BASIN-EDGE EFFECTS FROM SH-WAVE MODELLING WITH REFERENCE TO THE LOWER HUTT VALLEY, NEW ZEALAND

A thesis
submitted in partial fulfilment
of the requirements for the Degree
of
Doctor of Philosophy in Civil Engineering

by

Brian Mark Adams

Department of Civil Engineering
University of Canterbury
Christchurch, New Zealand

October 2000

ABSTRACT

A study is made of seismic wave propagation at the edge of sedimentary basins and valleys, and the subsequent amplification of earthquake shaking that occurs. The aim of this thesis is to determine the geological and seismic conditions that control the occurrence and nature of basin-edge effects.

In the first half of the thesis, elastic SH-wave propagation is investigated at the edge of a two-dimensional semi-infinite homogeneous layer above a homogeneous half-space, first with a geometrical ray-path and wavefront analysis and then with finite-element modelling of plane incident Ricker wavelets. It is shown that Love waves generated at an edge produce characteristic patterns of amplification across the layer in both the time and frequency domains. In addition, occurrences of localised amplification at the edge of the layer are categorised into three different classes based on their mechanisms of development. The *Airy-phase edge effect* occurs when the input frequency is close to the fundamental frequency of the layer; the *wedge effect* occurs above shallow sloping edges; and the *basin-edge effect* occurs above deep basins adjacent to steeply dipping edges.

The second half of the thesis makes a case study of seismic amplification and edge effects in the Lower Hutt Valley. It is found that the anti-plane seismic response is characterised by multi-dimensional resonance across the full width, and the basin-edge effect and strong differential motion adjacent to the vertically-dipping Wellington fault. Love waves generated at each edge are the primary cause of such spatially varying ground motions. Modelling results are compared with an analysis of weak ground motions recorded on a dense linear array of instruments across the fault-bounded edge of the valley. A high degree of similarity is found. Discussion is also made concerning the use of the two-dimensional elastic SH-wave analysis for predicting seismic response during strong ground shaking.

PREFACE

The author commenced research toward this thesis in March 1997. The majority of research has been carried out at the Department of Civil Engineering at the University of Canterbury under the supervision of Professor Rob Davis and Dr John Berrill, and Dr John Taber of the School of Earth Sciences at Victoria University of Wellington (now Senior Visiting Fellow at the University of Canterbury).

In October and November 1997 six weeks were spent using the finite-element computational package, Archimedes, at Carnegie Mellon University, Pittsburgh, PA. The work was supervised by Professor Jacobo Bielak in the Department of Civil and Environmental Engineering. Archimedes software was subsequently installed in the Department of Civil Engineering at the University of Canterbury.

Part of the research presented in this thesis was originally intended to be submitted in partial fulfilment of the requirements for a Master of Civil Engineering degree. This includes the bulk of Chapters 2, 3, 7 and 8, which were subsequently presented along with additional material as a University of Canterbury Civil Engineering Research Report to the EQC (Adams et. al., 1999).

A large section of work carried out but not presented in this thesis was a two-dimensional finite-element modelling study of the Aburrá Valley at Medellín, Colombia. The results are not directly related to basin-edge effects yet many of the ideas and methods developed during this study have been drawn on to understand the response of the Lower Hutt valley. The research, which took place between September 1999 and March 2000, has also been presented as a University of Canterbury Civil Engineering Research Report to the EQC (Adams et. al., 2000).

CONTENTS

ACKNOWLEDGEMENTS

This research was funded by the University of Canterbury and the Earthquake Commission of New Zealand (EQC).

Sincere thanks to my supervisors, Rob Davis and John Berrill, whom I have been very privileged to work with. Both these blokes have gone out of their way to throw opportunities and encouragement and comical stories my way. Kia ora, kia ora, kia ora koutou.

Thanks to John Taber (School of Earth Sciences, Victoria University of Wellington) who has played a crucial role with many discussions and idea-throwing sessions concerning seismic observations and modelling results in Lower Hutt. Thanks also to Neal Osborne and Emma Winthrop for their work collecting and processing the array data.

Thanks to Jacobo Beilak, Jifeng Xu (Department of Civil and Environmental Engineering, Carnegie Mellon University, Pittsburgh, PA.) and Dave O'Hallaron (Department of Computer Science, CMU) for their help with the Archimedes computation.

Thanks to Nick Perrin, Peter Wood, John Haines, Rafael Benites, Bill Stephenson and others at the Institute of Geological and Nuclear Sciences, Lower Hutt, for their useful discussions and help with collation of the geological data.

Thanks to many departmental staff, especially Brandon Hutchison and Melody Callaghan for their help with computing and graphics.

To an overwhelming number of office mates, flatmates, climbers, runners, general assorted friends, whanau, and of course the ever-present Big G; with whom I have shared countless adventures and kai-ups and campfires and all-nighters. May the adventure continue.

LIST OF NOTATION

α	Half phase-angle shift on total reflection
β	Shear wave velocity
β_1	Shear wave velocity of the layer or medium 1
β_2	Shear wave velocity of the half-space or medium 2
β^*	Dimensionless shear wave velocity
Δf	Frequency step
Δt	Time step
Δx	Displacement on total reflection
ε	Volumetric strain
ζ	Damping ratio
γ_0	Dimensionless velocity constant
γ_1	Dimensionless velocity term
γ_2	Dimensionless velocity term
η	Dimensionless frequency
η_c	Dimensionless Ricker wave central (characteristic) frequency
η_{cn}	Dimensionless cut-off frequency for n^{th} mode
θ	Angle of propagation
θ_c	Critical angle
$\theta_{E\text{-}max}$	Angle of max conversion to inhomogeneous energy
$\theta_1{}^b$	Angle of base-refraction
$\theta_1{}^{e1}$	Angle of edge-refraction by the direct wavefront
$\theta_1{}^{e2}$	Angle of edge-refraction by the downward-travelling wavefront
λ	Wavelength
λ_c	Ricker wave central wavelength
λ_n	Wavelength of the n^{th} mode Love wave
λ_{cn}	Cut-off wavelength of the n^{th} mode Love wave
μ	Shear modulus
μ_1	Shear modulus of the layer or medium 1
μ_2	Shear modulus of the half-space or medium 2
π	3.14159265358979
ρ	Bulk Density
ρ_1	Bulk Density of the layer or medium 1
ρ_2	Bulk Density of the half-space or medium 2
ψ	Edge-slope angle
ω	Circular frequency
ω_0	Reference circular frequency
ω_{cn}	Cut-off frequency for n^{th} mode Love wave
Ω_n	n^{th} mode dimensionless frequency
a	Rayleigh damping parameter
a_m	Haskell-Thompson transfer matrix for layer m
A	Combined Haskell-Thompson transfer matrix for all layers
A_1	Wave amplitude in layer 1
A_2	Wave amplitude in layer 2
A_i	Incident wave amplitude
A_{m}	Wave amplitude in half-space after the m^{th} reflection within the layer

b	Rayleigh damping parameter
B_{m}	Wave amplitude in layer after the m^{th} reflection within the layer
c	Phase velocity
c_x	Apparent horizontal velocity
c_z	Apparent vertical velocity
$c_x^{\,b}$	Apparent horizontal velocity of base-refracted wavefront
$c_x^{\,e1}$	Apparent horizontal velocity of first edge-refracted wavefront
$c_x^{\,e2}$	Apparent horizontal velocity of second edge-refracted wavefront
$c_z^{\,e1}$	Apparent vertical velocity of first edge-refracted wavefront
$c_z^{\,e2}$	Apparent vertical velocity of second edge-refracted wavefront
C	Global damping Matrix
C^e	Element damping Matrix
E	Energy content
EN	Edge normal
EP	Edge parallel
f	Frequency
f_0	1-D resonant frequency of the fundamental mode
f_c	Ricker wave central (characteristic) frequency
f_{cn}	Cut-off frequency of the n^{th} higher mode
f_n	1-D resonant frequency of the n^{th} higher mode
f_{mn}	2-D resonant frequency
F	Fourier transform
F	Ratio of incident energy made inhomogeneous
FN	Fault normal
FP	Fault parallel
FSR	Fourier spectral ratio
h_n	Layer n thickness
H	Fourier transfer function
H	Layer thickness
i	Impedance ratio
k	Wavenumber
K	Global stiffness matrix
K^e	Element stiffness matrix
L	Valley width
M	Global mass matrix
M^e	Element mass matrix
PGA	Peak ground acceleration
PGD	Peak ground displacement
PGV	Peak ground velocity
Q	Damping quality factor
R	Rate of energy travel
t	Time
t^*	Dimensionless time
t_c	Time of constructive interference at the surface
t_m	Time that wavefront touches basement after m reflections
t_r	Time between Ricker peaks
t_{r1}	Time that direct wavefront reaches lower vertex
t_{r2}	Time that reflected wavefront returns to lower vertex
t_{S1}	Shear wave travel time in soil
t_{S2}	Shear wave travel time in rock
$t_{SR,r}$	Surface arrival time of the r^{th} reflection from the base
u	In-plane displacement in the x-direction
U	Group velocity
v	Anti-plane displacement in the y-direction
$\dot{v}$	Anti-plane velocity

$\ddot{v}$	Anti-plane acceleration
v_n	n^{th} mode Love wave displacement
v_{mn}	2-D resonant mode displacement
w	In-plane displacement z-direction
x	In-plane horizontal coordinate
x^*	Dimensionless x-coordinate
x^c	Position of constructive interference on the surface
$x_r^{\,c}$	Position of constructive interference by r^{th} reflection
$x_{nm}^{\,c}$	Position of multiple constructive interferences for harmonic input
x^b	Position of base-refracted wavefront at the surface
x^{e1}	Position of 1st edge-refracted wavefront at the surface
x^{e2}	Position of 2nd edge-refracted wavefront at the surface
$x_{mi}^{\,E}$	i^{th} extremum point of the m^{th} horizontal mode resonance
$x_{ni}^{\,E}$	i^{th} extremum point of the n^{th} mode Love wave
$x_{mi}^{\,N}$	i^{th} nodal point of the m^{th} horizontal mode resonance
$x_{ni}^{\,N}$	i^{th} nodal point of the n^{th} mode Love wave
y	Anti-plane horizontal coordinate
z	In-plane vertical axis (elevation)
z^*	Dimensionless z-coordinate
∇^2	Laplacian operator

PART I

PRELIMINARIES

Chapter 1: INTRODUCTION

Edge effects, in the genre of engineering seismology, is a term given to the amplification of seismic energy at the margins of sedimentary deposits. Their importance is apparent in the aftermath of recent major earthquakes such as Northridge (1994) and Kobe (1995) where anomalously severe damage occurred on deep soft sediments adjacent to a basin edge.

In the recent years following the Kobe and Northridge events, a significant amount of research in the form of numerical modelling has been made to simulate the strong basin-edge amplification. While many different mechanisms (including focussing, surface wave action, constructive interference, and resonance) were ascribed as physical causes of such amplifications, the most convincing and universally accepted result of these studies is that both basin-edge effects developed by constructive interference between edge-generated surface waves and the delayed direct arrival through the sediments.

The existence of a deep fault-bounded edge in the Lower Hutt sedimentary valley in New Zealand prompted the initiation of this research. It was obvious that given the physical similarities between Kobe (Figure 1.1) and Lower Hutt (Figure 1.2), the possibility of a similar damaging basin-edge effect exists in the latter. After some preliminary finite-element modelling of wave propagation within the geological structure of the Lower Hutt valley, it became clear that there was a lack of physical understanding of the processes associated with basin-edge effects. For this reason it was difficult to predict the likely occurrence or characteristics associated with a possible basin-edge effect in the Lower Hutt or indeed any other location.

1.1 HYPOTHESIS

Although the basic mechanism of basin-edge amplification is clear, there are still notable uncertainties as to its details, especially with regard to the frequencies involved, the geological and seismic source conditions that are required and its relationship with other basin effects. It is thus the aim of this research to begin to answer these questions, to develop an understanding of when and where damaging edge effects may occur, and of the

magnitude and characteristics of the associated amplification. It is hoped that a comprehensive physical understanding of the edge effects will lead toward the effective prediction of seismic shaking at basin margins.

Figure 1.1. Kobe is built on a 900m-deep sedimentary basin adjacent to the granitic Rokko mountains. The Rokko fault system runs along the foot of the mountains. Photo courtesy of John Berrill.

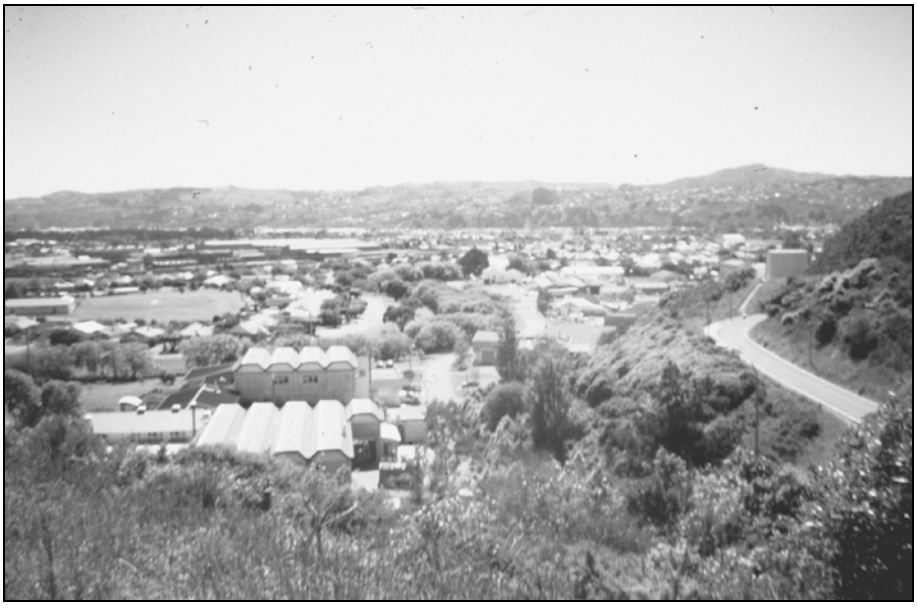

Figure 1.2. Lower Hutt City lies on a 300m-deep sedimentary valley, bounded on the far side by the near-vertical dip of the Wellington fault.

1.2 BACKGROUND

Sub-surface geological irregularities of any kind have the effect of locally distorting the incoming wave field by processes such as bending, scattering and focussing. Such distortions are generally called site effects and are often as, if not more, important than the source processes. Soft sedimentary deposits in particular have the effect of both amplifying and trapping seismic energy by internal reflections. When such sediments are laterally confined by a more rigid basement rock as in an alluvial basin or valley, the seismic behaviour becomes highly multi-dimensional. Interaction of the incoming wave field with the basin edges generates horizontally-propagating surface waves which subsequently reflect back and forth across the width of the basin and significantly increase the duration of shaking. The lateral confinement also gives rise to multi-dimensional modes of frequency-dependent resonance.

The study of edge effects is strongly tied to that of the seismic response of soft sedimentary valleys and basins. There is a strong interaction between the behaviour of a basin as a whole and the behaviour of sediments near the edges, especially for basins where the dimensions are of similar magnitude to the wavelength of seismic motion. Edge-effects are in general associated with the edge-generated surface waves which develop at lateral discontinuities in material properties. The resultant dispersive surface waves (Rayleigh and Love waves) travel at a frequency dependent velocity due to a post-critical and complex interaction at the base of the sediments.

While it has been clearly shown that edge effects are a reality and are able to be successfully modelled after they occur, it is the goal of the engineering seismologist to be able to predict such anomalous amplification so that appropriate measures may be taken to guard against foreseeable disaster. Such a goal necessitates both an understanding of the physical processes associated with edge effects, as well as the ability to be able to fit them together and forecast the likely response.

Recent exponential growth in information technology and data handling capabilities have begun to make possible the modelling of complex physical processes. The nature of computational modelling, however, requires that an outer boundary must be defined at one end, and a limiting resolution at the other. It is only possible to include a finite number of the determining physical processes and relationships in any model or interlinking set of

models. The modelling undertaken in this study is limited at the upper end by computational capabilities to a local boundary in the order of several kilometres, not much larger than the sedimentary deposit, while at the lower end to a resolution of several metres defined by available geological information.

1.3 SCOPE

Research presented here falls within the field of study of seismic site effects, in particular concerned with the amplification of seismic waves at the edge of sedimentary deposits. It aims to understand the physical mechanisms involved in the edge-amplification process in the hope of being better able to predict zones where there is a risk of anomalously strong shaking.

A multi-faceted approach is taken to understanding edge effects, beginning in Part II with a simple geometrical analysis of plane-wave propagation at the edge of a semi-infinite layer. The dispersive mechanisms of diffraction and total reflection that necessarily develop at such a discontinuity later require the use of approximate numerical techniques to continue the analysis. Plane wave propagation at the edge is then investigated with the help of finite-element methods.

In Part III the finite-element method is again employed to investigate the seismic behaviour of the Lower Hutt sedimentary valley. The surface response of the model is compared with an analysis of weak ground motions recorded on a linear seismic array across the fault-bounded edge of the valley. Ideas developed in the analysis of the semi-infinite layer in Part II are drawn on to explain the observations and modelling results in Lower Hutt.

For mathematical simplicity, the geometrical analysis and finite-element modelling is limited to two dimensions, and to anti-plane particle motion. This confines the study to that of horizontally-polarised shear waves (SH-waves) and Love waves, not considering the in-plane motions associated with SV, P and Rayleigh waves. We thus consider only the case of the SH-Love-wave-controlled basin-edge effect, although its application to understanding basin-edge effects in general is possibly quite significant.

With two-dimensional modelling of wave propagation in a cross-section aligned perpendicular to the valley or basin edge, the in-plane (P-SV and Rayleigh) waves form the

edge-normal (EN) and vertical components of motion, whilst the anti-plane (SH and Love) waves form the edge-parallel (EP) component. In the common case of the edge being formed by a steeply dipping fault, the components are often referred to as fault-normal (FN) and fault-parallel (FP). In this thesis, the terms EP and EN will be used in an attempt to distinguish basin-edge effects as *site* effects, whereas FP and FN are terms referring to the source.

Seismic source effects and source-to-site propagation effects are (along with site effects) fundamental to the ground motion felt at a given site. Given the generally close proximity of earthquakes capable of generating strong ground motion, the teleseismic source-to-site propagation effects fundamental to the study of global seismology are generally insignificant, whereas the nature of the source mechanism is of central importance to defining the characteristics of the incoming wave field. Such source effects are not explicitly studied, yet a discussion of their ability to influence edge effects is made in Chapter Eleven.

Research is limited to a linear elastic ground response. Numerical modelling is based on linear stress-strain models. In addition, the weak ground motions recorded in Chapter Nine are all assumed to have produced an elastic response in the near-surface geology. The significance of non-linear material behaviour is discussed at the end of Chapter Ten.

While this thesis is primarily concerned with understanding the nature of seismic amplification at the edge of sedimentary deposits, we have concurrently discussed two additional topics. The first of these is Love wave generation and propagation at the edge of a semi-infinite layer, and the second is multi-dimensional resonant effects in enclosed basins. Both topics are in every way linked with edge effects and while at times they may appear like padding to the primary thesis, their understanding has been fundamental to that of edge effects. As such, a good proportion of the literature review in Chapter Two is devoted to multi-dimensional basin effects, while Love-waves and SH-wave propagation in general are extensively reviewed in Chapter Four. On the same note, significant discussion has been made concerning Love wave propagation some distance from the edge in Chapter Six, and in Chapters Eight and Ten we concurrently present results both just at the edge and across the whole valley.

1.4 THESIS OUTLINE

The thesis has been divided into four parts. Part I (Chapters 1, 2 and 3) presents preliminary information on related research and computational methods. Part II (Chapters 4, 5 and 6) presents an analysis of SH wave propagation at the edge of a semi-inifnite homogeneous layer, the simplest of basin-edge geometries. Part III (Chapters 7, 8, 9 and 10) makes a case study of the Lower Hutt valley, and investigates the possibility of a Kobe-like basin-edge effect adjacent to the fault-bounded edge. Finally, in Part IV (Chapters 11, 12 and 13), the observations and ideas developed in Parts I, II and III are discussed with the express intent of shaping them into a useful form for practitioners and researchers.

Chapter 2: LITERATURE REVIEW

While the bulk of this Chapter is devoted to a discussion of current literature concerning basin-edge effects, we can not bypass the issue of the seismic response of the whole basin. For this reason, an overview of the huge amount of literature on basin site response is presented as an introduction to edge effects. Details are provided on the subject of two-dimensional basin-resonance that will be drawn on in later chapters.

Several other literature reviews are made in later chapters. Chapter Three contains a brief overview of the various numerical techniques that are used in wave propagation studies. Chapter Four provides a review of SH wave propagation in homogeneous structures as an introduction to the analysis in Part II. In Chapter Seven we discuss current literature concerning geology, earthquake hazard and seismic site response studies that have been made in the Lower Hutt valley and greater Wellington region.

2.1 SEISMIC RESPONSE OF SEDIMENT-FILLED BASINS

Sedimentary basins have received a lot of attention in recent years, as more and more examples of damage by strong shaking within such structures have come to light and as computers have become more accessible and powerful as a tool for modelling large-scale ground motions. Much of the earliest work on basin response was analytical in nature with exact and approximate solutions to displacement response in the time-domain being found for several simple basin-configurations. These solutions (eg. Trifunac, 1971) are still widely used for checking the accuracy of numerical schemes.

The most significant numerical work in basin response in the time-domain is generally accredited to Bard and Bouchon (1980a,b) who used a two-dimensional Aki-Larner technique (Aki and Larner, 1970) in the time-domain to study several hypothetical basins of simple geometrical shape. They showed that local surface waves are generated at the edge of basins and propagate back and forth to produce a response of both high amplification and long-duration. They also demonstrated that for the case of incident SH waves, Love waves (Love, 1911) are produced; and for incident SV or P waves, Rayleigh waves (Rayleigh, 1885) are produced from the basin edge.

Good overviews of basin response and various techniques that have been used in the analysis thereof may be found in Sanchez-Sesma (1987), Aki (1988, 1993), Bard (1994), Bouchon (1995), Graves and Sommerville (1995), Kazuyoshi (1995), Hisada and Yamamoto (1996), Sanchez-Sesma et al. (1996), Rassem et al. (1997) and Bielak et al. (2000).

2.1.1 MULTI-DIMENSIONAL BASIN RESONANCE

When a basin is bounded by bedrock on two opposing sides such as in a valley, it may develop modes of resonance not just with depth but also in the horizontal orientation. This will occur when the incoming seismic energy and the subsequent wave fields that reflect around inside the basin are able to excite it at the appropriate frequency. A significant amount of analytical work has been done to determine the eigenfrequencies and mode shapes of such resonant motions, while the results have been verified by various numerical methods and limited observation. Good overviews on problems of basin resonance are given in both Rial and Ling (1992) and Wirgin (1995).

A closed form exact solution to the anti-plane displacement field of a two-dimensional semi-circular valley within a homogeneous elastic half-space was found by Trifunac (1971). While he did not specifically define the response as resonant in nature or find the associated resonant frequencies they have been recently derived by Wirgin (1995). The cylindrical semi-circular basin problem is of unique canonical value in that it has an exact solution for an open system (ie. the displacement field of both the soft inclusion and the half-space). Wong and Trifunac (1974) later extended the original theory to a 2-D basin of semi-elliptical shape yet were unable to derive a closed form solution. Sánchez-Sesma and Esquivel (1979) present a method for computing the anti-plane response of various other shapes including triangles and sine-shapes.

Bard and Bouchon (1985) investigate the resonant response of sine-shaped 2-D valleys using the Aki-Larner technique for both in-plane (P-SV) and anti-plane (SH) motion. In the course of their investigation they derive an exact solution to the anti-plane resonant frequencies of a 2-D rectangular basin within a rigid half-space. Such a soft inclusion within a rigid half-space is often referred to as a Helmholtz resonator, which is essentially a closed system (no leakage of energy into the surrounding medium). The Helmholtz

resonant frequencies may thus be used to approximate real open systems where the velocity contrast between the inclusion and half-space is high.

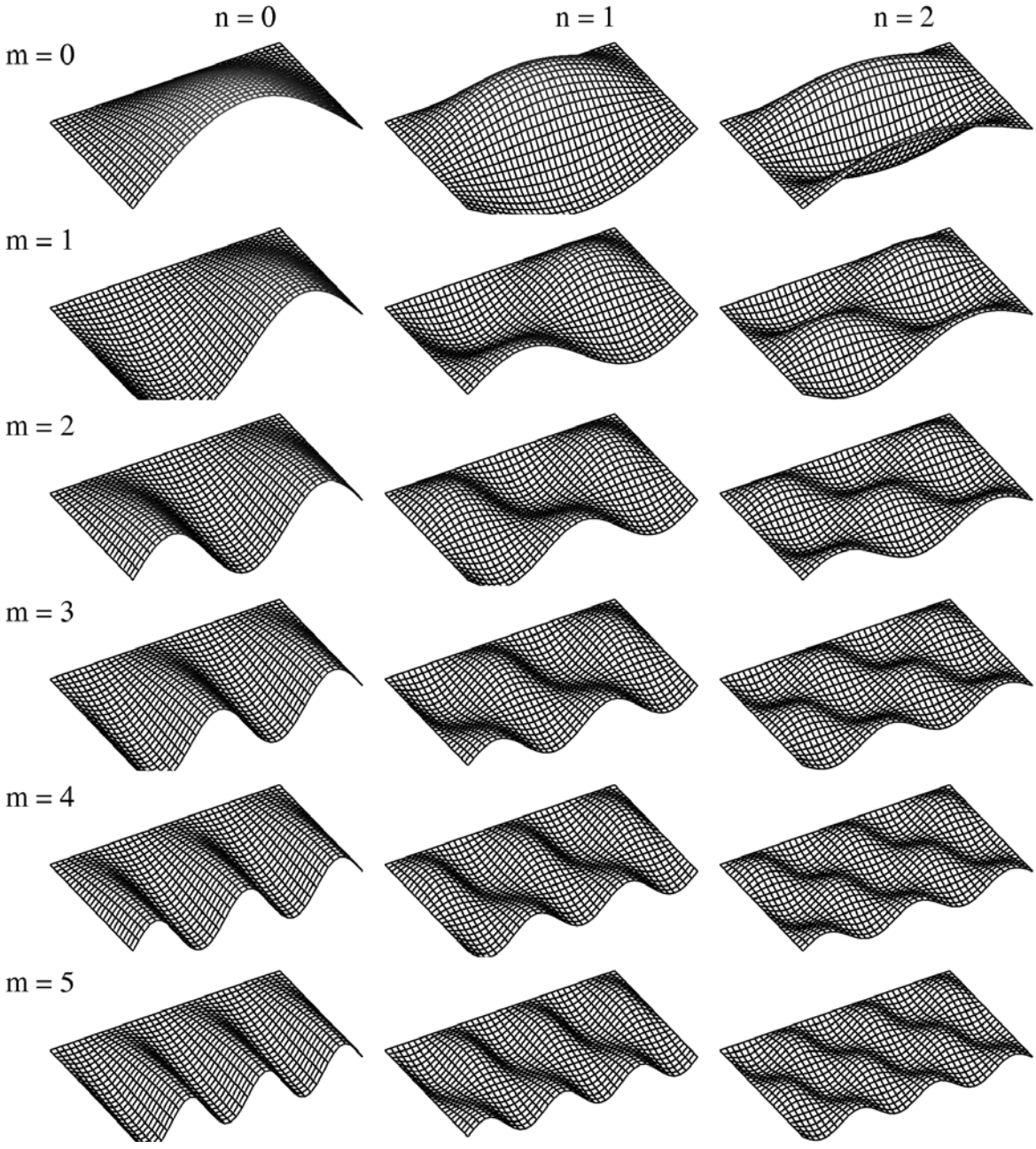

Figure 2.1. Anti-plane modeshapes, v_{nm}, of two-dimensional resonance in a rectangular cross-section bounded on three sides by a rigid basement. Each cross-section is aligned so that the unbounded (free) surface is on the lower right, with depth increasing toward the top left of the figure. The first three vertical (*n*) modes are shown, each with the first six horizontal (*m*) modes.

The analytical solution of Bard and Bouchon for the anti-plane eigenfrequencies of the rectangular Helmholtz resonator may be expressed by

$$f_{nm} = \frac{\beta}{4H}\sqrt{(2n+1)^2 + (m+1)^2\left(\frac{2H}{L}\right)^2} \qquad n,m = 0,1,2,...\infty \qquad [2.1]$$

where H is the valley depth, L is the width, β is the shear wave velocity of the elastic inclusion, and f_{nm} is the eigenfrequency corresponding to the n^{th} vertical eigenmode and m^{th} horizontal eigenmode. Thus eigenfrequencies are a function only of the valley dimensions and sediment shear velocity. In the limit as $L \to \infty$, the solution reduces to that of one-dimensional vertical resonance of anti-plane (SH) ground motion in an infinitely wide and uniform soft layer, given by (Haskell, 1960).

$$f_n = \frac{\beta}{4H}(2n+1) \qquad n = 0,1,2,...\infty \qquad [2.2]$$

Bielak et al. (1999) helps explain the physical nature of the 2-D rectangular solution, which may be visualised by the displacement associated with each anti-plane resonant modeshape, $v_{nm}(x,z)$, given by

$$v_{nm}(x,z) = \sin\frac{(2n+1)\pi z}{2H}\sin\frac{(m+1)\pi x}{L} \qquad n,m = 0,1,2,...\infty \qquad [2.3]$$

where the origin of the x-z coordinate system is the lower left corner of the cross-section, z is measured vertically up and the x-axis is horizontal. These modeshapes have been plotted in Figure 2.1. For each vertical mode, n, there exists a set of m horizontal modes. The ground surface response for an input frequency, f_{nm}, will have m+1 extremum (E) points and m+2 nodal (N) points. The x-position (across the valley) for each is given by (Bielak, et al., 1999)

$$x_{mi}^{E} = \frac{2i+1}{2(m+1)}L \qquad i = 0,1,2,...m \qquad [2.4]$$

$$x_{mi}^{N} = \frac{i}{m+1}L \qquad i = 0,1,2,...m+1 \qquad [2.5]$$

where L is again the valley width. Each point on Figure 2.2 represents an extremum (crest or trough) or a nodal (zero displacement) point in the mode shape expression on the surface. If the input contains a range of frequencies, we would expect the surface response (in the frequency-domain) to exhibit a pattern of extremum points as shown, with each higher vertical mode (and corresponding set of m horizontal modes) overlaying the

previous vertical mode set. Thus the higher the frequency, the more complex the mode shape. Extremum points and nodal points for each vertical set lie on a distinctive set of curves. Bielak et al. (1999) uses the terms extremum line and nodal line to describe them.

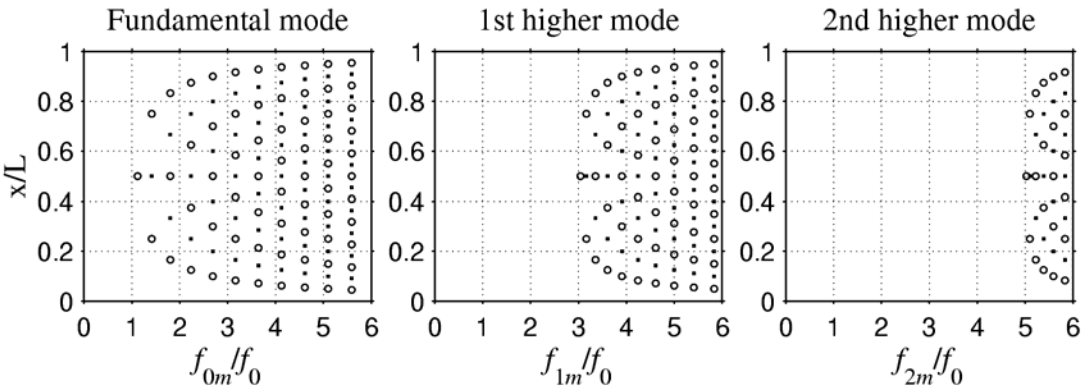

Figure 2.2. Theoretical resonant response of a dimensionless rectangular cylindrical valley set in a rigid half-space. Locations of extremum points (crests and troughs) are marked with an open circle, nodal (stationary) points are marked with a small dot (after Bielak et al., 1999).

Ling and Rial (1994) later use the Einstein-Brillouin-Keller (EKB) method borrowed from quantum physics, along with a local wedge approximation (LWA) to determine resonant frequencies at particular locations in Helmholtz (rigidly bounded) basins of various shapes. The method was then validated with a finite-element method with excellent results, and again validated with a boundary element method by Kouoh-Bille and Wirgin (1995).

Resonant responses of 3-D basins are much more complex. Rial (1989a) draws on early mathematical work by Keller and Rubinow (1960) and Weinstein (1969) to develop approximate solutions to resonant frequencies occurring near the centre of 3-D semi-ellipsoidal basins, surrounded below by a rigid half-space (a 3-D Helmholtz resonator). Rial uses a WKB solution to the wave equation and an asymptotic method that only holds at high frequencies. The solutions reduce to 2-D (cylindrical) shapes and the flat-layer case at the appropriate limits. Rial (1989b) discusses unstable and chaotic modes of resonance that also occur within 3-D basins. In a later paper Rial and Ling (1992) compare the 2-D anti-plane (SH) case of their analytical solutions to the numerical results of finite element modelling, with varying success.

Rodríguez-Zúñiga et al. (1995) consider the 2-D rectangular Helmholz resonator of Bard and Bouchon (1985) and derive an exact solution to the total anti-plane displacement field due to a moving rigid base. Making several approximations that are later validated with rigorous numerical solutions, Rodríguez-Zúñiga et al. then extend their solution to 3-D open-system configurations subject to oblique incidence and find substantial differences between the 2-D and 3-D basin response. Various other authors have studied the 2-D and 3-D resonant response of sediment-filled basins including Zhou and Dravinski (1994) with an eigenvalue and spectral search method who found that resonant frequencies are indeed independent of the impedance contrast, an assumption made by Bard and Bouchon (1985).

Stephenson (1974, 1975) has made observations of ground motion in the Lower Hutt Valley, New Zealand, which suggest the action of horizontal resonant modes of response in the valley. He proposes that this "directed resonance" is directed by the shape of the valley rather than the orientation of incoming wave fields. In a later paper, Stephenson (1989a) develops a solution for the resonant frequencies associated with a "cellular mode resonant response" of a 3-D cylindrical inclusion in a rigid or elastic half-space. The equation reduces to the 2-D rectangular case of Bard and Bouchon (1985) in the appropriate limit.

Other observations by King and Tucker (1984) and Tucker and King (1984) in the Chusal valley, Califiornia, found that valley response was strongly dependant on the input signal's frequency and the cross-valley position, indicating some form of 2-D resonance. Seligman et al. (1989) develops a solution for a Helmholtz equation with boundary conditions approximating the soft clay region within Mexico City and finds a frequency-dependent pattern of anti-nodal points that supposedly match damage zones in downtown Mexico.

2.1.2 NUMERICAL STUDIES ON THE RESPONSE OF HYPOTHETICAL 2-D AND 3-D BASINS

Since the foundational work of Bard and Bouchon (1980a,b), a large variety of numerical techniques have been used to investigate both the 2-D and 3-D seismic response of valleys and basins of various shapes, generally in the time-domain. Such non site-specific studies have been made with the source method (Dravinski, 1982a,b,c), the indirect boundary integral method (Dravinski, 1983), ray methods (Sánchez-Sesma et al., 1988a), boundary methods (Bravo, et al., 1988, 1989; Chávez-Pérez et al, 1989), the discrete wave-number

method (Sánchez-Sesma et al., 1989) the discrete wave-number boundary element method (Kim and Papageoriou, 1993; Papageoriou and Pei 1994), boundary-integral methods (Luco and De Barros, 1995), combined boundary-integral and finite-element methods (Bouden et al., 1989; Khair et al., 1989, 1991; Zeng and Benites, 1998), finite-element methods (Luokakis and Bielak, 1995), boundary-element methods (Shibuya, 1992; Pei and Papageoriou, 1993; Sánchez-Sesma et al., 1993; Takemiya and Fujiwara, 1994; Ahmad et al., 1995) and the weighted residual method (Manoogian and Lee, 1995). Various results highlighted by these works are referred to in later chapters.

2.1.3 SITE RESPONSE STUDIES AND NUMERICAL MODELLING OF ACTUAL SEDIMENTARY BASINS AND VALLEYS

The seismic response of many different sedimentary basins around the world have now been analysed with the help of numerical modelling. Some of these studies have attempted to simulate strong ground motions recorded during notable earthquakes, while the results of other studies have been matched against weak motions or noise recordings. One of the earliest studies of this type was made by Seed et al. (1970) who used a 2-D elastic finite-element method to investigate the response of the Caracus basin, Venezuela, to explain spatially-variable damage noted during the 1967 earthquake. The same basin has more been recently studied by Semblet et al. (1999) who found a clear two-dimensional pattern of amplification in their modelling.

Similar two-dimensional analyses have been made of the soft basin in Mexico City to understand the cause of strong shaking during the 1985 Michoacan Earthquake (eg. Sanchez-Sesma et al., 1988b; Kawase and Aki, 1989), the San Fernando Valley during the 1971 San Fernando (Vidale and Helmberger, 1988) and 1994 Northridge (Pitarka and Irikura, 1996) earthquakes, the Los Angeles Basin during the 1994 Northridge earthquake (Schrivner and Helmberger, 1994; Graves, 1995; Pitarka and Irikura, 1996), the Coachella Valley, California, during the 1992 Landers/Big Bear aftershock sequence (Field, 1996), the La Molina Valley, during the 1974 Lima, Peru earthquake (Espinosa et al., 1977; Zahradnik and Hron, 1987), the Kanto Basin, Japan during the 1984 Nagano earthquake (Yamanaka et al., 1989), the Ashigara Valley, Japan during the 1990 Odwara earthquake (Pitarka et al., 1994, 1996b), and Kirovakan, Armenia, during the 1988 earthquake (Bielak et al., 1999). Both Zhang and Papageogiou (1995) in a study of the of the highly 3-D Marina District, San Francisco, and Pitarka et al. (1994) for the Ashigara Valley conclude

that a far more computationally efficient 2-D model, despite its shortcomings, is very useful for estimating ground motions for engineering considerations.

More recently, three-dimensional simulations of basin response from Californian earthquakes (Frankel and Vidale, 1992; Frankel, 1993a,b; Graves, 1993; Olsen and Archuleta, 1996) have been made using the finite-difference method and a double-couple point source to combine the effects of a fault rupture into in a three-dimensional velocity model. Other 3-D studies have been made in the San Fernando Valley with a finite-element method (Bao et al., 1998) and the Kanto Basin, Japan, with the Gaussian beam method (Kato et al., 1993) and the boundary-element method (Hisada et al., 1993).

2.2 BASIN-EDGE EFFECTS

The literature is full of observations of amplification or intense damage at basin margins. Historically, there are sketchy reports in Prescott (1982) for the 1868 California earthquake and Weischet (1963) for the city of Valdivia during the 1960 Chile earthquake, which describe occurrences of basin-edge effects. Moczo and Bard (1993) mention bands of intense damage adjacent to geologic lateral discontinuities from the 1909 France, 1979 Montenegro (Italy) and 1980 Irpinia (Italy) earthquakes. Other occurrences of bands of damage along basin edges have been reported following the Skopje, Yugoslavia earthquake of 1963 (Poceski, 1969), the Miyagiken-Oki, Japan earthquake of 1978 (Kubo and Isoyama, 1980) and the Shidian basin (China) during the 1976 Longlin earthquake (Yuan et al., 1992).

The 1995 Hyogo-ken Nanbu earthquake which devastated Kobe, Japan, and surrounding cities was characterised by a narrow band of intense damage about 0.8 to 1.0 km south of the Rokko fault system, a strong lateral discontinuity between granitic bedrock and deep Pliocene and Pleistocene sediments of Osaka Bay. The band of intense damage extended parallel to the fault for some 30km between Kobe and Nishinomiya (Finn et al., 1996; Park et al., 1995). A similar band of intense damage was found some distance out from the Santa Monica Mountains in Los Angeles following the 1994 Northridge Earthquake on a blind thrust fault 20km north of the site (Gao et al, 1996).

2.2.1 THE "BASIN-EDGE EFFECT"

Kawase (1996) hypothesised that amplification causing the damage belt in Kobe was due (at least in part) to constructive interference between horizontally propagating Rayleigh waves and the direct shear wave propagating vertically through the sediments a short distance away from the basin edge, a phenomenon he subsequently termed the "basin-edge effect". The waves from a rupture at depth reach the ground surface earlier through the rock and generate surface waves that travel across the basin. For the case of Kobe, the surface wave had travelled a horizontal distance of 0.8-1.0km before the direct shear-waves arrived through the sediment. Kawase (1996) used a finite-element method to analyse a two-dimensional velocity model of the deep Osaka basin and bounding bedrock to substantiate his hypothesis.

Motosaka and Nagano (1995, 1996, 1997) made a similar 2D analysis of in-plane propagation within the deep underground structure. Their conclusions are very similar to those of Kawase (1996), finding the zone of greatest structural damage to coincide with interference between horizontally propagating Rayleigh waves and vertical shear wave arrivals (the fault-normal component). Similar but smaller peak ground motions were also found in the vertical component, closer to the basin-edge. Motosaka and Nagano referred to the phenomenon as 'a focussing effect, in its broadest sense'. Higashi (2000) shows the same phenomena of constructive interference with a time-domain pseudospectral method.

Graves et al. (1998) identify the band of damage found in Santa Monica following the 1994 Northridge earthquake as an example of this same basin-edge effect. The damage occurred just south of the 3km deep, complex basin-edge structure formed by the actively thrusting strand of the Santa Monica Fault. They use a 2-D finite difference method to calculate the P-SV and SH wave responses in the damaged area. Results show conclusively a peak in displacements some 2km south of the fault trace. They point out that the variety of building types damaged may indicate a broad-band nature in the amplification, suggesting that it may be due to interference between the short-period direct body waves and the longer-period basin-generated surface waves.

Several other researchers have attempted to explain the damage concentrations in Kobe and Santa Monica by various other mechanisms. Gao et al. (1996) describe the damage in Santa Monica as a result of focusing of waves by the deep basin structure, similar to the

focusing effects apparent in Sherman Oaks (Hartzell et al., 1997) during the same earthquake. The lens-like deep basin model proposed by Gao et al. (1996) and Hartzell et al. (1997) is certainly capable of focusing amplifying the high frequency ($f > 2$Hz) ground motions in Santa Monica, yet is apparently inconsistent with the known sub-surface geological structure in the area (Graves et al., 1998). Alex and Olsen (1998), with a 2-D finite-difference model, also dismiss focussing as the primary cause of heavy damage in the area and suggest the action of the constructive basin-edge effect.

Takemiya and Adam (1996) use a 2-D linear finite-element and boundary-element method to model the top 20m or so of soft sediments in order to explain the damage belt in Kobe. Although the paper suggests a similar mechanism to the basin edge effect, which they call the "bump effect", their simulation results fail to show it occurring in the location of the disaster zone. Their idea of surface wave propagation in the soft layer has also been discounted on the grounds of non-linear behaviour by Kawase (1996). Adam and Takemiya (1997) later make a non-linear analysis that 'adequately approximates the response within the disaster belt'.

Inoue and Miyatake (1997) investigated the effect of rupture directivity as the cause of the damage belt in Kobe. They simulated ground motions up to 1.0Hz with a 3-D finite difference method incorporating a dynamic fault model, and demonstrated how directivity alone can account for a band of damage along the basin edge. It is found that this only occurs when the correct fault and basin-edge configuration exists, as it does in Kobe. Pitarka et al. (1997) have since termed this type of amplification the 'guided directivity effect'. Although admitting the influence of constructive interference effects (Kawase, 1996) and possible focusing effects, Inoue and Miyatake (1997) assert that rupture directivity is a necessary condition for the basin-edge effect observed in Kobe, an assertion that is strongly refuted by Kawase et.al. (1997).

Defining 'The Basin-Edge Effect'

In light of these differing views on the cause of the observed damage belts, the question arises as to whether the basin-edge effect is a phenomenon associated solely with strike-slip ruptures on basin-bounding faults – as observed in Kobe – thus insinuating rupture directivity as a necessary causal-mechanism of the basin-edge effect. The implications of this question are significant, as many sedimentary basins and valleys – while not bounded

by active strike-slip faults – may still be capable of exhibiting the basin-edge effect during ground shaking. The observation of a damage belt in Santa Monica hints that perhaps the basin edge is indeed a more general phenomenon, capable of occurring in a far-field situation, so long as the necessary basin-edge properties exist.

While Inoue and Miyatake (1997) are undoubtedly correct to consider rupture directivity as a causal factor of the damage concentration in Kobe, it is not a fundamental or necessary condition for the development of a band of damage, as has been reasoned by several authors. Kawase et al. (1997) use a 3-D finite difference scheme to show that for three different types of input (a plane SV wave, a point dislocation and a radially ruptured fault), the spectral ratios show the same characteristics, thus implying that the relative amplification caused by the basin-edge effect is independent of the incident-wave field. Observations of the basin-edge effect within aftershock array records in Kobe (Pitarka et al, 1996a, 1997), and outside the zone of forward directivity in Santa Monica (Graves et al., 1998) also imply its independence from the source process.

The case for the cause of the damage belt in Kobe is summed up well by Pitarka et al. (1998) who use a 3-D finite difference method to model FN, FP and vertical components under the action of a kinematic rupture on a fault bounding the Osaka Basin in Kobe. They found the near-source ground motions to be controlled firstly by source radiation and rupture directivity effects. Close to the fault on a weathered rock site, the ground motion at Kobe University (KBU) is characterised by two distinctive low-frequency pulses in which FN components dominate over FP components. This directivity-controlled ground motion was then essentially the input to the deep basin structure, and was subsequently amplified by the basin edge effect. Hence the damage zone in Kobe was primarily caused by fault-normal high-amplitude long-period pulses, a coupling of both source and basin-edge effects.

Kawase et al. (2000) present the most comprehensive analysis of strong ground motion for the Kobe earthquake to-date. They use a 3-D geological structure and a heterogeneous-slip rupture model to show the belt-like damage zone identified by amplified peak ground velocities. They then calculate the response of the model without the influence of edge-generated surface waves (achieved by suppressing the direct shear waves in the rock) and find that amplified PGV's in the damage belt effect do not occur; thus showing the critical nature of the surface waves in generating the basin-edge effect.

The basin-edge effect is thus, as initially defined by Kawase (1996), purely a multipathing effect, caused by the constructive interference between direct body waves and basin generated surface waves. It is a local phenomenon, completely independent of the rupture process. Other factors such as focusing, soft-sediment amplification, directivity in general and the guided-directivity effect may enhance the amplification produced by the basin-edge effect, yet are not causes of it. This above definition of "the basin-edge effect" will be assumed hereinafter.

Additional Research on the Basin Edge Effect in Kobe

Later studies have attempted to further characterise the mechanism of the basin-edge effect in Kobe. Nagano (1998) use the so-called Thin Layer Method (TLM) to determine the type of surface wave involved in the constructive interference effect at Kobe. The TLM allows decomposition of the wave field into surface waves and body waves. Nagano shows that the first three modes of the Rayleigh wave are the strongest, and are excited in the neighbourhood of their respective Airy phases. He concludes that the 2nd-higher mode Rayleigh wave contributes the most to the basin-edge effect, while the 1st-mode travels too slow to make a significant contribution. Maruo et al. (1998) look at spectral amplifications in aftershock records of the 1995 event and conclude that within the disaster belt the motion is characterised by wider-band frequency amplification than other areas.

The number of strong ground motion studies in the Kobe area increased dramatically after 16 different research groups agreed to take part in a simultaneous simulation of the Hyogo-ken Nanbu earthquake and aftershocks (Kawase and Iwata, 2000). These studies included both 3-D (eg. Hisada, et al. 1998) and 2-D numerical modelling. The results were of varying accuracy when compared both against observed ground-motion and against each other, the differences being larger when the modelling was performed blind (without knowledge of observed data).

2.2.2 EDGE EFFECTS NOTED IN NUMERICAL MODELLING

Prior to the recognition of its cause, several modelling studies have given results that suggest the action of basin-edge effects. Seed et al. (1970) use a 2-D finite-element method in order to explain the unusual damage distribution that occurred during the 1967 Caracus earthquake, Venezuela, and find variably-amplified peak ground motions across the width

of the valley with the highest peaks occurring near the edges. Vidale and Helmberger (1988) using a 2-D elastic finite-difference method attributed amplification at the edge of the San Fernando Valley to the action of edge-generated waves. Larkin and Marsh (1991) found that amplification effects were most significant at the valley edges by 2-D non-linear finite difference modelling of idealised basins. Sanchez-Sesma and Luzon (1995) using a 3-D boundary-element method noted very large amplification of incident SH waves and attributed it to the 'constructive interference of various refracted waves'. Pitarka et al. (1994, 1996b) found amplification at the basin edge for incident SH waves using a 2-D elastic FDM to approximate 3-D wave propagation from a double-couple point source in the Ashigara Valley during the 1990 Odawara (Japan) earthquake. They attributed the amplification to the basin structure. Pitarka and Irikura (1996) with a similar 2-D elastic FDM and double-couple point source found amplification along the northern edge of the Los Angeles basin during the 1994 Northridge earthquake, and accredited it to constructive contributions from both site effects and source processes.

Niousha and Motosaka (1998) noticed strong directionality in a sediment-site record in Hachinohe City from the 1994 Sanriku Haruka oki earthquake. They use a 2-D model of the assumed underground structure and model the propagation of vertically-incident SH and SV waves, finding constructive interference between SH and Love waves occurs closer to the edge of the basin than that between SV and Rayleigh waves. The former amplification is the largest, and occurs approximately at the Airy phase frequency of the Love wave which also corresponds to the frequency content of the incident wave.

Three different examples have been found in the literature of numerical studies of wedge-shaped basins with similar cross-sectional shape to the Lower Hutt valley, although quite different in size. The smallest of these is the Shidian basin, China, where a local irregular distribution of damage was found after the 1976 Longlin earthquake. Yuan et al. (1992) uses a 2-D finite-element method to model SH wave action in a cross-section of the elongated basin. The cross-section is approximately 1500m wide, fault-bounded with a 45° dip on one side and a gently sloping edge on the other. The maximum depth of sediments in only 36m, with an shear wave velocity of 150-300m/s. The worst damage occurred in a band between 100 and 360m out from the fault-bounded edge. While the modelling results of Yuan et al. (1992) do not show a higher peak ground motions in the zone of damage, they do show smaller peaks nearer the edges, as well as strong surface wave action which is undoubtedly associated with the damage.

On a larger scale, Hill et al. (1990) study SH wave amplification in Salt Lake valley, Utah, a 15km-wide alluvial valley. Unconsolidated Quaternary and semi-consolidated Tertiary alluvium with shear-wave velocities 980m/s and 1420m/s reach a maximum depth of 1500m at the eastern edge adjacent to the steeply-dipping Wastach Fault. While not explicitly mentioned in the paper, the finite-difference synthetic seismograms presented show a clear basin-edge effect resulting from interaction between strong edge-generated Love waves and the delayed first arrival in the deep sediments, occurring about 800m from the valley edge.

In another example, Tanaka et al. (2000) used both 2-D and 3-D finite difference schemes to investigate the likelihood of a Kawase-type basin-edge effect occurring adjacent to the near-vertical Yoro Fault on the western edge of the Nobi plain, Japan. The basin is essentially a huge wedge-shaped structure some 47km wide and 2.4km deep containing sediments with shear-wave velocities between 400 and 1600m/s above a 2800m/s basement. Both the 2-D and 3-D time domain results show clear constructive interference between edge-generated surface waves and the direct arrival some distance out from the fault. Investigating both the in-plane and anti-plane motions, they find that the interference effect associated with SH (anti-plane) motion occurs closer to the edge, related to the lower dispersive velocity for Love waves than Rayleigh waves in the given sedimentary structure.

2.2.3 NUMERICAL STUDIES OF HYPOTHETICAL BASIN EDGES

Dezfulian and Seed (1970, 1971) use both 1-D and 2-D finite-element methods to study the seismic response at the surface above plane sloping edges to a semi-infinite layer using real input motions. Edge slopes range between 1:1 and 1:12. Their results show clearly that the presence of the edge has a large influence on the response of the layer. The magnitude and extent of the influence may vary within a wide range depending on the edge-slope and depth of the layer.

Moczo and Bard (1993) model a semi-infinite layer with a vertical edge in a homogenous elastic half-space under excitation by vertically incident plane SH waves. Twelve different configurations of material parameters were investigated with a finite-difference technique. Displacement time-histories at the surface of all 12 models show both the direct arrival and the generation of surface waves that propagate away from the discontinuity into the soft

layer. The maximum displacement peak occurs just to the soft side of the lateral break. Although its cause was not explicitly outlined, it appears to be, in the light of recent findings an example of the basin-edge effect defined by Kawase (1996); constructive interference between the horizontally propagating surface wave and the direct wave traveling vertically through the sediments. In frequency domain, transfer functions for the soft layer appear to be a superposition of 1D vertical resonance and of "oscillatory patterns corresponding to the interference between the direct and diffracted waves". The frequency spacing of these oscillations shortens and their amplitude decreases with distance from the discontinuity.

2.2.4 Analytical Solutions to SH Waves at Corners and Wedges

Insights into amplification of anti-plane motion at shallow dipping sedimentary basin edges have been made by analytical analyses of SH wave propagation at simple geometrical corners between the plane edges of homogeneous solids. The most relevant example in the literature is of a wedge where one side is fixed to a rigid boundary, approximating a dipping basin-edge bounded below by stiff bedrock and above by a free surface. Hudson (1963) finds an approximate solution for a line source within the dipping layer as input. The solution shows that Love waves exist in the wedge when the apex angle is small. Sánchez-Sesma and Velázquez (1987) then produce a tidy analytical solution for the displacement field on the free surface when the input is in the form of a moving rigid lower boundary. Maximum amplification of peak ground motion is found a short distance from the edge where pulses constructively interfere. This is an important result for ground motion above a relatively shallow dipping edge.

The analytical solution of Sánchez-Sesma and Velázquez (1987) is, however, not so applicable to a steeply dipping wedge where the finite depth of the wedge and the characteristics of the diffracted wave field produced at the lower vertex become important controlling factors of the response. Nor does this or the solution of Hudson (1963) consider an elastic subjacent half-space which has a significant effect on the characteristics total reflection and the response of the low-frequency end of the spectrum.

Several less applicable but nevertheless noteworthy examples include a general solution for amplification on the surface of a wedge where both edges are stress free is found by Sánchez-Sesma (1985), with earlier work on the problem having been done by Abo-Zena

and King (1973). The application of this is the surface amplification at the crest of hills. In another example Hudson and Knopoff (1964) take the case of a Love wave incident on a wedge with stress free edges, a problem related to seismic behaviour at continental margins and mountain roots.

Chapter 3: COMPUTATIONAL METHODS

Finite-element methods (FEM) are used extensively throughout this research in order to understand seismic response due to sub-surface geology. The aim of this thesis is not to analyse or develop such numerical techniques, but to merely use them as a tool toward a better understanding of wave-propagation at basin edges. An introduction is here provided to describe the software used in Parts II and III, as well as techniques of post-processing and viewing output data. Archimedes is the software used for two-dimensional elastic analyses of anti-plane SH wave propagation through theoretical geology in Chapter Six and real geological cross-sections of the Lower Hutt valley in Chapters Eight and Ten. A one-dimensional FEM similar to the Archimedes computation is also used for comparison. Displacement data captured at the surface and at depth is analysed with various post-processing techniques described here also.

3.1 A Brief Review of Numerical Techniques for Investigating Seismic Wave Propagation

Over the last 25 years with the rapid advances in computing technology, numerical methods for modelling the seismic behaviour of underground geology have become increasingly more refined and easy to use. A result has been much two- and three-dimensional modelling of sedimentary basins in an effort to understand their seismic behaviour.

Solutions to the propagation of seismic waves in inhomogeneous material and non-uniform geometries have generally been found through numerical techniques such as the finite-element method (e.g. Constantino et al., 1967; Douglas, 1970; Drake, 1972a,b; Lysmer and Drake, 1971, 1972; Smith, 1975) and finite-difference method (e.g. Boore, 1970, 1972; Helmberger and Vidale, 1988), that have the ability to analyse irregular, realistic geometries. Other common techniques include the ray-theory method (e.g. Jackson, 1971, Sanchez-Sesma et al., 1988a), boundary-integral equation method (e.g. Dravinski and Mossissian, 1987), boundary-element method (e.g. Shibuya, 1992; Sanchez-Sesma and Luzon, 1995), discrete wavenumber or Aki-Larner method (Aki and Larner, 1970; Boore et al., 1971; Bouchon and Aki, 1977) discrete wavenumber boundary-element method

(Kawase, 1988; Kawase and Aki, 1990; Bouchon, 1996), and other hybrid combinations thereof (e.g. Touhei and Yoshida, 1988; Zhang and Papageorgiou, 1995). Sanchez-Sesma (1987), Aki (1988), Helmberger and Vidale (1988) and Fah (1996) give good summaries of these techniques. Several other more obscure techniques include the Gaussian beam method, dynamic ray tracing, the Maslov method, the phase front method and the Kirchoff integral method (Kato et al., 1993).

3.1.1 FINITE ELEMENT METHODS

Two-dimensional finite-element methods have been used in recent years for modelling idealised valleys (eg. Ohtsuki and Harumi, 1983; Loukakis and Bielak, 1995) and site-specific response studies (eg. Bardet et al., 1992; Bielak et al., 1999; Adams and Jaramillo, 2000). Kawase (1996) used a 2-D FEM to investigate the basin-edge effect in Kobe during the 1995 earthquake. Finite-element methods have also been used in 2-D to model source processes (Loo and Jin, 1984). Three-dimensional finite-element techniques have been used to model 3-D basin resonance (Rial et al., 1992), basin-edge induced love-wave propagation (Toshinawa and Ohmachi, 1992) and general basin response (Bao et al., 1998; Hisada et al., 1998).

Loukakis and Bielak (1995) discuss two issues concerning the use of finite-element methods for modelling seismic motions in unbounded domains. The first is the need to limit the domain with an artificial boundary. Viscous boundaries using a spring dashpot model (Lysmer and Kuhlemeyer, 1969), transmitting boundaries (Lysmer and Waas, 1972), non-reflecting boundaries by averaging fixed (Dirichlet) and free (Neumann) boundary conditions (Smith, 1974) and Kosloff's Method (Kosloff and Kosloff, 1986; Seki and Nishikawa, 1988) have all been used to successfully counter the problem of reflections. The second issue is how to incorporate excitation into the finite-element mesh, a problem that has been solved by an effective force method and domain decomposition technique (Bielak and Christiano, 1984; Cremonini et al., 1988). Other solutions involve the use of an internal source (eg. Hisada et al., 1998).

3.2 ARCHIMEDES FOR TWO-DIMENSIONAL ANALYSIS

Archimedes (Bao et al., 1998) is an integrated set of computational software tools for performing large finite element method (FEM) simulations on parallel computers. It was

originally developed for two-dimensional elastic simulations (eg. Bielak et al., 1999; Adams and Jaramillo, 2000), while three-dimensional (eg. Hisada et al., 1998) and non-linear techniques are now possible. In this research, Archimedes is used to solve the problem of elastic SH wave propagation within two-dimensional cross-sections of real and theoretical basins.

Archimedes was developed as part of the National Science Foundation (NSF) Grand Challenge Quake Project, a joint venture between the Department of Civil and Environmental Engineering and the Department of Computer Science at Carnegie Mellon University (Pittsburgh, PA.), the Southern California Earthquake Center at the University of Southern California and the National University of Mexico. The Quake project has the goal of developing computer simulation methods for the prediction of ground motion in sedimentary basins during strong earthquake shaking.

Input to Archimedes includes (a) the geometry and properties of the geological model and (b) an FEM algorithm. The tool set, developed by Dave O'Hallaron and Jonathan Shewchuk of the Department of Computer Science at CMU, includes the following:

1. ***Triangle*** (Shewchuck, 1996) is a two-dimensional triangular mesh generator designed specifically for FEM's. It uses Delaunay triangulation algorithms to create an efficient, unstructured mesh. Input to Triangle includes the geometry of layer boundaries, free-surfaces and computational boundaries, maximum triangle area and minimum internal angle; all in the form of an ASCII data file (.poly extension). It also has the option of creating quadratic elements (six nodes per element) for more efficient computation. Output from Triangle consists of a set of three data files (.node, .ele, and .poly extensions) describing the coordinate points of each node and the nodes associated with each element. The 3-D equivalent, ***Pyramid***, uses similar techniques to generate a three-dimensional unstructured tetrahedral mesh.

2. ***Show Me*** is a C program for graphically displaying on the screen meshes generated by Triangle. It also has functions for writing images to postscript files and for viewing the input geometry to Triangle.

3. A set of three programs - ***Absorb***, ***Slice*** and ***Parcel*** - are used to refine, partition and reorganise the mesh data into a form that may be used on parallel processors. For our purposes, these programs were run with the input argument of only one processor.

Parcel also requires an extra input file (with a .fi extension) containing five lines describing the input ricker-wave central frequency, the time-step size and the simulation length.

4. ***Author*** is the central tool of Archimedes. As input it uses data files (with extensions .adj, .def, .ele, .node, .pack, .part and .ri) from the previous tools, as well as an FEM code file (with a .arch extension) written in ANSI C and containing an element-level description of the finite-element approximation, and a high-level description of the finite-element algorithm. The job of Author is to compile these files into a processor code for running the simulation.

Up-to-date information and a description of the Archimedes tool chain may be found on the World Wide Web at http://www.cs.cmu.edu/~quake/archimedes.html. Complete documentation for the use of Archimedes has not yet been published, although complete instructions on the use of Triangle, the two-dimensional triangular mesh generator may be found at http://www.cs.cmu.edu/~quake/triangle.html.

3.2.1 MESH GENERATION

Finite element methods allow the use of an unstructured mesh, enabling elements of differing sizes and proportions to give a high degree of geometric detail. Node spacing can be tailored in proportion to the local shear-wave velocity to give similar numerical accuracy and high computational efficiency throughout the geometry of the problem. In order to achieve reasonable accuracy, it is desirable to use a maximum node spacing in the finite-element mesh of one-eighth (Kuhlemeyer and Lysmer, 1973) to one-fifth (Lysmer et al., 1975) the shortest wavelength. Triangle and Archimedes conveniently allow the use of six-noded quadratic-triangular elements, with an intermediate node between each vertex. A maximum element size of $\lambda_{min}/4$ is thus used to achieve a maximum node spacing of $\lambda_{min}/8$. In order to simulate seismic motions within the frequency range $0 \le f \le f_{max}$, the corresponding maximum element size is required to be less than $\lambda_{min}/4 = \beta/4f_{max}$, where β is the shear-wave velocity of the unit. Part of the mesh generated for the Lower Hutt cross-section at the site of the array is shown in Figure 3.1.

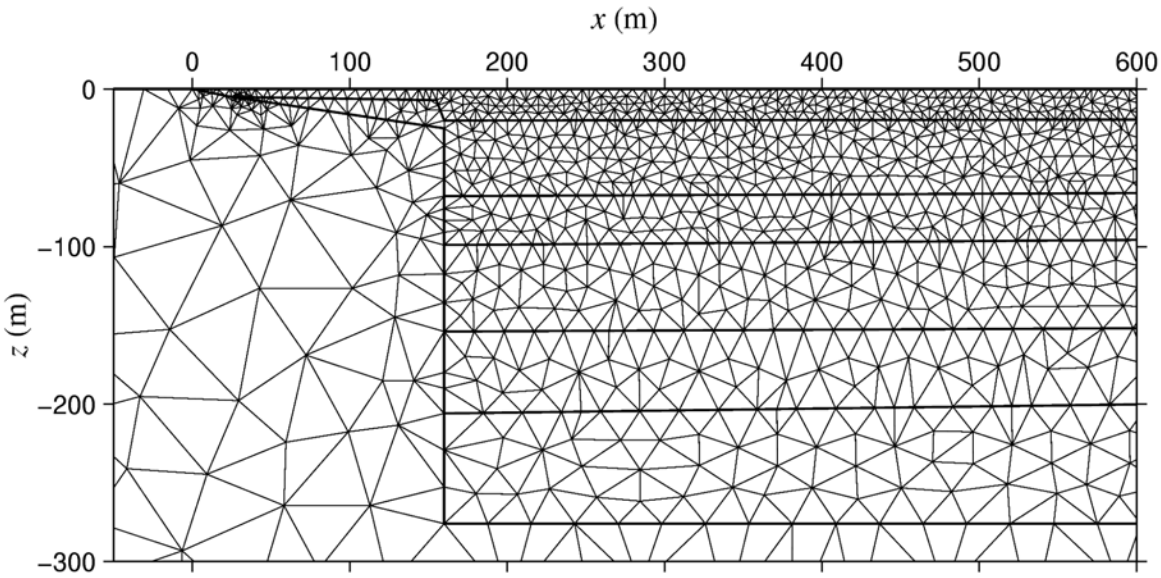

Figure 3.1. A section of the unstructured mesh developed by *Triangle* for a cross-section through the Lower Hutt valley (see Chapter Ten). Mesh size is tailored to the shear-wave velocity in each stratigraphic unit and the maximum frequency of interest.

For problems such as modelling the Lower Hutt, with shear-wave velocities differing by as much as a factor of 15 (100m/s and 1500m/s), large reductions in computation requirements can be made by using an unstructured mesh. For example, the cross-section through the Lower Hutt at Petone contains only 37,787 nodes compared to the ~200,000 nodes which would have been required in a uniform (structured) mesh of the same cross-section. Accordingly, the simulations are able to be run on a single 512MB DEC Alpha processor operating on a UNIX platform. Processing time for our modelling is in the order of 4-12 hours, while large 3-D simulations may be run on parallel machines in a few hours (eg. Bao et al., 1998).

3.2.2 THE FINITE ELEMENT ALGORITHM

In general terms, the problem is one of elastic horizontally-polarised (SH) shear-wave propagation within a soft basin surrounded by a homogeneous half-space of rock. The half-space is idealised as of uniform cross-section and infinite-length (often called a cylindrical cross-section). An FEM analysis allows a treatment of the whole basin so that the out-of-plane displacement field, v, within each element, satisfies the wave equation

$$\frac{\partial^2 v}{\partial t^2} = \beta^2 \nabla^2 v \qquad [3.1]$$

Boundary conditions are imposed which require the continuity of force and displacement across each element, and the absence of tractions at the free surface. The equation of motion over the computational domain can then be expressed as a system of ordinary differential equations of the form

$$[M]\ddot{v} + [C]\dot{v} + [K]v = f(t) \qquad [3.2]$$

where [*M*], [*C*], and [*K*] are the global mass, damping and stiffness matrices; v, $\dot{v}$ and $\ddot{v}$ are the time-dependant nodal displacements, velocities and accelerations respectively, and $f(t)$ is the applied nodal force.

3.2.3 MATERIAL DAMPING

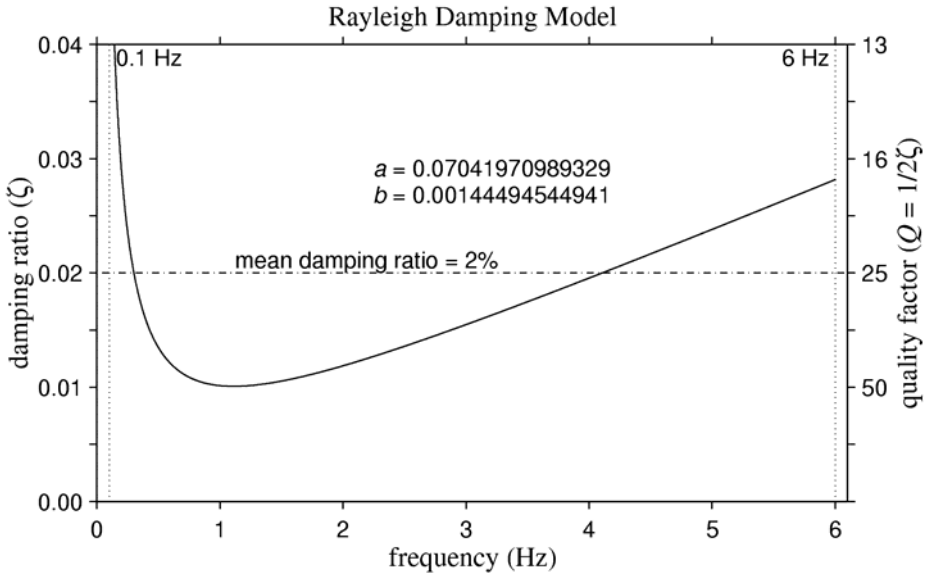

Figure 3.2. The viscous Rayleigh damping model used to approximate a constant 2% damping over the desired frequency range. The *a* and *b* values are those used in the Archimedes simulations for the Lower Hutt.

Damping has the effect of soaking up energy within the soil matrix thus inhibiting wave propagation. Likely values for the damping ratio, ζ, have been assigned to each layer. Archimedes uses a two-parameter (*a* and *b*) viscous Rayleigh damping model. Within each finite element, the damping matrix, [C^e], has the form (Bielak et al, 1999)

$$\left[C^e\right] = a\omega_o\left[M^e\right] + \frac{b}{\omega_o}\left[K^e\right] \qquad [3.3]$$

where ω_o is a reference frequency and $[M^e]$ and $[K^e]$ are the element mass and stiffness matrices. The Rayleigh damping model thus varies with frequency, so we select the a and b parameters in such a way that the damping ratio averages out to the desired value across the frequency range of interest, as shown in Figure 3.2 for a frequency range 0.1-6.0Hz and a damping ratio, $\zeta = 2\%$.

3.2.4 INPUT SIGNAL

The input motion is a single Ricker wavelet propagating up through the model as a continuous plane wavefront. The angle of incidence of the input wavelet may be varied throughout 180 degrees from horizontal to vertical. In the time-domain, the displacement trace, $v(t)$, is given by (Ricker, 1940)

$$v(t) = A\left[\, 1 - \frac{1}{2}\left(\omega_c t\right)^2 \right] e^{-\frac{1}{2}\left(\omega_c t\right)^2} \qquad [3.4]$$

where $\omega_c = 2\pi f_c$, and f_c is the central (dominant or characteristic) frequency. A is the wavelet amplitude. In the FEM modelling, this same wave is approximated by

$$v(t) = \begin{cases} a_1\left(\omega_c t\right)^4 + a_2\left(\omega_c t\right)^6 + a_3\left(\omega_c t\right)^8 & 0 \le t < \frac{\sqrt{6}}{\omega_c} \\ \left[\, \frac{1}{4}\left(\omega_c t - 3\sqrt{6}\right)^2 - 0.5 \right] e^{-\frac{1}{4}\left(\omega_c t - 3\sqrt{6}\right)^2} - \dfrac{13e^{-13.5}}{0.5 + 13e^{-13.5}} & \frac{\sqrt{6}}{\omega_c} \le t < \frac{5\sqrt{6}}{\omega_c} \\ a_1\left(\omega_c t - 6\sqrt{6}\right)^4 + a_2\left(\omega_c t - 6\sqrt{6}\right)^6 + a_3\left(\omega_c t - 6\sqrt{6}\right)^8 & \frac{5\sqrt{6}}{\omega_c} \le t < \frac{6\sqrt{6}}{\omega_c} \\ 0 & \textit{elsewhere} \end{cases} \qquad [3.5]$$

where a_1, a_2 and a_3 are polynomial coefficients. Here the wavelet has been given finite start and finish points by substituting 3rd order polynomials at the start and end of the function. The Ricker waveform can be visualised in terms of its displacement trace, $v(t)$, and its Fourier amplitude spectrum as shown in Figure 3.3.

The Ricker pulse contains frequencies between 0 and $3f_c$. The peak displacement now occurs at $3\sqrt{6}/\left(2\pi f_c\right)$ seconds and the time between arrivals of each of the three peaks in the wavelet, t_r, is given by

$$t_r = \frac{\sqrt{6}}{2\pi f_c} \qquad [3.6]$$

The excitation is incorporated into the computational domain along a smaller semi-circular arc inside the absorbing boundary. The time of excitation of each node on the arc is adjusted so to represent a pulse starting simultaneously over the width of the mesh from the same depth. The method used is that developed by Bielak and Christiano (1984) and Cremonini et al. (1988) whereby nodal forces are applied along this inner arc of finite elements.

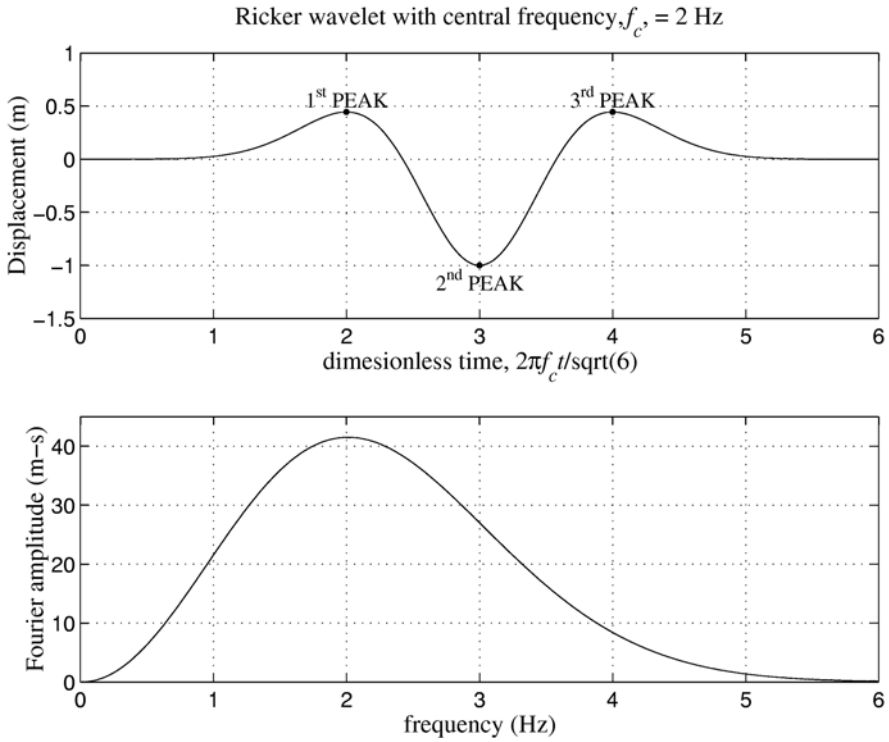

Figure 3.3. Plot of a Ricker wavelet in time domain and the corresponding Fourier amplitude spectrum of displacement showing the central frequency and distribution of amplitude in the frequency domain.

3.2.5 ABSORBING BOUNDARY

Bedrock extends many kilometres below and to the sides, away from the soft basin. To keep memory requirements and calculation time to a minimum, we require a finite computational domain extending no more than a few hundred metres (several node spacings) into the rock. This introduces the problem of reflections from the artificial outer

boundary, which need to be removed from the system. Al-Hunaidi (1989) describes and compares various solutions to this particular problem, one of which is the viscous boundary technique used here. A semi-circular absorbing boundary has been placed around the lower extent of the model, with the viscous boundary conditions, a distributed set of spring and dashpot models, imposed on the arc. The circular boundary has the advantage of being easy to describe mathematically as a singular bounding segment.

3.2.6 VERIFICATION BY AN ANALYTICAL SOLUTION FOR RESONANT FREQUENCIES IN A 2-D RECTANGULAR VALLEY

A brief side trip allows us to build confidence in the Archimedes FEM technique. The solution for resonant frequencies in a homogeneous rectangular inclusion in a rigid half-space (Bard and Bouchon, 1985) is given in Equation 2.1, while the position of extremum points defined by Bielak et al. (1999) is given in Equation 2.4. The solution is ideal for verification of the Archimedes method because while the exact solution was developed for a rigid-base closed system (a Helmholtz resonator), the resonant frequencies still hold exactly in the open system with an elastic half-space (Zhou and Dravinski, 1994). The position of extremum points defined in Equation 2.4 are not exact for the open system, yet are expected to be very close for a high impedance constrast.

Here we take a 1000m wide by 100m deep 2-D rectangular basin with a shear-wave velocity of 300m/s, surrounded by a homogeneous half-space with a shear-wave velocity of 1500m/s, and excite it with a vertically incident plane Ricker pulse with a characteristic frequency of 2.0Hz. The velocity contrast between the layer and half-space is 5. Material damping is omitted to show wave propagation more clearly. Surface displacements calculated by the Archimedes method are shown on the top plot of Figure 3.4. The frequency response in the form of a Fourier spectral ratio (see Section 3.3) is plotted on the lower axis in Figure 3.4. On top of this is plotted the 2-D resonant frequencies of order $n = 0$, calculated by the analytical method (Bard and Bouchon, 1985) and previously shown in Figure 2.2. Symmetrical horizontal modes are cancelled out due to the symmetry of the problem.

Excellent comparison between the analytical and numerical result is seen for two-dimensional mode shapes belonging to the first vertical mode ($n = 0$). Every 2nd of the first 31 (n = 1,3,5, … ,31) horizontal resonant frequencies are identifiable on the spatial plot of

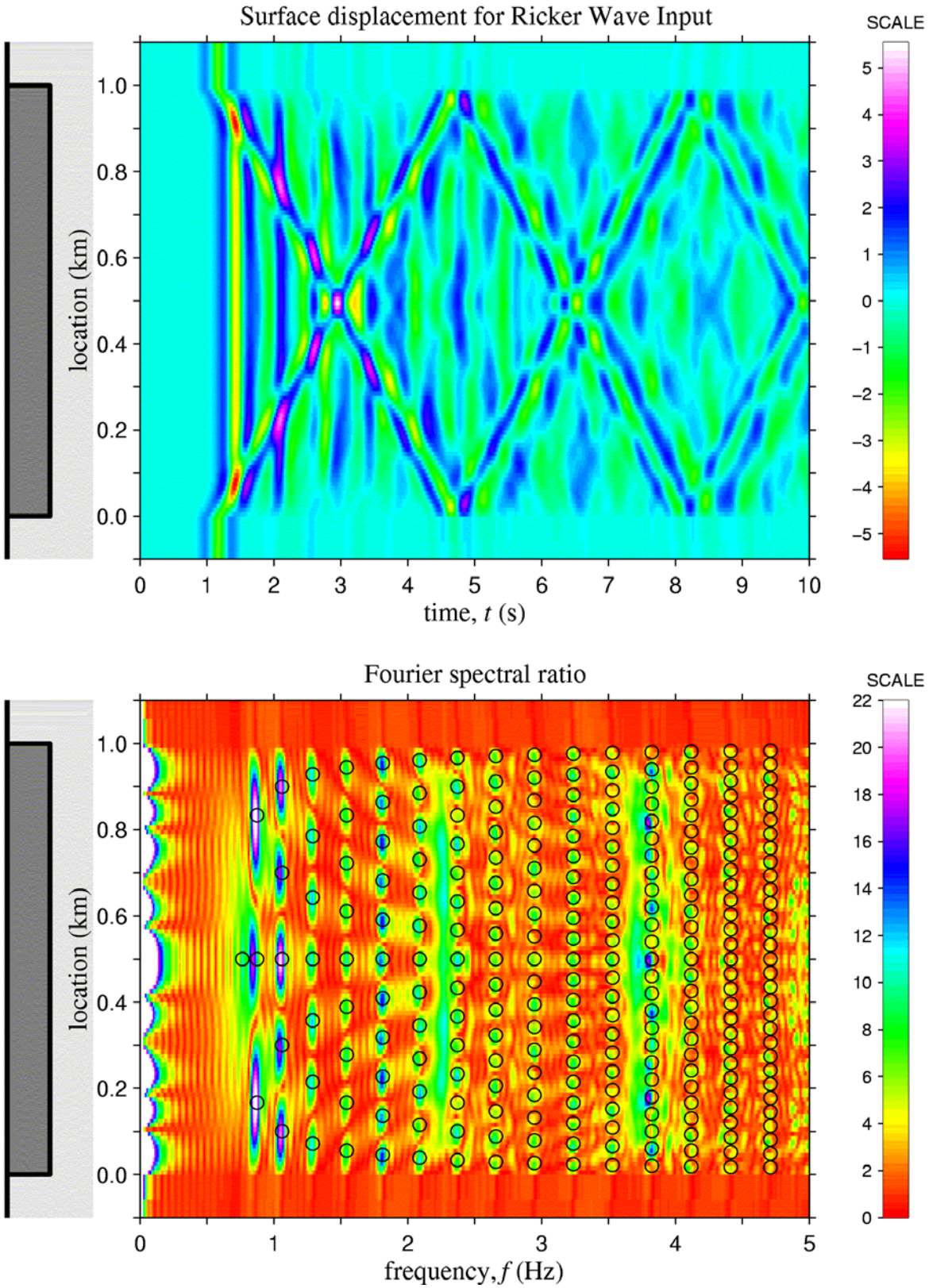

Figure 3.4. Results of two-dimensional time-domain FEM modelling in a soft homogeneous rectangular basin. The colour plots show the Archimedes output, while the circles indicates the position of extremum points calculated by an analytical method. The first three vertical modes appear on the plot.

transfer function. It appears that nearly all of the peaks shown belong to the horizontal modes for which $n = 0$. Broad and diffuse amplification at $f = 2.25$Hz and $f = 3.75$Hz correspond to the first few horizontal modes for each of the 1st higher ($n = 1$) and 2nd higher ($n = 2$) vertical resonant frequencies. Higher m^{th}-order eigenmodes for $n \geq 1$ appear to be very small in amplitude.

3.3 THE ONE-DIMENSIONAL ANALYSIS

A short code written in MATLAB is used to calculate the time-domain response of an SH wave travelling vertically within an uncoupled column of elastic and homogeneous soil and rock units. The computation is in many ways similar to the two-dimensional Archimedes code. The input excitation is again a Ricker wavelet as was shown in Figure 3.3, while damping and the absorbing boundary are also incorporated in the same fashion to the two-dimensional method.

The one-dimensional method requires that the waves be constrained to propagate in only one orientation (the vertical). In this way we rule out the possibility of focussing, surface-wave generation and other effects caused by non-horizontal geometry and of non-vertical wave incidence. The result seen for each given soil column is identical to that given by assuming a uniform stratigraphy extending to infinity in both horizontal directions, and bounded below by a uniform half-space.

3.3.1 VERIFICATION BY AN ANALYTICAL SOLUTION FOR ONE-DIMENSIONAL RESONANT FREQUENCIES

The Haskell-Thompson matrix method (Thompson, 1950; Haskell, 1953) provides an exact analytical solution to the frequency response of several homogeneous layers over a uniform half-space. Here we take a simple system of four uniform layers above a stiff elastic basement. The configuration and properties of the model are presented in Table 3.1. The effect of material damping is not considered. Results of the finite-element method are compared with the analytical solution in Figure 3.5. As for the 2-D FEM, the comparison is good. Only small discrepancies exist at higher frequencies.

Table 3.1. Configuration and material properties of the four-layer soil model analysed to compare the FEM solution with the analytical.

Layer	Depth (m)	Shear-wave velocity (m/s)	Bulk density (kg/m^3)
1	10	150	1500
2	20	300	1800
3	20	350	1800
4	30	375	1850
Basement	inf	2000	2700

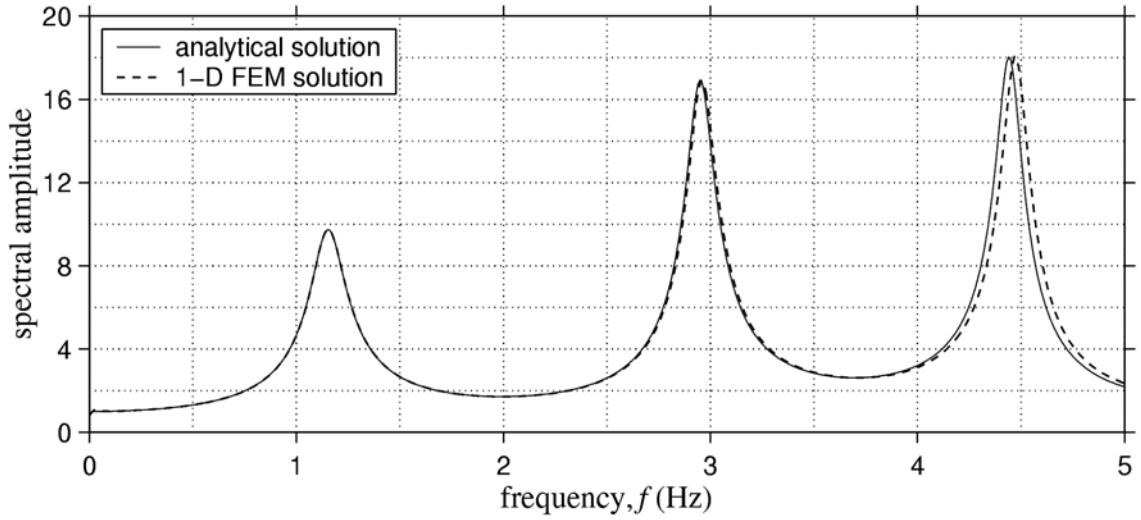

Figure 3.5. Normalised Fourier amplitude showing resonant frequencies of vertically reflecting SH waves in a uniform homogeneous layer over a homogenous half-space. Results calculated by the 1-D FEM method are very close to the analytical result.

3.4 POST-PROCESSING TECHNIQUES

Output from both the one-dimensional and two-dimensional finite-element analyses is in the form of displacement, velocity or acceleration time-histories recorded at each time step thorough the simulation. Time-history data may be captured from any of the nodes within the model. In most cases, it is taken from some 100-400 nodes across the surface of the model (akin to recording information from an extensive, closely-spaced set of seismographs). Displacement records are also taken from a selection of nodes throughout

the depth of the cross-section so that the movement of pulses up through the model may be plotted.

3.4.1 TIME HISTORY DATA

Closely spaced records from surface nodes allow displacement to be presented as a continuous function of both location and time, as shown in the top plot of Figure 3.4. Using this approach we can visualise both the arrival of body-waves through the medium, and the paths of surface waves along the ground. On space-time axes (eg. distance, x, vs. time, t) a vertically-propagating body wave arrives simultaneously across the width of the model at the same time. A wave front which, on the other hand, has been bent from the vertical by refraction or some other process to will have an apparent horizontal velocity which will be given by the slope of the pulse on x-t axes. In the same way the phase velocity of surface waves may be directly read from the graph.

3.4.2 SPECTRAL ANALYSIS

Displacement, velocity and acceleration time histories are converted into the frequency domain using a radix-2 fast Fourier transform algorithm built into the MATLAB function library (Mathworks, 1997). Time sequences of 4000 points are typically padded with trailing zeros to a length, N, of 2^{14} (16384) in order to give sufficient accuracy in the frequency-domain. A typical time-step, Δt, of 0.005 seconds in the time-history record produces a frequency-step, Δf, of $1/(N\Delta t) = 1/(2^{14} \times 0.005) = 0.0122$ Hz on the frequency plot; and permits the frequency response up to the Nyquist critical frequency, $f_{Nyquist}$, of $1/(2\Delta t) = 1/(2 \times 0.005) = 100$ Hz. The frequency response is, however, generally limited to a maximum frequency of $2.5f_c$ by the frequency content of the Ricker wavelet.

In the frequency domain, spectral amplification resulting from the geological structure of the cross-sections is presented as soil to rock Fourier spectral ratios (FSR). These may also be plotted as a continuous function of position and frequency, a technique proved useful for viewing resonant behaviour in the sediments and the associated patterns of surface amplification. The FSR is defined (Borcherdt 1970) as the ratio of the Fourier amplitude from a recording on the *soil surface* to the Fourier amplitude from a simultaneous recording on a *bedrock outcrop*,

$$FSR(\omega) = \frac{\left|F_{soil\,surface}(i\omega)\right|}{\left|F_{rock\,outcrop}(i\omega)\right|} \qquad [4.6]$$

where ω is the frequency, $F_{soil.surface}(i\omega)$ is the complex Fourier transform of the output seismogram at the soil surface and $F_{rock.outcrop}(i\omega)$ is the Fourier transform of the output on a rock outcrop. All phase information is lost in the calculation of the FSR. The purpose of the FSR is to cancel out the effect of the input motion and reduce the results to show only the effect of the soft near-surface geology. Thus, in theory, the results should be earthquake-independent, and a function only of the surface layers.

For the case of a uniform half-space of perfectly elastic rock, the outcrop surface motion (ie. the output from the simulation) is expected to have twice the amplitude of the bedrock basement motion (ie. the input to the simulation). The actual response from the numerical computer simulations is slightly erratic, although of similar amplitude and shape to the analytical solution. Thus to obtain a smoother FSR from model results, it is calculated directly from the input motion,

$$\begin{aligned} FSR(\omega) &= \frac{\left|F_{o,surface}(i\omega)\right|}{2\left|F_{i,bedrock}(i\omega)\right|} \\ FSR(\omega) &= \frac{1}{2}\left|H(i\omega)\right| \end{aligned} \qquad [4.7]$$

where, the subscripts *i* and *o* refer to input and output respectively and $H(i\omega)$ is the complex transfer function between the basement and the surface.

PART II

SH WAVES AT THE EDGE OF A SEMI-INFINITE SURFACE LAYER

Chapter 4: A REVIEW OF THEORY ON SH-WAVE PROPAGATION

This chapter provides a review and discussion of the fundamental mathematical concepts concerning the propagation of horizontally-polarised shear (SH) waves in two-dimensional space. Many of the concepts and equations presented here will be drawn on heavily throughout the rest of Part II. A good proportion of the current mathematical theory of elasticity and seismic wave propagation was developed by great mathematicians such as Hooke, Navier, Cauchy, Poisson and Stokes. Later work by Rayleigh (1888) and Love (1911) saw the discovery of surface waves, while the more recent efforts around the mid 1950's by Jeffreys, Hudson, Thompson, Haskell and Brekhovskikh and others have greatly added to the current understanding of seismic-waves. Much of the review here has been compiled from standard seismology and wave mechanics texts such as Ewing, Jardetzky and Press (1957), Brekhovskikh (1980), Tolstoy (1973), Aki and Richards (1980), Hudson (1980) and Ben-Menahem and Singh (1981). While most of the ideas here are now considered common knowledge in the field, references have been made to original contributors, where appropriate.

4.1 SH Waves in a Homogeneous Material

If we constrain SH wave propagation to the *x*-*z* plane (with *x* horizontal and *z* vertical upwards) then the horizontally-polarised displacement is constrained to act in the anti-plane horizontal *y*-direction. The wave equation for displacement, *v*, in the *y*-direction is given by

$$\rho \frac{\partial^2 v}{\partial t^2} = (\lambda + \mu) \frac{\partial \varepsilon}{\partial y} + \mu \nabla^2 v \qquad [4.1]$$

where μ and λ are Lame's constants, ρ is the bulk density, ε is the volumetric strain

$$\varepsilon = \frac{\partial u}{\partial x} + \frac{\partial v}{\partial y} + \frac{\partial w}{\partial z} \qquad [4.2]$$

and ∇^2 is the Laplacian operator

$$\nabla^2 = \frac{\partial^2}{\partial x^2} + \frac{\partial^2}{\partial y^2} + \frac{\partial^2}{\partial z^2} \qquad [4.3]$$

The in-plane displacements u and w in the x- and z-directions are non-existant, while the anti-plane displacement, v, is a function of time and space in the x-z plane. For harmonic waves, $v(x,z,t)$ has a general solution of the form

$$v(x,z,t) = Ae^{i(kx-\omega t)} \qquad [4.4]$$

where A describes the amplitude of v, and $e^{i(kx-\omega t)}$ describes the harmonic waveform.

4.2 SH WAVES AT A MATERIAL INTERFACE

Here we take the case of a plane harmonic horizontally-polarised shear wave, incident on a plane boundary of a stiffer material at an angle of incidence θ_i, measured from a line normal to the boundary. The problem is depicted in Figure 4.1.

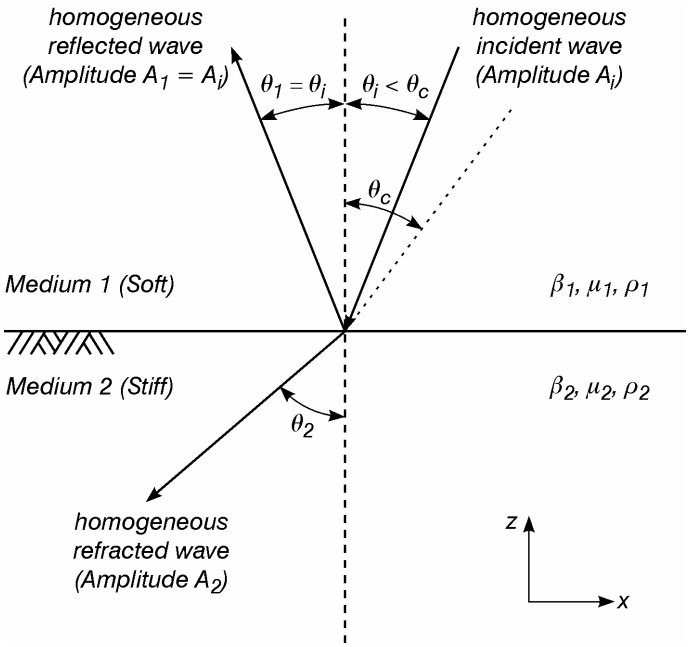

Figure 4.1: Subcritical contact ($\theta_i < \theta_c$) of a SH wave with an interface between two half-spaces. The incident wave produces both a reflected and a refracted wave.

The shear-wave propagation velocity in the first medium is denoted by β_1, and in the second medium β_2.

$$\beta_1 = \sqrt{\frac{\mu_1}{\rho_1}} \qquad \text{and} \qquad \beta_2 = \sqrt{\frac{\mu_2}{\rho_2}} \tag{4.5}$$

where μ_1 and μ_2 are the shear moduli and ρ_1 and ρ_2 are the bulk densities of the respective mediums. Since the upper material is softer than the lower, $\beta_1 < \beta_2$, and $\mu_1 < \mu_2$. Displacements of the SH wave are in the horizontal anti-plane direction, perpendicular to the direction of propagation.

4.2.1 SUBCRITICAL CONDITIONS OF REFLECTION AND REFRACTION

Subcritical conditions are defined by the generation of both a homogeneous reflected wave and a homogeneous refracted wave at an interface. For the case of an incident wave propagating towards and perpendicular to the interface ($\theta_i = 0$), a homogeneous wave is reflected back into the soft layer, and a homogeneous wave is transmitted (refracted) into the stiff layer. The amplitudes of the reflected and transmitted waves are given by

$$A_1 = A_i \frac{\rho_1\beta_1 - \rho_2\beta_2}{\rho_1\beta_1 + \rho_2\beta_2} = A_i \frac{1-i}{1+i} \tag{4.6}$$

$$A_2 = A_i \frac{2\rho_1\beta_1}{\rho_1\beta_1 + \rho_2\beta_2} = A_i \frac{2}{1+i} \tag{4.7}$$

where A_i, A_1 and A_2 are the amplitudes of the incident, reflected and transmitted waves respectively, and i is the impedance ratio between the two materials

$$i = \frac{\rho_2\beta_2}{\rho_1\beta_1} \tag{4.8}$$

When $\theta_i \neq 0$, the wave is reflected back into the first medium with an angle $\theta_1 = \theta_i$; while the wave in the second medium is refracted with an angle of θ_2 given by Snell's law

$$\frac{\sin\theta_2}{\beta_2} = \frac{\sin\theta_i}{\beta_1} = \frac{\sin\theta_1}{\beta_1} \tag{4.9}$$

The amplitudes of the reflected and refracted waves are now given by

$$A_1 = A_i \frac{\rho_1\beta_1\cos\theta_i - \rho_2\beta_2\cos\theta_2}{\rho_1\beta_1\cos\theta_i + \rho_2\beta_2\cos\theta_2} \tag{4.10}$$

$$A_2 = A_i \frac{2\rho_1\beta_1 \cos\theta_i}{\rho_1\beta_1 \cos\theta_i + \rho_2\beta_2 \cos\theta_2} \qquad [4.11]$$

Since $\beta_2/\beta_1 > 1$, as θ_i increases from 0 the angle of refraction, θ_2, approaches $\pi/2$ (parallel to the interface) much more quickly than does the angle of incidence, θ_i. The angle of incidence for which $\theta_2 = \pi/2$ has been termed the *critical angle of incidence*, θ_c, and is given by

$$\sin\theta_c = \frac{\beta_1}{\beta_2} \qquad [4.12]$$

This condition is known as *critical refraction*, and the refracted wave which is now travelling parallel to the boundary in the stiffer material ($\theta_2 = \pi/2$) and is known as the critically refracted wave or *head wave*.

4.2.2 TOTAL REFLECTION

As θ_i increases beyond θ_c, the angle of refraction, θ_2, becomes complex and we have a post-critical condition known as *total reflection*, shown in Figure 4.2.

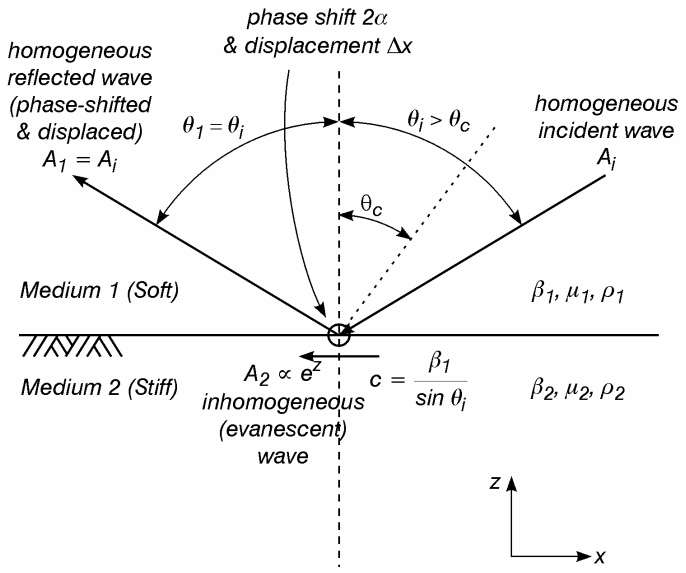

Figure 4.2: Total reflection (post-critical contact, $\theta_i < \theta_c$) of an SH wave. An inhomogeneous wave is produced in the stiffer material, while a phase shifted wave is reflected back into the soft material.

The reflected wave again leaves the interface and travels with an angle $\theta_1=\theta_i$, yet it undergoes a phase shift to lead the incident wave by a phase angle of 2α (Hudson, 1962), where

$$\tan\alpha = \frac{\mu_2}{\mu_1}\frac{\sqrt{\sin^2\theta_i - \sin^2\theta_c}}{\cos\theta_i} \qquad [4.13]$$

For a vacuum or liquid as the second medium (μ_2, $\beta_2 = 0$) no phase change would exist, while for a rigid second medium (μ_2, $\beta_2 = \infty$) the wave would be reflected $2\alpha = 180°$ out of phase. At the same time, for critical incidence when $\theta_i = \theta_c$ there is no phase change, and as θ_i increases to 90°, 2α goes to 180°.

As well as a undergoing a change in phase angle, the reflected wave is displaced a frequency-dependant distance Δx along the interface (Hudson, 1962)

$$\Delta x = \begin{cases} \dfrac{2\beta_1}{\omega\sin\theta_i}(\alpha) & for\ \ 0 \le \alpha \le \dfrac{\pi}{4} \\ \dfrac{2\beta_1}{\omega\sin\theta_i}\left(\dfrac{\pi}{2}-\alpha\right) & for\ \ \dfrac{\pi}{4} < \alpha \le \dfrac{\pi}{2} \end{cases} \qquad [4.14]$$

where ω is the harmonic frequency. The idea of total reflection implies that there is no loss of energy across the interface out of the soft medium. While this is true on average, it can be shown (Hudson, 1962) that there is in fact a continual transfer of energy back and forth across the interface between the two media. Instead of a homogeneous wave there is now an inhomogeneous wave generated in the stiffer medium. At the same time and same rate as the energy is transmitted into the stiffer medium, energy is transmitted back into the soft medium from the inhomogeneous wave, such that there is a net transfer of zero energy into the second medium. The ratio, F, of incident energy that is transmitted into the stiffer medium to travel as an inhomogeneous wave is given by (Hudson, 1962)

$$F = \frac{2}{\pi}\sin\left(\frac{\omega\sin\theta_i}{\beta_1}\Delta x\right) \qquad [4.15]$$

The relationship between F, Δx and α with the angle of incidence is shown in Figure 4.3. The amount of energy transfer back and forth across the interface reaches a maximum when the angle of incidence $\theta_i = \theta_{E\text{-}max}$ (Hudson, 1962)

$$\sin^2 \theta_{E-\max} = \frac{\mu_1 + \mu_2 \sin^2 \theta_c}{\mu_1 + \mu_2} \qquad [4.16]$$

The angle, $\theta_{E\text{-}max}$, that produces the strongest inhomogeneous wave is generally very close to the critical angle, θ_c, especially when the impedance ratio is large.

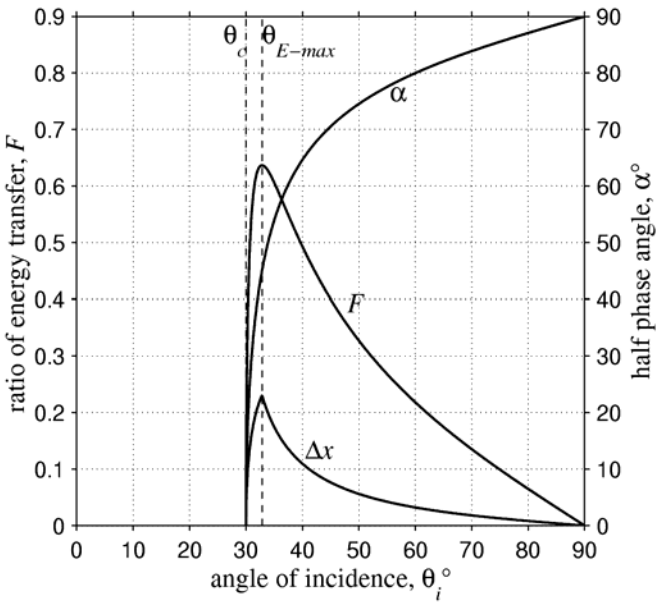

Figure 4.3: Relationship between the phase shift, 2α, displacement shift, Δx, and the ratio of energy transmitted back and forth across the interface, F, for various angles of post-critical incidence, $\theta_i < \theta_c$. Here plotted for $\beta_2/\beta_1 = 2$ and $\mu_2/\mu_1 = 4$.

The inhomogeneous wave is often called an *evanescent* wave since its amplitude decays exponentially with depth. It appears to travel parallel to the interface with a phase velocity, c, given by Snell's law

$$c = \frac{\beta_1}{\sin \theta_i} \qquad [4.17]$$

which we will later show to be equivalent to the phase velocity of a Love wave in a soft surface layer. The evanescent wave is therefore essentially the product of the bi-directional leaking of energy back and forth across an interface when the conditions of total reflection are satisfied. This should not be confused with the refracted or leaky rays that are the product of a net transfer of energy across an interface under sub-critical conditions.

Historically, evanescent waves have been studied in the context of the somewhat canonical configuration of two homogeneous fluid half-spaces excited by a point source (Brekhovskikh, 1980) or line source (Drijkoningen and Chapman, 1988) of acoustic *P*-waves. Hudson (1962) and Abramovici et al. (1989) have extended the theory to the case of *SH* motion in two solid half spaces. Hudson (1962) then provides a comprehensive discussion on the total reflection of SH waves in a low-velocity surface layer, and the generation of inhomogeneous waves in the subjacent half-space.

The inhomogeneous wave may also be called a *tunnelling* or *pseudo-surface* wave due to its tendency to travel laterally through sub-surface higher velocity layers. On a global scale, evanescent P waves have been observed on tele-seismic recordings after tunnelling through sub-crustal lithosphere (eg. Fuchs and Schulz, 1976). More recently Lomnitz et al. (1999) has shown on a local scale how coupling between evanescent P waves and a Rayleigh waves along an interface can set up standing patterns of constructive and destructive interference within sedimentary basins.

4.3 SH Waves in a Soft Surface Layer

The preceding ideas may be applied to the case of a horizontal surface layer of soft material above a stiff basement. When waves are incident from the half-space below, the energy transmitted into the layer is constrained to travel up and down at angles less then the critical. On the other hand, when a condition of total reflection is set up on the lower boundary (by a point source within the layer, for example), a Love wave is generated within the layer.

4.3.1 Vertical Resonance in a Infinite Layer

Consider an incident plane wave of amplitude A_i, travelling vertically upward through the stiff half-space (with properties ρ_2, β_2 and μ_2) and into the soft layer (with properties ρ_1, β_1 and μ_1). Most of the energy that reaches the interface is transmitted up into the softer material with a reduced amplitude, A_1, given by replacing A_2 with A_1 in Equation 4.7, while a smaller proportion is reflected back down into the half-space with an amplitude, A_2, given by replacing A_1 with A_2 in Equation 4.6.

The transmitted wave subsequently travels up through the layer and is reflected back down from the free surface without a change in phase. The lack of phase change requires the amplitude of the wave to double at the free surface, under constructive interference between up-going and down-going waves. This phenomenon is commonly referred to as *free-surface doubling* whereby the amplitudes of displacement, velocity and acceleration recorded on the surface are twice that recorded below ground.

Upon encountering the basement interface again, most of the energy is reflected back up into the layer with a phase change of 180°, and a somewhat reduced amplitude. A smaller proportion of energy is transmitted back into the half-space with each subsequent reflection at the lower interface, the loss of energy often being referred to as *leaky energy*. In this way a low velocity layer essentially traps and amplifies incident seismic energy. The degree to which energy is trapped depends on the impedance contrast between the layer and half-space and the internal angle of reflection.

Once the wave has undergone this phase change twice (by repeated reflection within the layer), it is back in phase with the original signal, and constructive interference occurs to produce a standing resonant wave. This occurs at successive periods given by four times the travel time through the layer (Haskell, 1960), or at the eigenfrequencies, f_n, of the n^{th} higher mode

$$f_n = \frac{\beta_1}{4H}(2n+1) \qquad n = 0,1,2,\ldots\infty \qquad [4.18]$$

where H is the thickness of the layer. The fundamental vertical frequency, f_0, of a layer over a half-space is thus given by

$$f_0 = \frac{\beta_1}{4H} \qquad [4.19]$$

When a plane wave travels up through the half-space at an angle, θ_i, between 0 (vertical) and $\pi/2$ (horizontal), it is refracted into the layer with a lesser angle, θ_1, which is always less than θ_c. This implies that it is impossible to generate a condition of total reflection within a plane infinite homogeneous surface layer by the incidence of homogeneous waves from a subjacent stiff half-space.

4.3.2 LOVE WAVES AND THE TOTAL REFLECTION OF SH WAVES WITHIN A SOFT LAYER

In order to achieve total reflection within a flat horizontal soft layer at the ground surface, the waves within the layer must be somehow set to travel at angles greater than that of the critical. This may be achieved either by the source being within the layer, or by an upward travelling wave being induced to travel in a more horizontal fashion in the layer. The former often occurs naturally on a global scale as earthquakes are sourced in the earth's crust which overlies the denser mantle. The latter occurs on a more local scale when upward travelling seismic waves from sub-surface earthquakes are bent horizontally into soft surface layers by irregular interfaces and topography or lateral inhomogeneities of material properties. It is correspondingly obvious that the condition of total reflection is a very common phenomenon in the real inhomogeneous world. The following chapter will look more closely at the special case where total reflection is set up by the lateral interface at the bounding edge of a layer.

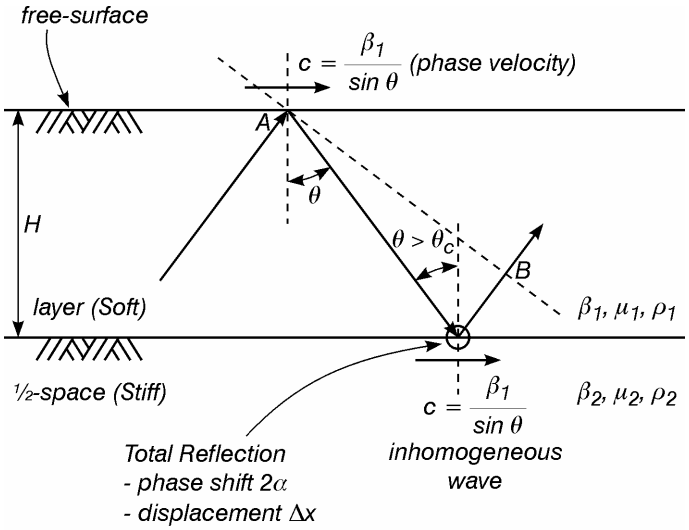

Figure 4.4: Constructive interference between trapped SH waves produces a Love wave when points A and B on the same ray path are in phase after total reflection at the lower interface.

The following theory assumes that total reflection has been set up within the layer. The post-critically trapped SH waves undergo repeated reflection between the free surface and the lower interface as shown in Figure 4.4. A Love wave (Love, 1911) is set up by constructive interference between in-phase wavefronts, such that there is an apparent

propagation in the horizontal direction at a phase velocity given by Equation 4.17. Because the waves within the layer are incident on the basement interface at some angle between the horizontal and critical, they tend to transmit a substantial amount of energy into the basement as evanescent waves; while at the same time there is an equal and opposite transfer of energy from the basement back into a homogeneous waveform within the layer. The net effect is a zero energy loss from the layer into the half-space. The amplitude of Love waves in homogeneous media hence does not decay except by geometric spreading in the horizontal plane.

The total internal reflection of SH waves within a soft surface layer can be described by the wave equation written in the form

$$\frac{\partial^2 v}{\partial t^2} = \frac{\mu_1}{\rho_1}\left(\frac{\partial^2 v}{\partial x^2} + \frac{\partial^2 v}{\partial z^2}\right) \qquad \text{in the layer for } 0 \le z \le H \qquad [4.20a]$$

and

$$\frac{\partial^2 v}{\partial t^2} = \frac{\mu_2}{\rho_2}\left(\frac{\partial^2 v}{\partial x^2} + \frac{\partial^2 v}{\partial z^2}\right) \qquad \text{in the half-space, } z \ge H \qquad [4.20b]$$

This describes both the totally reflected homogeneous waves within the layer, and the inhomogeneous waves that are generated by total reflection and which tunnel through the half-space parallel to the interface. If we apply the conditions of zero tractions at the free surface and continuity of displacement and stress at the interface, we can construct a solution for harmonic SH waves using the general form in Equation 4.4. The n^{th} mode displacement of the ground, v_n, is given as a function of time and space by

$$v_n(x,z,t) = 2A\cos\left(\omega\sqrt{\frac{1}{\beta_1^2} - \frac{1}{c_n^2}}\; z\right) e^{i(kx-\omega t)} \qquad n = 0,1,2\ldots\infty \qquad 0 \le z \le H \qquad [4.21a]$$

$$v_n(x,z,t) = 2A\cos\left(\omega\sqrt{\frac{1}{\beta_1^2} - \frac{1}{c_n^2}}\; H\right)\exp\left(-\omega\sqrt{\frac{1}{\beta_1^2} - \frac{1}{c_n^2}}\;(z-H)\right) e^{i(kx-\omega t)} \qquad z \ge H \qquad [4.21b]$$

where H is the depth of the layer, A is a coefficient of amplitude, c_n is the frequency dependent phase velocity of the n^{th} mode Love wave ($c = \lambda f$), ω is the angular frequency ($\omega = 2\pi f$) and k is the Love wave number ($k = 2\pi/\lambda$, $k = \omega/c$). Equation 4.21 shows that the displacement of the homogeneous wave within the layer has a sinusoidal shape with

depth, with n nodes and n+1 antinodes, while the displacement of the evanescent wave in the half-space decays exponentially with depth.

Phase Velocity

The phase velocity of the n^{th} mode, c_n, can be found by the solution of (eg. Aki and Richards, 1980)

$$\tan\left(\omega H\sqrt{\frac{1}{\beta_1^2}-\frac{1}{c_n^2}}-n\pi\right)=\frac{\mu_2}{\mu_1}\frac{\sqrt{\frac{1}{c_n^2}-\frac{1}{\beta_2^2}}}{\sqrt{\frac{1}{\beta_1^2}-\frac{1}{c_n^2}}} \qquad n=0,1,2,\ldots\infty \qquad [4.22]$$

which is commonly referred to as the *Love wave dispersion equation* or *frequency equation* for a single layer. It can also be written in the form (eg. Ewing et al, 1957)

$$\tan\left(kH\gamma_{1,n}-n\pi\right)=\frac{\mu_2}{\mu_1}\frac{\gamma_{2,n}}{\gamma_{1,n}} \qquad n=0,1,2,\ldots\infty \qquad [4.23]$$

where $$\gamma_{1,n}=\sqrt{\frac{c_n^2}{\beta_1^2}-1} \qquad [4.24]$$

and $$\gamma_{2,n}=\sqrt{1-\frac{c_n^2}{\beta_2^2}} \qquad [4.25]$$

The phase velocity is the apparent horizontal velocity of the peaks and troughs of the wave as they travel across a surface. Because the phase velocity is a function of frequency, Love waves are dispersive by nature. The phase velocity for each mode, plotted in Figure 4.5, decreases with increasing frequency but always lies between the shear wave velocity of the half-space, β_2 and the shear wave velocity of the layer, β_1. A solution to the n^{th} mode phase velocity, c_n, only exists when $\omega > \omega_{cn}$, where ω_{cn}, is the cut-off frequency of the n^{th} mode

$$\omega_{cn}=n\pi\frac{\left(\beta_1/H\right)}{\sqrt{1-\frac{\beta_1^2}{\beta_2^2}}} \qquad n=0,1,2,\ldots\infty \qquad [4.26]$$

This can be written in the form of the dimensionless cut-off frequency of the n^{th} mode, η_{cn}, normalised against the fundamental layer frequency from Equation [4.19]

$$\eta_{cn} = \frac{2n}{\gamma_0} \qquad n = 0,1,2,\ldots\infty \qquad [4.27]$$

where $$\gamma_0 = \sqrt{1 - \frac{\beta_1^2}{\beta_2^2}} \qquad [4.28]$$

When the velocity contrast, β_2/β_1, becomes very high, γ_0 tends toward unity, and η_{cn} tends toward $2n$. At frequencies less than the cut-off, the waves are not completely trapped in the layer and form leaky modes.

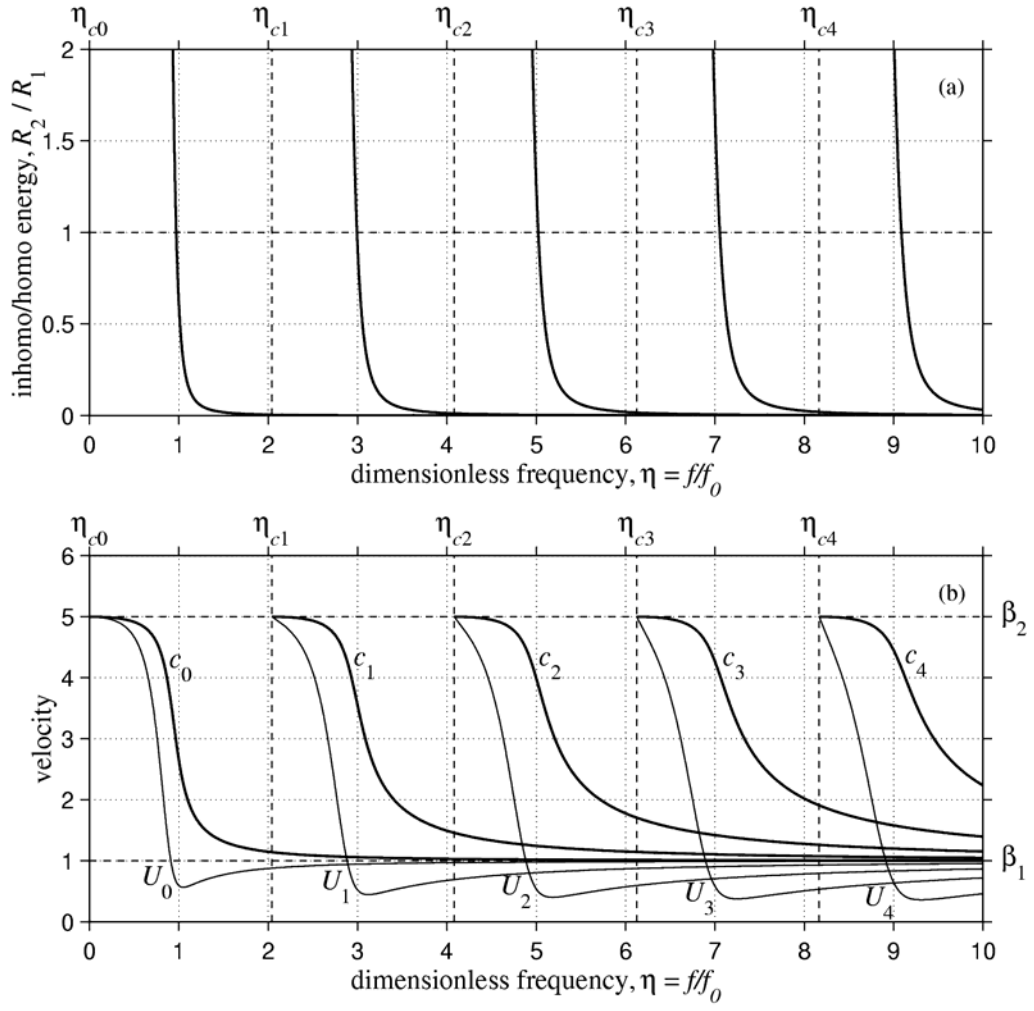

Figure 4.5: (a) The ratio, R_2/R_1, of inhomogeneous to homogeneous energy in a harmonic Love wave. Evanescent waves dominate at frequencies below the resonant of the layer ($\eta = 1$). After Hudson (1962), here plotted for $\beta_2/\beta_1 = 5$ and $\mu_2/\mu_1 = 25$. (b) Dispersion curves showing the relationship between phase velocity, c, group velocity, U, and frequency for the 1st 5 modes of a Love wave in a single layer over a half-space. A real solution to the nth mode velocity exists only for frequencies greater than the cut-off, $\eta > \eta_{cn}$.

Group Velocity

Energy is transported by the Love wave at a rate known as the group velocity, U, which is given by differentiation of the Love wave frequency Equation 4.22.

$$U = \frac{d\omega}{dk} = c + k\frac{dc}{dk} \qquad [4.29]$$

or from the phase velocity curves in Figure 4.5(b) using the expression

$$\frac{1}{U} = \frac{1}{c} - \frac{\omega}{c^2}\frac{dc}{d\omega} \qquad [4.30]$$

The group velocity of the n^{th} mode, U_n, can thus be expressed in the form (eg. Ben-Menahem, 1981)

$$U_n = \frac{\beta_1^2}{c_n}\left(\frac{c_n^2/\beta_1^2 + \Omega_n}{1+\Omega_n}\right) \qquad [4.31]$$

where Ω_n is a dimensionless frequency term given by

$$\Omega_n = \omega H\sqrt{\frac{1}{c_n^2} - \frac{1}{\beta_2^2}}\left[\frac{\rho_1}{\rho_2}\left(\frac{c_n^2 - \beta_1^2}{\beta_2^2 - \beta_1^2}\right) + \frac{\mu_2}{\mu_1}\left(\frac{\beta_2^2 - c_n^2}{\beta_2^2 - \beta_1^2}\right)\right]$$

$$\text{or} \qquad \Omega_n = kH\gamma_{2,n}\left(\frac{\mu_1}{\mu_2}\frac{\gamma_{1,n}^2}{\gamma_0^2} + \frac{\mu_2}{\mu_1}\frac{\gamma_{2,n}^2}{\gamma_0^2}\right) \qquad [4.32]$$

This result for the group velocity can also be obtained by considering energy transport within the layer and the half space (Hudson, 1962). First he defines R_1 and R_2 as the rates of energy travel in the x-direction in the layer and half-space respectively.

$$R_1 = \int_0^H \left(-\mu_1\frac{\partial v_1}{\partial x}\right)\left(\frac{\partial v_1}{\partial t}\right)dz \qquad [4.33]$$

$$R_2 = \int_H^\infty \left(-\mu_2\frac{\partial v_2}{\partial x}\right)\left(\frac{\partial v_2}{\partial t}\right)dz \qquad [4.34]$$

where $\partial v/\partial x$ is a term of shear strain and $\partial v/\partial t$ is the anti-plane particle velocity. R_1 and R_2 both have SI units of *Nm/s* (or *J/s.m*) per unit distance in the anti-plane y-direction. The

ratio R_1/R_2 indicates the proportion of energy that travels within the layer as a homogeneous trapped SH wave compared to the energy that travels as an inhomogeneous evanescent wave in the half-space, and is given by

$$\frac{R_1}{R_2} = \frac{\mu_1^2}{\mu_2^2}\left(\frac{2(\alpha + n\pi) + \sin 2\alpha}{2\cos^2 \alpha}\right)\tan\alpha \qquad [4.35]$$

which is plotted for the first few Love wave modes in Figure 4.5(a). The lower frequency components are transported most effectively by the inhomogeneous fraction. The ratio R_1/R_2 depends on the phase shift angle, 2α, which is a function of both the impedance contrast at the interface and the frequency content of the wave

$$\alpha = \omega H \sqrt{\frac{1}{\beta_1^2} - \frac{1}{c_0^2}}$$

$$\text{or} \qquad \alpha = kH\gamma_{1,0} \qquad [4.36]$$

Summing the rates of energy travel, R_1 and R_2, and integrating over a wavelength in the x-direction, gives R_{ave}, the average rate of energy that is transported within a love wave

$$R_{ave} = \frac{1}{\lambda}\int_0^{\lambda} (R_1 + R_2)\, dx \qquad [4.37]$$

which has the SI units J/s. Now the total of the potential and kinetic energy is each layer is given by

$$E_1 = \frac{\mu_1}{2}\int_0^{H} \left[\frac{1}{\beta_1^2}\left(\frac{\partial v_1}{\partial t}\right)^2 + \left(\frac{\partial v_1}{\partial x}\right)^2 + \left(\frac{\partial v_1}{\partial z}\right)^2\right] dz \qquad [4.38]$$

$$E_2 = \frac{\mu_2}{2}\int_H^{\infty} \left[\frac{1}{\beta_2^2}\left(\frac{\partial v_2}{\partial t}\right)^2 + \left(\frac{\partial v_2}{\partial x}\right)^2 + \left(\frac{\partial v_2}{\partial z}\right)^2\right] dz \qquad [4.39]$$

with the SI units J/m^2. And the average energy content within a wavelength of the Love wave is given by

$$E_{ave} = \frac{1}{\lambda}\int_0^{\lambda} (E_1 + E_2)\, dx \qquad [4.40]$$

with the units J/m or energy per unit distance in the anti-plane direction. The group velocity of the Love wave is given by the average velocity of energy being transported by the total of the homogeneous and evanescent parts of the wave

$$U = \frac{R_{ave}}{E_{ave}} \qquad [4.41]$$

For the case of plane harmonic waves, the group velocity of the n^{th} mode, U_n, it thus given by (Hudson, 1962)

$$U_n = \frac{\beta_1^2}{c_n}\left[\frac{(\alpha + n\pi)\sin\alpha + \left(\sin^2\alpha + \frac{\mu_2}{\mu_1}\cos^2\alpha\right)\cos\alpha}{(\alpha + n\pi)\sin\alpha + \frac{\beta_1^2}{c_n^2}\left(\sin^2\alpha + \frac{\mu_2}{\mu_1}\cos^2\alpha\right)\cos\alpha}\right] \qquad [4.42]$$

which produces the same curve as Equation 4.31, a differentiation of the frequency equation. The phase velocity is found by solution of the frequency Equation 4.22 and the half phase angle, α, is given by Equation 4.36.

Airy Phase

The local minimum in the group velocity curves shown in Figure 4.5(b) implies that a significant range of frequencies travel with a similar velocity. The associated amplified arrivals commonly seen in tele-seismic recordings have been termed the *Airy phase*. As the velocity contrast between the layer and the half-space increases, the Airy phase frequency decreases toward the fundamental frequency of the layer, f_0, and the minimum group velocity tends toward zero. For the special case when the lower medium is rigid ($\beta_2,\mu_2 \to \infty$), the n^{th} mode group velocity can be given by

$$U_n^{rigid} = \frac{\beta_1^2}{c_n} \qquad [4.43]$$

which tends toward zero as the phase velocity tends toward infinity at the Airy phase frequency, that now forms a lower cut-off value, f_{cn}, given by

$$f_{cn} = \frac{\beta_1}{4H}(2n+1) \qquad [4.44]$$

which is equivalent to the vertical resonant frequency of the layer, f_0, in Equation 4.19.

4.3.3 LOVE WAVES IN A MULTI-LAYERED HALF SPACE

Consider a homogeneous half-space overlain by M–1 horizontal homogeneous layers of depth h_m, and elastic parameters β_m, ρ_m, and μ_m. The M^{th} layer is the half-space with the elastic parameters β_M, ρ_M, and μ_M. Again we will let the input be an plane harmonic SH wave of frequency, $\omega = 2\pi f$, and wave number, $k = \omega/c$. The phase velocity or apparent horizontal velocity, c, of the wave in each layer is the same

$$c = \frac{\beta_1}{\sin\theta_1} = \frac{\beta_2}{\sin\theta_2} = ... = \frac{\beta_m}{\sin\theta_m} = ... = \frac{\beta_M}{\sin\theta_M} \qquad [4.45]$$

where θ_m is the angle of wave propagation in the m^{th} layer. The dispersion equation for a Love wave travelling in multiple layers may be written as (Haskell, 1953)

$$A_{21} = -\mu_M \gamma_M A_{11} \qquad [4.46]$$

where A_{21} and A_{11} are coefficients of the matrix A

$$A = \begin{bmatrix} A_{11} & A_{12} \\ A_{21} & A_{22} \end{bmatrix} = a_{M-1} a_{M-2} ... a_m ... a_1 \qquad [4.47]$$

and a_m is the Haskell-Thompson transfer matrix for layer m

$$a_m = \begin{bmatrix} \cos\alpha_m & i\mu_m^{-1}\gamma_m^{-1}\sin\alpha_m \\ i\mu_m\gamma_m\sin\alpha_m & \cos\alpha_m \end{bmatrix} \qquad m = 1,2,3,...,M-1 \qquad [4.48]$$

$$\alpha_m = kh_m\gamma_m \qquad [4.49]$$

$$\gamma_m = \begin{cases} +\sqrt{\dfrac{c^2}{\beta_m^2} - 1} & c > \beta_m \\ -i\sqrt{1 - \dfrac{c^2}{\beta_m^2}} & c < \beta_m \end{cases} \qquad [4.50]$$

For the case of a single layer over a half-space (M = 2), $A = a_1$, and the Love wave dispersion equation reduces to

$$\tan\alpha_1 = i\frac{\mu_2}{\mu_1}\frac{\gamma_2}{\gamma_1} \qquad [4.51]$$

which is equivalent to the fundamental-mode Love wave in Equation 4.23, where γ_1 and γ_2 are equivalent to Equations 4.24 and 4.25 respectively, and $h_1 = H$. The calculation of dispersion curves for more than one layer requires an iterative technique.

4.4 SUMMARY

The behaviour of waves at an interface depends heavily on their angle of incidence and the velocity contrast. Waves are totally reflected when incident on a stiffer material at angles greater than the critical. Total reflection is a frequency dependent process that shifts the phase of and displaces the reflected wavefront. In the case of SH waves trapped by total reflection within a soft surface layer, Love waves develop by constructive interference between repeatedly-reflected and in-phase wavefronts.

Love waves are dispersive and propagate horizontally with a frequency-dependent velocity. The apparent phase velocity, c, of pulses travelling along the surface is often significantly faster than the velocity of energy propagation, the group velocity, U. Some of the energy in a Love-wave is transported horizontally as an inhomogeneous (evanescent) wave, the amount being greater for low frequency motions. The above ideas are for Love waves that are fully set up within a layer extending to infinity is both directions. The following two chapters investigate the generation of a Love wave at the edge of a semi-infinite layer.

Chapter 5: THEORETICAL DEVELOPMENTS

Ray path and wavefront analyses are used to investigate SH-wave propagation at the plane edge of a semi-infinite soft layer (sediments) above a stiff half-space (rock), and to illustrate the mechanisms involved in the generation of a Love wave. Constructive interferences between plane undispersed wavefronts refracted from the base and edge are found to occur inside the layer. In Section 5.4 mathematical expressions are developed to calculate their transient positions. The analysis is then simplified to the cases of vertical incidence and a rectangular (vertical) edge, while the nature of the input wave is also discussed with a comparison between pulse and harmonic inputs. Finally, characteristic patterns of amplification at the edge of the layer due to edge-generated Love waves are proposed in Section 5.5.

5.1 PROBLEM GEOMETRY

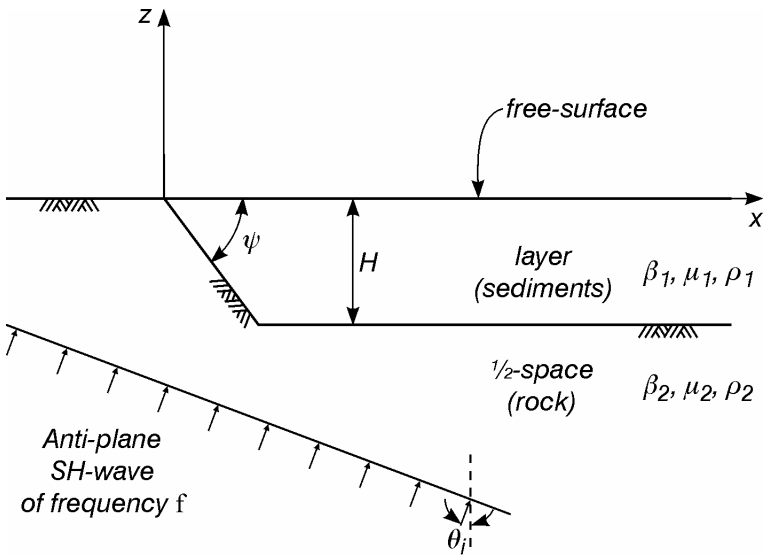

Figure 5.1: Geometry of the problem in Part II. A semi-infinite layer of depth *H* with various angles of edge-slope overlies a uniform half-space. The input is a plane SH wave with particle displacement parallel to the out-of-plane *y*-axis.

The geometry of the problem is shown in Figure 5.1. The layer has a thickness, H, and an edge-slope angle, ψ, in the range $[0 < \psi < \pi]$, measured clockwise from the horizontal (+ve

x-axis). The layer and half-space are both homogeneous and isotropic with shear-wave velocities and bulk densities given by β_1, β_2, and ρ_1, ρ_2, respectively. The incoming (direct) plane wave field is infinite in width and propagates toward the free surface with an angle of incidence, θ_i, in the range $[-\pi/2 < \theta_i < \pi/2]$ measured clockwise from the vertical (–ve *z*-axis).

Graphical results are presented in a non-dimensional form by taking the depth of the layer, *H*, as the characteristic distance to give dimensionless *x** and *z** coordinates

$$x^* = \frac{x}{H} \qquad [5.1]$$

$$z^* = \frac{z}{H} \qquad [5.2]$$

Shear wave velocities in the layer and half-space are normalised against β_1, respectively

$$\beta_1^* = \frac{\beta_1}{\beta_1} = 1 \qquad [5.3]$$

$$\beta_2^* = \frac{\beta_2}{\beta_1} \qquad [5.4]$$

Bulk densities are assumed equal in the layer and half-space ($\rho_1 = \rho_2$) such that the impedance ratio, *i*, is equivalent to both the shear-wave velocity ratio and the dimensionless velocity of the half-space

$$i = \frac{\rho_2 \beta_2}{\rho_1 \beta_1} = \frac{\beta_2}{\beta_1} = \beta_2^* \qquad [5.5]$$

The ratio of shear moduli is thus given by the square of the impedance ratio

$$\frac{\mu_2}{\mu_1} = \frac{\rho_2 \beta_2^2}{\rho_1 \beta_1^2} = i^2 \qquad [5.6]$$

The vertical travel-time of a shear wave through the layer, H/β_1, is taken as the characteristic time such that a dimensionless time, *t**, is given by

$$t^* = \frac{\beta_1 t}{H} = 4 f_0 t \qquad [5.7]$$

where f_0 is the fundamental vertical frequency of the layer. A dimensionless frequency, η, normalised against f_0, is defined as

$$\eta = \frac{f}{f_0} = \frac{4H}{\beta_1} f \qquad [5.8]$$

5.2 AN INTRODUCTION BY WAY OF A RAY-PATH ANALYSIS

Figures 5.2 and 5.3 show the propagation paths of rays that are incident at the sloping edge of a layer. The former shows an example where the edge-slope angle and angle of incidence are such that the incoming wave field is directly incident on the edge. The latter describes the opposite case where the edge of the layer lies in a shadow zone.

Clearly, in both examples, the edge initiates occurrences of both total reflection and diffraction, and generally points a significant proportion of the incoming wave field to propagate as a post-critically trapped SH wave in the positive x-direction. In addition, it can be seen that waves leaving the edge (either by refraction, total reflection or diffraction) will in general cross paths with the waves refracted or reflected up from the base.

For the case shown in Figure 5.2, waves are refracted into the layer from the edge at an angle θ_1^{e1} given by Snell's law

$$\sin\theta_1^{e1} = \frac{\beta_1}{\beta_2}\sin(\theta_i - \psi) \qquad [5.9]$$

and then arrive at the surface with an angle from the vertical given by $\psi + \theta_1^{e1}$. Waves refracted in from the base of the layer propagate upwards and meet the surface with an angle of incidence, θ_1^b, also given by Snell's law

$$\sin\theta_1^b = \frac{\beta_1}{\beta_2}\sin\theta_i \qquad [5.10]$$

Interference at the surface between the two refracted wave paths is thus always constrained to lie between x_1 and x_2.

$$x_1 = H\left[\tan(\pi/2 - \psi) + \tan\theta_1^b\right] \qquad [5.11]$$

$$x_2 = H\left[\tan(\pi/2 - \psi) + \tan(\psi + \theta_1^{e1})\right] \qquad [5.12]$$

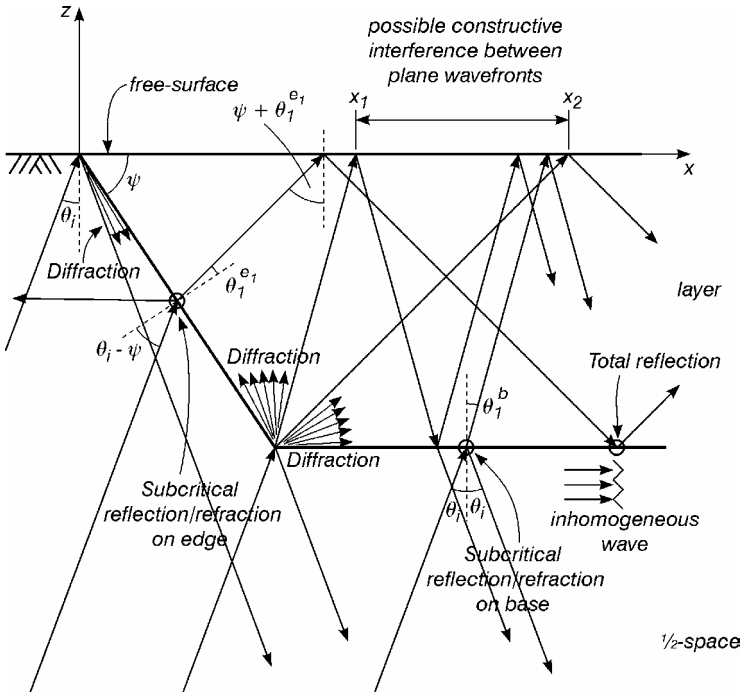

Figure 5.2: Ray path diagram of wave propagation for one possible combination of θ_i, ψ and β_2/β_1. In this case a homogeneous plane wave is refracted up towards the surface from both the edge and the base, while diffraction occurs within the layer at the lower vertex. The edge-refracted wave is subsequently trapped in the layer by total reflection.

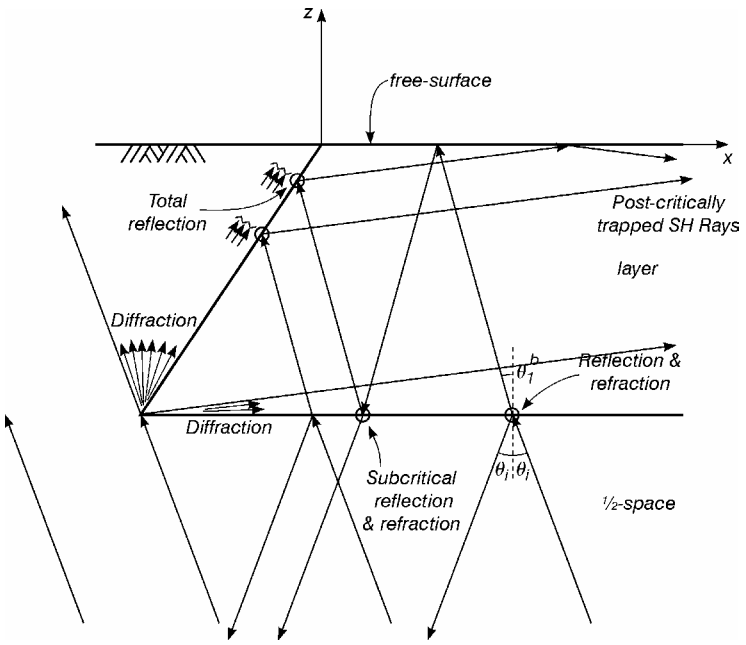

Figure 5.3: Ray path diagram of wave propagation for a second possible combination of θ_i, ψ and β_2/β_1. In this case constructive interference occurs at the surface between waves that have been dispersed by total reflection on the edge or diffraction at the vertices.

In Section 5.4, simple geometrical expressions are derived to determine the exact position of constructive interference between plane refracted wavefronts. Interference at the surface between waves that have been totally reflected or diffracted such as in Figure 5.3 is, however, a much more complex problem, and will be left for FEM modelling in the following chapter.

The characteristics of SH wave response at the edge is dependent on a number of variables:

1. The impedance ratio $\rho_2\beta_2/\rho_1\beta_1$, and velocity contrast, β_2/β_1, which determine the change of direction and amplitude of waves at the rock-soil interface.

2. The edge-slope angle, ψ.

3. The angle of incidence of the direct wavefield, θ_i.

4. The frequency of the input, f, which determines the characteristics of diffraction and total reflection.

Refraction is limited to occur along the base of the layer by the upward travelling direct wave, and along the edge of the layer by upward travelling direct wave and the downward travelling surface reflection of the direct wave. Diffraction is a frequency dependent scattering and phase shifting process that bends and spreads energy from the vertices of the edge. Diffraction may also occur in the stiff half-space near the vertices. The refracted and diffracted waves within the layer then set-up a dispersive Love wave by total reflection.

5.3 A WAVEFRONT ANALYSIS FOR PLANE INCIDENT WAVES

The propagation of plane wavefronts from the half-space into the layer is analysed for all possible angles of incidence, edge-slope angles, and velocity contrasts. The time variable is set such that $t_0 = 0$ occurs when the wavefront travelling up through the rock reaches the free surface at the edge of the layer ($x = 0$, $z = 0$), ie. the upper vertex. The direct wavefront thus reaches the lower vertex of the layer ($x = H/\tan\psi$, $z = -H$) at time, t_{r1}, given by

$$t_{r1} = \frac{H}{\beta_2}\frac{\sin(\theta_i - \psi)}{\sin\psi} \qquad [5.13]$$

which is negative in the usual case where $\theta_i < \psi$, and the wavefront meets the lower vertex some time before the origin. In the less common case of $\theta_i > \psi$, where the incidence is near horizontal or the edge-slope very flat, the wavefront may meet the origin first and t_{r1} will be positive. Refraction along the base of the layer occurs while $t > t_{r1}$ for $\theta_i > 0$, and while $t < t_{r1}$ for $\theta_i < 0$. Refraction may also be generated along the edge of the layer by the upward travelling wavefront when t lies between t_{r1} and t_0. The surface reflection of the direct wave in the rock then returns to meet the lower vertex at t_{r2}, given by

$$t_{r2} = \frac{H}{\beta_2}\left(1 + \frac{\tan\theta_i}{\tan\psi}\right)\cos\theta_i \qquad [5.14]$$

so that the refraction that may occur again along the edge by the downward travelling surface reflection when t lies between t_0 and t_{r2}. For vertical incidence (discussed later), t_{r1} and t_{r2} simplify to $-H/\beta_2$ and H/β_2, respectively.

Figures 5.4-5.7 illustrate the propagation of wavefronts at the edge for a representative range of edge-slope angles, $\psi = 30°$ (Figure 5.4), $\psi = 60°$ (Figure 5.5), $\psi = 90°$ (Figure 5.6) and $\psi = 120°$ (Figure 5.7). The first two will be defined as having normal edge slopes ($\psi < 90°$), while the third has a vertical edge ($\psi = 90°$) and the last a reverse or overhanging edge-slope ($\psi > 90°$). In addition, for each value of ψ, we look at three different angles of incidence, (a) $\theta_i = 45°$, (b) $\theta_i = 0°$ and (c) $\theta_i = –45°$. A velocity contrast, $\beta_2/\beta_1 = 5$, is used such that the critical angle is 11.537° (from Equation 4.12), measured clockwise from a line normal with the interface. Constructive interference between wavefronts is indicated with a small star, and a big star when it reaches the surface. Total reflection is shown with a black dot, while diffraction occurs at either the upper and lower vertices when a wavefront diverges from an interface.

A wavefront analysis such as this can account only for homogeneous undispersed plane waves within the system. The frequency dependent processes of diffraction and total reflection are described qualitatively. Leaky waves transmitted back out of the layer and the waves reflected back into the half-space from the layer are neglected, as their amplitudes are small and they add nothing to the response within the layer.

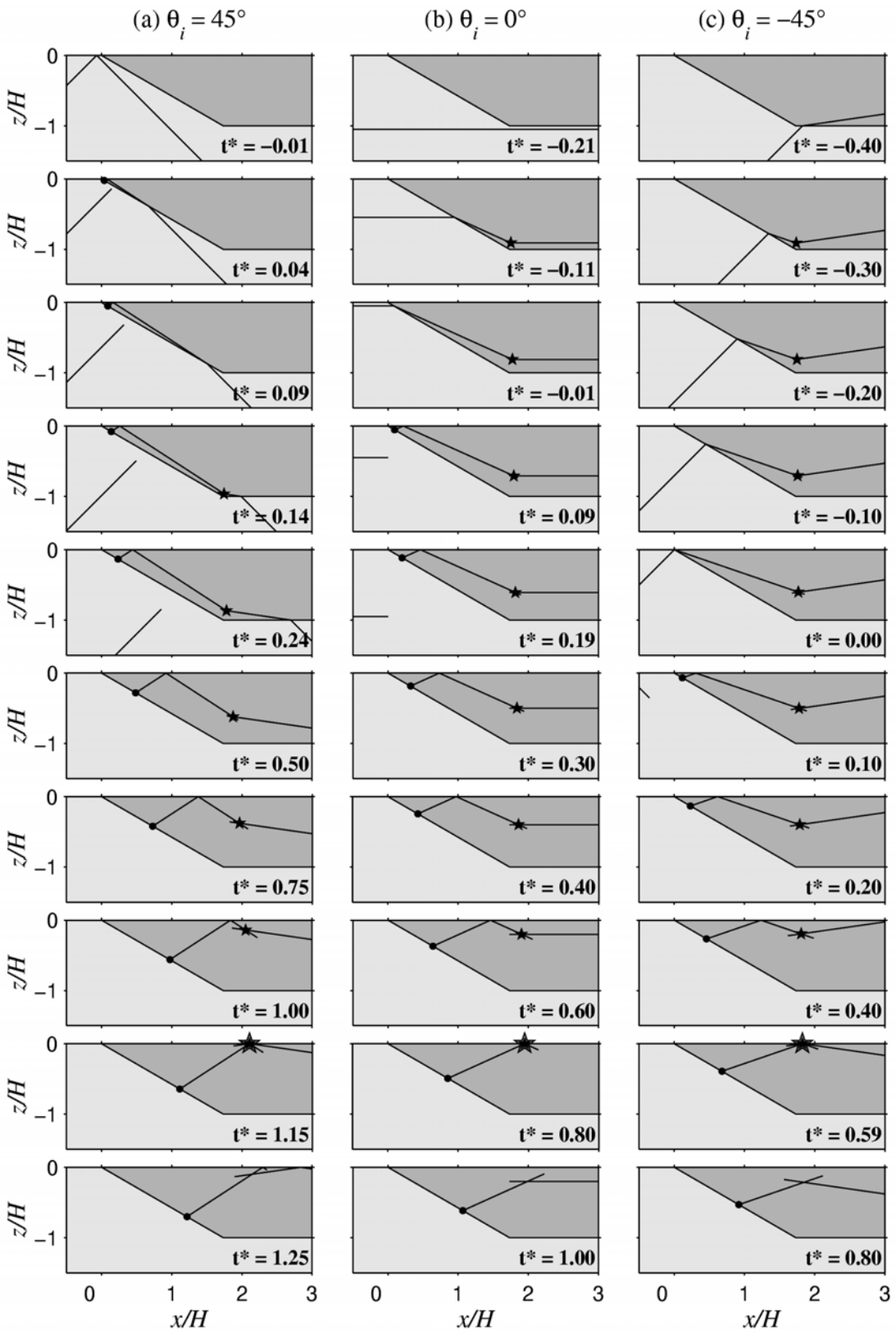

Figure 5.4: Wavefront anaylsis for SH propagation at a shallow-angled normal edge-slope, $\psi = 30°$ and $\beta_2/\beta_1 = 5$. Ten frames for each angle of incidence show the location of plane wavefronts at successive dimensionless time intervals ($t^* = \beta_1 t/H$).

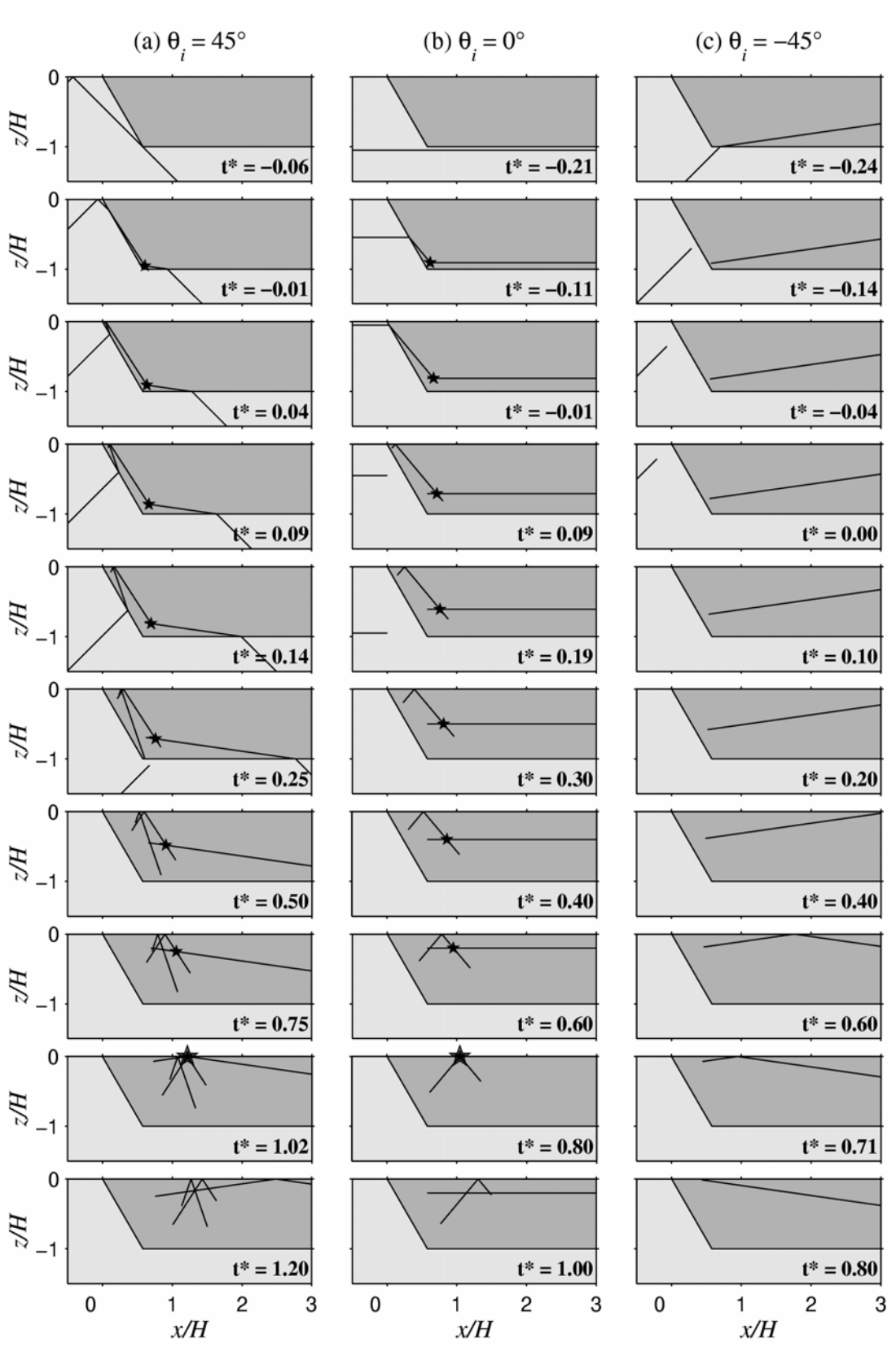

Figure 5.5: Wavefront anaylsis for SH propagation at a steeply-dipping normal edge-slope, $\psi = 60°$, and $\beta_2/\beta_1 = 5$. The transient location of wavefronts is shown with ten consecutive frames for each angle of incidence.

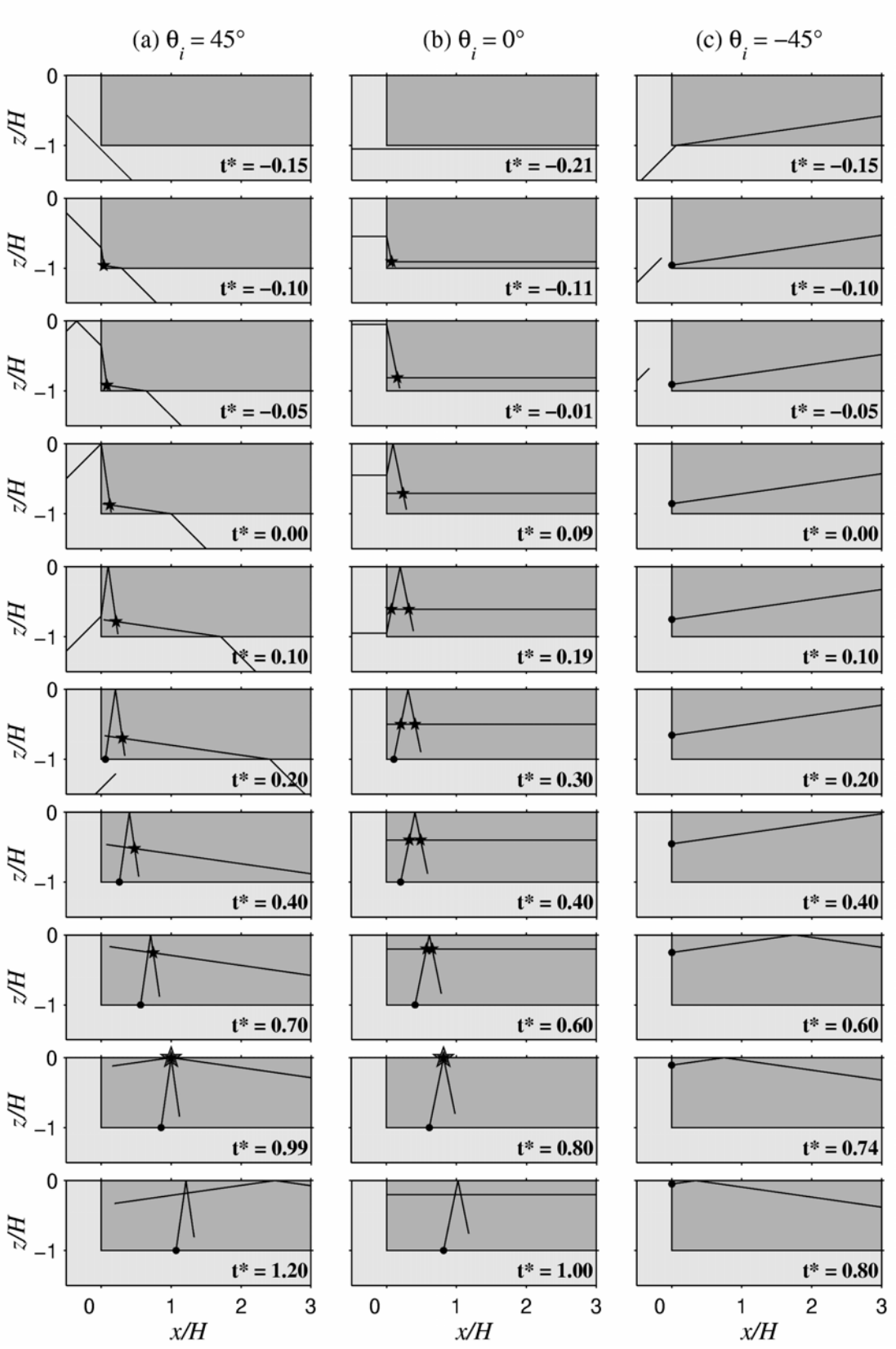

Figure 5.6: Wavefront anaylsis for SH propagation at a vertical (rectangular) edge-slope, $\psi = 90°$, and $\beta_2/\beta_1 = 5$. The transient location of wavefronts is shown with ten consecutive frames for each angle of incidence.

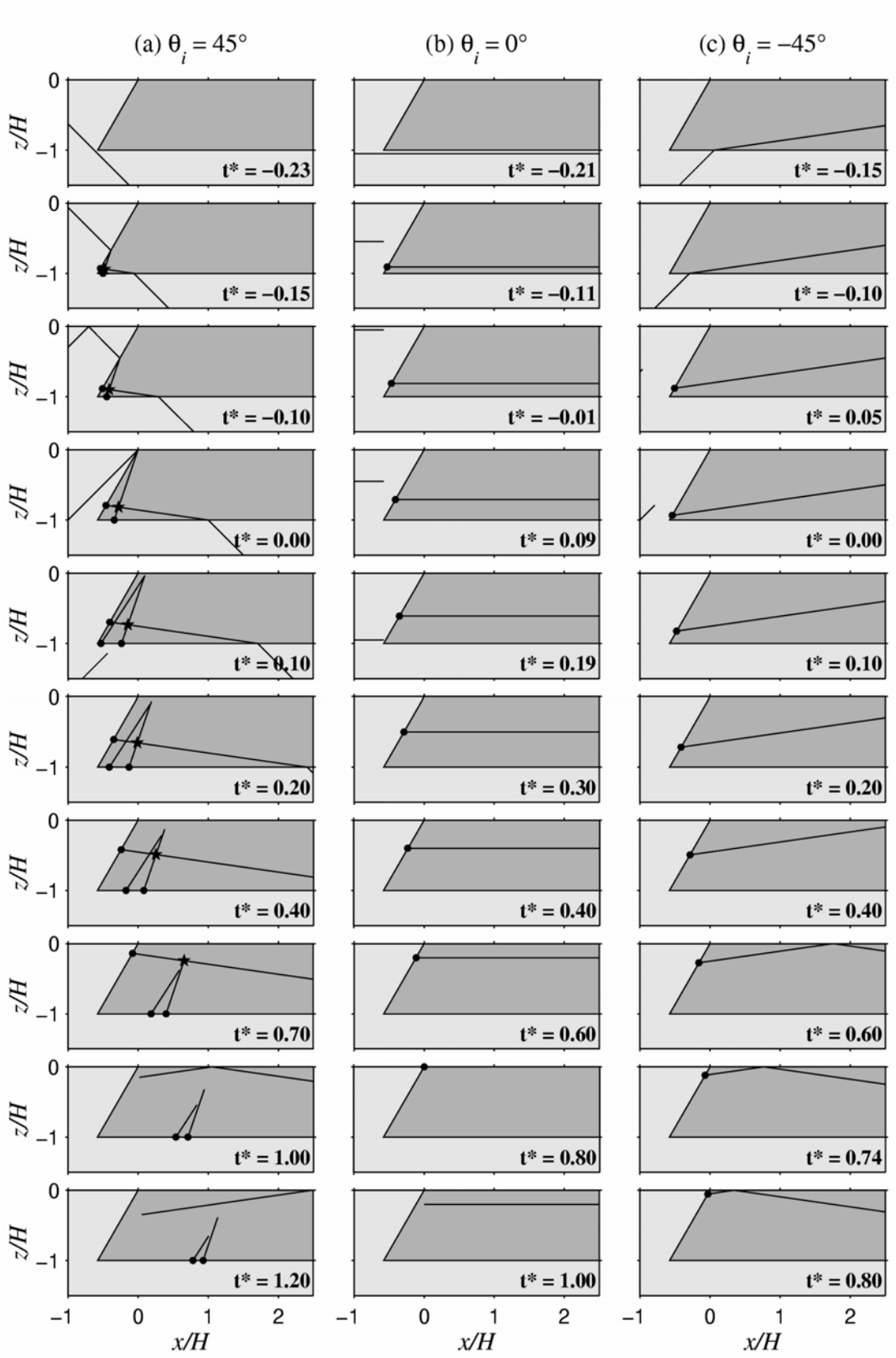

Figure 5.7: Wavefront anaylsis for SH propagation at a steeply-dipping reverse edge-slope, $\psi = 120°$, and $\beta_2/\beta_1 = 5$. The transient location of wavefronts is shown with ten consecutive frames for each angle of incidence.

5.3.1 REFRACTION AT THE BASE OF THE LAYER FROM THE UPWARD TRAVELLING WAVE

The horizontal impedance contrast along the base of the layer acts to transmit a wave into the layer for all angles of incidence,

$$-\pi/2 < \theta_i < \pi/2 \qquad \text{Condition [5.A]}$$

at an angle-of-refraction less than the critical, given by Equation 5.10. The wave refracted from the base is thus always constrained to subcritical reflection up and down within the layer The behaviour of this base-refracted wave at the edge of the layer, however, may involve total reflection or diffraction, dependent on the combination of the edge-slope angle and the angle of base-refraction:

[5.A-1] If edge-slope angle, $\psi < \theta_1^b + \pi/2$, the base-refracted wave does not touch the edge and diffraction occurs at the lower corner. This occurs in all six cases in Figures 5.4 and 5.5.

[5.A-2] If the edge-slope angle lies within the range $\theta_1^b + \pi/2 \le \psi < \theta_1^b - \theta_c + \pi$, the base-refracted wavefront is totally reflected at the edge, generating an inhomogeneous wave to travel up the edge toward the surface. For all angles of incidence, this generally occurs only when the edge is near vertical or overhanging, as in Figure 5.7, where total reflection on the edge is marked with a dot.

[5.A-3] In the rare case where $\psi \ge \theta_1^b - \theta_c + \pi$ and the edge is strongly overhung, the base-refracted wave is sub-critically reflected back into the layer and refracted into the overhanging edge.

5.3.2 INTERACTION BETWEEN THE UPWARD TRAVELLING DIRECT WAVE AND THE LAYER EDGE

The edge of the layer, unlike the base, may sometimes lie in a shadow zone and is not always directly hit by the upcoming wave front. This occurs when

$$\theta_i < \psi - \pi/2 \qquad \text{Condition [5.B]}$$

The resulting divergence causes diffraction in the rock at the lower vertex such as in Figure 5.7(b) and (c). In this case most of the action within the layer is due to the wave refracted from the base, or from a surface-reflected wave refracting at the edge (see Section 5.3.3).

A direct hit and subsequent refraction into the layer occurs thus only when

$$\theta_i \geq \psi - \pi/2 \qquad \text{Condition [5.C]}$$

The upward travelling wave in the half-space has an angle of incidence of $\theta_i - \psi$ with respect to the edge (Figure 5.2), and the wave transmitted into the layer has an angle of refraction given by Equation 5.9.

When the angle of edge-incidence is positive ($\theta_i > \psi$) the direct wavefront touches the top corner first and travels down the edge with a positive angle of refraction. More commonly, however, the angle of edge-incidence is negative ($\theta_i < \psi$) and the wavefront reaches the lower corner first before travelling up the edge with a negative angle of refraction. In both cases, the edge-refracted wavefront is now travelling semi-horizontally within the layer. Its behaviour depends on whether it is inclined upward to the surface, or downward to the basement interface.

[5.C-1] When $\psi < \pi/2 - \theta_1^{e1}$, the propagation is inclined upward to meet the free surface with an angle of incidence given by $\psi + \theta_1^{e1}$. In this case we get diffraction in the layer at the lower corner as the wavefront parts from the basement, and reflection at the free-surface. The wave that is reflected down from the free-surface may or may not have further contact with the edge.

> [5.C-1.1] If $2\psi < \pi/2 + \theta_1^{e1}$, the surface reflection of the edge-refracted wave again meets the edge and generates an inhomogeneous wave on total reflection. This occurs in the example shown in Figure 5.4.
>
> [5.C-1.2] If $2\psi > \pi/2 + \theta_1^{e1}$, the surface reflection of the edge-refracted wave diverges from the edge, and diffraction occurs at the upper corner of the layer, such as in Figure 5.5(a) and (b).

[5.C-2] When $\psi > \pi/2 - \theta_1^{e1}$, the propagation of the edge-refracted wavefront is inclined downward to meet the basement with an angle of incidence given by $\pi - \psi - \theta_1^{e1}$. This will

generally occur only with an overhanging edge and large angles of incidence such as in Figure 5.7(a). In most cases, total reflection will occur along the base, while for very steeply overhung edges subcritical conditions may exist along the basement (when $\psi > \pi - \theta_1^{e1} - \theta_c$).

5.3.3 INTERACTION BETWEEN THE DOWNWARD TRAVELLING SURFACE REFLECTION AND THE LAYER EDGE

When the direct wave in the rock reaches the free surface (on the left hand side of the model) it is reflected back down into the half-space, sometimes incident on the edge for a second time, and sometimes diverging from the edge. The downward travelling surface reflection diverges from the edge and diffraction occurs in the rock at the top corner when

$$\theta_i < \pi/2 - \psi \qquad \text{Condition [5.D]}$$

The diffracted energy spreads downward between the diverging wavefront and the edge, some of which is undoubtedly refracted into the layer at the critical angle.

On the other hand, the surface reflection is incident on the edge and refracts a second plane wave into the layer when

$$\theta_i > \pi/2 - \psi \qquad \text{and} \qquad \theta_i > 0 \qquad \text{Condition [5.E]}$$

This second angle of edge-incidence is given by $\pi - \theta_i - \psi$, and the second angle of edge-refraction by Snell's law

$$\sin\theta_1^{e2} = \frac{\beta_1}{\beta_2}\sin(\pi - \theta_i - \psi) \qquad [5.15]$$

Both these angles of incidence and refraction are positive, except for cases of strongly overhung edges and near-horizontal incidence. This second edge-refracted wavefront also travels semi-horizontally within the layer, inclined either slightly upward or downward.

[5.E-1] When $\psi < \pi/2 - \theta_1^{e2}$, the propagation is inclined upward to meet the free surface with an angle of incidence given by $\psi + \theta_1^{e2}$. This occurs only for a small range of normal edge-slopes and positive angles of incidence such as in Figure 5.5(a).

[5.E-1.1] If $2\psi < \pi/2 + \theta_1^{e2}$, the surface reflection of the edge-refracted wave again meets the edge and generates an inhomogeneous wave on total reflection.

[5.E-1.2] If $2\psi > \pi/2 + \theta_1^{e2}$, the surface reflection of the second edge-refracted wave diverges from the edge, and diffraction occurs at the upper corner of the layer as in Figure 5.5(a).

[5.E-2] In the much more common case when $\psi > \pi/2 - \theta_1^{e2}$, the propagation is inclined downward to meet the basement with an angle of incidence given by $\pi - \psi - \theta_1^{e2}$, which is usually large enough to produce total reflection.

5.3.4 DIFFRACTION AT THE LOWER CORNER FROM THE DOWNWARD TRAVELLING SURFACE REFLECTION

As a corollary of Condition [5.A], the downward travelling surface reflection in the rock is not incident on the basement interface, rather diffraction occurs at the lower corner of the layer, spreading energy through the rock along the base of the layer. A certain amount of energy is expected to refract into the layer at the critical angle. The amount of refracted energy being greatest for angles of incidence tending toward the horizontal ($\theta_i \to \pi/2$).

5.4 CONSTRUCTIVE INTERFERENCE BETWEEN UNDISPERSED EDGE- AND BASE-REFRACTED WAVEFRONTS

The location of constructive interference in the *x*-*z* plane between undistorted wavefronts is determined first for the general case, and the analysis is then simplified to the case of vertical incidence and still further to the case of a rectangular edge.

5.4.1 THE GENERAL CASE

Constructive interference occurs between the base-refracted wavefront and the wavefront refracted in from the edge by the *upward* travelling wave (hereafter called the 1st edge-refracted wavefront) only when Condition [5.C] is satisfied ($\theta_i \geq \psi - \pi/2$) and for $t > t_{r1}$. Another occurrence of constructive interference takes place between the base-refracted wavefront and the wavefront refracted in from the edge by the *downward* travelling wave

(hereafter called the 2nd edge-refracted wavefront) only when Condition [5.E] is satisfied satisfied ($\theta_i > \pi/2 - \psi$ and $\theta_i > 0$) and for $t > t_0$. Each of these is discussed in turn.

Constructive Interference with the First Edge-Refracted Wavefront

The point of constructive interference starts at the lower vertex and moves in a sloping linear path upward to the surface with a time-dependent position given by

$$x(t) = \left[H\left(\frac{\tan\theta_1^b}{\tan\theta_i} - 1 \right) + \beta_1 t \left(\frac{1}{\cos\theta_1^b} - \frac{1}{\cos(\psi + \theta_1^{e1})} \right) \right] \frac{1}{\tan\theta_1^b - \tan(\psi + \theta_1^{e1})} \qquad [5.16]$$

$$z(t) = \frac{\beta_1 t - x(t)\sin(\psi + \theta_1^{e1})}{\cos(\psi + \theta_1^{e1})} \qquad [5.17]$$

This constructive interference reaches the surface at time, t^c, and at a distance from the edge, x^c. These are best given by determining the movements of the edge-refracted and base-refracted wavefronts at the surface, and finding the time and distance at which their paths cross. The edge-refracted wave has an apparent horizontal velocity, c_x^{e1}, and time-dependent surface position, x^{e1}, given by

$$c_x^{e1} = \frac{\beta_1}{\sin(\psi + \theta_1^{e1})} \qquad [5.18]$$

and

$$x^{e1}(t) = c_x^{e1} t \qquad [5.19]$$

while the base-refracted wave has an apparent horizontal velocity, c_x^b, and time-dependent surface position, x^b, given by

$$c_x^b = \frac{\beta_1}{\sin\theta_1^b} \qquad [5.20]$$

and

$$x^b(t) = c_x^b t - \frac{H}{\tan\theta_1^b} + \frac{H}{\tan\theta_i} \qquad [5.21]$$

Constructive interference at the surface occurs when $x^{e1}(t) = x^b(t)$, at a time, t^c (the superscript denotes constructive interference), given by

$$t^c = \frac{\left(\frac{H}{\tan\theta_i} - \frac{H}{\tan\theta_1^b}\right)}{\left(\frac{\beta_1}{\sin(\psi + \theta_1^{e1})} - \frac{\beta_1}{\sin\theta_1^b}\right)} \qquad [5.22]$$

and a distance, x^c, given by

$$\begin{aligned} x^c &= c_x^{e1} t^c \\ x^c &= \frac{\beta_1 t^c}{\sin(\psi + \theta_1^{e1})} \end{aligned} \qquad [5.23]$$

which is in fact the solution to Equation 5.16 when $z = 0$.

For a given layer of depth, H, shear-wave velocity, β_1, and velocity contrast, β_2/β_1, the surface position, x^c, depends most strongly on the horizontal phase velocity of the edge-refracted pulse, c_x^{e1}. The phase velocity is, in turn, a function of the angle at which the edge-refracted pulse travels within the layer.

Equation 5.23 may be plotted in the ψ-θ_i plane with contour height representing the distance of constructive interference from the layer edge, x^c. The result is shown in Figure 5.8 for two different velocity contrasts. The blank region below the line $\theta_i = \psi - \pi/2$ represents Condition 5.B where the edge of the layer lies within a shadow zone of the incoming wavefront and a (plane) wave is unable to be refracted into the layer. The blank region in the top right corner represents the region where the edge-refracted wave does not touch the surface and travels down toward the base (Condition 5.C-2).

Changing the angle of incidence has little effect on the angle that the wave is refracted into the layer. Especially for high velocity contrasts, an input wave from any angle tends strongly toward the normal when entering the soft material. As θ_i varies between $-\pi/2$ and $+\pi/2$, the angle of refraction varies only between $-\theta_c$ and $+\theta_c$. The angle of the edge-slope on the other hand has a significant effect on the angle of propagation within the layer, especially for high velocity contrasts. As ψ varies between 0 and $\pi/2 - \theta_1^{e1}$ (Condition 5.C-1), the angle of propagation within the layer may vary between θ_c and $\pi/2$, such that the phase velocity of the edge refracted pulse, c_x^{e1}, may vary over the full range possible, between β_1 and β_2, and the distance x^c may vary between x_1 and ∞.

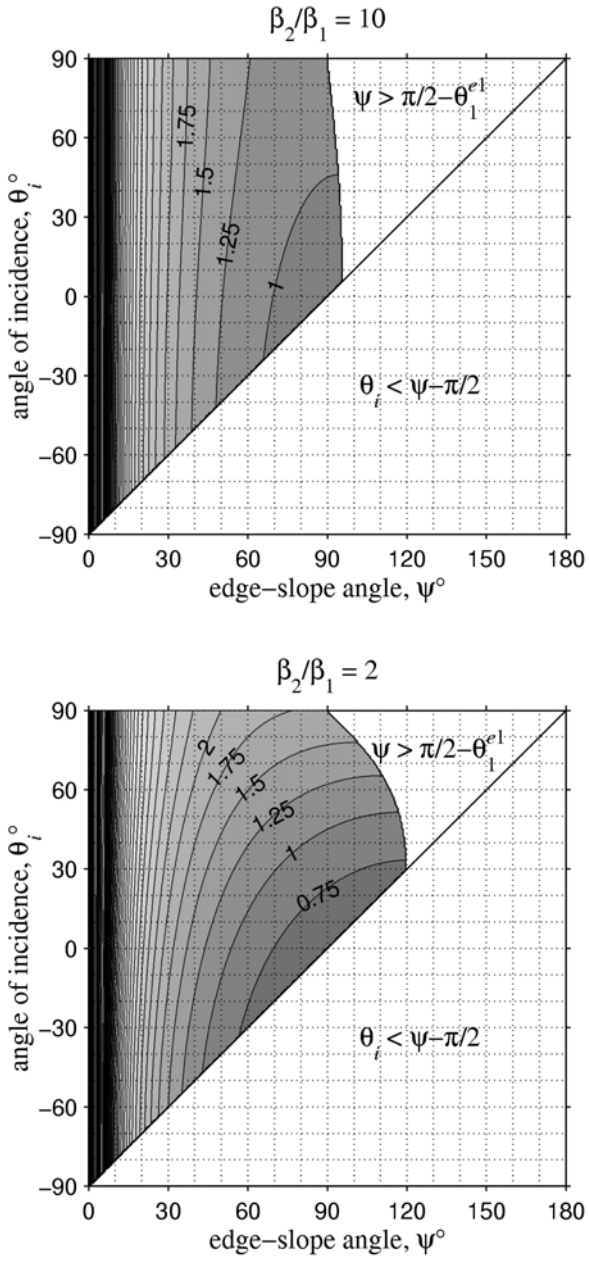

Figure 5.8: A graphical interpretation of Equation 5.23 for two different velocity contrasts. Contour height represents the distance, x^c, of constructive interference between undispersed refracted waves from the edge and base of the layer.

Constructive Interference with the Second Edge-Refracted Wavefront

The second edge-refracted wave has an apparent horizontal velocity, c_x^{e2}, given by

$$c_x^{e2} = \frac{\beta_1}{\sin(\psi + \theta_1^{e2})} \qquad [5.24]$$

which is always slower than c_x^{e1} because θ_1^{e2} is always greater than θ_1^{e1} (the latter being generally negative). The corresponding time-dependent surface position, x^{e2}, is given by

$$x^{e2}(t) = c_x^{e2} t \qquad [5.25]$$

such that constructive interference at the surface between the base-refracted wave and this second edge-refracted wave occurs when $x^{e2}(t) = x^b(t)$, at a time, t^{c2}, given by

$$t^{c2} = \frac{\left(\frac{H}{\tan\theta_i} - \frac{H}{\tan\theta_1^b}\right)}{\left(\frac{\beta_1}{\sin(\psi + \theta_1^{e2})} - \frac{\beta_1}{\sin\theta_1^b}\right)} \qquad [5.26]$$

and a distance, x^{c2}, given by

$$\begin{aligned} x^{c2} &= c_x^{e2} t^{c2} \\ x^{c2} &= \frac{\beta_1 t^{c2}}{\sin(\psi + \theta_1^{e2})} \end{aligned} \qquad [5.27]$$

which is always a lesser distance from the edge than x^c. Examples of this are Figures 5.5(a), 5.6(a) and (b) and 5.7(a). The occurrence of refraction along the edge by the downward travelling wavefront is, however, much less common than by the upward travelling wave. In addition to the narrow range of θ_i and ψ for which it can occur, there is commonly a hill-slope adjacent to the layer that will act to reflect direct waves away from the edge. When this second edge refraction does occur it often has a downward angle of propagation within the layer, and is more importantly associated with the constructive set-up of a love wave than with constructive interference at the surface.

Constructive interference is hence most important between the first edge-refracted wavefront and the base-refracted wavefront. It may only occur at the surface when Condition 5.C is satisfied, such that a edge-refraction travels at an angle upward toward the surface. Within the small range of parameters that will produce a upward-travelling second edge-refracted pulse (Condition 5.E), the constructive effect at the surface occurs very close to that which occurs for the first edge-refracted pulse. An example of this is shown in 5.5 (a).

5.4.2 THE CASE OF VERTICAL INCIDENCE

The preceding ideas will be reduced to the case of vertically incident wave pulses ($\theta_i = 0$), as a preamble to the numerical modelling of vertical incidence presented in the next chapter. We can define vertical travel-times of the shear wave from the base of the soft layer ($z = -H$) to the surface through the soft layer and rock, respectively

$$t_{S1} = \frac{H}{\beta_1} \qquad [5.28]$$

and

$$t_{S2} = \frac{H}{\beta_2} \qquad [5.29]$$

The upward travelling horizontal wavefront reaches the base of the layer at time $t_{r1} = -t_{S2}$. At time $t_0 = 0$, the wavefront reaches the surface through the rock across the whole left hand side of the model ($x \le 0$). The surface reflection of the direct wave then arrives back at $z = -H$ at time $t_{r2} = t_{S2}$.

On the way up, the direct wave is refracted into the layer from the edge for normal or vertical edge-slopes only ($0° < \psi \le 90°$). The upward travelling wave makes an angle of incidence with the edge that is equivalent to minus the edge-slope angle, $-\psi$, and the angle of refraction into the layer is correspondingly given by θ_1^{e1}, from Equation 5.1,

$$\sin\theta_1^{e1} = \frac{\beta_1}{\beta_2}\sin(-\psi) \qquad [5.30]$$

which is always negative. When the edge-slope is reverse ($90° < \psi < 180°$), diffraction occurs in the rock at the bottom vertex (eg. Figure 5.7b), and only a lesser amount of energy may be refracted from the edge at the critical angle. On the way back down from the surface, the direct wave does not come into contact with the edge, unless the edge is vertical, in which case there is grazing incidence and a second edge-refracted wave enters the layer with a refraction angle $\theta_1^{e2} = \theta_c$, as in Figure 5.6(b).

Since the incidence is vertical, the wavefront transmitted into the layer through the base undergoes no change in direction, and travels up though the layer to reach the surface at a time given by $t_{S1} - t_{S2}$. For normal edge-slopes, the upward travelling wave in the layer

generates diffraction at the lower vertex, while for reverse edge-slopes there is total reflection generated on the hanging wall.

Constructive Interference

Constructive interference between the (first) edge-refracted and base-transmitted wavefronts occurs first at the lower vertex, and travels up through the layer with parametric coordinates given by

$$x(t) = \frac{H}{\tan\psi} + \beta_1\left(t + \frac{H}{\beta_2}\right)\left(\frac{\cos(\psi + \theta_1^{e1}) - 1}{\tan(\psi + \theta_1^{e1})} + \sin(\psi + \theta_1^{e1})\right) \qquad [5.31]$$

$$z(t) = \beta_1\left(t + \frac{H}{\beta_2}\right) - H \qquad [5.32]$$

The point of construction now reaches the surface at the same time as the base-transmitted wavefront, at a time, t^c, given by

$$t^c = t_{S1} - t_{S2} = \frac{H}{\beta_1} - \frac{H}{\beta_2} \qquad [5.33]$$

and at a distance x^c from the edge of the layer now given by

$$x^c = \frac{\beta_1}{\sin(\psi + \theta_1^{e1})}\left(\frac{H}{\beta_1} - \frac{H}{\beta_2}\right) \qquad [5.34]$$

Equation 5.34 is essentially the product of the horizontal phase velocity of the edge-refracted wave from Equation 5.18 and the time it has to travel across the layer before the base-refraction arrives at the surface ($t_{S1} - t_{S2}$).

5.4.3 THE CASE OF A RECTANGULAR EDGE

The mechanism of Love wave generation and constructive interference between plane refracted wave fronts can be further illustrated by considering the most simple of cases, that of a plane SH wave pulse propagating vertically upward toward a rectangular edge ($\theta_i = 0$ and $\psi = \pi/2$) as shown in Figure 5.6(b). Both the up-going and down-going waves in the rock travel at grazing incidence and act like a head wave with respect to the vertical

edge. The edge-refracted wavefronts in this case, form a single continuous wavefront and enter the basin with angles of refraction given by

$$\theta_1^{e1} = -\theta_c \qquad [5.35]$$

and

$$\theta_1^{e2} = +\theta_c \qquad [5.36]$$

where θ_c is the angle of critical refraction given in Equation 4.12. The horizontal phase velocity of both refracted pulses are thus equal and given by

$$c_x^{e1} = \frac{\beta_1}{\sin\left(\pi/2 + \theta_1^{e1}\right)} = \frac{\beta_1}{\cos\theta_c} \qquad [5.37]$$

$$c_x^{e2} = \frac{\beta_1}{\sin\left(\pi/2 + \theta_1^{e2}\right)} = \frac{\beta_1}{\cos\theta_c} \qquad [5.38]$$

while their vertical phase velocities are of equal magnitude but in opposing directions

$$c_z^{e1} = \frac{\beta_1}{\sin\theta_c} = \beta_2 \qquad [5.39]$$

$$c_z^{e2} = \frac{-\beta_1}{\sin\theta_c} = -\beta_2 \qquad [5.40]$$

such that the first edge-refracted wave travels at an angle up toward the surface while the second travels at an angle down towards the lower interface.

Constructive Interference

Constructive interference involving the first edge-refracted pulse begins at time t_{r1} as soon as it enters the soft layer from the lower corner and interacts with the vertically propagating direct pulse. This point of interference moves away from the lower corner with a time-dependant position given by

$$x(t) = \frac{\beta_1}{\cos\theta_c}\left(1 - \frac{\beta_1}{\beta_2}\right)\left(t + \frac{H}{\beta_2}\right) \qquad [5.41]$$

$$z(t) = \beta_1 t - H\left(1 - \frac{\beta_1}{\beta_2}\right) \qquad [5.42]$$

Constructive interference between the second edge-refracted pulse and the slowly propagating base-transmitted wave occurs only after the up-going direct wave in the layer passes the down-going reflected wave in the rock when

$$t > \frac{H}{(\beta_1 + \beta_2)}\left(1 - \frac{\beta_1}{\beta_2}\right) \qquad \text{Condition [5.F]}$$

and has a time-dependant position given by

$$x(t) = \frac{\beta_1}{\cos\theta_c}\left[\left(1 + \frac{\beta_1}{\beta_2}\right)t - \left(1 - \frac{\beta_1}{\beta_2}\right)\frac{H}{\beta_2}\right] \qquad [5.43]$$

$$z(t) = \beta_1 t - H\left(1 - \frac{\beta_1}{\beta_2}\right) \qquad [5.44]$$

The point of constructive interference reaches the surface (z = 0) at time t^c, given by Equation 5.33, which when substituted into either Equation 5.41 or 5.43, gives a distance, x^c, out from the vertical edge,

$$x^c = \frac{\beta_1}{\cos\theta_c}\left(\frac{H}{\beta_1} - \frac{H}{\beta_2}\right) \qquad [5.45]$$

which is again the product of the phase velocity of the edge-refracted wave and the difference in time between the surface arrivals of the direct and base-refracted waves.

Constructive Interference with Vertically Reflected Waves within the Layer

Further constructive and destructive interferences may occur at successive intervals of distance and time across the basin between the edge-refracted pulse and vertical reflections of the base refracted pulse. The r^{th} reflection arrives back at the surface in phase with the original at time $t_{SR,r}$, given by

$$\begin{aligned} t_{SR,r} &= t_{S1} - t_{S2} + \frac{4H}{\beta_1}r \\ &= \frac{H}{\beta_1}(1 + 4r) - \frac{H}{\beta_2} \qquad r = 0,1,2,\ldots < \tfrac{1}{4}(\beta_2/\beta_1 - 1) \end{aligned} \qquad [5.46]$$

The condition on r is imposed because only a certain number of vertical reflections may occur before the edge-refracted wavefront is completely reflected down from the surface. The aforementioned wavefront may only be seen at the surface while

$$t < t_{r1} + \frac{H}{\beta_1 \sin\theta_c} = \frac{H}{\beta_2}\left(\frac{\beta_2^2}{\beta_1^2} - 1\right) \qquad \text{Condition [5.G]}$$

and thus constructive interference may only be seen at the surface while

$$t^c = t_{SR,r} < \frac{H}{\beta_2}\left(\frac{\beta_2^2}{\beta_1^2} - 1\right) \qquad \text{Condition [5.G-1]}$$

The surface positions of the constructive interference with the r^{th} reflected arrivals and the edge-refracted wavefront occur at successive distances given by

$$x_r^c = \frac{\beta_1}{\cos\theta_c}\left(\frac{H}{\beta_1} - \frac{H}{\beta_2} + \frac{4H}{\beta_1} r\right) \qquad r = 0,1,2,... < \tfrac{1}{4}\left(\beta_2/\beta_1 - 1\right) \qquad [5.47]$$

the same condition on r implies that

$$x_r^c < \frac{H}{\tan\theta_c} \qquad \text{Condition [5.G-2]}$$

For example, in the case of a velocity contrast, $\beta_2/\beta_1 = 10$, r is required to be less than 2.25, such that there will be two additional points of surface constructive interference between the first edge-refracted wavefront and the base-reflected wavefronts, as well as the initial point of construction ($r = 0$). These occur at positions and times given by ($x_0^c = 0.905H$, $t_0^c = 0.9H/\beta_1$), ($x_1^c = 4.905H$, $t_1^c = 4.9H/\beta_1$) and ($x_2^c = 8.905H$, $t_2^c = 8.9H/\beta_1$). The edge-refracted wavefront is then completely reflected below the surface at ($x = 9.950H$, $t = 9.900H/\beta_1$).

5.4.4 THE CASE OF MULTIPLE LAYERS

Here we take the case of a system of M–1 homogeneous horizontal layers extending to infinity in the positive x-direction from the edge. A simple extension of the previous analysis in Section 5.4.2 where the angle of incidence is vertical ($\theta_i = 0°$) gives travel times through the layered sediments and half-space, respectively

$$t_{S1} = \frac{h_1}{\beta_1} + \frac{h_2}{\beta_2} + \ldots + \frac{h_m}{\beta_m} + \ldots + \frac{h_{M-1}}{\beta_{M-1}} \qquad [5.48]$$

$$t_{S2} = \frac{H}{\beta_M} \qquad [5.49]$$

where h_m and β_m are the depth and shear-wave velocity of the m^{th} layer, and the total depth of all the layers is given by $H = h_1 + h_2 + \ldots + h_m + \ldots + h_{M-1}$. The M^{th} layer refers to the half-space. The distance, x^c, out from the edge where constructive interference occurs between undispersed wavefronts is thus given by

$$x^c = \frac{\beta_1}{\sin(\psi + \theta_1^{e1})}\left[\frac{H}{\beta_M} - \left(\frac{h_1}{\beta_1} + \frac{h_2}{\beta_2} + \ldots + \frac{h_m}{\beta_m} + \ldots + \frac{h_{M-1}}{\beta_{M-1}}\right)\right] \qquad [5.50]$$

where ψ and θ_1^{e1} are edge-slope angle and angle of refraction associated with the edge of the top layer. The constructive distance is still a function of the difference in travel times through the rock and sediments, and the apparent horizontal velocity of the edge-refracted wave in the top layer.

5.4.5 ON THE NATURE OF THE INPUT MOTION

For a train of direct wave pulses arriving through the half-space, a corresponding train of edge-refracted pulses is generated in the layer. The 1st edge-refracted pulse may construct with the 1st, 2nd, 3rd, 4th, … and m^{th} pulse of the base-refracted wave train as it travels further out from the edge. In a similar fashion, the 2nd, 3rd, 4th, … and n^{th} pulses of the edge-refracted wave train may interact with the whole suite of pulses in the base refracted wave. The net effect of this would likely be a continuously amplified broad width of ground shaking adjacent to the edge.

For simplicity we will consider a vertically propagating plane input of harmonic SH waves of frequency f. The 1st peak (m = 1) in the harmonic wave train reaches the base of the sediments ($z = -H$) below the ground surface at time $t = t_{r1}$. The 2nd peak of the same sign (m = 2) arrives at $z = -H$ one period later at time $t = t_{r1} + T$, where $T = 1/f = 2\pi/\omega$. Thus the m^{th} peak arrives at the base of the sediments at a time given by $t_{r1,m}$

$$t_{r1,m} = \frac{2\pi}{\omega}(m-1) - \frac{H}{\beta_2} \qquad m = 1,2,3,\ldots\infty \qquad [5.51]$$

On the down-thrown side of the basin edge the m^{th} pulse arrives at the surface through the sediments at time $(t_{S1} - t_{S2})_m$, while on the up-thrown side it arrives through the rock at time $t_{0,m}$,

$$(t_{S1} - t_{S2})_m = \frac{H}{\beta_1} - \frac{H}{\beta_2}\frac{2\pi}{\omega}(m-1) \qquad [5.52]$$

$$t_{0,m} = \frac{2\pi}{\omega}(m-1) \qquad [5.53]$$

at which time the corresponding harmonic train of horizontally propagating edge-refractions sets out across the surface of the sediments with a phase velocity, c_x^{e1}, given in Equation 5.18. Letting the m^{th} direct arrival generate the n^{th} surface wave pulse, the n^{th} pulse will have travelled a distance x across the basin at time t_n, given by

$$t_n = \frac{x}{c_x^{e1}} + \frac{2\pi}{\omega}(n-1) \qquad n = 1,2,3,...\infty \qquad [5.54]$$

Constructive interference occurs when the m^{th} peak in the direct arrival and the n^{th} pulse in the surface wave arrive simultaneously at the same location, $x^c_{m,n}$, out from the basin edge. By setting $t_n = (t_{S1} - t_{S2})_m$ and solving for x we get

$$x^c_{n,m} = c_x^{e1}\left(\frac{H}{\beta_1} - \frac{H}{\beta_2} + \frac{2\pi}{\omega}(m-n)\right) \qquad [5.55]$$

In practice, both n and m will have upper bounds placed on them at the point where the edge-refracted wave is completely reflected back down from the surface, as in the case of interference from sequential reflections (Condition 5.G).

The situation may be further complicated by considering the effect of vertical reflections of the direct arrival within the soft layer. The r^{th} reflection of the m^{th} direct pulse reappears with the same sign at the ground surface at time $t_{SR,m,r}$ given by

$$t_{SR,m,r} = t_{S1,m} + \frac{4H}{\beta_1}r \qquad [5.56]$$

and constructive interference occurs between these reflected arrivals and the n^{th} pulse of the surface wave when $t_n = t_{SR,m,r}$, and at a distance from the edge given by

$$x^{c}_{n,m,r} = c_x^{e1}\left(\frac{H}{\beta_1} - \frac{H}{\beta_2} + \frac{2\pi}{\omega}(m-n) + \frac{4H}{\beta_1}r\right) \qquad [5.57]$$

Thus for a given harmonic input frequency, we can determine the phase velocity of the edge-refracted pulses, c_x^{e1}, and predict a whole suite of locations of constructive interference measured from the edge, so long as the edge-refracted pulse exists at the surface.

5.5 SURFACE RESPONSE DUE TO AN EDGE-GENERATED LOVE WAVE

While Love waves travel away from the edge with the dispersive characteristics described in Section 4.3.2, the presence of the edge creates unique patterns at the surface in both the time and frequency domains. Here we propose theoretical patterns of displacement and frequency amplification set up by edge-generated Love waves.

5.5.1 A PATTERN IN THE TIME-DOMAIN

For any given harmonic (single frequency) input, the relationships in Section 4.3.2 may be used to calculate a phase velocity, c, and a group velocity, U. For all frequencies, the n^{th} mode phase velocity is always greater than or equal to the n^{th} mode group velocity ($c_n \geq U_n$). The energy of the Love wave travels with a constant average velocity given by the group velocity. Nevertheless, it is the phase velocity of pulses travelling along the surface that will be observed in seismograms. And each phase must be constrained to last for only a short while at the surface, such that a set of parallel phases develops, the centroid of which travels across the basin at the group velocity.

Figure 5.9 displays the dispersion characteristics and travel paths of Love waves at the edge of a layer. The slope of lines is representative of velocity. Plots (a) and (d) show fundamental-mode dispersion curves for two different shear-wave velocity contrasts. We make the assumption that the energy centroid of the Love wave leaves the edge of the layer ($x = 0$) at $t = 0$, and look at the pattern of energy propagation from the edge in a dimensionless x-t plane.

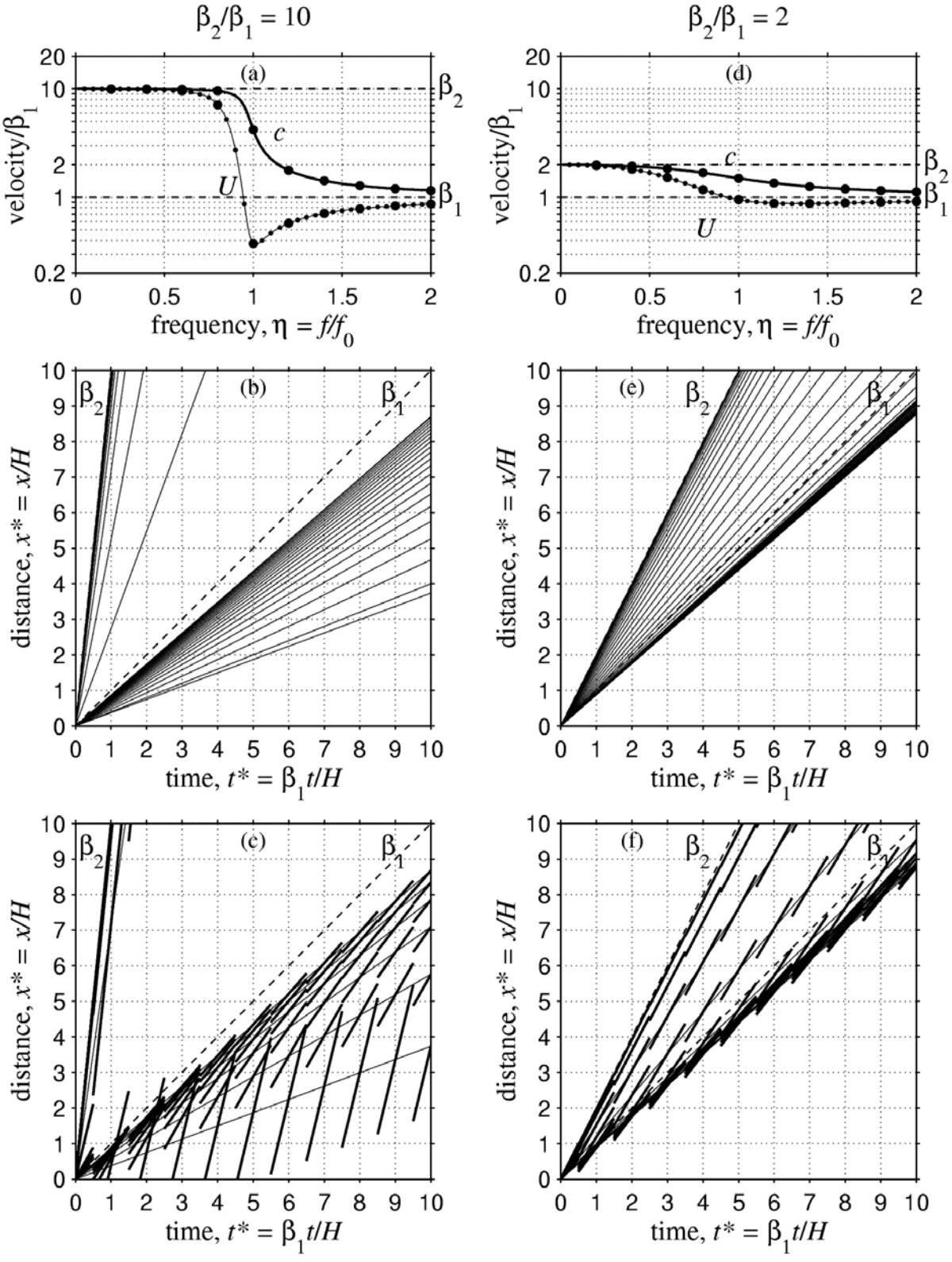

Figure 5.9: Love wave propagation in the time domain from a point source for two different velocity contrasts. Plots (a) and (d) show dispersion curves, (b) and (e) the distribution of group velocity, while (c) and (f) show the proposed pattern of phase velocity (dark lines) observed in surface seismograms, plotted atop an even distribution of group velocity (thin lines).

At frequency intervals of 0.05 (marked by small dots on the group velocity curves), discrete values of group velocity have been plotted on *x*-*t* axes (b) and (e). The slopes of β_1 and β_2 are also shown. Most of the low-frequency energy travels with a velocity at or just less than β_2, while frequencies greater than $\sim f_0$ ($\eta = 1$) travel at a velocity less than the shear-wave velocity of the layer, β_1. The frequency associated with the minimum point on the group velocity curve is the Airy phase frequency.

The lower plots (c) and (f) show a likely pattern of phase paths plotted atop a set of group velocity slopes at frequency intervals of $0.2f_0$ (marked by the large dots on axes (a) and (d)). While the group velocity associated with the Airy phase is often significantly lower than β_1, the associated phase velocity slope is significantly greater than β_1. At low frequencies both the phase velocity and group velocity tend toward β_2, while at high frequencies they both tend toward β_1.

The pattern shown is what we would expect to see from a point source of Love waves, initiated at $x = 0$ and $t = 0$, and containing an evenly spaced set of discrete harmonic frequencies. In the case of a high impedance ratio (Figure 5.9a) the interaction between frequencies travelling at different velocities creates (apparently) flattening lines of phase velocity curving from the Airy phase velocity to the shear wave velocity of the layer. In the low impedance ratio case, there are (apparently) steepening lines of phase velocity between β_1 and β_2. The situation could be complicated with the inclusion of higher modes of Love waves. The pattern is also likely to be strongly dependent on the shape and frequency content of the input waves.

5.5.2 A PATTERN IN THE FREQUENCY DOMAIN

A Love wave is in essence a constructive interference pattern set up between totally reflected SH waves in the layer. The edge of the layer is required to be a nodal point in the standing resonant pattern. Further nodes occur at wavelength intervals across the layer from the edge such that the i^{th} nodal (N) point belonging to the n^{th} mode Love wave occurs at a frequency-dependent position given by

$$x_{ni}^{N} = \lambda_n i \qquad n, i = 0,1,2,...\infty \qquad [5.58]$$

while the m^{th} extremum (E) point (antinode) occurs at

$$x_{ni}^{E} = \lambda_n (i + 0.5) \qquad n, i = 0,1,2,...\infty \qquad [5.59]$$

where λ_n is the frequency-dependent n^{th} mode Love wavelength given by

$$\lambda_n = \frac{c_n}{f} \qquad [5.60]$$

and c_n is found by solution of the dispersion equation (4.22). The extremum lines defined by Equation 5.45 are plotted on dimensionless axes in Figure 5.10. The first three modes are shown. At the cut-off frequency of the nth mode, f_{cn}, a maximum cut-off wavelength, λ_{cn} is defined by

$$\lambda_{cn} = \frac{c_n}{f_{cn}} \qquad [5.61]$$

The cut-off wavelength of the fundamental mode has a value of infinity, while for higher modes a real cut-off frequency exists and can be seen by the flaying branches in Figure 5.10.

5.6 DISCUSSION

The edge sets up refracted, diffracted, and totally reflected wave fields within the layer. Constructive interference occurs between base and edge-refracted pulses, and reaches the surface some distance in from the edge. At the same time, total reflection on the base and edge of the layer and diffraction at the vertices generates frequency-dependent dispersion. Constructive interference between totally reflected wavefronts eventually sets up a Love wave that travels away from the edge.

In Sections 5.2 and 5.3, SH-wave propagation at the edge was qualitatively analysed in order to define the mechanisms of reflection, refraction, total reflection and diffraction that occur at the edge. In Section 5.4 the occurrence of constructive interference between undispersed wavefronts was analysed in detail, with disregard to the frequency-dependent mechanisms of Love-wave set-up which are known to occur. In Section 5.5 patterns of amplification by Love waves travelling away from the edge were proposed, assuming that the dispersive Love wave develops immediately at the edge.

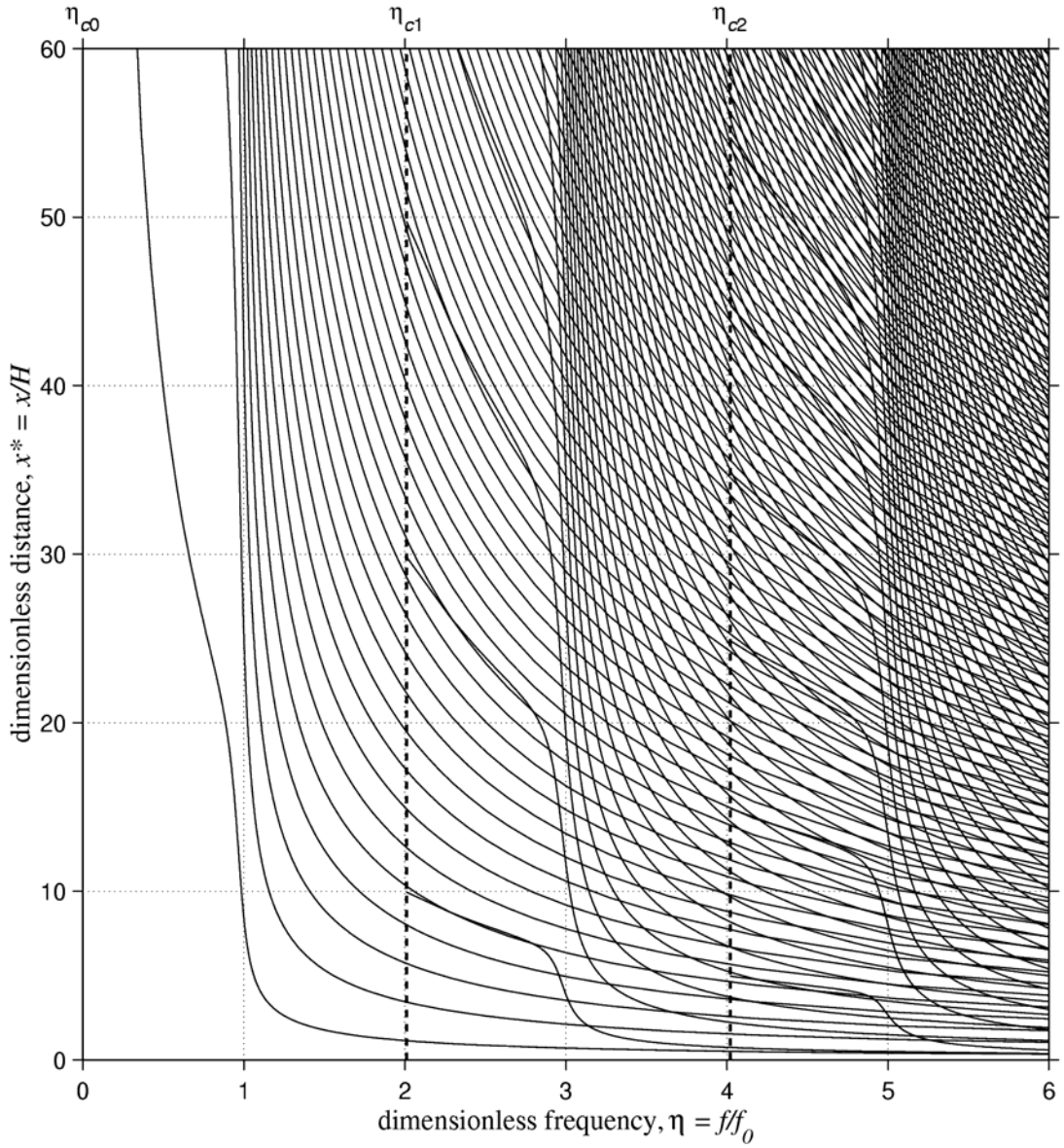

Figure 5.10: A proposed pattern of extremum lines in the interference pattern resulting from an edge-generated Love wave for $\beta_2/\beta_1 = 10$ and $\rho_2/\rho_1 = 1$. The distance between extremum lines is equivalent to the wavelength.

5.6.1 DEVELOPMENT OF A LOVE WAVE

The largest uncertainty in the above analyses is the speed with which the dispersive Love wave develops at the edge. Undoubtedly it will be determined by the characteristics and propagation paths of the diffracted and refracted wavefronts within the layer, and hence a function of the frequency content of the input, as well as the relative angles of edge-slope and incidence and the velocity contrast which determine the angle of refraction and the

critical angle. A rapidly set-up Love wave may mask the effect of constructive interference between undispersed wavefronts, while a slowly set-up Love wave will not show the characteristics proposed in Section 5.4.

Since Love waves are in essence a horizontally propagating mode of constructive interference between totally reflected wavefronts trapped within the layer, they can only be set-up after more than two successive reflections, once at the free surface and once at the base of the layer, as shown in Figure 4.4. For a wavefront to be post-critically trapped within the layer, it must be persuaded to travel sub-horizontally by refraction (Figure 5.2) or total reflection (Figure 5.3) from the edge, or diffraction from the vertices.

Diffraction (Figures 5.2 and 5.3) will usually emit a dispersed wavefront into the layer as soon as the first edge-refracted wavefront is generated at the lower vertex, at time t_{r1}. The diffracted rays travel at a frequency-dependent angle with a velocity, β_1. The apparent horizontal phase velocity of these diffracted rays is thus frequency-dependent, yet it will generally take more than one travel-time through the layer before any frequency dependent effect from the lower vertex will be seen at the surface. It would then be expected that the diffracted wavefield also makes at least two successive reflections before a Love wave can develop.

5.6.2 AMPLIFICATION BY CONSTRUCTIVE INTERFERENCE AT THE EDGE

Interference between *undispersed* edge-refracted and base-refracted wavefronts may occur only over half the range of possible incidence angles and edge-slope angles, when the input is directly incident on the edge, and then it only reaches the surface when the edge-refracted pulse is set to travel up toward the surface. Its range of occurrence is shown by the shaded area in Figure 5.8. On the other hand, it is clear (with reference to Figures 5.2 and 5.3) that constructive interference between *dispersed* (diffracted or totally-reflected) wavefronts will occur for all angles of incidence and edge-slope angles. While we can predict the timing and position of the former with the neat geometrical expressions developed in Section 5.3, it is important to understand that constructive edge-amplification also likely to be highly dependent on dispersive effects.

In the wavefront analysis in Sections 5.3 and 5.4, it was asserted that there was only one peak in the input and hence only one wavefront. In contrast, any real seismic motion

contains a multitude of peaks of various shape and timing. With a single-peak input, constructive interference at the surface occurs only for an instant in time and space as the base-refracted wave constructs with edge-refracted wave, creating a unique position across the layer where peak ground motions are amplified. With a multi-peaked input, however, a complex pattern of interference is likely to occur anywhere out from the edge and the nature of amplification is highly dependent on the frequency content and timing of peaks.

Further constructive interference may occur at successive distances between horizontally travelling wavefronts and vertical reflections of the base-refracted wave. Such later episodes of amplification by constructive effects are, however, likely to be counterbalanced by deamplification due to the dispersive spreading of energy by the surface wave and the loss of energy due to material damping and subcritical leakage into the half-space.

A second assertion made in the wavefront analysis is that the wavelength is small compared to the depth of the layer such that there is no interference between subcritically-trapped base-refracted waves. Low frequency input pulses are thus expected to behave quite differently in that the prescribed constructive effects may be masked by the aforementioned interference.

5.6.3 DESTRUCTIVE INTERFERENCE BY WAVEFRONTS TRAVELLING PARALLEL TO AN INTERFACE

When a wavefront within the layer is set to travel parallel to the edge or the base, a complete loss of amplitude occurs by destructive interference. An example of this is the case of vertical incidence and a vertical edge, as in Figure 5.6(b), where the base-transmitted wavefront travels parallel to the edge. In addition, when the wavefront is diffracted at the lower vertex as in Figure 5.2, some of the energy is bent to travel parallel with the edge and the base.

The phenomenon occurs when the wavefront touches the edge of a stiffer layer with a grazing incidence, $\theta_i = \pi/2$. From Equation 4.13 the phase shift $2\alpha = 180°$, and 4.14, $\Delta x = 0$, such that the reflected wave completely cancels out the incident wave by destructive interference (Hudson, 1962). At the same time, no energy can be transmitted

into the stiffer material by this upward travelling base-refraction, since $R_1/R_2 = \infty$ from Equation 4.35. Displacements on either side of the edge thus are non-existant.

5.7 SUMMARY

A wavefront analysis was used to define the effect of the angle of incidence, θ_i, and the edge-slope angle, ψ, on SH wave propagation at the plane edge of a semi-infinite homogeneous layer. The mechanisms of refraction, diffraction and total reflection of plane SH waves at the edge of the layer are shown to generate total internal reflection and a horizontally propagating Love wave. For certain combinations of ψ and θ_i, it is found that constructive interference occurs within the layer between undispersed plane waves refracted from the base and edge. Simple expressions have been developed to determine the transient *x*-*z* coordinates of this interference. The analysis was simplified to the case of vertical incidence and a rectangular edge, and the effect of vertical resonance, multi-pulse inputs and multi-layered geometry on the constructive interference was discussed. Constructive interference between totally reflected and/or diffracted wavefronts is also likely to occur, yet is much more difficult to describe geometrically and has been left for the FEM analysis in the next chapter. Finally, amplification patterns unique to Love wave propagation at the edge of a semi-infinite layer were proposed in both the time and frequency domains.

Chapter 6: FEM MODELLING OF A LAYER EDGE

Two-dimensional elastic finite-element modelling using Archimedes is used to investigate the anti-plane response near the edge of the semi-infinite layer for a Ricker pulse input. The model has the same properties and geometry as that analysed in Chapter Five. We look at the importance of the input frequency, the layer depth, the edge-slope angle, the shear-wave velocity and the velocity contrast on its dynamic behaviour. The difference between FEM results and the wavefront analysis in Chapter Five indicates the importance of diffraction and total reflection as well as the input signal shape.

Similar previous studies include those of Dezfulian and Seed (1970, 1971) who made an FEM analysis of response immediately at the shallow sloping edge of a semi-infinite layer. More recently, Moczo and Bard (1993) used a finite difference method to investigate the response for a rectangular edge to a semi-infinite layer, the results of which are discussed later in this chapter.

6.1 METHOD OF ANALYSIS

The geometry of the model is the same as that used in the ray path analysis in Figure 5.1. Both the layer and the half-space are again assigned homogeneous elastic properties β_1, β_2 and ρ_1, ρ_2. Zero material damping ($\zeta_1,\zeta_2 = 0$, $Q_1,Q_2 = \infty$) is used because the interest is in the mechanisms of wave propagation rather than the amplitude. The force-input boundary in the layer lies at a distance $x = 23.2H$, while the absorbing boundary lies at $x = 24.7H$. Input to the model is an SH Ricker wavelet with a dimensionless characteristic frequency, η_c, given by

$$\eta_c = \frac{f_c}{f_0} = \frac{4H}{\beta_1} f_c \qquad [6.1]$$

and a dimensionless characteristic wavelength, λ_c*, given by

$$\lambda_c * = \frac{\lambda_c}{H} = \frac{\beta_1}{f_c H} \qquad [6.2]$$

The anti-plane SH Ricker wavelet is input as a continuous plane wavefront across the whole model, propagating with an angle of incidence, θ_i, with respect to the vertical, which is 0° (vertical input) in the testing.

6.1.1 TESTING PROCEDURE

In all 16 simulations are made, a full list of which is given in Table 6.1.

Table 6.1. A summary of FEM simulations made on the semi-infinite layer model. Tests F5, V3 and S6 are identical ($\eta_c = 2$, $\psi = 90°$, $\beta_2/\beta_1 = 10$).

variable	test code	characteristic frequency $\eta_c = f_c/f_0$	velocity contrast $i = \beta_1/\beta_2$	edge-slope angle ψ
input frequency	F1	0.50	10	90°
	F2	0.75	10	90°
	F3	1.00	10	90°
	F4	1.50	10	90°
	F5	2.00	10	90°
	F6	5.00	10	90°
velocity contrast	V1	2.00	2	90°
	V2	2.00	5	90°
	V3	2.00	10	90°
edge-slope angle	S1	2.00	10	15°
	S2	2.00	10	30°
	S3	2.00	10	45°
	S4	2.00	10	60°
	S5	2.00	10	75°
	S6	2.00	10	90°
	S7	2.00	10	105°
	S8	2.00	10	120°
	S9	2.00	10	135°

The first six simulations (F1-F6) are carried out on a vertical-edge model ($\psi = 90°$) with an impedance ratio of 10 ($i = \beta_2/\beta_1 = \beta_2^* = 10$), using input pulses of different characteristic frequencies ranging from $\eta_c = 0.5$ to $\eta_c = 5.0$. From the relationship in Equation 6.1 it can be seen that increasing the frequency is equivalent to either increasing the layer depth or decreasing the shear-wave veolocity, β_1. For example, a dimensionless input frequency of

η_c = 2.0, may equate to a (f_c, H, β_1) combination of (0.5Hz, 100m, 100m/s) or (5.0Hz, 20m, 200m/s) or (25.0Hz, 10m, 500m/s). The shear-wave velocity in the rock, β_2, must also be scaled the same amount as β_1 in order to preserve the velocity contrast. Further simulations are carried out to determine the effect of different velocity contrasts (V1-V3), and edge-slope angles (S1-S9).

6.1.2 Additional Details on the Finite Element Method

The analysis of a semi-infinite layer introduces two new problems into the Archimedes analysis. The first is do to with the input of motion within the layer, and the second involves the removal of dispersed wave fields at the absorbing boundary.

Force Input within the Semi-Infinite Layer

The layer, of different properties to the half-space is required to extend through the force-input boundary in the positive x-direction. The input to the system in the region of the layer is thus required to account for the amplification, reflection and refraction that occurs at the interface between the layer and half-space.

When the upcoming wave reaches the base of the soft layer, a wave is transmitted into the layer and another is reflected back down into the half-space. In addition, at each successive cycle of reflection of the wave within the layer, a leaky wave is transmitted back into the half-space. It is a reasonably simple process to account for each of these waves on the input boundary by applying Equations 4.6 and 4.7. For a vertically incident input motion with amplitude A_i, the wave reflected back down into the half-space off the interface has an amplitude, B_0, given by

$$B_0 = A_i \left(\frac{1 - 1/i}{1 + 1/i} \right) \qquad [6.3]$$

while the amplitude A_0 of the wave transmitted into the layer is

$$A_0 = A_i \left(\frac{2}{1 + 1/i} \right) \qquad [6.4]$$

where i is the impedance ratio given in Equation [4.8]. The wave trapped within the layer decays exponentially with the number of times it touches the lower interface. After m reflections from the basement, this multiply reflected wave has an amplitude, A_m, given by

$$A_m = A_i \left(\frac{2}{1+1/i} \right) \left(\frac{1-i}{1+i} \right)^m \qquad m = 0,1,2,...\infty \qquad [6.5]$$

The amplitude thus decays more quickly for lower impedance ratios. For an impedance ratio of 10, $A_0 = +1.818A$, $A_5 = -0.666A$ and $A_{10} = +0.244A$ after 0, 5 and 10 reflections from the interface; while for a lower impedance ratio of 5, $A_0 = +1.666A$, $A_5 = -0.216A$ and $A_{10} = +0.029A$. The amplitude, B_m, of the leaky wave transmitted back into the half-space is given by

$$B_m = A_i \left(\frac{2}{1+1/i} \right) \left(\frac{2}{1+i} \right)^m \qquad m = 1,2,3,...\infty \qquad [6.6]$$

Reflection m at the basement interface occurs at time, t_m, after the upcoming incident wavefront initially touches the interface, given by

$$t_m = \frac{2H}{\beta_1} m \qquad m = 0,1,2,...\infty \qquad [6.7]$$

which is equivalent to two travel times through the layer between each successive reflection.

Equations 6.3-6.7 hold only for vertical incidence and materials with zero damping where no energy is dissipated during transmission through the layer. For non-vertical incidence we can apply Equations 4.10 and 4.11 to give amended versions of Equations 6.3-6.6, respectively

$$B_0 = A_i \left(\frac{\rho_2 \beta_2 \cos\theta_i - \rho_1 \beta_1 \cos\theta_1}{\rho_2 \beta_2 \cos\theta_i + \rho_1 \beta_1 \cos\theta_1} \right) \qquad [6.8]$$

$$A_0 = A_i \left(\frac{2\rho_2 \beta_2 \cos\theta_i}{\rho_2 \beta_2 \cos\theta_i + \rho_1 \beta_1 \cos\theta_1} \right) \qquad [6.9]$$

$$A_m = A_i \left(\frac{2\rho_2\beta_2 \cos\theta_i}{\rho_2\beta_2 \cos\theta_i + \rho_1\beta_1 \cos\theta_1} \right) \left(\frac{\rho_2\beta_2 \cos\theta_i - \rho_1\beta_1 \cos\theta_1}{\rho_2\beta_2 \cos\theta_i + \rho_1\beta_1 \cos\theta_1} \right)^m \qquad m = 0,1,2,\ldots\infty \quad [6.10]$$

$$B_m = A_i \left(\frac{2\rho_2\beta_2 \cos\theta_i}{\rho_2\beta_2 \cos\theta_i + \rho_1\beta_1 \cos\theta_1} \right) \left(\frac{2\rho_1\beta_1 \cos\theta_1}{\rho_1\beta_1 \cos\theta_1 + \rho_2\beta_2 \cos\theta_i} \right)^m \qquad m = 1,2,3,\ldots\infty \quad [6.11]$$

where θ_i is the angle of incidence of the initial disturbance from the half-space, θ_1 is the angle of propagation of the wave within the layer given by Snell's law

$$\sin\theta_1 = \frac{\beta_1}{\beta_2} \sin\theta_i \qquad [6.12]$$

which lies between 0 and the critical angle, θ_c, for vertical and horizontal inputs respectively. The angle $\theta_2 = \theta_i$ is the propagation angle of the down-going waves in the half-space. The wavefront in the layer now has an apparent horizontal velocity, c_x, given by

$$c_x = \frac{\beta_1}{\sin\theta_1} = \frac{\beta_2}{\sin\theta_i} \qquad [6.13]$$

which lies between ∞ and β_2 for vertical and horizontal inputs respectively; and an apparent vertical velocity, c_z, given by

$$c_z = \frac{\beta_1}{\cos\theta_1} = \frac{\beta_1}{\sqrt{1 - \frac{\beta_1^2}{\beta_2^2} \sin^2\theta_i}} \qquad [6.14]$$

which is generally quite close to β_1. Equation 6.7 can thus be revised to account for different angles of incidence. Reflection at a point on the lower interface now occurs at successive times given by

$$t_m = \frac{2H}{\beta_1} \left(1 - \frac{\beta_1^2}{\beta_2^2} \sin^2\theta_i \right)^{\frac{1}{2}} m \qquad m = 0,1,2,\ldots\infty \qquad [6.15]$$

after the initial contact. Equations 6.3-6.7 are used in Archimedes in order that the correct amplitudes and timing of reflected and refracted pulses occur along the force input boundary within the layer and half-space. While the procedure is still reasonably straight forward, an analysis for different angles of incidence has been omitted because it is deemed (from the previous chapter) to have a lesser effect on the edge response than the velocity contrast, edge-slope angle and input frequency.

Errors Associated with Reflection at the Absorbing Boundary

Although the absorbing boundaries used in Archimedes effectively remove the plane waves generated by simple reflection and refraction in the model, they are unable to completely remove the dispersive Love waves travelling horizontally through the layer and subjacent half-space in the positive x-direction. When the Love waves reach the right-hand extent of the model, a proportion of their energy is reflected back into the model as Love waves travelling in the opposite direction. While this is not easily seen in the results shown, it is apparent in surface displacement plots at greater distances and longer time. Some of the peakedness in FSR for $1.2 < \eta < 2.5$ in Figure 6.6(a) and $3.2 < \eta < 5.0$ in Figure 6.6(c) is thought to be attributed to interference with low-amplitude surface wave reflections.

The low frequency components in the Love wave travel fastest (with a phase velocity, $c \leq \beta_2$) and are the first to generate erroneous pulses in the opposite direction. The amplitude of these phases, however, is generally quite insignificant compared to the direct waves in the system, and appear to have little significant influence on the results. The bulk of the energy arrives at the right-hand extent of the model much later at a time given by the dominant group velocity of the Love wave. For high frequency inputs this is close to the velocity of the layer, β_1, while for frequencies close to the, f_0, the dominant group velocity may be significantly less than β_1. The majority of the error generated by this mechanism has thus been crudely discounted by stopping the simulation prior to the bulk of the Love wave components reaching the right-hand side of the model.

6.1.3 Analytical Estimates of Response that are Expected to be Evident in the Modelling

Using the ideas described in the previous two chapters, we can define a number of features that are expected to show up in the FEM results. These include the appearance of vertically propagating wavefronts at the surface, the initial apparent velocity of edge-refracted pulses, the position and time of constructive interference between undispersed refracted wavefronts, and the phase and group velocities of a Love wave travelling away from the edge.

A phenomenon that has been overlooked in previous discussion is the distortion of pulses due to the dispersive mechanisms of diffraction and total reflection. Equation 4.14 gives a frequency dependent displacement of each harmonic component within a waveform. A pulse containing a range of frequencies is thus not only displaced but its shape is deformed at each cycle of total reflection. This undoubtedly has significant effects on the resultant surface displacement and may explain many of the discrepancies between the modelling and the wavefront analysis.

Vertically Propagating Wavefronts

With time $t^* = 0$ set to occur when the first peak of the Ricker wavelet reaches the surface through the rock, the second and third peaks of the wavelet are expected to arrive at t_r^* and $2t_r^*$, respectively, where t_r^* is the dimensionless time-gap between each of the three peaks in the Ricker pulse. From Equation 3.6

$$t_r^* = \frac{2\sqrt{6}}{\pi \eta_c} \qquad [6.16]$$

Values of t_r^* for each of the different input frequencies are presented in the 3rd column of Table 6.2.

For a characteristic input frequency of $\eta_c = 2$, the first peak will arrive at the surface through the rock at $t^* = 0$, the 2nd at $t^* = t_r^* = 0.78$ and the 3rd at $t^* = 1.56$. Peaks transmitted into the soil through the base, on the other hand, arrive at a time given by the difference in travel times through the rock and soil ($t_{S1} - t_{S2}$, Equation 5.33). After two further travel times later ($2t_{S1}$) the 1st reflection from the base arrives back at the surface

180° out of phase, and another two travel times later ($4t_{S1}$) the 2nd reflection from the base arrives back at the surface in-phase with the original.

Table 6.2. Dimensionless surface arrival times of the vertically travelling Ricker pulse (see Figure 3.3). The sense of displacement (+ or -) of each peak changes after subcritical reflection at the lower interface.

			1st arrival in rock			1st arrival in soil			1st base reflection			2nd base reflection		
η_c	λ_c*	t_r*	1st peak (+)	2nd peak (-)	3rd peak (+)	1st peak (+)	2nd peak (-)	3rd peak (+)	1st peak (-)	2nd peak (+)	3rd peak (-)	1st peak (+)	2nd peak (-)	3rd peak (+)
0.50	8.00	3.12	0.00	3.12	6.24	0.90	4.02	7.14	2.90	6.02	9.14	4.90	8.02	11.14
0.75	5.33	2.08	0.00	2.08	4.16	0.90	2.98	5.06	2.90	4.98	7.06	4.90	6.98	9.06
1.00	4.00	1.56	0.00	1.56	3.12	0.90	2.46	4.02	2.90	4.46	6.02	4.90	6.46	8.02
1.50	2.67	1.04	0.00	1.04	2.08	0.90	1.94	2.98	2.90	3.94	4.98	4.90	5.94	6.98
2.00	**2.00**	**0.78**	**0.00**	**0.78**	**1.56**	**0.90**	**1.68**	**2.46**	**2.90**	**3.68**	**4.46**	**4.90**	**5.68**	**6.46**
5.00	0.80	0.31	0.00	0.31	0.62	0.90	1.21	1.52	2.90	3.21	3.52	4.90	5.21	5.52

Table 6.2 lists the arrival time at the surface of waves through the rock, through the soil, and after one and two reflections from the base of the layer. For low frequencies where $\eta_c < 2$, the time between peaks of the Ricker wavelet is long enough that constructive interference occurs at the surface between vertically reflecting pulses. In the case of $\eta_c = 1.5$ we would expect destructive interference between the first and third peaks, while for $\eta_c = 0.75$ we would expect constructive interference between the 2nd and 1st peaks, and then again between the 3rd and 2nd peaks. For input frequencies of $\eta_c = 2$ and $\eta_c = 5$, the wavelets are expected to be completely reflected back down from the surface before the next one arrives.

Undispersed Edge-Refracted Pulses and associated Constructive Interference

In accordance with the wavefront analysis in Chapter Five, an edge-refracted and undispersed Ricker pulse is expected to travel across the surface away from the edge, provided $\psi \leq 90°$. It should have a phase velocity, c_x^{e1}, given by Equation 5.18, and travel a distance x_2 (Equation 5.12) out from the edge before being completely reflected below the surface. Table 6.3 lists the dimensionless values of these variables for the normal edge-slope simulations. Constructive interference between the edge-refraction and the vertically

travelling base-refraction occurs at position x^c from Table 6.3, and at the time of first arrival through the soil given in Table 6.2.

Table 6.3. Theoretical angles of edge-refraction (Equation 5.9), edge-refracted-wave phase velocities (Equation 5.18), positions of constructive interference (Equation 5.34) and x_2 (Equation 5.12) expected to be seen in the FEM results for $\beta_2/\beta_1 = 10$.

ψ°	$\theta_1^{e1}{}^\circ$	c_x^{e1}/β_1	x^c/H	x_2/H
15	-1.48	4.278	3.851	3.97
30	-2.87	2.193	1.973	2.24
45	-4.05	1.526	1.373	1.87
60	-4.97	1.220	1.098	2.01
75	-5.54	1.068	0.961	2.94
90	-5.74	1.005	0.905	9.95

Properties of a Fully Developed Love Wave

Figure 6.1 compares the frequencies contained within each Ricker pulse (lower plot) with the dispersion curves of a Love wave in the layer. Ricker wavelets with central frequencies less than the resonant frequency of the layer ($\eta_c \leq 1$) contain most of their energy solely within the domain of the fundamental Love wave mode. Higher frequency wavelets on the other hand, for example $\eta_c = 5$, contain energy covering a large number of modes. The Airy phase frequencies and velocities are given in Table 6.4.

Table 6.4: Airy phase frequencies, group velocities and phase velocities for the n^{th} mode Love wave taken from Figure 6.1 (c) for $\beta_2/\beta_1 = 10$. Velocities are normalised against β_1.

n	η_n^{Airy}	U_n^{Airy}	c_n^{Airy}
0	1.012	0.366	3.74
1	3.031	0.275	4.83
2	5.049	0.243	5.36
3	7.067	0.225	5.68
4	9.083	0.213	5.95

A pulse departing from the origin of a *t-x* plot and travelling horizontally at the maximum Love wave velocity, $\beta_2 = 10\beta_1$, would have a very steep slope (taking only one unit of time to travel 10 units of distance). A pulse travelling at β_1* would have a unit slope, while energy at the minimum 1st mode group velocity, $U_0^{Airy} = 0.366\beta_1$ would have a very low-angled path.

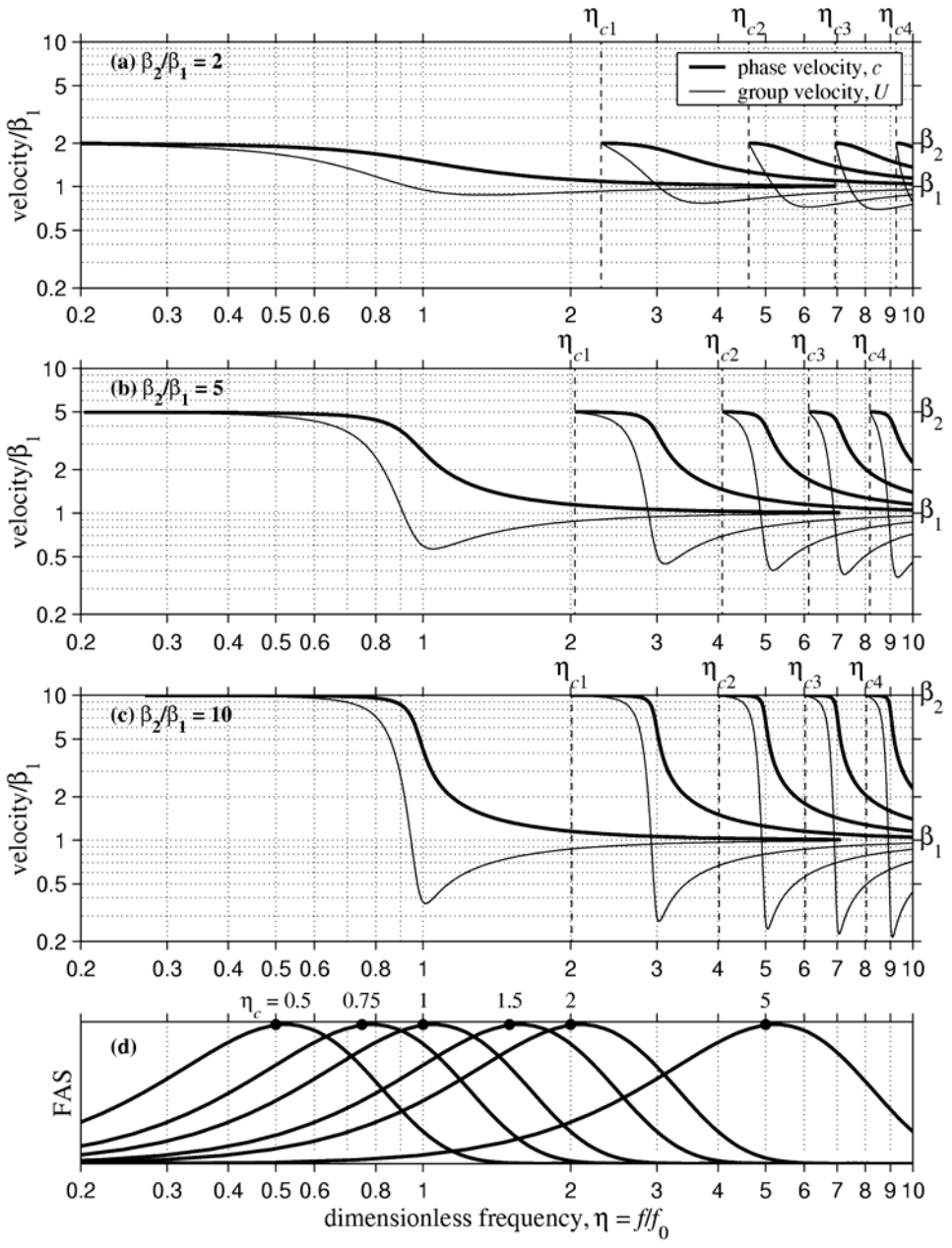

Figure 6.1. Dimensionless Love wave dispersion curves for a single layer over a half-space. Three different shear-wave velocity contrasts are shown; (a) $\beta_2/\beta_1 = 2$, (b) $\beta_2/\beta_1 = 5$, (b) $\beta_2/\beta_1 = 10$. In all cases $\rho_1 = \rho_2$. Plot (d) shows the Fourier amplitude spectra (FAS) of Ricker wavelets with the six different characteristic frequencies used in the simulations.

6.2 RESULTS

Results from the 16 simulations are presented here to determine the pattern of amplification adjacent to the edge for a pulse-type input. The significance of the frequency content, layer depth and shear-wave velocity is analysed with the first set of results (simulations F1-F6). The shear-wave velocity contrast and the edge-slope angle and are then analysed with the results from simulations V1-V3 and S1-S9.

The results from simulations F1-F6 and V1-V3 are plotted to a distance of $x = 20H$, and from these we discuss the characteristics of the Love wave which travels across the layer. The results are compared with the dispersive features of a fully developed Love wave reviewed in Section 4.3.2 and discussed further in Section 5.4.

Results from simulations S1-S9 are plotted to a maximum distance of $x = 8H$ and used to investigate constructive interference and amplification close to the edge. Results are compared with those of the wavefront analysis in Chapter Five to determine if constructive interference between undispersed refracted wavefronts is a significant factor in edge amplification, or whether constructive edge amplification is governed by totally-reflected and diffracted phases that were not analysed in Chapter Five.

6.2.1 SIMULATIONS F1-F6: TESTS ON THE INPUT FREQUENCY, LAYER DEPTH AND SHEAR-WAVE VELOCITY

Displacement and Fourier spectral ratios at the surface are plotted to a distance of $x = 20H$ from the vertical layer edge. While the effect of changing the dimensionless frequency of the input is discussed, the same arguments could be equally applied to changing the shear-wave velocity or the layer depth, using the relationship in Equation 6.1.

Displacement Response

Figures 6.2-6.4 show contour plots of transient surface displacement as a continuous function of horizontal distance across the layer. The displacement at four discrete locations ($x = 0H$, $5H$, $10H$ and $15H$) is also sketched over the top in the more traditional form of a line plot. Peak displacement across the layer is shown on the right hand side, while a cross-section of the layer is shown on the left.

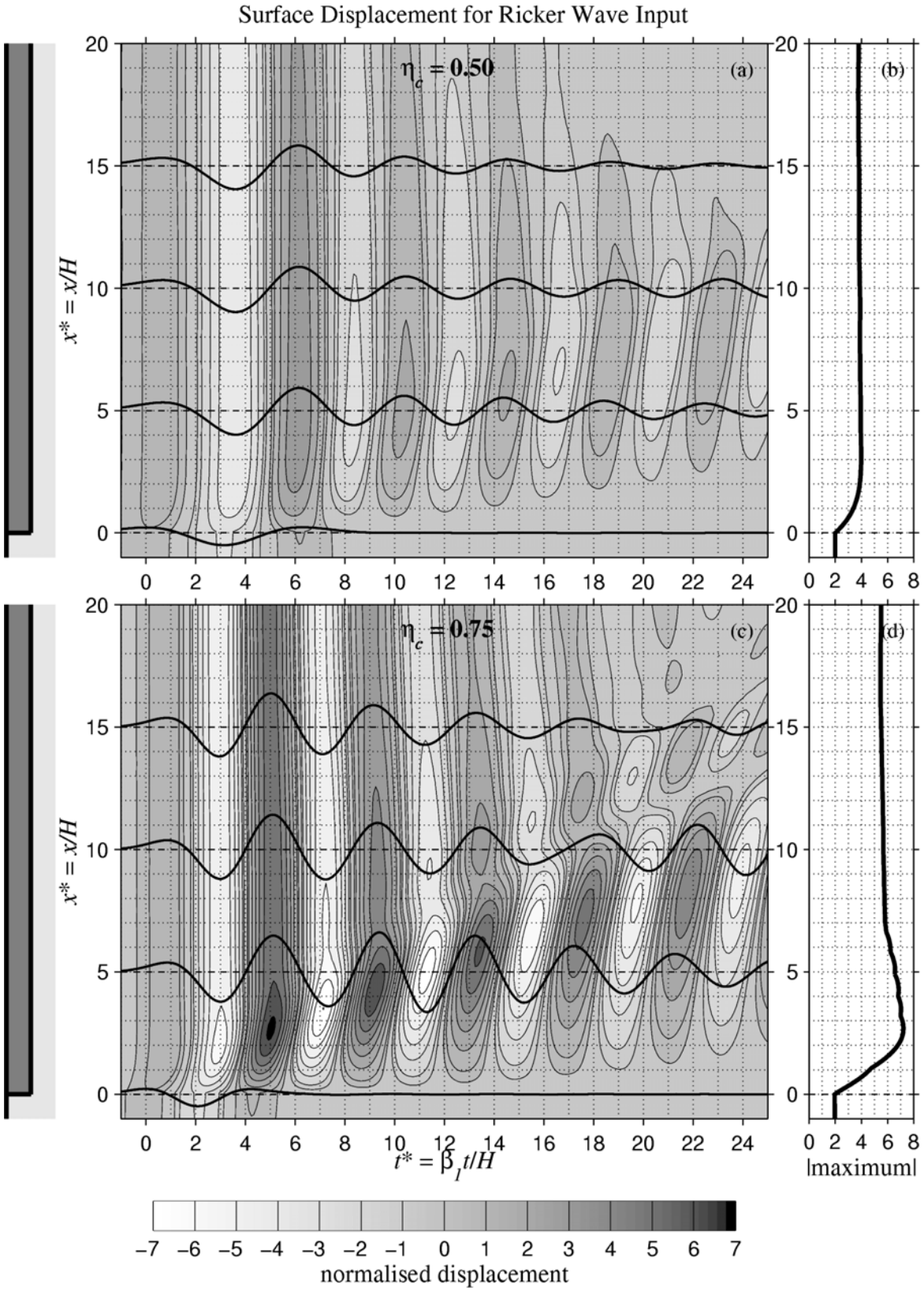

Figure 6.2. Contour plots of transient surface displacement for tests F1 (η_c = 0.50) and F2 (η_c = 0.75). Maximum displacement is shown on the right-hand plots.

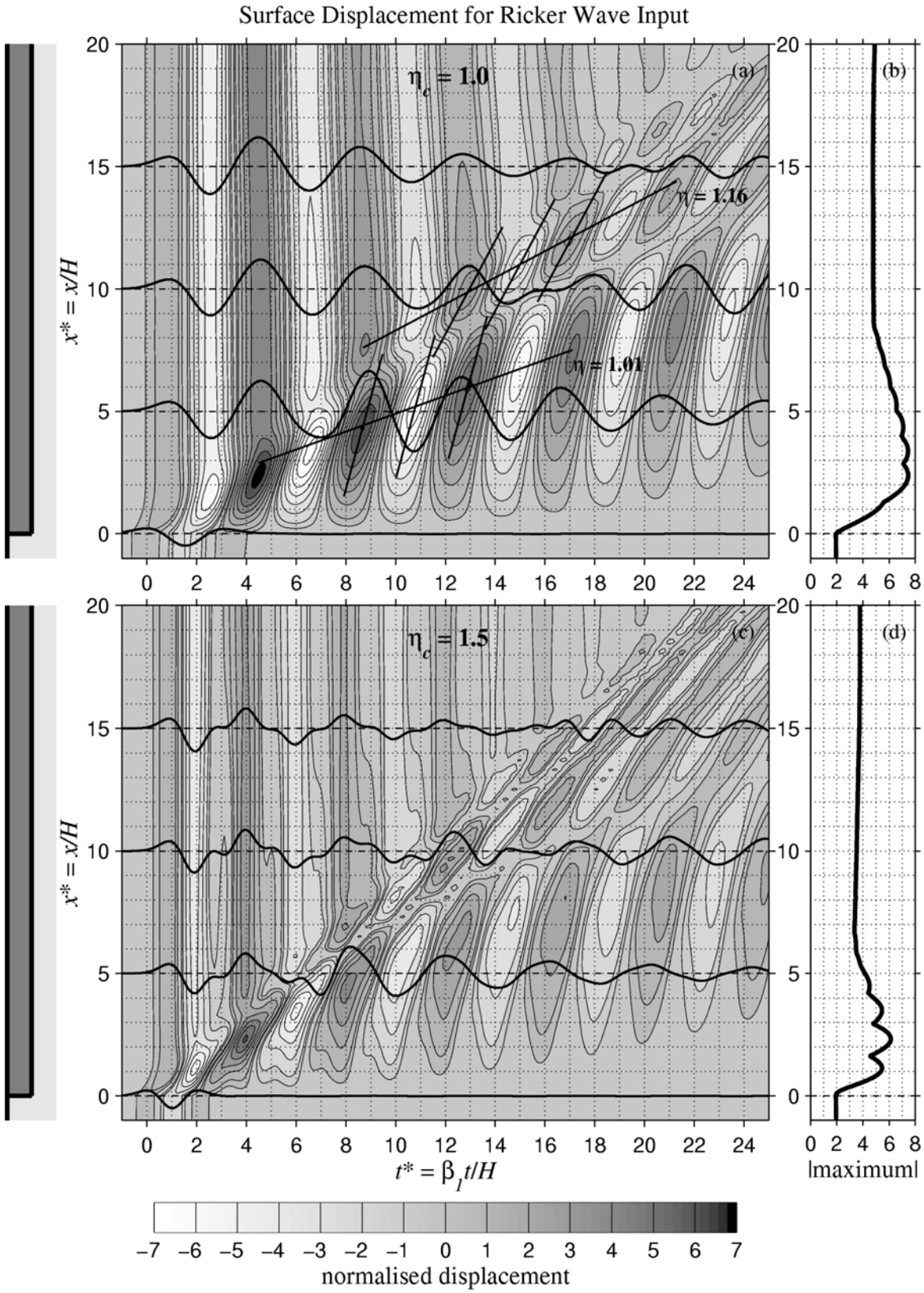

Figure 6.3. Contour plots of transient surface displacement for tests F3 (η_c = 1.0) and F4 (η_c = 1.5). Maximum displacement is shown on the right-hand plots.

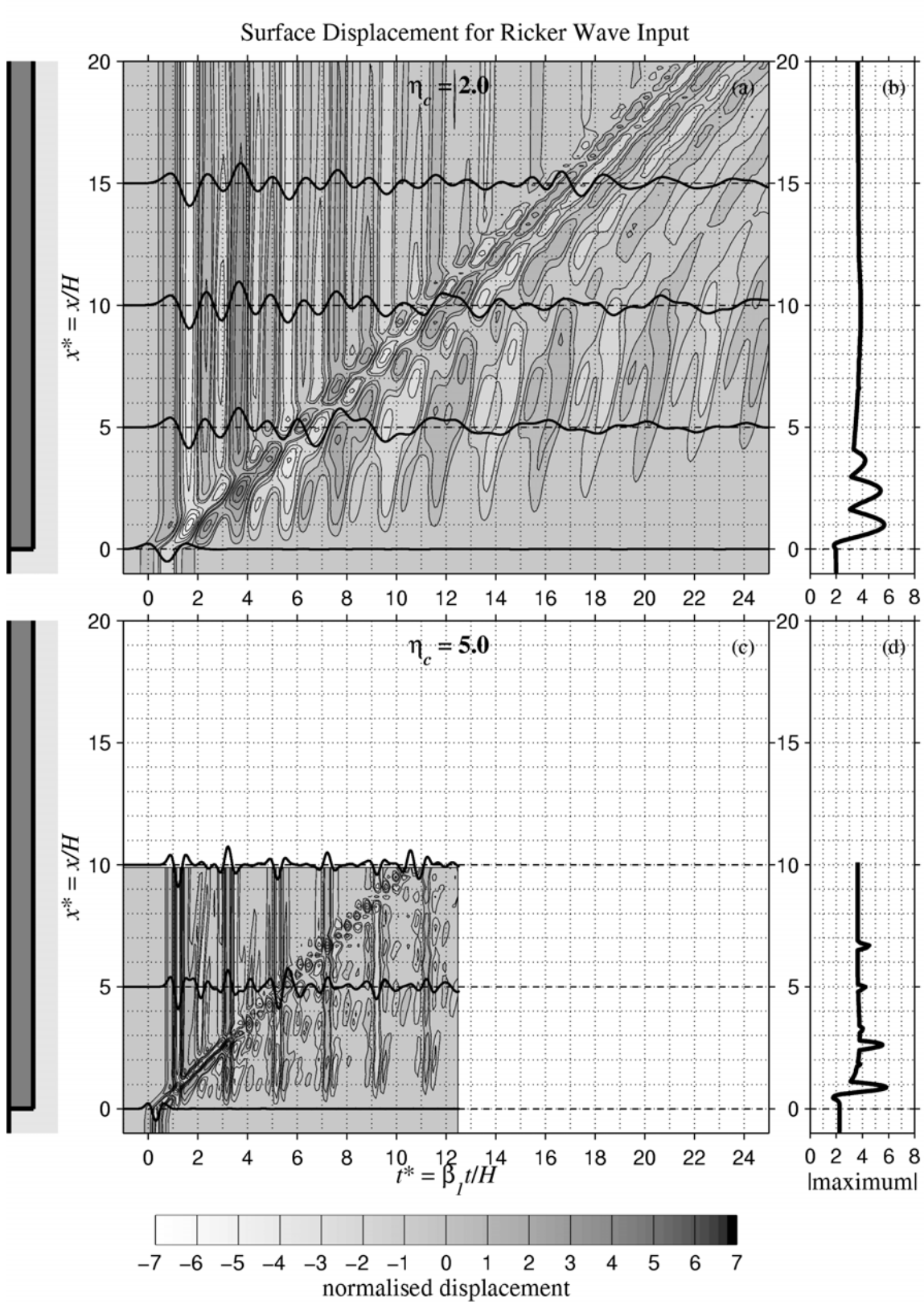

Figure 6.4. Contour plots of transient surface displacement for tests F5 (η_c = 2.0) and F6 (η_c = 5.0). Maximum displacement is shown on the right-hand plots. The high frequency simulation (F6, η_c = 5.0) was limited to $x = 10H$ and $t = 12.5H/\beta_1$ due to the higher node density and correspondingly high computation cost.

For a high dimensionless pulse frequency, $\eta_c = 5$ (Figure 6.4), the characteristic wavelength is short compared to the depth of the layer, and a discrete Ricker pulse can be seen to arrive at the surface at successive times given in Table 6.2. The amplitude of these arrivals maybe calculated by Equation 6.4 and accounting for free-surface doubling, to give the peak displacement of 3.64 seen across the majority of the model width. In addition, well-defined Love waves originate from the edge and propagate horizontally across the layer. They are clearly composed of pulses with slopes (phase velocities) close to β_2, and pulse with slopes close to β_1. The slope joining the centroid of pulse amplitude (the group velocity) varies between β_2 and ~0.2 the latter of which roughly corresponds to the minimum group velocity of a higher mode Love wave (Table 6.4). Sharp peaks in displacement occur near the edge, clearly a result of interference between the Love wave and vertical arrivals within the layer.

At the other extreme a low input frequency, $\eta_c = 0.5$, produces an almost constant peak displacement across the width of the layer. Peak amplitude is a function only of the impedance contrast rather than surface wave action. A small amount of energy, however, can be seen to travel across the basin at approximately the Airy group velocity of the fundamental mode (Table 6.4). Characteristic frequencies of $\eta_c = 0.5$ and $\eta_c = 0.75$ correspond to group and phase velocities close to β_2 (Figure 6.1), yet there is little evidence of phases travelling across the layer at this velocity. Figure 4.5(a), however, indicates that most of the energy at frequencies below $\eta \approx 1$ travels in the form of an inhomogeneous wave in the half-space and is therefore not seen at the surface.

At $\eta_c = 0.75$ and $\eta_c = 1.0$, there is (as predicted in Table 6.2) constructive interference between vertically reflecting wavelets within the layer. As a result, peak displacement is greater across the full width of the layer. Both these input wavelets also contain a large proportion of energy at the Airy phase frequency (Figure 6.3) and there is a correspondingly strong amplification generated by energy travelling at the fundamental mode Airy phase velocity.

The proportion of energy travelling at the Airy group velocity (U_0^{Airy}) increases as the characteristic Ricker frequency increases from $\eta_c = 0.5 \rightarrow 1.0$, where it is approximately equal to the fundamental mode Airy phase frequency ($\eta_0^{Airy} \approx 1.0$). Then for $\eta_c > \eta_0^{Airy}$, the proportion of energy at the Airy phase decreases, and most of the energy tends to travel at

velocities closer to that of the layer, β_1. At the same time, when $\eta_c > 1$, we begin to see velocities associated with higher mode Love waves, best evidenced by the irregular shaped (double) peaks in the Airy phase for $\eta_c = 2$.

In general, there is a pattern in the results similar to that presented in Figure 5.9, with phase velocities that apparently curve and flatten as in the high velocity-contrast case. The strength of different frequencies (and hence velocities) depends on the proportion and range of frequencies contained within each Ricker pulse. It appears, however, that only certain frequencies of the Love wave are amplified, while the input wavelet contains a smooth distribution of frequencies. This is likely to be simply a feature of the dispersion curve, which shows that velocities may change quite rapidly for small shifts in frequency, leaving the uneven distribution of velocities in the *x*-*t* plane (also seen in Figure 5.9).

For any set of peaks moving across the layer, a line can generally be drawn through their centroids to give the group velocity, and a line may be drawn along the trajectory of each peak to give its phase velocity. Both these velocities correspond to a common frequency on Figure 6.1 (c). Two examples of this for frequencies $\eta = 1.16$ and $\eta = 1.01$ have been plotted on Figure 6.3 (a). The latter example is the Airy phase frequency. The steep lines correspond to phase velocities, while the flatter lines to group velocities. It can now be observed that the slopes of the group velocities do not run linearly back toward the origin as expected from a point source (Figure 5.9). It appears that high frequency components (like those travelling at β_1 for $\eta_c = 5$) are set up the closest to the edge, while lower frequency energy is set up some distance from the edge.

Interference between various up-going, down-going and horizontally-travelling pulses is the most significant contributor to variable amplification at the edge. In the high frequency cases ($\eta_c = 2$ and $\eta_c = 5$), there are successive sharp points of constructive interference across the layer, clearly between edge-refracted pulses travelling at a velocity close to β_1, and base-refracted (then reflected) pulses. For $\eta_c = 5$, the first occurs at $x \approx 0.9H$ from the edge, which is the same result as given by the undispersed wavefront analysis (Equation 5.45).

For lower frequencies, the nature of interference between vertically and horizontally propagating pulses is significantly different to that described for undistorted pulses in Chapter Five, indicative of strong dispersive effects governing the response. While peak

displacement clearly occurs where phases of the Love wave cross paths with the base-refracted wavefronts, the amplitude appears also to be strongly dependent on interference between vertically reflecting peaks of the Ricker pulse. The highest displacement for $\eta_c = 0.75,\ 1.0$ and 1.5 occurs at around $x = 2.3H$ due to a coupling between vertical resonance and the Airy phase of the Love wave.

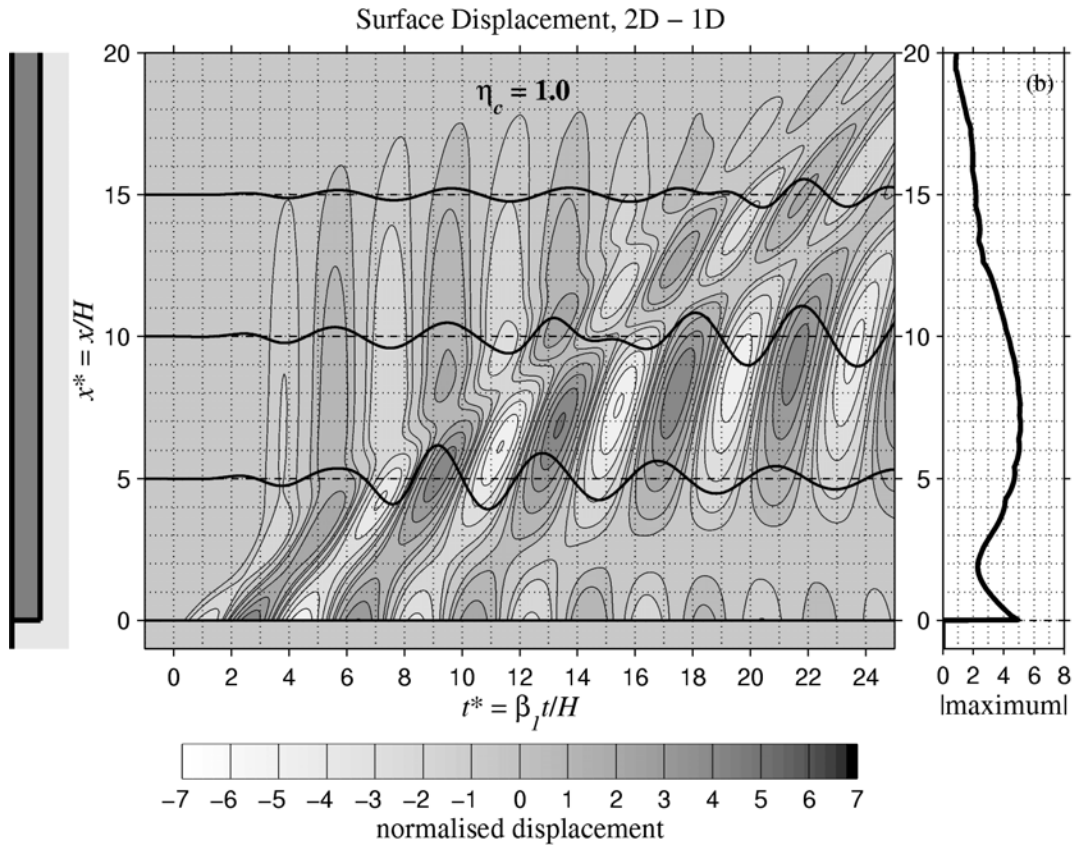

Figure 6.5. Transient surface displacement from simulation F3 ($\eta_c = 1.0$) after results from a one-dimensional analysis have been subtracted. Amplitude is now a result exclusively of effects at the edge.

The final observation we make in this section is that the amplitude of displacement due to vertical reflections within the layer is clearly greater than that of the surface waves, and as a result, surface waves are often masked by the dominance of vertical reflections. For example in Figure 6.5 we show the result of taking simulation F3 ($\eta_c = 1$) and subtracting from it the results of a one-dimensional analysis. It now contains (in theory) only the displacements that arise due to the effect of the edge. Amplitudes are significantly lower

than the 2-D result, but we can now see low-amplitude phases propagating at velocity β_2 across the basin, where they were previously masked by the vertical reflections.

Results in this section have shown that the surface displacement response changes dramatically as the input frequency changes. More precisely, the response is strongly dependent on the ratio of wavelength to the depth of the layer, where the wavelength within the layer is a function of both the frequency of the input and the shear-wave velocity of the layer. High input frequencies, low shear-wave velocities and deep layers tend to produce a narrow constructive edge-amplification, the position of which is able to be adequately predicted by the wavefront analysis in Chapter Five. For long-period inputs, stiff sediments and shallow layers, the edge-response is much more a function of interaction between the dispersive Love wave and the resonant qualities of the layer.

Frequency Response

Figure 6.6 presents Fourier spectral ratios (FSR) calculated with the displacement data from simulations F3 ($\eta_c = 1$) and F5 ($\eta_c = 2$). Both plots show a similar picture, although the domain of the plot for $\eta_c = 2$ extends to 5Hz because the wider range of frequencies in the input wavelet. Line plots showing FSR at three locations ($x = 5H$, $10H$ and $15H$) are sketched atop the contour plots, as are the theoretical extremum curves from Section 5.5.2.

The fit between theoretical extremum curves and the modelling result is very good. Peak FSR reaches a maximum value of 16 at $x \approx 6H$, approximately in the position where the first extremum line constructs with the fundamental resonant frequency of the layer ($\eta = 1$). It is interesting that while this peak in the frequency domain corresponds with the Airy phase frequency, it does not correspond with peak displacement in the time domain. The frequencies most outstanding in the results change with distance from the edge. At the same time, while we have not made a comprehensive time-frequency analysis, it is clear that the dominant frequency of shaking changes with time as the surface waves pass each position across the layer.

The frequency response adjacent to the edge essentially consists of a superposition between the classical one-dimensional resonance pattern and of an oscillatory pattern generated by Love waves. This observation has previously been made by Moczo and Bard (1993) in the results of finite difference modelling. They however, attribute the oscillatory

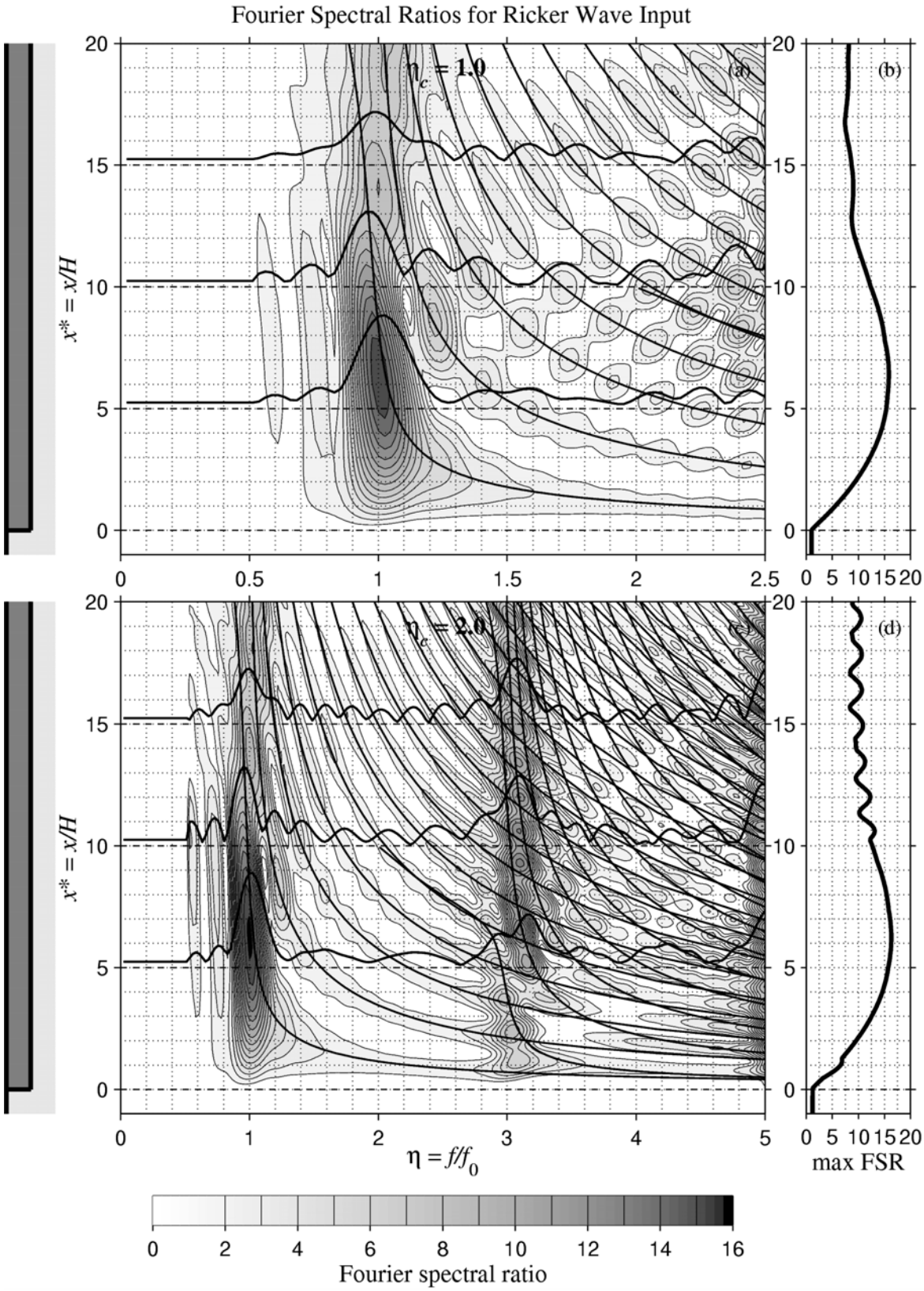

Figure 6.6. Contour plots of Fourier spectral ratios (FSR) for simulations F3 ($\eta_c = 1.0$) and F5 ($\eta_c = 2.0$). Maximum FSR is shown on the right. Line plots of FSR at three locations ($x = 5H$, $10H$, $15H$) are sketched atop the contour plots, as are the theoretical extremum curves from section 5.4.2

pattern to "interference between the direct (body) and diffracted (surface) waves", whereas we have shown here the pattern to be a function of the Love wavelength when constrained by the edge of the layer, as defined in Section 5.5.2.

6.2.2 SIMULATIONS V1-V3: TESTS ON THE VELOCITY CONTRAST

The effect of reducing the shear-wave velocity contrast (β_2/β_1) between the layer and the half-space is discussed with reference to surface displacement and Fourier spectral ratios to $x = 20H$. Results may be compared with the simulation V3 = F5 ($\eta_c = 2$, $\beta_2/\beta_1 = 10$) in Figures 6.4 and 6.6. The first thing to note is that the range of velocities within which the Love wave may travel is reduced as the velocity contrast decreases (Figure 6.1), and the path of Love-wave propagation shown in Figure 5.9 is correspondingly much more constrained. Airy phase frequencies and cut-off frequencies also increase slightly.

Displacement Response

Figure 6.7 shows surface displacements from simulations V1 ($\beta_2/\beta_1 = 2$) and V2 ($\beta_2/\beta_1 = 5$) due to a ($\eta_c = 2$) Ricker pulse input. For $\beta_2/\beta_1 = 5$, most of the Love wave travels across the layer with a group velocity just less than β_1, and the Airy phase is much less well developed than for $\beta_2/\beta_1 = 10$. For $\beta_2/\beta_1 = 2$, Love wave propagation is much less regular although apparently steepening curves of phase velocity can be seen as predicted in Section 5.5.1.

Both simulations show a noticeable peak in the displacement of pulses travelling at a velocity near β_2 at a distance $x \approx 9H$ from the edge, strongest in the low contrast case. While the peak appears to be a result of constructive interference with a vertically reflected wavefront in the case of $\beta_2/\beta_1 = 5$, it is difficult to account for in the case of $\beta_2/\beta_1 = 2$. Closer to the edge, constructive amplification between the Love wave and the vertically travelling pulse creates displacement peaks approximately at positions given by Equation 5.45 ($x^c = 0.817H$ and $x^c = 0.577H$, for $\beta_2/\beta_1 = 5$ and $\beta_2/\beta_1 = 2$, respectively).

Frequency Response

Figure 6.8 shows contour plots of Fourier spectral ratio (FSR). Line plots showing FSR at three locations ($x = 5H$, $10H$ and $15H$) are sketched atop the contour plots, as are the

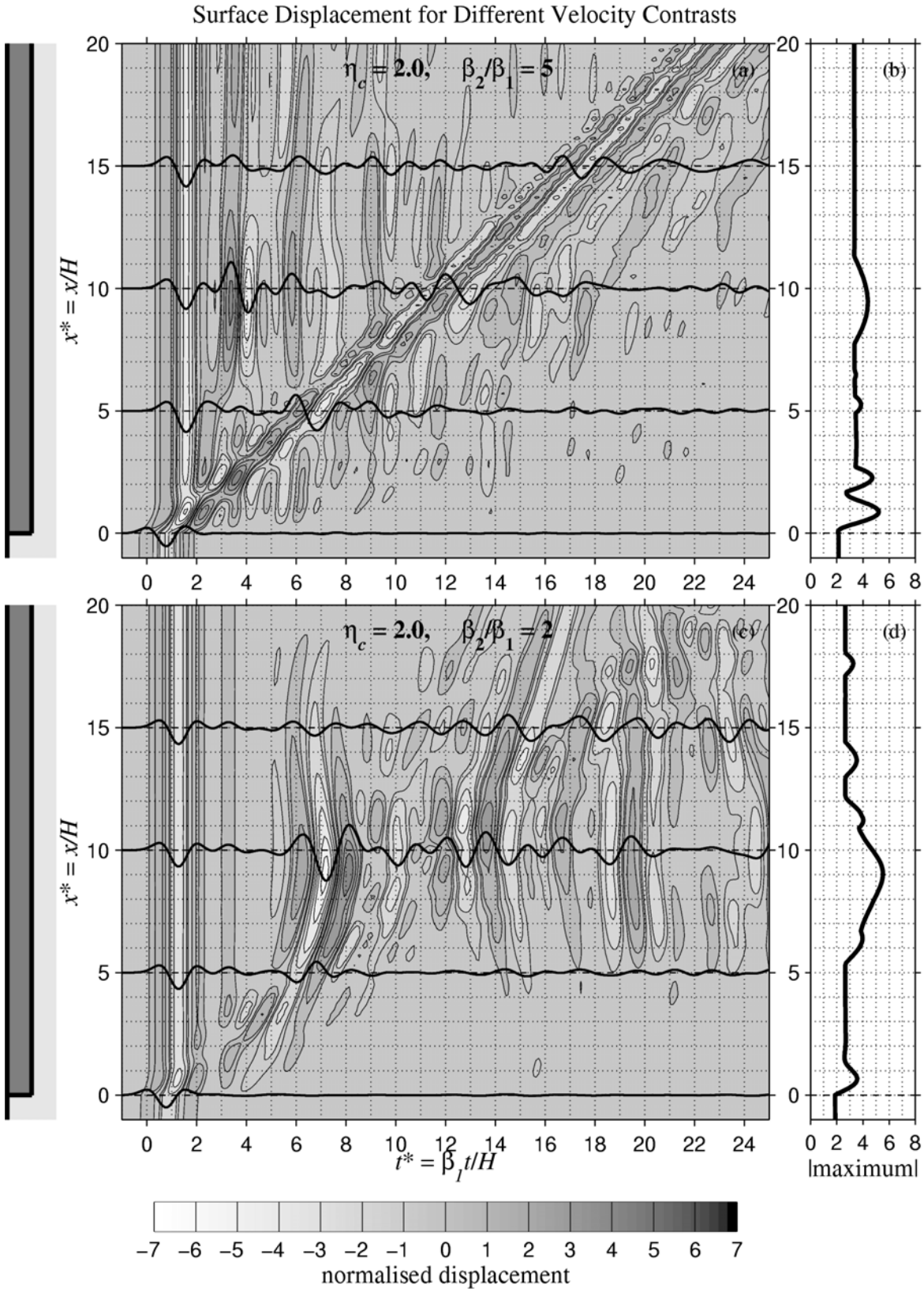

Figure 6.7. Transient surface displacement for two different velocity contrasts V2 ($\beta_2/\beta_1 = 5$) and V1 ($\beta_2/\beta_1 = 2$). The characteristic input frequency, $\eta_c = 2.0$ in both cases. Maximum displacement is shown on the right.

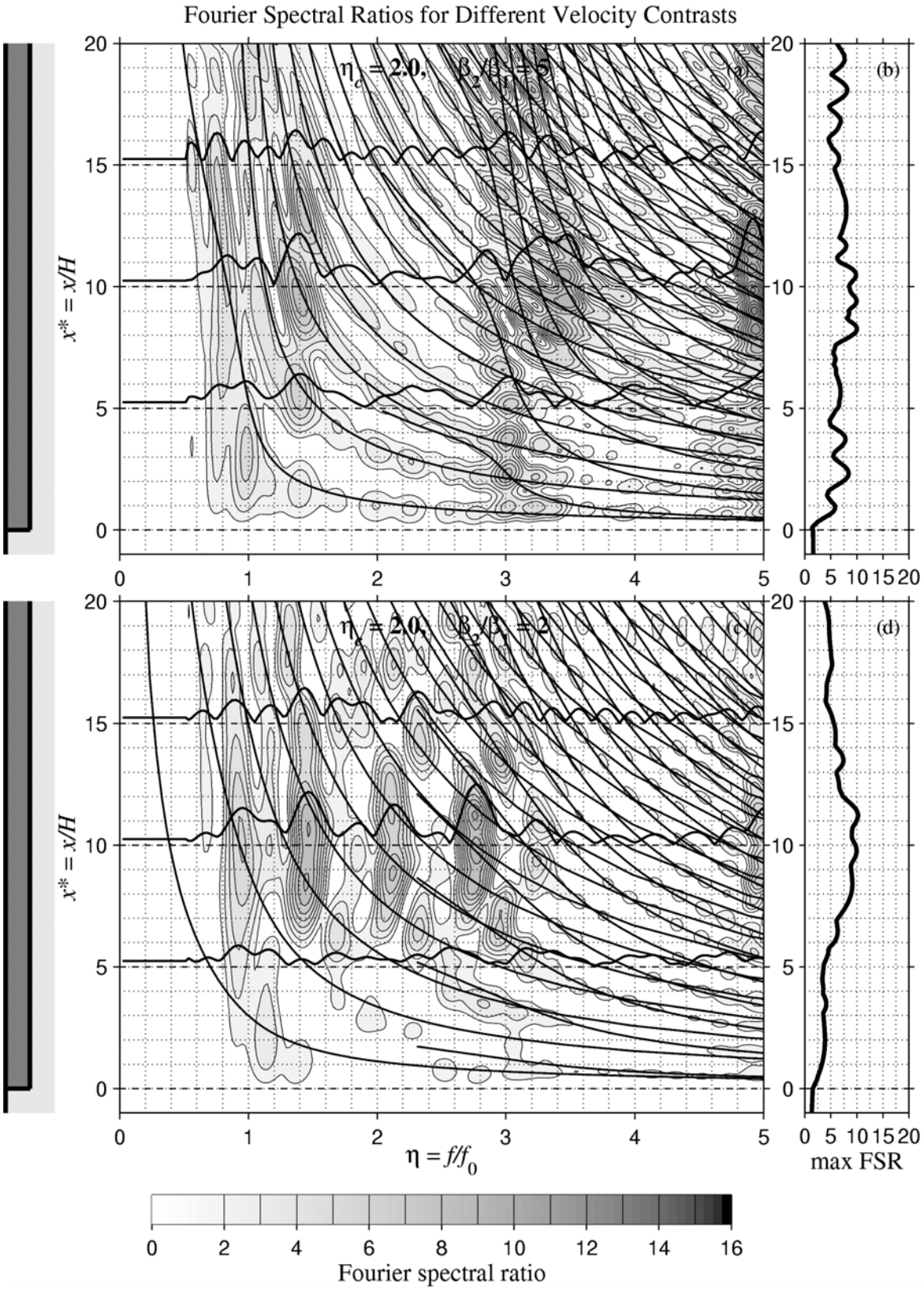

Figure 6.8. Contour plots of Fourier spectral ratios (FSR) for simulations V2 ($\beta_2/\beta_1 = 5$) and V1 ($\beta_2/\beta_1 = 2$). Maximum FSR is shown on the right. Line plots of FSR at three locations ($x = 5H$, $10H$, $15H$) are sketched atop the contour plots, as are the theoretical extremum curves from section 5.4.2

theoretical extremum curves from Section 5.5.2. Both $\beta_2/\beta_1 = 2$ and $\beta_2/\beta_1 = 5$ are quite different to the high contrast case ($\beta_2/\beta_1 = 10$). Frequency-domain amplification close to the edge decreases significantly as the velocity contrast decreases. At low contrasts the resonant frequencies of the layer have much less influence, and the effect of the Love wave becomes much more important, clearly dominating the response. At the same time, the pattern of amplification is less inclined to fit the pattern prescribed in Section 5.5.2, especially for low frequencies.

6.2.3 SIMULATIONS S1-S9: TESTS ON THE EDGE-SLOPE ANGLE

The effect of different edge-slope angles on response close to the edge is investigated. The propagation of waves within the model is compared with the wavefront analysis in Chapter Five, and the differences between the two are ascribed to frequency dispersion and pulse-shape effects.

Displacement Response

Figures 6.9-6.11 present contour plots of surface displacement for nine different edge-slope angles, ψ, ranging between 15° and 135°. Horizontal dashed lines indicate the position of the edge and lower vertex. Over the top, three solid lines are plotted to indicate the surface arrival of each of the three peaks in the Ricker pulse. The sloping lines from the edge show the expected path of undistorted edge-refracted pulses travelling at velocity (slope) c_x^{e1} (Table 6.3) to a maximum distance, x_2, and constructing with the base refracted pulse at x^c, in the position of the small star (Table 6.3). For $\psi > 90°$, the wavefront analysis has shown that there is no undistorted edge-refracted wavefront, and thus no lines are plotted.

Figures 6.12-6.14 show successive time frames of contoured displacement in the x-z plane at the edge of the layer. Displacement at the surface of each frame is identical to that shown in Figures 6.9-6.11 at each respective time-step. The first three seconds of each simulation are shown at dimensionless time intervals of $0.25\beta_1 t/H$. On top of the contours has been plotted the theoretical positions of each of the three peaks of the Ricker pulse, similar to the plots in Figures 5.5-5.7. Again, a small star is plotted at the expected position of interference between undistorted wavefronts, x^c, on the surface.

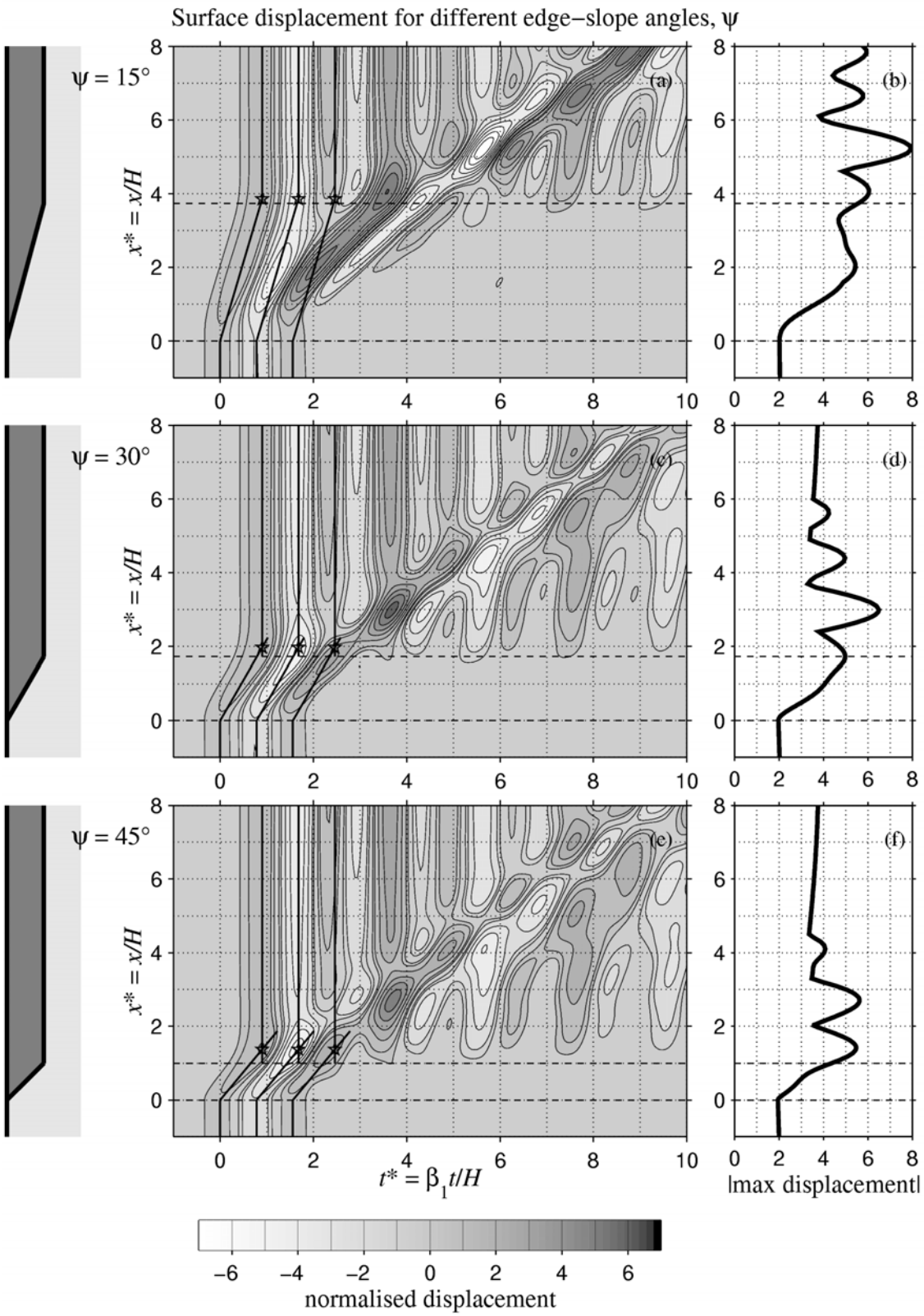

Figure 6.9. Transient surface displacement at the layer edge for simulations S1 ($\psi = 15°$), S2 ($\psi = 30°$) and S3 ($\psi = 45°$). Maximum displacement is shown on the right. The small pentagrams mark the theoretical positions of constructive interference between undistorted base- and edge-refracted wavefronts.

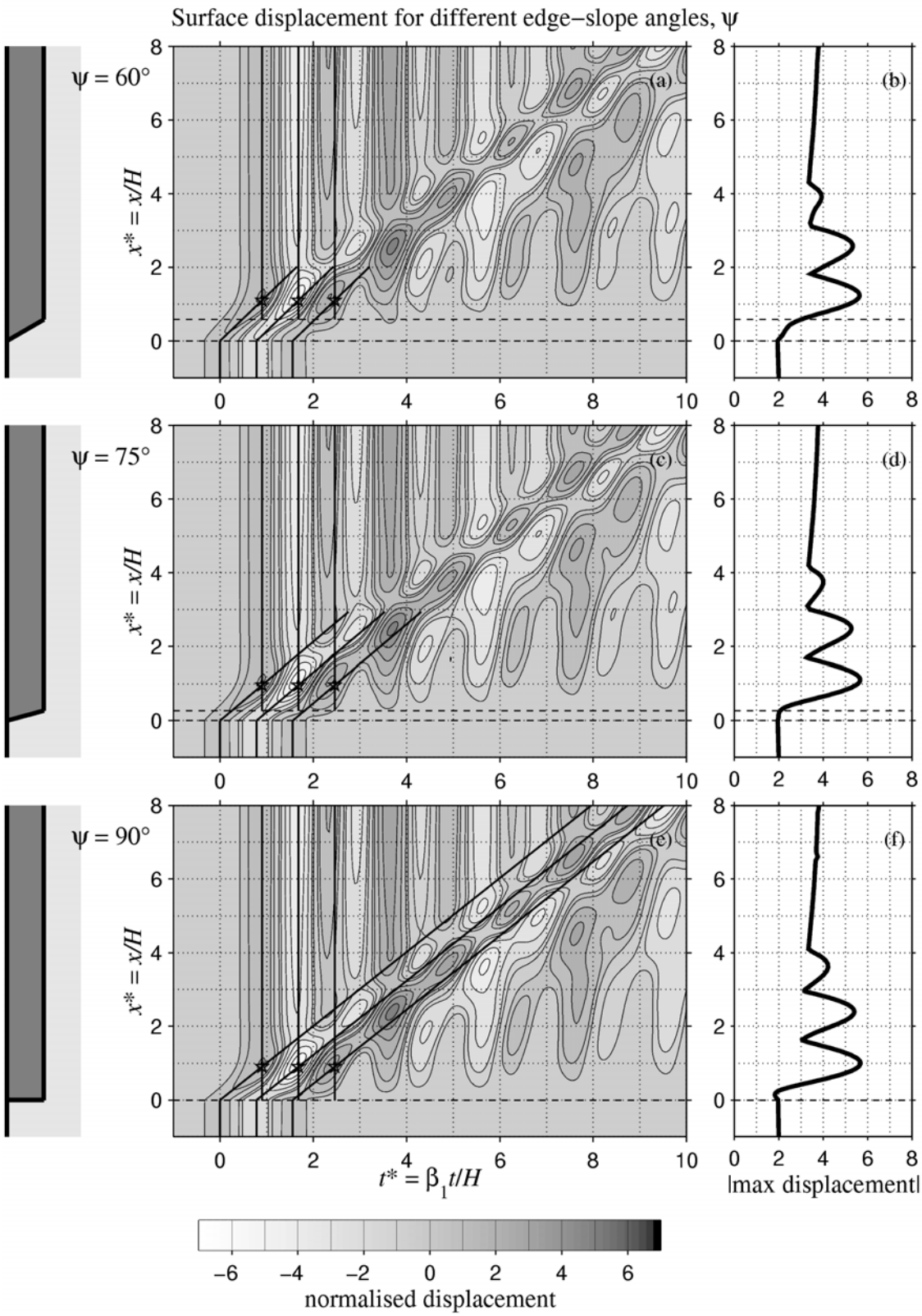

Figure 6.10. Transient surface displacement at the layer edge for simulations S4 ($\psi = 60°$), S5 ($\psi = 75°$) and S6 ($\psi = 90°$). Maximum displacement is shown on the right. The small pentagrams mark the theoretical positions of constructive interference between undistorted base- and edge-refracted wavefronts.

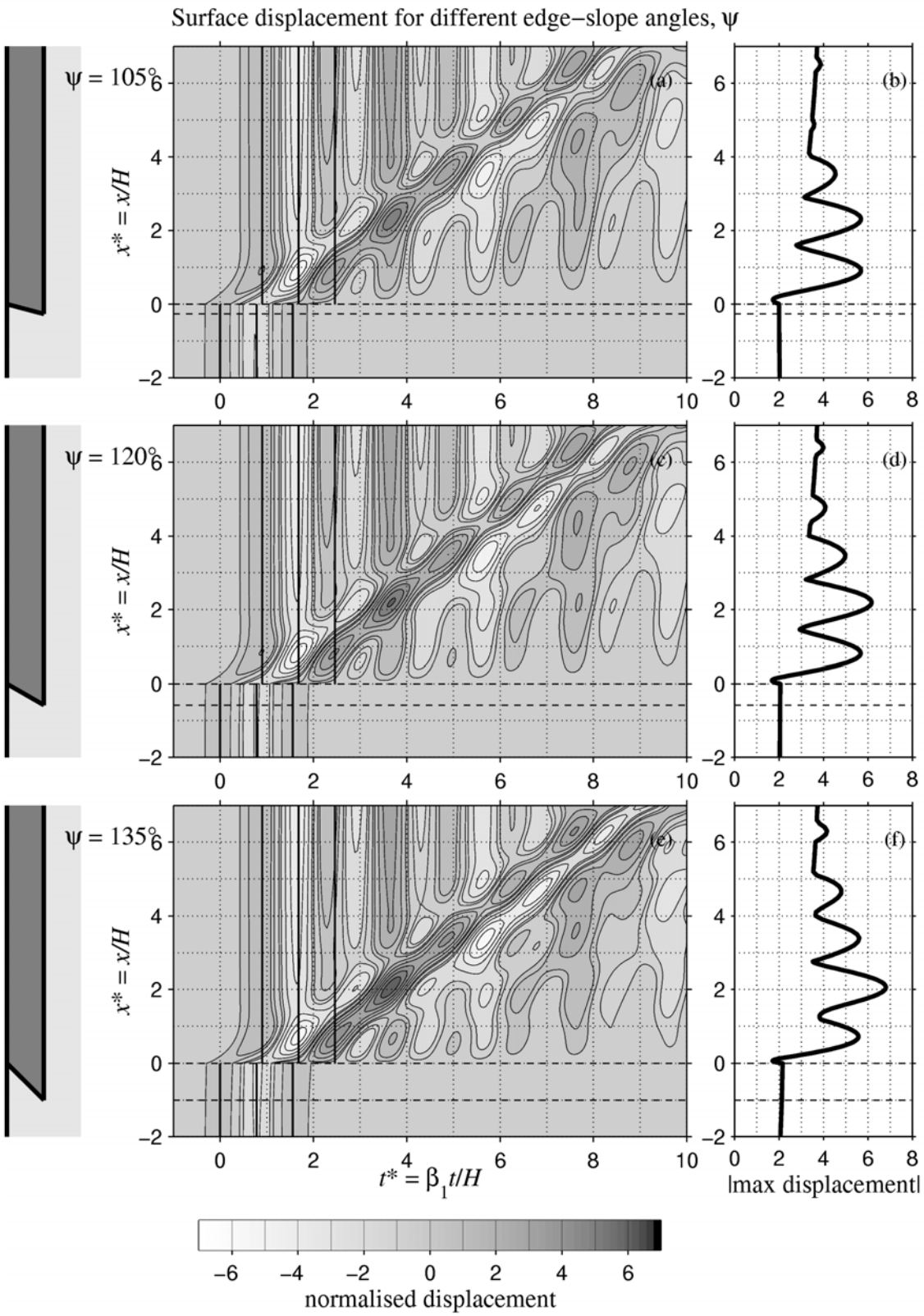

Figure 6.11. Transient surface displacement at the layer edge for simulations S7 ($\psi = 105°$), S8 ($\psi = 120°$) and S9 ($\psi = 135°$). Maximum displacement is shown on the right. Straight lines show the expected surface arrivals of each of the three peaks of the Ricker wavelet

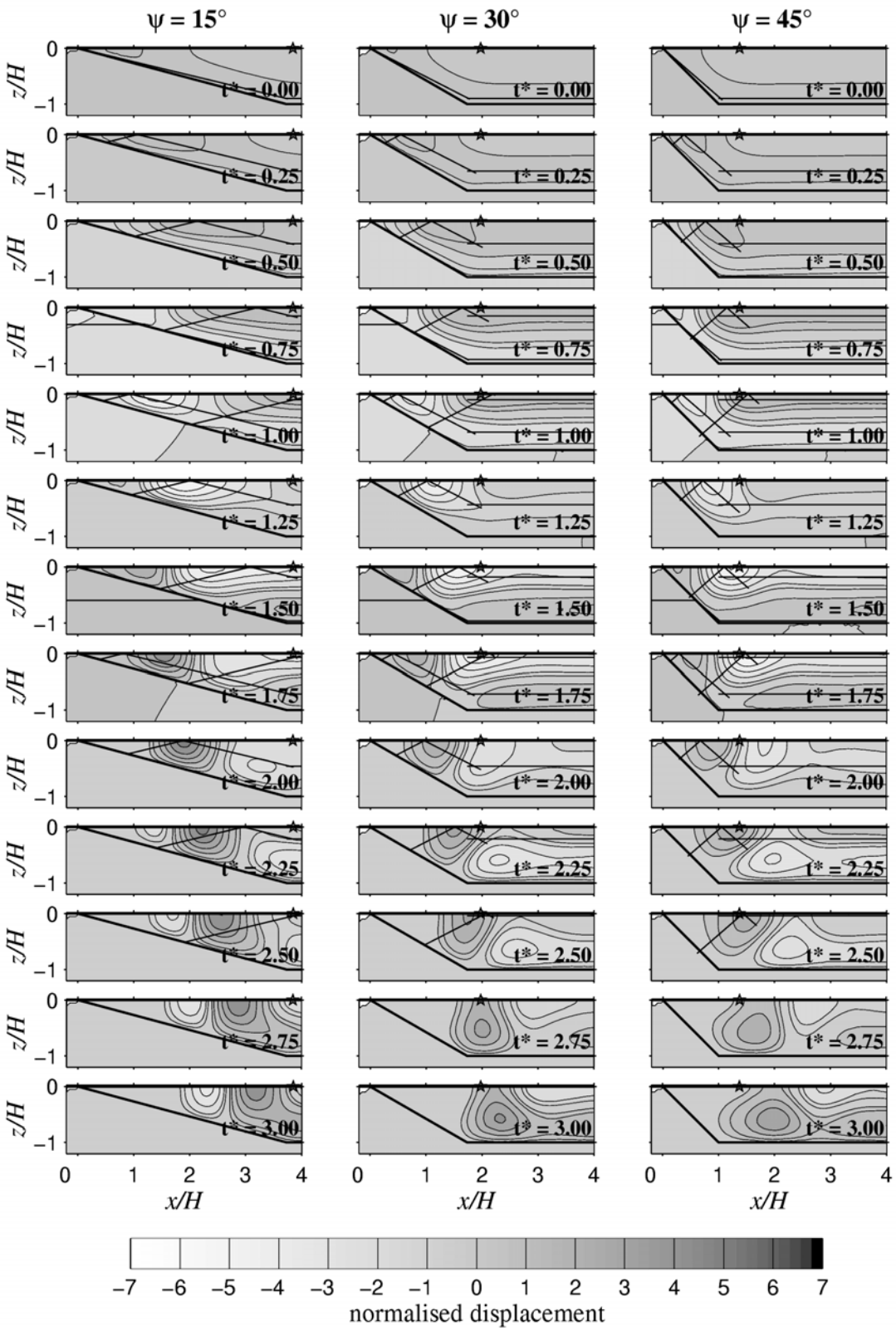

Figure 6.12. Consecutive frames of displacement in the *x*-*z* plane for simulations S1 ($\psi = 15°$), S2 ($\psi = 30°$) and S3 ($\psi = 45°$). The boundary of the layer is shown with a solid line. Thin lines show the expected positions of the each of the Ricker wavelet peaks, prior to surface amplification at the pentagram.

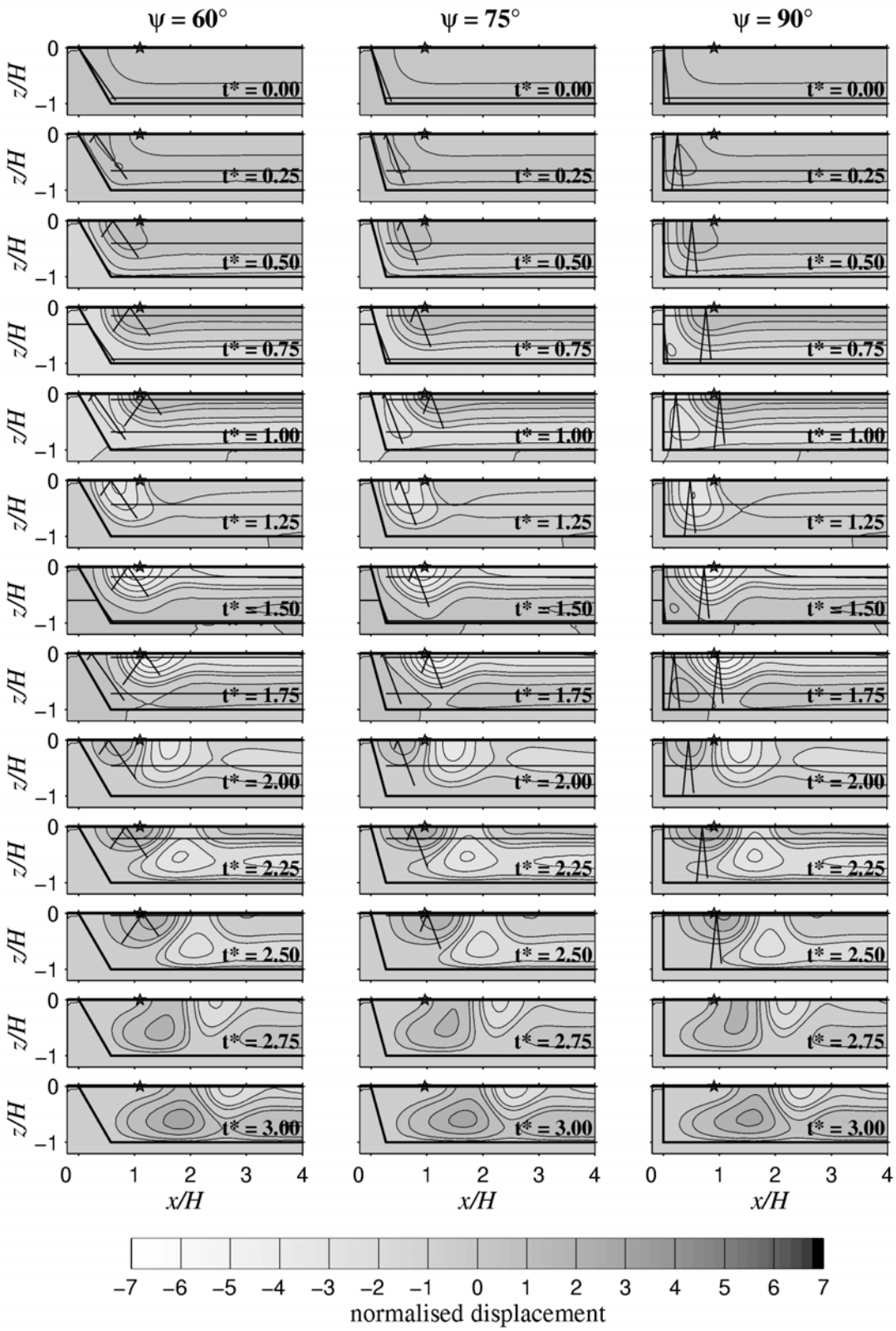

Figure 6.13. Consecutive frames of displacement in the *x*-*z* plane for simulations S4 ($\psi = 60°$), S5 ($\psi = 75°$) and S6 ($\psi = 90°$). The boundary of the layer is shown with a solid line. Thin lines show the expected positions of the each of the Ricker wavelet peaks, prior to surface amplification at the pentagram.

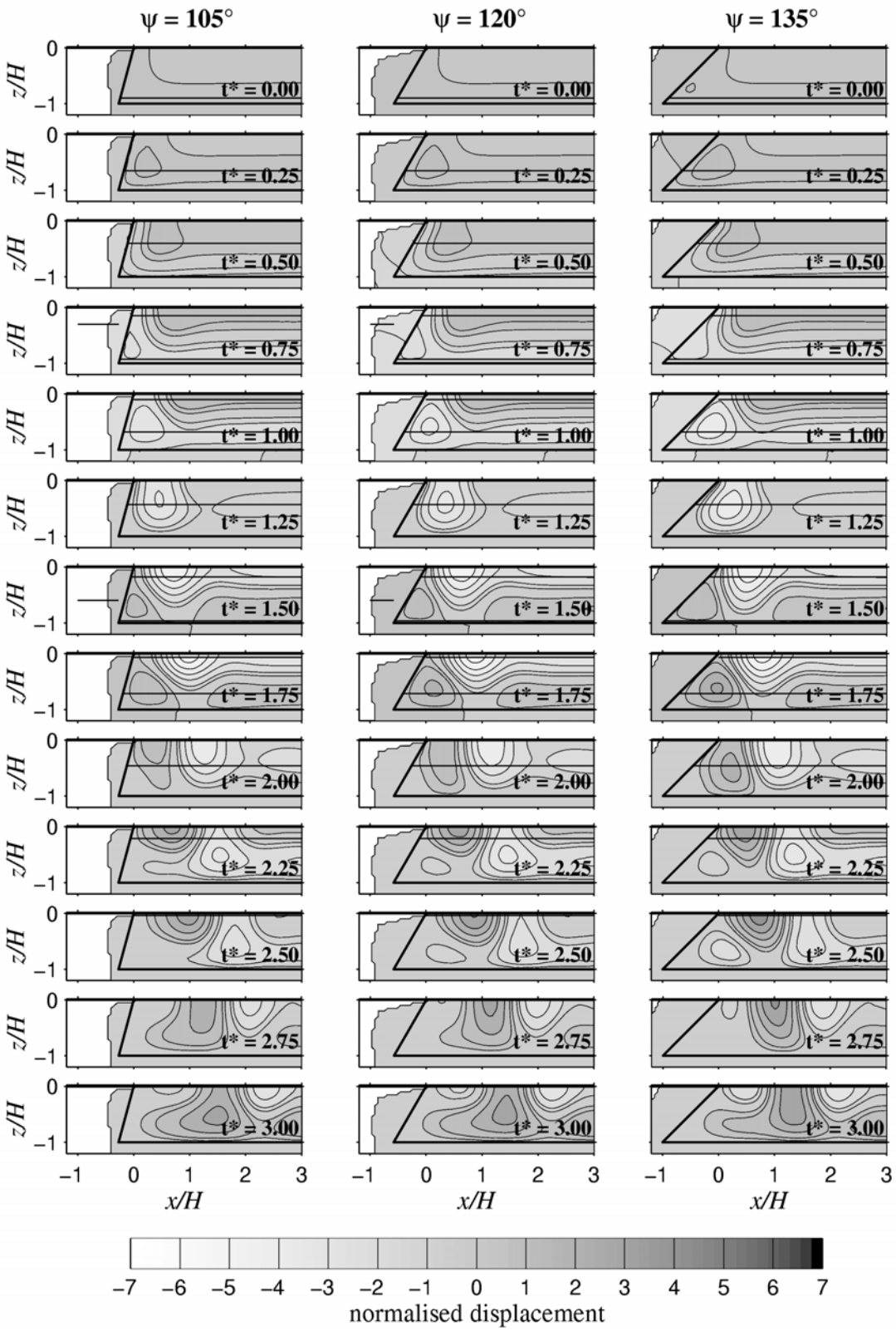

Figure 6.14. Consecutive frames of displacement in the *x*-*z* plane for simulations S7 ($\psi = 105°$), S8 ($\psi = 120°$) and S9 ($\psi = 135°$). The boundary of the layer is shown with a solid line. Thin lines show the expected positions of the each of the Ricker wavelet peaks, prior to surface amplification at the pentagram.

While the base-refracted wavefronts from the FEM modelling do follow their expected position up through the cross-section, there is often interference between up-going and down-going peaks in the Ricker wavelet which makes each individual peak hard to follow. A similar situation exists for edge-refracted pulses where interference from diffracted and totally reflected wavefields significantly distorts the shape of the sub-critically refracted pulse. Nevertheless, a poorly defined point of constructive interference can be seen to form at the lower vertex for $\psi \geq 60°$. The small peak travels upwards on an angle toward the surface which it meets at approximately $x = x^c$. This occurs three times, once for each peak of the Ricker pulse.

On the *t-x* plots in Figures 6.9-6.11 this same process can be seen as a pulse following the theoretical sloping line to meet the arrival of the base refracted wavefront at x^c, marked by a small star. This constructive interference between undistorted wavefronts occurs for all $\psi \geq 90°$, as expected. The interference, however, causes very little amplification when the phase velocity of the Love wave is significantly different to c_x^{e1}.

The dominant phase velocity of the Love wave has been measured from the *t-x* plots for each of the nine cases. All lie within the narrow range $c = 1.15 \pm 0.1\beta_1$, which (not surprisingly) corresponds to the phase velocity associated with the characteristic frequency of the input ($\eta = 2$) on the Love wave dispersion curve in Figure 6.1(c). A significantly lower group velocity, $U = 0.87$, at this frequency means that energy is quickly transferred from one phase to the next. Referring to Table 6.3, c_x^{e1} is significantly greater than $c(\eta = 2) = 1.15\beta_1$ for $\psi \geq 45°$, while for $\psi = 60°$ and $\psi = 75°$ it is about the same and for $\psi = 90°$ it is slightly lower.

For edge-angles other than vertical, the first pulse of the Love wave does not lead directly back to the origin of the plot, as we might expect for an undistorted horizontally travelling pulse. For normal edge-slopes the Love wave is initiated a short distance into the layer from the edge, while for reverse edge-slopes the pulse appears to originate from a point back into the rock from the edge. In general, the first pulses are initiated at a point on the edge where the layer depth is one-third of the full depth, *H*.

It is clear that the strongest constructive effect at the surface occurs between vertically reflected pulses within the layer and pulses of the Love wave. Amplification by interference between vertically reflected pulses and undistorted edge-refracted pulses

appears to be minimal, except when the phase velocity of the latter matches the dominant phase velocity of the Love wave. The position and strength of the amplification is thus highly dependent on the nature of the edge-generated Love wave.

Constructive interference is not limited to occur between the n^{th} peak of the base-refracted pulse and the corresponding n^{th} peak of the Love wave pulse. For all edge-slopes, there are several peaks in displacement across the width of the layer. The first (except for $\psi = 15°$), however, is due to interference between the n^{th} base-refracted peak and the n^{th} Love wave peak. Later peaks are associated with interference between base-*reflected* peaks and the Love wave, and are the site of the highest amplification in the results when the edge slope is less than 45° or overhanging. In the exception, when $\psi = 15°$, the first peak occurs above the shallow sloping edge, in the approximate position where the depth of the layer corresponds to a 1-D resonant frequency equivalent to the central frequency of the input. Amplification in this case is though still clearly influenced by the action the horizontally travelling dispersed wavefield.

Frequency Response

Plots of frequency response for different edge angles are presented in Appendix 1.1. As with the FSR from simulations F1-F6, amplification in the frequency domain shows little correlation with constructive interference at the edge. The pattern of amplification is in all cases similar to that described in Figure 5.10, yet is apparently offset some distance from the edge. The offset is perhaps an indicator of the nature of the Love wave development.

6.3 DISCUSSION

Two basic phenomena have been shown to occur when SH waves meet the edge of a soft layer. The first is the generation of sub-horizontally propagating wavefronts that quickly develop into a Love wave, and the second is constructive interference between these and wavefronts which are refracted in from the base to become sub-critically trapped within the layer. While these observations have certainly be made before, several important characteristics of each have been noted in the FEM modelling. Results from the 16 simulations have shown that the frequency of the input, the depth and properties of the layer, the velocity contrast and the edge-slope angle all influence the development and nature of the Love wave, as well as the nature of constructive interference at the edge.

6.3.1 LOVE WAVE GENERATION AT THE EDGE OF A LAYER

In Chapter Five it was demonstrated how incident pulses are refracted, diffracted or reflected from the edge of the layer into sub-horizontal paths of propagation within the layer. Such pulses are trapped by total internal reflection and subsequently generate a Love wave. The nature of the edge, the layer and half-space properties and the frequency all affect the speed and location of Love wave development. Once set-up, the Love wave propagates away from the edge with well known characteristics reviewed in Chapter Four.

Effect of Frequency

The dispersive nature of diffraction and total reflection indicates that Love wave development must also be highly dependent on frequency. This idea is supported by the results presented in Figures 6.2-6.4 where it appears that high frequencies develop into Love waves much more quickly than do low frequencies. The group velocity of low-frequency components of the Love wave do not lead directly back to the origin of the graph, while they do for high frequencies.

At the same time, the frequency response of the vertical-edge layer is approximately the same for any of the modelled input frequencies. The near-perfect matching between FEM modelling results and theoretical extremum lines from Section 5.5.2 implies that the interference pattern of the Love wave develops immediately adjacent to the edge (which becomes a nodal point in the pattern).

Effect of Edge-Slope Angle

The effect of the edge slope angle has only been investigated for a reasonably high dimensionless frequency ($\eta_c = 2$). While $45° \leq \psi \leq 135°$, each peak of the input Ricker pulse appears to generate a peak in the Love wave that initially travels at the dominant phase velocity across the layer. The dominating phase velocity is shown to correspond to the central frequency of the Ricker wavelet, calculated from the Love wave dispersion relationship (Equation 4.22).

Figures 6.9-6.11 show in the time-domain how Love wave peaks travelling at the phase velocity can be traced back to a point on the edge where they appear to be initiated. This distance from the edge where the Love waves originate is about one-third of the distance

between the upper and lower vertices. The pattern of frequency response also appears to develop at a distance controlled by the edge-slope angle.

6.3.2 AMPLIFICATION BY CONSTRUCTIVE INTERFERENCE AT THE EDGE OF A LAYER

It has been shown in the results that the most important constructive interference occurs between phases of the edge-generated Love wave and base-refracted pulses. Constructive interference between *undispersed* edge-refracted wavefronts and the base-refracted wave occurs in most simulations yet the associated amplification is usually small. For high frequency inputs it is much smaller than the amplification associated with the Love wave, while for low frequency inputs, its effects are masked by interference between vertically reflecting wavefronts. With a high frequency input and a steep normal edge-slope, however, the phase velocity of the undispersed edge-refracted wave is close to the phase velocity of the Love wave and the position of the peak displacement may be roughly approximated by x^c from Equation 5.34 in the wavefront analysis. The following discussion concentrates on constructive amplification associated with the horizontally propagating Love wave.

Effect of Frequency

For inputs where the dominant frequency is high compared to the fundamental resonant frequency of the basin ($\eta_c \geq 1.5$), the highest amplification at the edge clearly occurs due to discrete points of constructive interference between horizontally-propagating phases of the Love wave and vertically-propagating peaks that are refracted or later reflected from the base of the layer.

For lower input frequencies, the amplification is also a function of interference between sub-critically reflecting peaks within the layer. It then becomes very much a function of the shape of the input waveform. When the input frequency is close to both the fundamental of the layer and the Airy phase frequency ($\eta_c \approx \eta_0 = 1.0 \approx \eta_0^{Airy}$), edge amplification is very strong and develops by a coupling between vertical resonance within the layer and Love wave energy travelling at the Airy phase group velocity. For input frequencies lower than the fundamental, most of the Love-wave energy travels in an inhomogeneous form in the half-space and little amplification is seen at the surface.

Effect of Edge-Slope Angle

As previously discussed, the edge-slope angle has the apparent effect of displacing the point of initiation of the Love wave by about one-third of the distance between the upper and lower vertices. The position of constructive interference between the vertical arrival and the Love wave, x^c, can therefore be given by the dominant phase velocity multiplied by the difference in travel times plus the distance of Love wave initiation, x_i, from the edge

$$x^c = c\left(\frac{H}{\beta_1} - \frac{H}{\beta_2}\right) + x_i \qquad [6.17]$$

and $$x_i = \frac{H}{3}\tan(\pi/2 - \psi) \qquad [6.18]$$

where c is the dominant phase velocity of the Love wave and $H\tan(\pi/2-\psi)$ is the horizontal distance between the upper and lower vertices. This holds at least for a vertically incident $\eta_c = 2$ Ricker pulse input and for $45° \le \psi \le 135°$. Note that for a vertical edge ($\psi = 90°$), the point of initiation, $x_i = 0$.

Figure 6.15(a) shows maximum displacement across the layer for each of the different edge-slope angles. Shaded contours effectively interpolate between the results obtained for each test. Dashed lines indicate the position of the vertices of the layer. The thin solid line plots the distance x^c from Equation 5.34 where the undispersed wavefronts are expected to construct, while the thick solid line plots the distance x^c from Equation 6.17 where the Love wave is expected to construct with the base-refracted arrival. Figure 6.15(b) relates the horizontal phase velocity of the undispersed edge-refracted wavefront to the edge-slope angle.

For edge-slope angles between 45° and 90°, x^c from Equation 5.34 is just short of the first peak in maximum amplitude from the modelling. The small discrepancy is due to the small difference between c and c_x^{e1} over this range of edge-slopes, shown in Figure 6.15(b). Equation 6.17, on the other hand, plots almost exactly along the 1st constructive peak for $45° \le \psi \le 135°$. While the fit of Equation 6.17 is good, it is very limited in application, being only valid for vertically incident $\eta_c = 2$ Ricker wavelets, and even then only determining the 1st position of constructive amplification when for overhanging or very

shallow edges it is later points of constructive interference that produce the maximum amplification.

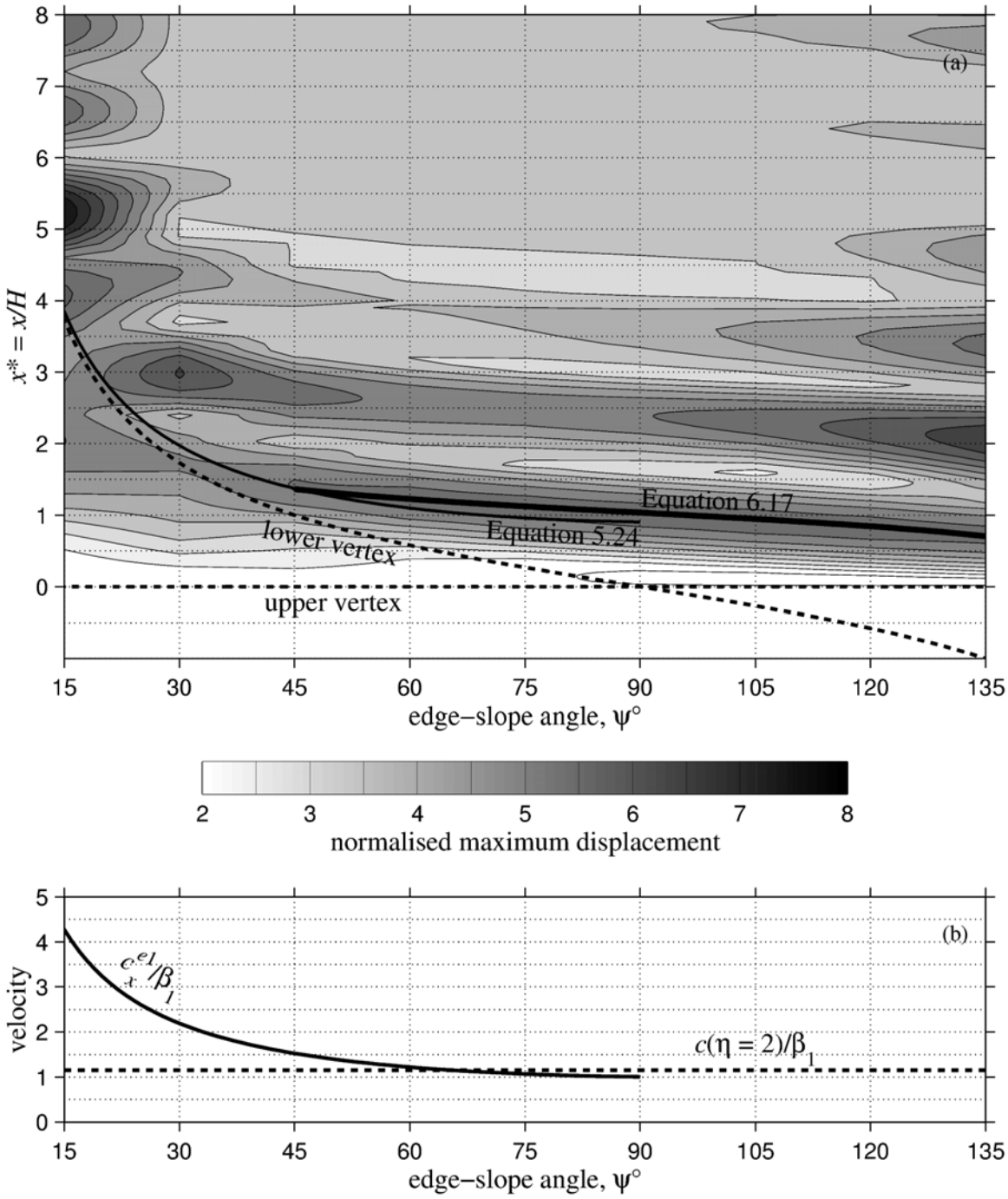

Figure 6.15. (a) Contour plot of maximum displacement out from the edge for each of the different edge-angles in simulations S1-S9. The data plotted here is the same as that shown on the right hand side of Figures 6.9-6.11. (b) A plot showing the relationship between the phase velocity of the undispersed edge-refracted wavefront, c_x^{e1} (Equation 5.9), and the edge-slope angle.

Subsequent occurrences of amplification further from the edge are a result of constructive interference between subcritical reflections of the base-refracted wave. These interferences are highly dependent on the shape and timing of peaks within the Ricker pulse. It would be possible to derive simple geometrical expressions to determine the exact position each peak, yet the result would be valid only for the $\eta_c = 2$ Ricker wavelet shape. In fact it would be possible to take any time-history, determine the dominant frequency and timing of each pulse, and compute a whole suite of points of constructive interference across the layer, in a similar fashion to the analysis of vertical reflections and multiple harmonic peaks in Section 5.3.5. Yet again the results would be valid only for the given time-history.

Perhaps an important factor that has been overlooked in the numerical analysis is the action of material damping, which would undoubtedly decrease the amplitude of later occurrences of constructive interference. The inherent material damping within real geological materials is thus likely to make the 1st peak of interference stand out in amplitude from later peaks.

6.4 SUMMARY

The Archimedes FEM code is used to study the dynamic response of a semi-infinite homogeneous layer over a uniform half-space to a vertically propagating plane Ricker wavelet. The problem is non-dimensionalised and the results are compared with those from the wavefront analysis in Chapter Five.

For vertical edge-slopes and input frequencies greater than the fundamental of the layer, the edge-generated love wave appears to develop immediately adjacent to the edge, and sets up a frequency-dependent amplification pattern matching that proposed in Section 5.5.2. This pattern explains the oscillations in Fourier amplitude noted by Moczo and Bard (1993), and is characteristic of Love wave generation at an edge. For non-vertical edge-slopes, the Love wave appears to originate about one-third the distance to the lower vertex from the upper corner of the edge, for $\eta_c = 2$ at least.

While the propagation of undistorted refracted pulses can be seen at the edge for high input-frequencies, the resultant constructive interference is found to be minor compared to that between the edge-generated Love wave and the base-refracted pulse. The position of

amplification by constructive interference at the edge is thus highly dependent on the dominant phase velocity of the Love wave and the position where it appears to be set-up.

The dominant frequency of the input determines the nature of the constructive interference. For input frequencies greater than twice the fundamental resonant frequency of the layer, one or more discrete points of amplification occur between horizontally and vertically propagating pulses. For input frequencies near the fundamental, a strong coupling develops between the Love wave travelling at the Airy phase and vertical resonance within the layer. Input frequencies significantly lower than the fundamental have little effect at the edge.

Such constructive amplification occurred for all edge-slope angles tested ($15° \leq \psi \leq 135°$). The largest amplification occurs between the Love wave and the initial surface arrival of the base-refracted pulse for steep normal edge-slope angles ($60° \leq \psi \leq 90°$), while for shallow or overhanging edges, the largest constructive amplification is associated with later vertical reflections of the sub-critically trapped pulse. The degree and position of peak amplification are a strong function of the shape of the input pulse. For very shallow edge-slopes, additional amplification occurs in the approximate position where the depth of the layer corresponds to a 1-D resonant frequency equivalent to the central frequency of the input. This amplification will later be defined as a wedge effect.

PART III

SEISMIC AMPLIFICATION AND EDGE EFFECTS IN THE LOWER HUTT VALLEY

Chapter 7: AN INTRODUCTION TO LOWER HUTT

Lower Hutt City lies some 15km north-east of Wellington City, atop a wedge of Quaternary sediments forming a long alluvial valley. On its western edge the sediments butt up against the near vertical wall of the potentially active Wellington Fault. Lower Hutt is home to 96,000 of the 340,000 people living in the greater Wellington region. Around 57,000 of these reside on the 35 square kilometres of flat land created by c.400,000 years of sedimentary deposition within the valley. The valley, shown in Figure 7.1, is approximately 12km long with a maximum width of 4.5km. It slopes and widens gently from Taita Gorge south-west down to the foreshore of the Wellington Harbour, dropping only 30 metres in elevation. The alluvial and marine sediments extend to a maximum depth of 300 metres in the south-western corner, adjacent to the Wellington Fault which forms a clear lineation along the true-right of the valley.

Figure 7.1. Lower Hutt Central viewed from the western hills above the Wellington fault.

The Wellington Fault is one of a number of active dextral strike-slip faults in the highly tectonic region situated above the shallow subduction interface between the Pacific the Australian Plates. It forms the southern end of the North Island Shear Belt, shown in

Figure 7.2. The Hutt Valley has been formed by the tilting action of the large bedrock block to the east of the Wellington Fault. On both sides it is bounded by a range of hills, each reaching around 300-400 metres in elevation. Seismic risk in the Lower Hutt is high for two reasons. The first is the abundance of active faults and tectonic activity in the area and the second is the nature of the local geology and topography which produce strong site effects.

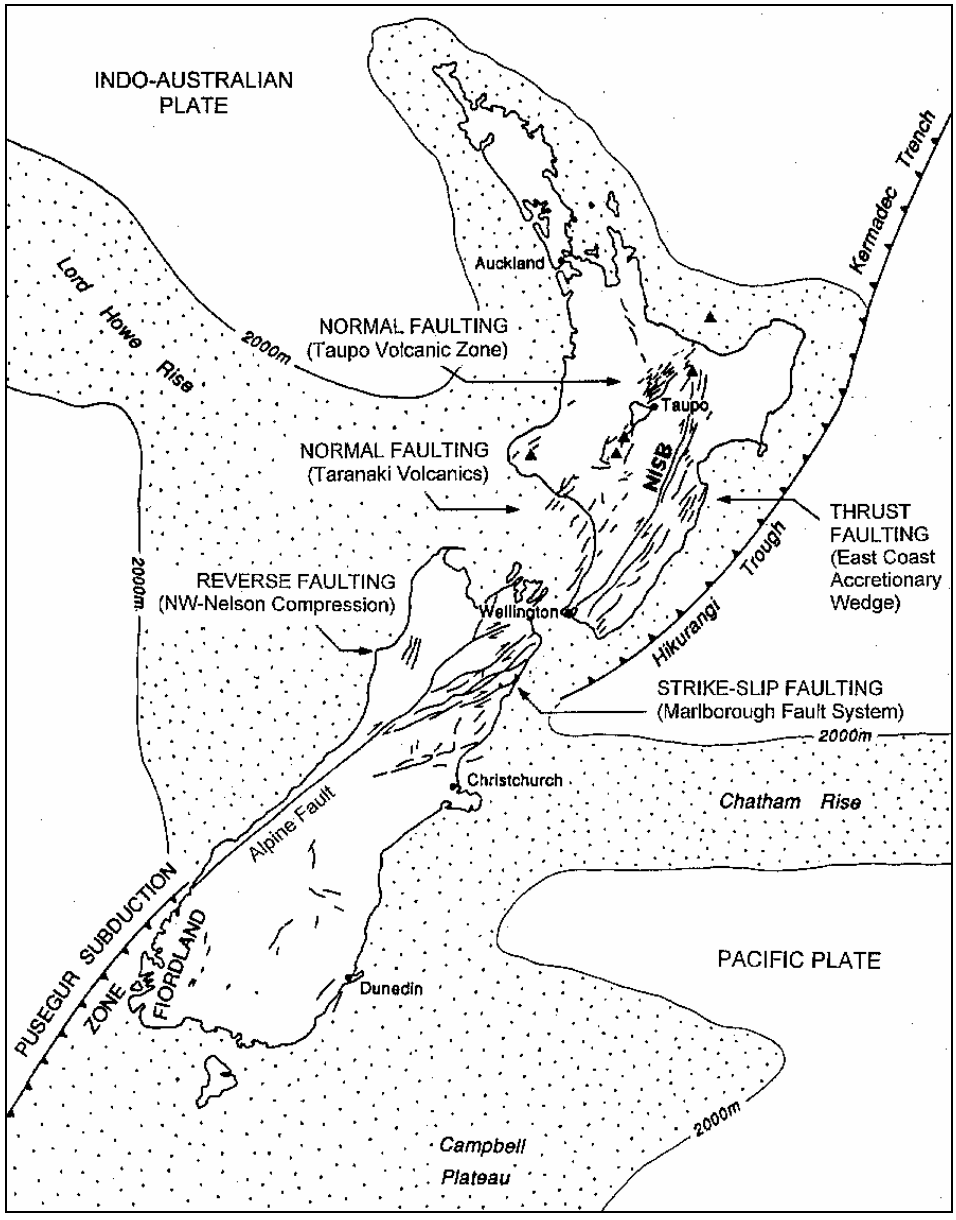

Figure 7.2. New Zealand plate tectonics indicating the major forms of seismic activity. Wellington lies in an active area between the southern end of the North Island Shear Belt (NISB) and the Marlborough Fault System, and directly above the shallow dipping Hikurangi subduction zone (after Cowan, 1994).

7.1 SEDIMENTARY GEOLOGY IN THE LOWER HUTT VALLEY

The Lower Hutt Valley is essentially a wedge of geologically young sediments that have accumulated within an actively subsiding basin adjacent to the Wellington Fault. The soft sediments are surrounded from below by a much more rigid basement bedrock. Begg and Mazengarb (1996), Stevens (1991, 1990, 1958), Cotton (1960) and Lensen (1958) all contain good descriptions of geology in the Wellington area.

7.1.1 BASEMENT ROCKS

The Wellington area is underlain by Upper Paleozoic to Mesozoic age basement rock of the Torlesse Complex. Interbedded layers of indurated sandstone (greywacke) and mudstone (argillite) were formed in a deep marine environment during a period of subduction at the continental margin. Small areas of basalt, chert, coloured argillite and limestones are also present (Begg and Mazengarb, 1996). The rocks have since been intensely folded and faulted in several directions, and are closely jointed. Intact bedrock is generally strong to very strong, although the rock mass is weaker due to the 0.1-0.5 m joint spacing, the presence of many sheared zones and weathering near the surface (Dellow et al., 1992; Grant-Taylor, 1959).

7.1.2 SEDIMENTS INFILLING THE VALLEY

Substantial depths of Quaternary sediments have accumulated in the Port Nicholson basin over the last 450,000 years (Begg and Mazengarb, 1996). The thickest record of sediments in the Lower Hutt Valley (299m) is from the Gear Meat Drillhole which reaches basement on the Petone foreshore. The sediments within the Lower Hutt-Port Nicholson basin are referred to as the Hutt Formation and were laid down in alluvial, estuarine and marine environments, during a succession of interglacial and glacial periods (Stevens, 1956a,b; Grant-Taylor, 1959).

The most recent (Holocene) sediments were deposited during the current interglacial. Taita Alluvium is the fluviatile veneer over the Hutt Delta and consists of gravels with minor silts and clays with an average depth of 13m, overlying Melling Peat, a thin highly fossiliferous layer. The Petone Marine Beds – silts and clays of some seven metres in thickness bounded below by an impervious aquiclude – complete the 20m+ depth of Holocene sediments.

Dellow et al. (1992) describes the near-surface Holocene materials above the aquifer as generally soft in nature, fine grained with high water contents and low SPT values (N<10). Coarser grained beds and lenses may form up to 40% of the total mass. Shear wave velocities of 168-190m/s have been measured with a seismic cone penetrometer (SCPT) in several locations in the bottom end of the valley, and is apparently fairly constant with depth (Stephenson and Barker, 1992). Their maximum thickness is 27 m in the lower, western valley, and they gradually thin and grade into the Taita Alluvium gravels up-valley. Only the lower half of the Hutt Valley is underlain by more than 10 m of soft sediments (Dellow et al., 1992).

Waiwhetu Artesian Gravels originate from the last (Otiran) Glacial and consist of compact sandy gravel to form an aquifer ranging between 30 and 50 metres thick. Many boreholes penetrate into the Waiwhetu aquifer as fresh water supply for the Lower Hutt City. Below the aquifer lie a series of glacial and interglacial units consisting of gravels, sands and silts. Included amongst these are the marine Wilford Shell Beds from the last Interglacial (Kaihinu), and the Moera and Nemona Basal Gravels. Begg and Mazengarb (1996), Dellow et al. (1992) and Stevens (1956b) all provide more complete descriptions of sediments in the Lower Hutt.

A layer of fill covers small parts of Lower Hutt and much of the Wellington inner city. Seaview, on the eastern side of the lower Hutt River is one such area, along with the Hutt Road up the western side of the valley. In Wellington, much of the city is sited on reclaimed land extending out into the harbour. Most of the central city has been built on more than two metres of fill, the majority of which is poorly compacted. The most commonly used material was weathered rock from nearby quarries, whilst hydraulic fill and demolished brickwork have been used in some areas (Begg and Mazengarb, 1996). These layers of fill have low strength and shear velocities and are likely to liquefy during strong shaking.

7.2 SEISMIC SOURCES THREATENING THE LOWER HUTT

Wellington frequently experiences many small magnitude earthquakes, sourced in both the overriding Australian Plate and the subducting plate. Historically it has also been shaken quite severely by a number of different events. Those that have had a felt intensity greater than MM VI are listed in Table 7.1. They range from close strike-slip ruptures such as the

1855 Wairarapa earthquake to distant thrust events such the 1929 Buller earthquake in the South Island.

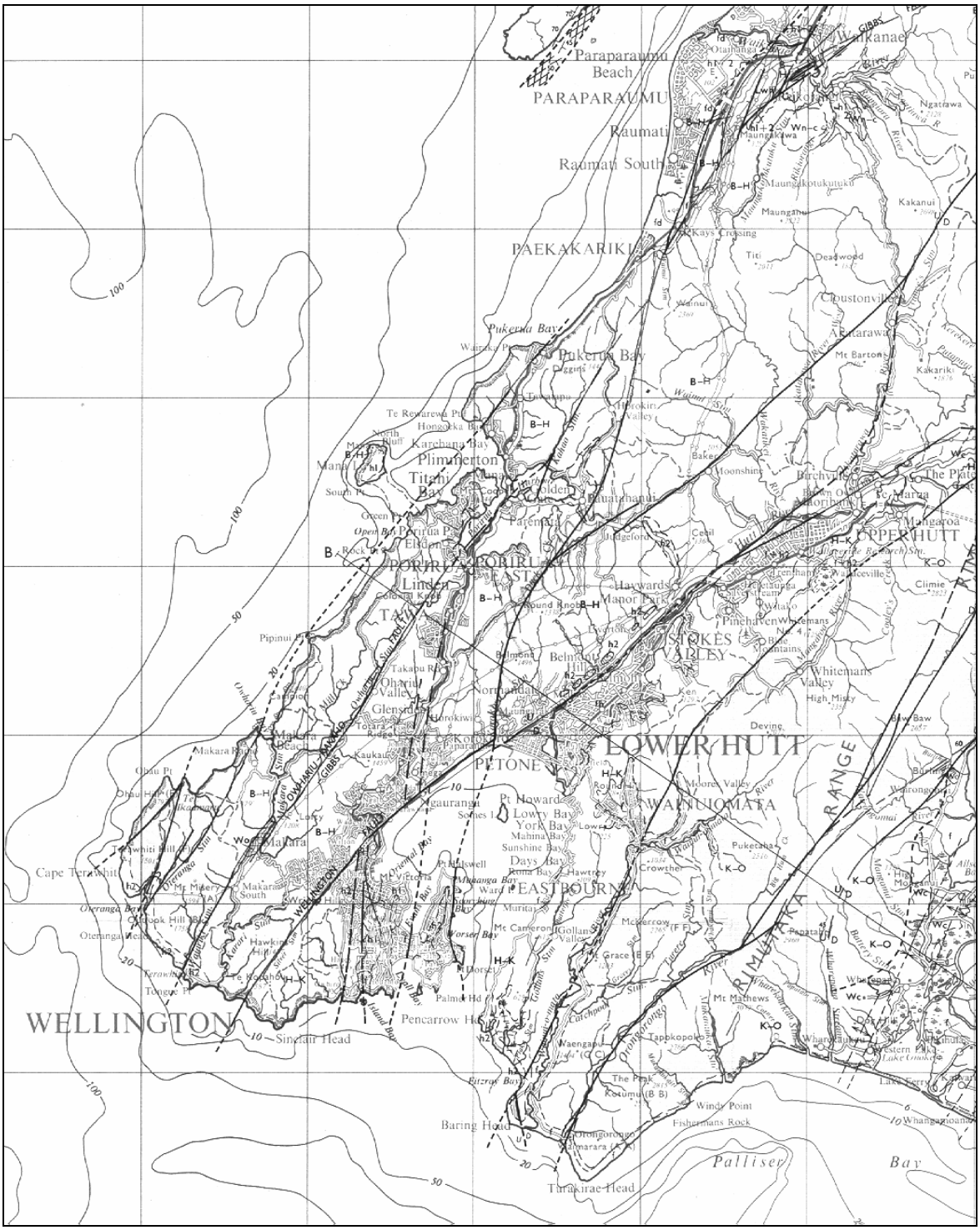

Figure 7.3. The Lower Hutt Valley extends northeast from the Wellington Harbour along the strike of the Wellington Fault. Several other major strike-slip faults (see Table 7.2) also run parallel to the valley (from Kingma, 1967).

Within 30km of the Lower Hutt Valley there are at least five active strike-slip faults (Figure 7.3), each capable of producing large magnitude events. Paleoseismic evidence summarised in Table 7.2 shows that recurrence intervals range from 500-5000 years, with the Wellington Fault being by far the most active. The only one of these Faults to have ruptured in European history is the Wairarapa, in 1855.

Table 7.1: Earthquakes felt in Wellington with an intensity greater than MM VI (after Adams, 1974, and updated from Downes, 1995).

Year	Date	Intensity MM	Magnitude M_L	Distance from Wellington	Epicentral Location
1840	26 May	VI	6	80?	
1843	08 Jul	VI	7.5	160?	
1848	16 Oct	VIII	7.1	65?	Marlborough
1855	23 Jan	X	8.1	30	Wairarapa
1893	12 Feb	VI	6.6	130	Nelson
1897	08 Dec	VI	6-7	160	
1904	09 Aug	VIII	7.5	190	Cape Turnagain
1914	08 Feb	VII	6	30	
1929	17 Jun	VI	7.8	220	Buller
1934	05 Mar	VI	7.6	110	Paihiatua
1942	24 Jun	VII	7.2	100	Masterton
1942	02 Aug	VII	7.0	100	Masterton
1943	26 Feb	VI	5.5	30	
1966	23 Apr	VI	6.0	50	
1968	01 Nov	VI	5.5	30	Cook Straight

In addition to the Wellington and other major strike-slip faults, there several other potential sources of strong shaking. These include the shallow interface of the Hikurangi subduction zone which lies some 30km directly beneath Wellington. Best guesses based on accumulated inter-plate strain and likely rupture area indicate a subduction zone earthquake is likely to have a recurrence interval of 2000 years and a moment magnitude M_W 8.2 (Van Dissen and Berryman, 1996). Other potential large earthquake sources include normal faulting within the down-going Pacific crust, distant thrust faults in the Wairarapa acretionary wedge and strike-slip faults in Marlborough, as well as possible unknown faults.

Table 7.2: Results of Paleoseismic studies on the five major strike-slip faults in the Wellington region (from Van Dissen et al., 1996).

Fault Name	Probable Magnitude (M_W)	Recurrence Interval (years)	Last Event (years ago)
Wairau	7.6	1000-2300	800+
Shepherds Gully	7.6	2500-5000	1200+
Ohariu	7.6	1500-5000	1105-1185
Wellington	7.6	500-770	335-485
Wairarapa	8.1	1160-1880	145

7.2.1 THE WELLINGTON FAULT

Perhaps the most striking landscape feature in the area is the Wellington Fault, which has created a highly visible lineation in a NE-SW direction from the south coast, over the hills, beside down-town Wellington, along the western shores of Port Nicholson, and up the western edge of the Hutt Valley before disappearing into the Tararua ranges to the north. The Wellington Fault is one of the major active dextral strike-slip faults in New Zealand and represents a significant hazard to the greater Wellington region. Both Lower Hutt City and the central business district of Wellington City lie immediately adjacent to the fault on essentially alluvial sediments forming a basin bounded by firm rock. The presence of the Wellington Fault was first recognised by McKay (1892), while it was named by Cotton (1912).

The 75 km long Wellington-Hutt Valley Segment of the Wellington Fault appears to behave in a characteristic fashion with the occurrence of maximum-magnitude ruptures at regular intervals. Paleoseismic studies (eg. Grant-Taylor, 1967; Lewis, 1989; Berryman, 1990; Van Dissen and Berryman, 1991; Van Dissen et al., 1992a; Van Dissen and Berryman, 1996) suggest a characteristic dextral offset of 3.2-4.7 metres with a small up-thrusting component of less than 1 in 10, or 0.3 metres (Berryman, 1990). The lateral slip rate has been a relatively constant 6.0-7.6 mm/year through the last 140 ka. (Berryman, 1990). The length of rupture and amount of slip have been used to estimate a probable surface-wave magnitude, M_S, of 7.1-7.8 (Berryman, 1990) and moment magnitude, M_W, of 7.3-7.9 (Van Dissen and Berryman, 1996). These figures indicate that a major rupture on the Wellington Fault would be of similar source characteristics, yet slightly larger than the 1995 Hyogo-ken Nanbu earthquake.

Elapsed time since the last rupture has been estimated at 340-490 years, and the second most recent, 710-770 (Van Dissen and Berryman, 1996). The average recurrence interval estimated from slip-rate data is given a value of 500-770 years, as shown in Table 7.2. The probability of rupture in the next 100, 300 and 1000 years has been estimated at 25 ± 20%, 60 ± 30% and 90 ± 10% respectively (Van Dissen and Berryman, 1990).

A Wellington Fault earthquake is expected to produce mainly strike-slip and some thrust movement from a hypocentre around 10 km deep. Rupture length and slip suggest that the fault plane is upper crustal and dipping slightly to the west, not reaching the shallow-dipping subduction plane like the nearby Wairarapa Fault. The path of seismic wave propagation will be essentially vertical, slightly inclined to the east. Source radiation (especially in the direction of the fault) is likely to be a significant factor, although the rupture could just as easily propagate in either or both directions.

7.3 A Review of Previous Research on Site Effects in the Lower Hutt Valley

Several studies have been conducted looking at the frequency-dependant amplification found in recorded data from Wellington and the Lower Hutt. The exclusive availability of only relatively weak-motion records places questionable limitations on the applicability of these results to the estimation of strong shaking, although their usefulness for correlation with elastic modelling is nonetheless highly valuable.

Stritharan and McVerry (1992) describe ground shaking in the Lower Hutt Valley from the strong-motion instrument data of nine earthquakes between 40 and 240 km away with peak ground accelerations (PGA) in the order of 0.01-0.15g. They calculated Fourier spectral ratios (FSR) up to a factor of 10 at some recorder sites in the deepest part of the valley, and constructed a microzone map of the Lower Hutt Valley, which indicates areas that received the strongest ground shaking. Unusually located peaks from some earthquakes suggested the influence of two, or even three-dimensional site amplification.

Taber and Smith (1992) describe the spectral amplification at 24 weak-motion sites in the Lower Hutt Valley. Amplification of shaking appears to increase gradually when moving down-valley from the Taita Gorge to the Petone foreshore. They find peak FSR up to a factor of 14 at the lower end of the valley. Amplification at most sites occurred over a broad frequency band from 0.5 to 5.0 Hz. In general, the highest spectral peaks occur in the

1 to 3 Hz range. Van Dissen et al. (1992b) have mapped out ground shaking hazard zones and estimated PGA in the Lower Hutt Valley due to a Wellington Fault rupture based on geological data and weak-motion data from the above studies.

Taber et al. (1993) compares strong motion recorded data (PGA's between 0.005 and 0.10g) to weak motions (PGA's between 0.00005 and 0.004g) at six sites in the Lower Hutt and ten sites in Wellington. Non-linear behaviour does not appear to be significant at these levels of shaking. For strong motions, deep sites in the Hutt Valley had a greater low frequency response while the peak amplification for a site near the edge occurred at higher frequencies.

Stephenson (1974, 1975, 1989b) observes strong directionality in the power spectra of several earthquakes in the Lower Hutt, including the 1968 Cook Straight event (Table 7.1, PGA = 0.15g) and other small events (0.0002-0.03g). He proposes that the 2.1-3.2Hz strong motion observed in the 45-65° direction (up-down valley) is a result of "directed" or horizontal resonance patterns within the flexible surface (Holocene) sediments.

Chapter 8: PRELIMINARY FEM MODELLING OF LOWER HUTT

Cross-sections through the Lower Hutt valley are analysed for anti-plane SH-wave propagation using the Archimedes FEM software described in Chapter Three. Input to the model is a plane Ricker wavelet with a central frequency of 2.0Hz. Initial results are presented in the form of transient anti-plane displacement, and sediment-to-rock Fourier spectral ratios (FSR). The results are later used in Chapter Nine to design an array across the fault-bounded edge of the valley. In Chapter Ten the geological model used here is calibrated with array results and a more comprehensive set of simulations and results are presented for the Lower Hutt valley.

8.1 METHOD OF ANALYSIS

Two cross sections of the Lower Hutt Valley are constructed form existing sub-surface geological data. Their positions are shown on Figure 8.1. One line (section AA) is taken through Petone and Seaview at the seaward end of the Hutt Valley, and the other (section BB) through Lower Hutt Central and Waiwhetu, 2.45 km up-valley. The cross sections are used to define the geometry of finite element meshes, and along with material properties are used as input to Archimedes.

8.1.1 MODEL GEOMETRIES

Both cross-sections were taken along a line running 38 degrees west of north. Cross-sections have been aligned in the x-z plane where the x-axis lies perpendicular to the Wellington Fault, approximately south-east from the north-western edge (rock-soil interface) of the basin and the vertical z-axis is negative below the ground surface. The out-of-plane horizontal y-axis runs fault-parallel down the length of the valley. The cross-sections are shown in Figure 8.2.

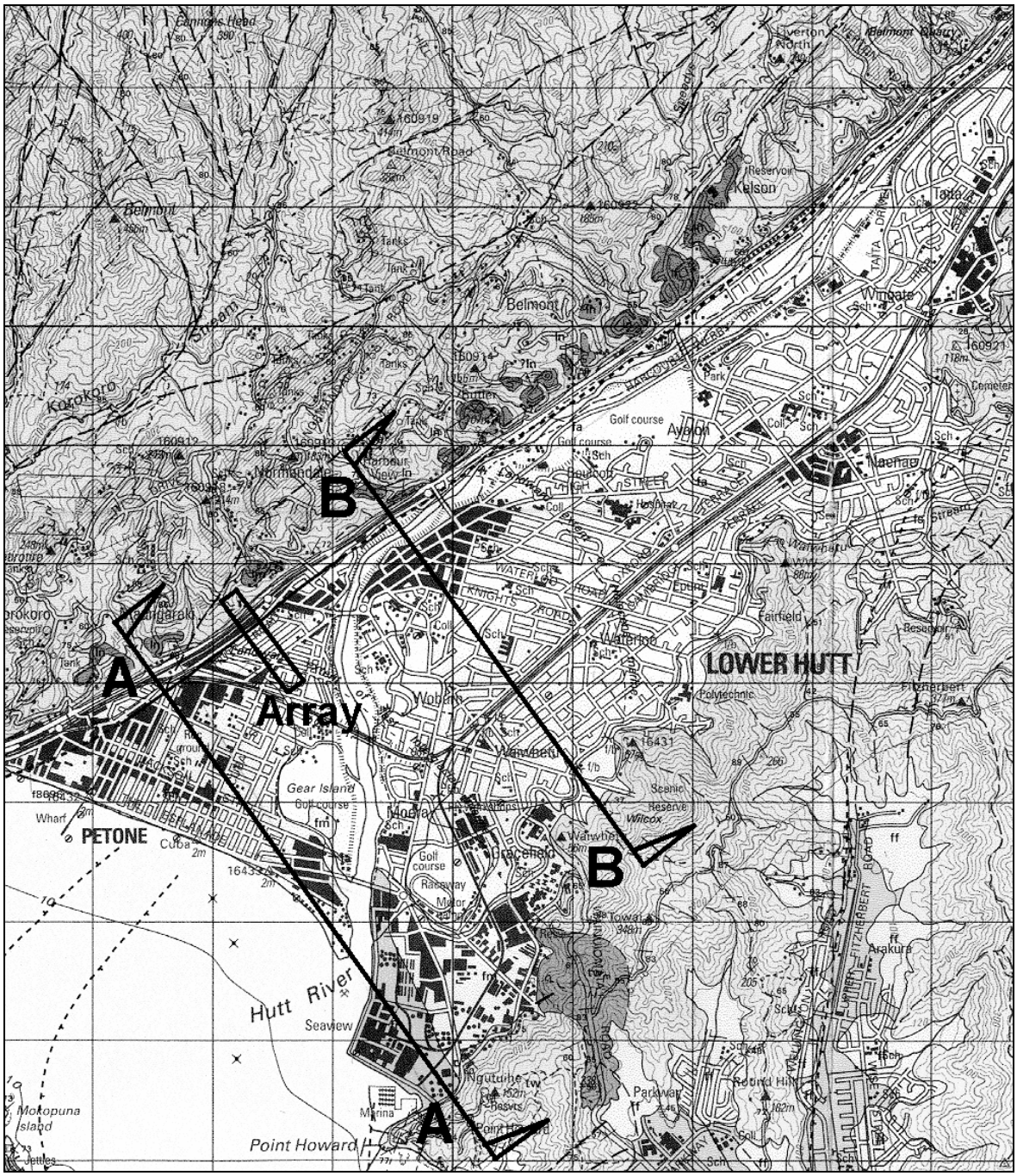

Figure 8.1. Map of the Lower Hutt Valley showing the position and orientation of the two geological cross-sections used in this chapter and the Array described in Chapter Nine (from Begg and Mazengarb, 1996).

The total sediment depth and contours of the bedrock-sediment interface have been estimated from a gravity survey (Cowan and Hatherton, 1968) with control provided by boreholes (Dellow et. al., 1992). The Institute of Geological and Nuclear Sciences (IGNS) in Wellington provided information from their database of borehole information for the Hutt Valley. Because of the artesian water supply in the Lower Hutt, numerous boreholes

and associated logs exist for depths to 30 metres, however deep information is limited to only a few boreholes at the lower end of the valley, only two of which reach bedrock. Borehole data was used to both locate layer interfaces and determine sediment properties. Geologic cross-sections of the valley were constructed from bedrock contours and borehole logs (N.D. Perrin, pers. comm.).

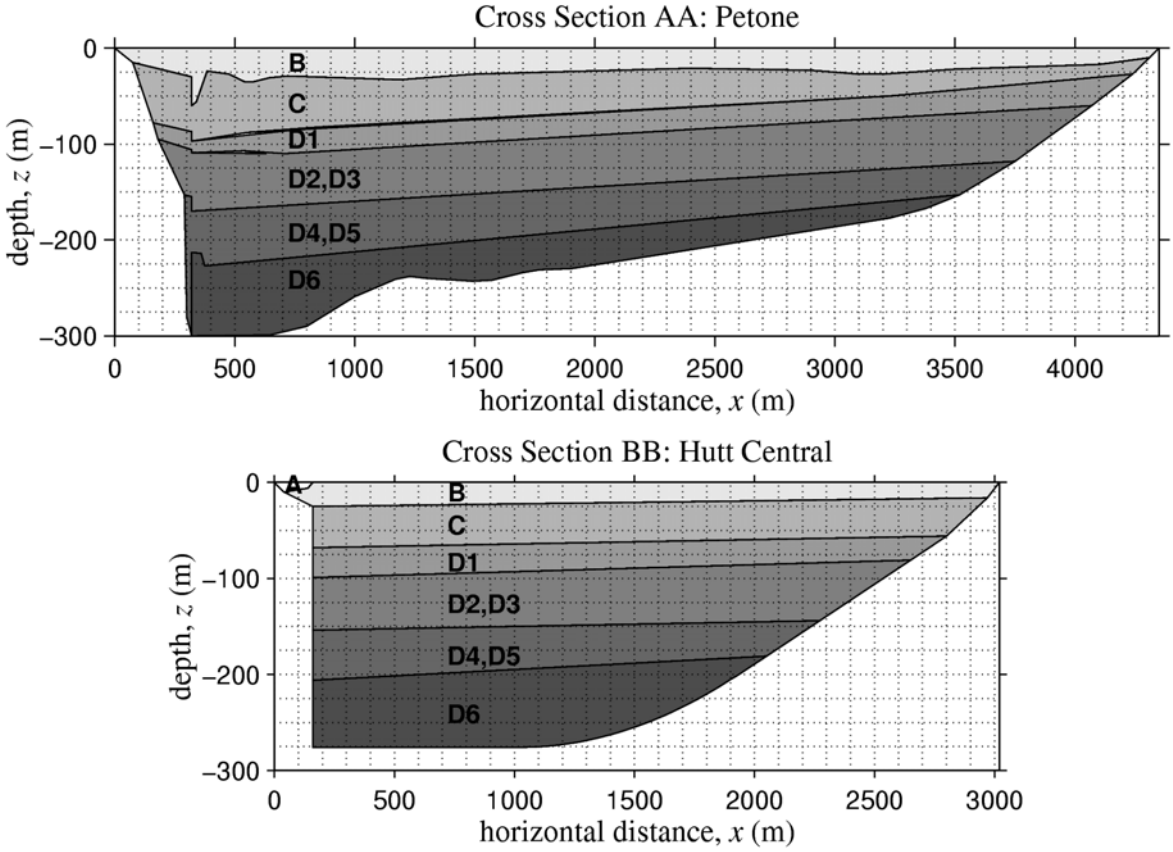

Figure 8.2. Section AA (top) through Petone and the seaward end of the Lower Hutt Valley and section BB (bottom) through Lower Hutt Central, 2.45km up-valley. Note the vertical exaggeration of 1:4.

The highly heterogeneous quaternary soil deposits in the Lower Hutt have been grouped into seven stratigraphic units according to their estimated elastic properties (Table 8.1). Shear-wave velocities of the sediments have been estimated based on the Borcherdt method (N.D. Perrin, pers. comm.), which uses data from San Fransico and Los Angeles, and are calibrated with SCPT measured data from unit B (Stephenson and Barker, 1992). Elastic properties of the basement greywacke have been estimated from measurements in the Wellington Motorway tunnel (Ingham, 1971) and at various other locations in the Wellington area (N.D. Perrin, pers. comm.).

Table 8.1. Elastic material properties of the eight different geological units modelled in Lower Hutt, used for input data to the FEM simulation. Material damping, ζ = 2% in all soft layers (n = 0-6), and ζ = 0 in rock (n = 7).

n	Shear wave velocity β_n (m/s)	Bulk Density ρ_n (kg/m^3)	Shear modulus μ_n (MN/m^2)	Layer	
0	100	1750	18	A	Artificial Fill
1	175	1750	54	B/Bb	Holocene Sediments
2	285	1800	146	C	Waiwhetu Artesian Gravels
3	325	1850	195	D1	Kaihinu Deposits
4	460	1900	402	D2/3	Waimea and Karoro Deposits
5	600	1950	702	D4/5	Moera Basal Gravels
6	675	2000	911	D6	Nemona Glacial Gravels
7	1500	2700	6075	E	Torlesse Basement Rock

Cross Section AA: Petone

The section chosen through Petone and Seaview crosses the southern end of the valley at its widest point (4.35 km) near the foreshore of the Wellington Harbour. The line intersects a mainly industrial and residential area of Lower Hutt, where buildings are between one and four storeys high. The fault trace and the position of the sub-surface vertical fault wall lie approximately 320m out from the western edge, while the Hutt River mouth is located approximately 3km further east.

Cross Section BB: Hutt Central

The second cross-section through the Hutt Valley shown in Figure 4.2(b) was chosen to intersect with the central business district of Lower Hutt (Lower Hutt Central). The Hutt River lies approximately 200m from the western edge, with the fault trace at approximately 160m. Lower Hutt Central contains commercial office blocks, shops and other buildings between one and seven storeys high, while the eastern two-thirds of the section across Waiwhetu is largely single and double-storey residential dwellings. The sedimentary valley is 3.02km wide at this point, and the sediment-bedrock interface extends to a maximum depth of 276m. Except for the top soft layer and the artesian gravels, which were plotted from nearby borehole data, layer interfaces have largely been extrapolated up-valley from the Petone cross-section (N.D. Perrin, pers. comm.). As with the first model, cross-section

BB includes no surface topography or elevation, disregarding the hills to either side of the valley.

8.1.2 ADDITIONAL FEM DETAILS

The degree of geometrical detail used for the bedrock and sediment-layer boundaries is on par with the degree of certainty we have from existing geological data in the Wellington region. The cross-sections are modelled with a set of straight and circular segments along layer boundaries. For cross-section AA, 70 segments were used to define the geological interfaces, while for cross-section BB, 40 segments were used. Greater complexity could easily be incorporated if better quality geological data existed.

Table 8.2 shows the element (mesh) size used for each of the Lower Hutt units based on a maximum frequency of 6.0Hz. The 2-D mesh generated by *Triangle* are both 6.5km wide by 1.0km deep. Mesh AA consists of 37,787 nodes forming 18,256 triangular elements, while mesh BB contains 27,676 nodes and 13,479 elements.

Table 8.2. Showing the mesh sizes used to model each geological unit in the Lower Hutt Valley. The minimum wavelength and maximum allowable element size are based on a maximum frequency, f_{max}, of 6.0 Hertz.

Layer	Shear-wave velocity β (m/s)	Minimum wavelength $\lambda_{min} = \beta / f_{max}$ (m)	Maximum element size $\lambda_{min}/4$ (m)
A	100	16.7	4
B	175	29.2	8
C	285	47.5	12
D1	325	54.2	14
D2/3	460	76.7	20
D4/5	600	100	25
D6	675	112.5	30
E	1500	250	60

8.1.3 ANALYSIS PROCEDURE

A simulation of each cross-section is made for a vertically-incident plane Ricker wavelet with a characteristic frequency of 2Hz. A 2Hz wavelet is used because it contains energy within a wide frequency band (0-6Hz). Tests are continued for 4000 iterations with a time

step of 0.005s to obtain 20 seconds of information. Transient displacement data is captured from approximately 200 points cross the surface of each model.

8.2 PRELIMINARY RESULTS

Both the Petone and Hutt Central cross-sections through the Lower Hutt valley yielded somewhat similar results. Throughout this section we will look at the results of the two models side-by-side in order to make comparisons and gauge a general picture of the valley as a whole.

8.2.1 TIME DOMAIN RESPONSE

In Figure 8.3, seismograms have been plotted close together on a position-time axis for each cross-section. The first motion on the seismogram occurs in the rock to either side of the valley. The time coordinate has been set such that the first peak of the Ricker pulse reaches the surface through the rock at $t = 0$. Free-surface doubling gives it an amplitude of twice the input, as it is reflected back down into the model to be removed by the absorbing boundary. In contrast, softer sediments in the valley delay the arrival of the Ricker pulse and amplify both the duration and intensity of shaking. The first arrival at the surface creates an inverted picture of the valley shape, and subsequent reflections between the free surface and the bottom of the valley lead to later arrivals that also mimic the valley shape with lower amplitude pulses. The first of these reflections returns to the surface approximately 1.3 seconds after the first arrival.

The most distinctive feature of the transient response is the generation of Love waves from each side of the valley. They are highly dispersive, with a dominant group velocity (taken from the slope of a line joining the highest amplitudes in the wave train) of 180-190m/s, and phase velocity (the slope of travelling wave peaks) of 320m/s. Phase velocities in fact vary between 230 and 520 m/s. The phases have an apparently steepening velocity, indicative of a low velocity contrast (eg. between the surface layers and lower layers). In section BB, strong vertical resonance in a soft layer on the western side has generated a number of Love waves at regular time intervals. Love waves significantly add to the duration of the record, especially in the central regions of the valley. They are initially of quite high amplitude yet attenuate rapidly as they travel across the basin.

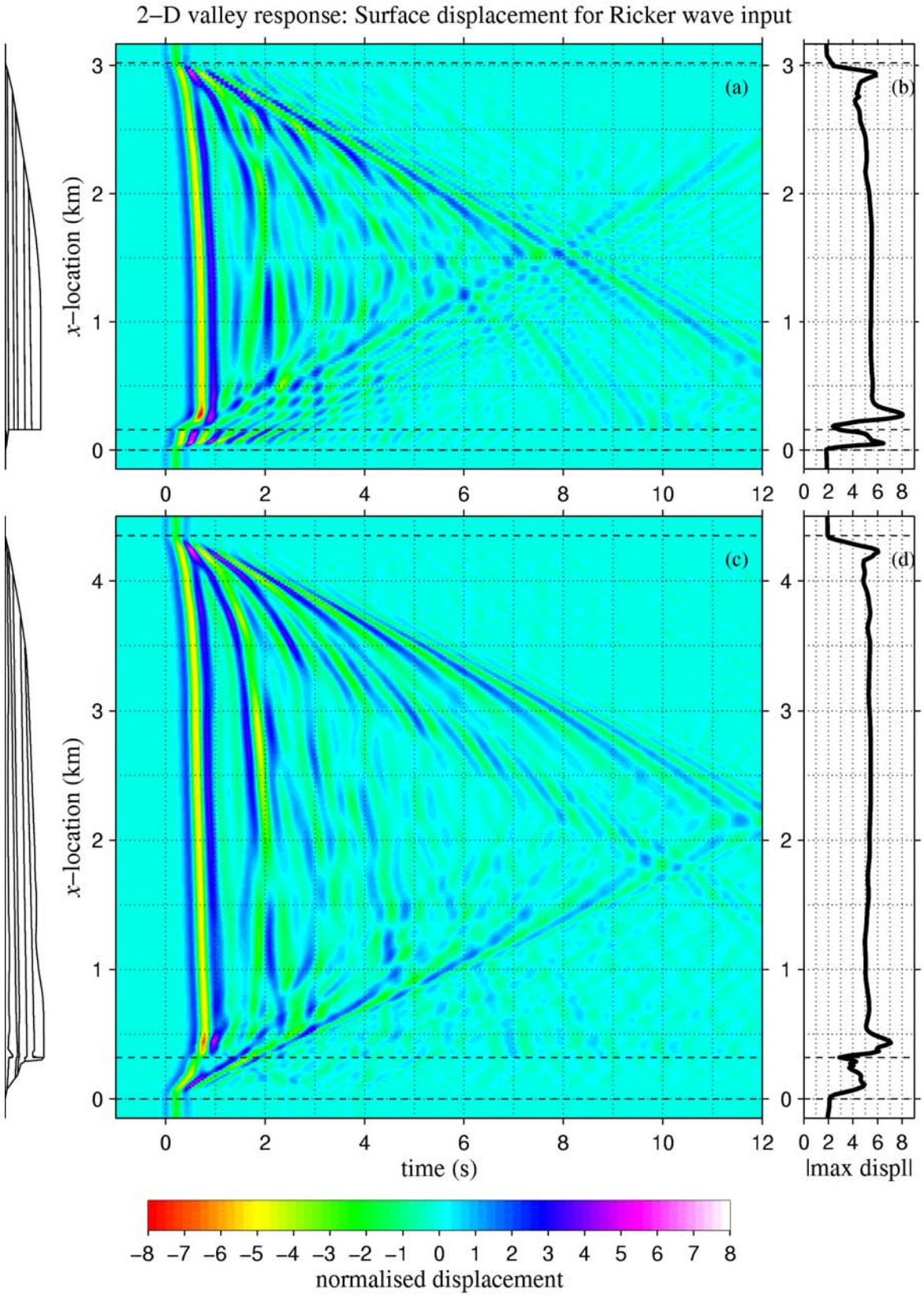

Figure 8.3. Surface displacement plotted as a continuous function of distance across the valley. Axes (a) and (c) show displacement with a colour scale for sections BB (Lower Hutt Central) and AA (Petone), respectively. Axes (b) and (d) show peak displacement across the valley.

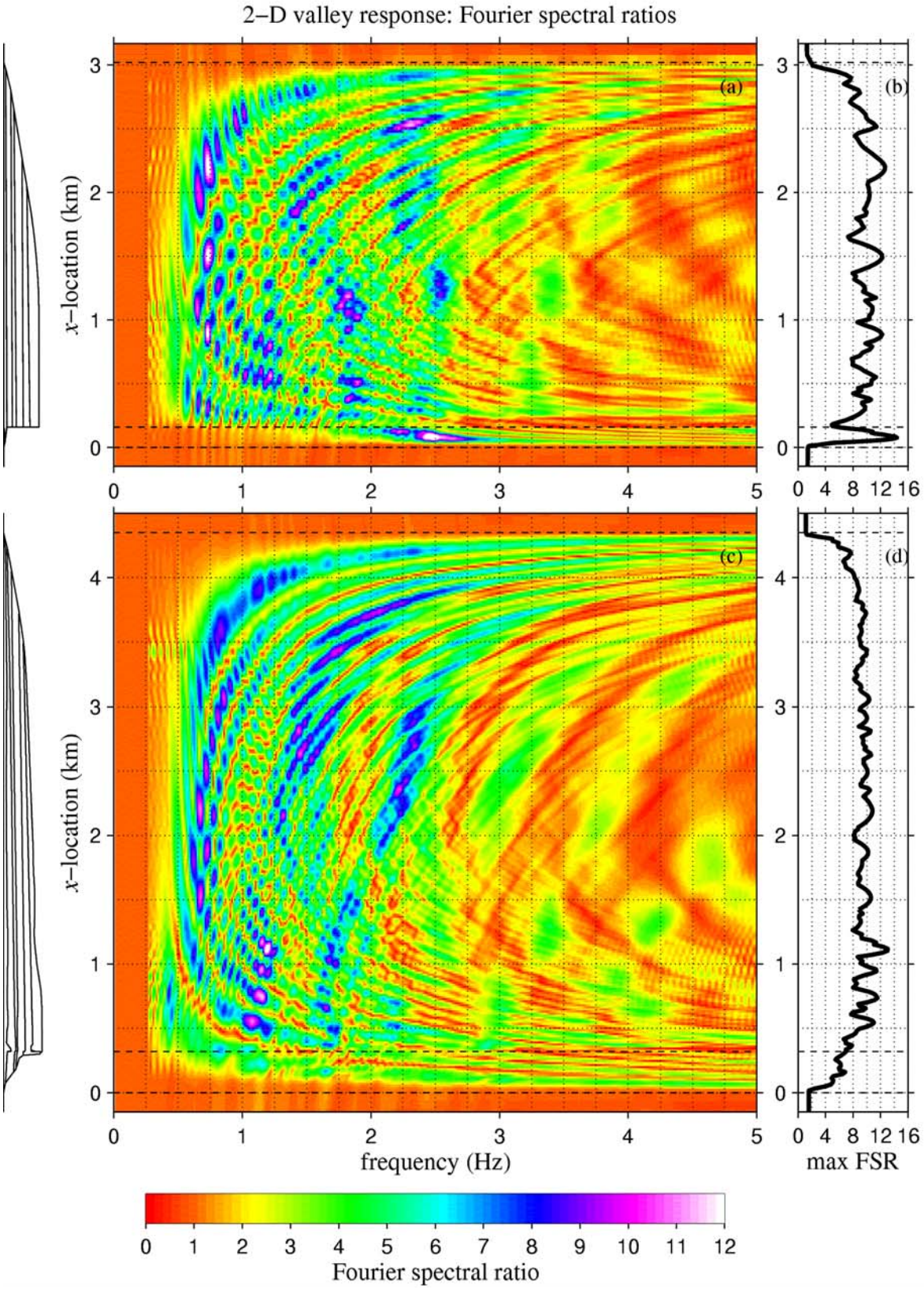

Figure 8.4. Soil to rock Fourier spectral ratios (FSR) plotted as a continuous function of distance across the valley. Axes (a) and (c) show FSR with a colour scale for sections BB (Lower Hutt Central) and AA (Petone), respectively. Axes (b) and (d) show maximum FSR (0-5Hz) across the valley.

The two line-plots on the right hand side of Figure 8.3 show peak ground displacement measured across the valley. There are three distinct locations where ground motions are highly amplified; the first two being located above the shallow-dipping bedrock at each edge, and the third a few hundred metres in from the fault-bounded edge. The peaks at the valley edges are lower in amplitude than the third peak, which is the site of the largest displacement. It occurs during the initial arrival of the Ricker pulse through the sedimentary basin, due to constructive interference with an edge-generated phase. In the Lower Hutt Central cross-section the edge-generated has an apparent horizontal velocity of 250m/s, while in the Petone cross-section, the constructing edge-generated pulse travels at 730m/s, much faster than the dominant Love wave phase velocity. The differences in valley-edge geometry obviously make a significant difference to the velocity of the initial edge-generated pulses, yet the maximum peak displacement occurs the same distance (120-130m) out from the deep vertical edge, which is appears to be the controlling geometrical feature.

8.2.2 FREQUENCY DOMAIN RESPONSE

Fourier spectral ratios have been plotted to form a continuum with across-valley position in Figure 8.4. FSR in the rock to each side of the basin is approximately unity, as expected. Within the valley, however, FSR ranges between 1 and 12, being highly dependent on both frequency and position. Widespread amplification occurs across the valley roughly within the range 0.5 to 3.5 Hz, and in a pattern indicative of two-dimensional resonance (eg. compare with Figure 3.4). Curving extremum lines of amplified motions are prominent features. The amplification is highly variable in both the spatial and frequency dimensions.

The first four vertical modes – each with a corresponding set of horizontal modes – can be recognised, occuring at 0.45, 1.10, 1.65 and 2.15Hz for Petone (lower plot), and at 0.49, 1.15, 1.80 and 2.50Hz in Hutt Central (top plot). On the whole, eigenfrequencies in Lower Hutt Central are around 5% to 20% higher than those in Petone. Amplification within any given vertical mode set (eg. for $m = 0$, $n = 0,1,2,\ldots$) appears to be strongly correlated with

the extremum lines, rather than particular eigenfrequencies. The extremum points tend to be centred toward the deepest part of the valley.

Amplification above the first higher vertical eigenfrequency ($f > 1.1$Hz) is dependant on constructive interference between the first ($m = 0$) and higher ($m = 1,2,3$) vertical-mode

sets. These interference effects (Wirgin, 1995) alter the apparent strength and position of the resonant amplification. The highest amplification on the plot in Figure 8.4(a) occurs at x = 1100 m and f = 1.15Hz where the second vertical mode set (n = 1) superimposes itself atop the 12^{th} to 17^{th} horizontal modes of the first vertical mode (n = 0, m = 12,13,..,17). Several other distinct patches of amplification in the region above 1.10 Hz also appear to occur due to interference.

8.3 SUMMARY

It has been shown using a 2.0Hz Ricker pulse that constructive interference between edge-generated phases and the first arrival of the Ricker pulse through the sediments creates strong amplification some 120 metres from the deep vertical edge. While different shallow edge geometry has a significant effect on the initial edge-refracted phases, the position of constructive interference appears to be controlled by the deep vertical edge. At the same time, dispersive Love waves are generated from both edges and significantly increase the duration of shaking across the full width of the valley.

Love wave propagation excites the valley into two-dimensional modes of resonance involving the full depth of sediments, while shallow sediments at both margins of the valley amplify ground motion by vertical resonance due to the sharp velocity contrast at the shallow sediments and bedrock. The pattern of amplification in the frequency domain is highly variable both in terms of cross-valley position and frequency. A complex pattern of interference between various resonant modes appears to determine the sites of highest spectral amplification.

Although the geometry of both the Lower Hutt Central and the Petone cross-sections are quite different, they develop similar patterns of response in both the time and frequency domains. The presence and location of strong basin-edge amplification by constructive interference observed in this modelling provided both the incentive and dimensions for which to design the array of seismographs detailed in the following chapter.

Chapter 9: ANALYSIS OF RECORDINGS FROM A WEAK MOTION ARRAY

As an adjunct to the research reported in this thesis an array of seismographs was deployed across the fault-bounded northwestern edge of the Lower Hutt valley during a six-week period from December 1998 to January 1999 in order to record weak ground motions from both near and distant events. The author of this thesis was involved in siting the instruments, while data collection and processing was carried out by Emma Winthrop and Neal Osborne, as part of an honours project in Geophysics (Osborne, 1999) supervised by John Taber at the University of Victoria, Wellington. In this chapter we make an analysis of the data with special interest in the features of basin-edge response, including edge-generated surface waves, local maxima in peak ground motions and spectral amplification. The results are compared with the FEM modelling in Chapter Ten.

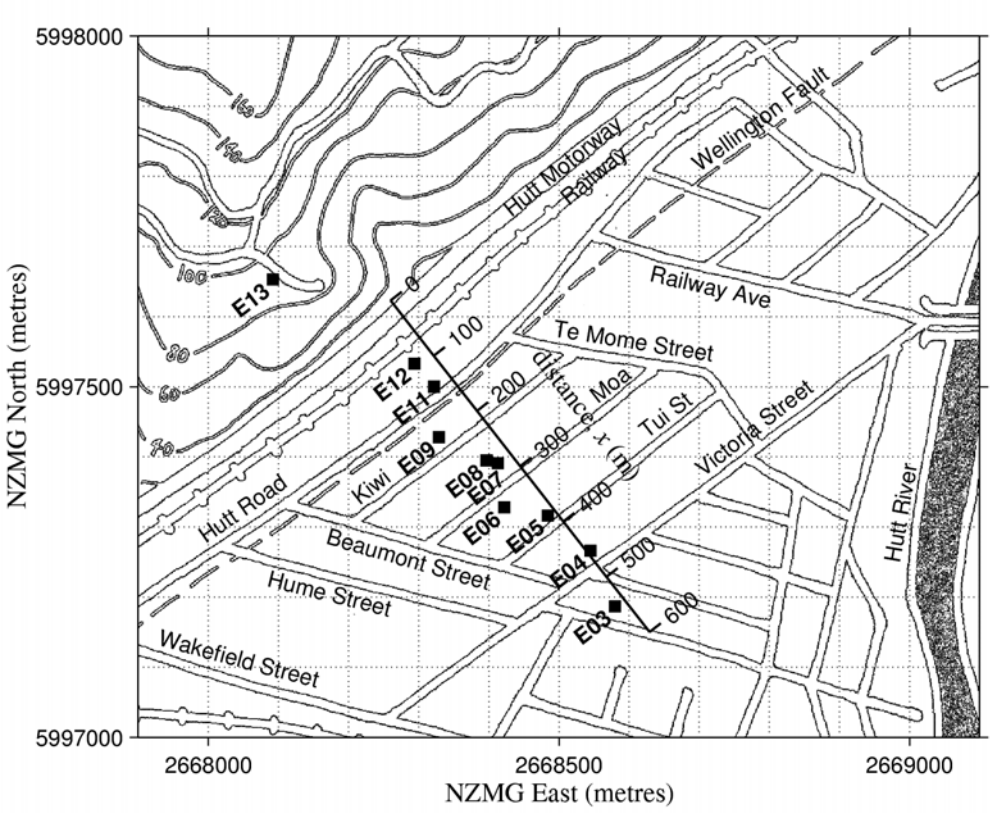

Figure 9.1. Location of the array recorder stations on the fault-bounded northwest edge of the Lower Hutt valley in Alicetown.

9.1 PRELIMINARIES

9.1.1 ARRAY DETAILS

Eleven digital seismographs were placed in a short linear array running from the base of the hill for a distance of 540 metres across the valley through the suburb of Alicetown. Figure 9.1 shows the positions of the stations, while Table 9.1 lists their coordinates and perpendicular distances relative to the valley edge. Due to the residential and industrial nature of the site, it was not possible to locate instruments in a perfectly straight line. The array also crosses a railway line, three busy arterial roads and three small residential streets. The surface trace of the Wellington Fault, shown in Figure 9.2, crosses the line of the array 160 metres from the base of the hills (x = 160m).

Table 9.1. Coordinates of the 11 array stations. The distance, x, is measured perpendicularly from the edge of the sediments. The trace of the Wellington fault lies 160 metres out from the edge.

	NZMG coordinates		Cross-valley distance	
Station Code	East	North	from base of hill x (m)	from fault x - 160 (m)
E01	2670990	5995280	3507	3347
E03	2668580	5997187	539	379
E04	2668545	5997266	455	295
E05	2668484	5997316	379	219
E06	2668422	5997328	332	172
E07	2668413	5997391	276	116
E08	2668397	5997395	263	103
E09	2668329	5997428	196	36
E11	2668322	5997500	134	-26
E12	2668294	5997533	91	-69
E13	2668092	5997653	-126	-286

Instruments were located on concrete floor slabs within private garages, shops and warehouses. The velocity sensors (Kinemetrics L4 3D seismometers) had a natural frequency of 1.0Hz and sampled at 100Hz, giving a frequency range of 0.5-50Hz. Additional details can be found in Osborne (1999).

Figure 9.2. A photograph looking west along Te Mome Street. The rise at the end of the street is the surface trace of the Wellington Fault. Station E13 is located on the skyline of the hill at the end of the street.

Figure 9.3. A photograph looking directly over the line of the array from near Station E13. The locations of Stations E04 and E03 are just visible over the roof of the houses, while Stations E01 is situated on the other side of the valley in the centre of the picture.

9.1.2 LOCAL GEOLOGY

Two of the stations in the array were located outside the sedimentary valley; E13 at an elevation of 80m part way up the hill above the northwestern edge, and E01 at the base of the hills on the other side. Figure 9.3 is a photograph taken from near E13 looking southeast across the array and valley to E01. Of the remaining nine stations, seven were situated above the ~300m deep sediments to the southeast of the Wellington fault; and two were located on the shallower sediments on the up-thrown side of the fault.

The sub-surface geology beneath the array has been estimated from clusters of shallow borehole data some 500 metres up-valley (Railway Avenue area) and down-valley (Wakefield Street area), as no boreholes exist in the immediate vicinity of the array. The estimated structure of the Holocene sediments (the top 20 metres) is shown on a geological cross-section in Figure 9.4 along with the locations of the recorders. Information on deep stratigraphy is limited to an interpolation of that described for the previously modelled cross-sections. The material on the up-thrown side consists of generally loose sands, silts and peat above a deposit of gravelly colluvial fan material to a maximum depth of around 25 metres.

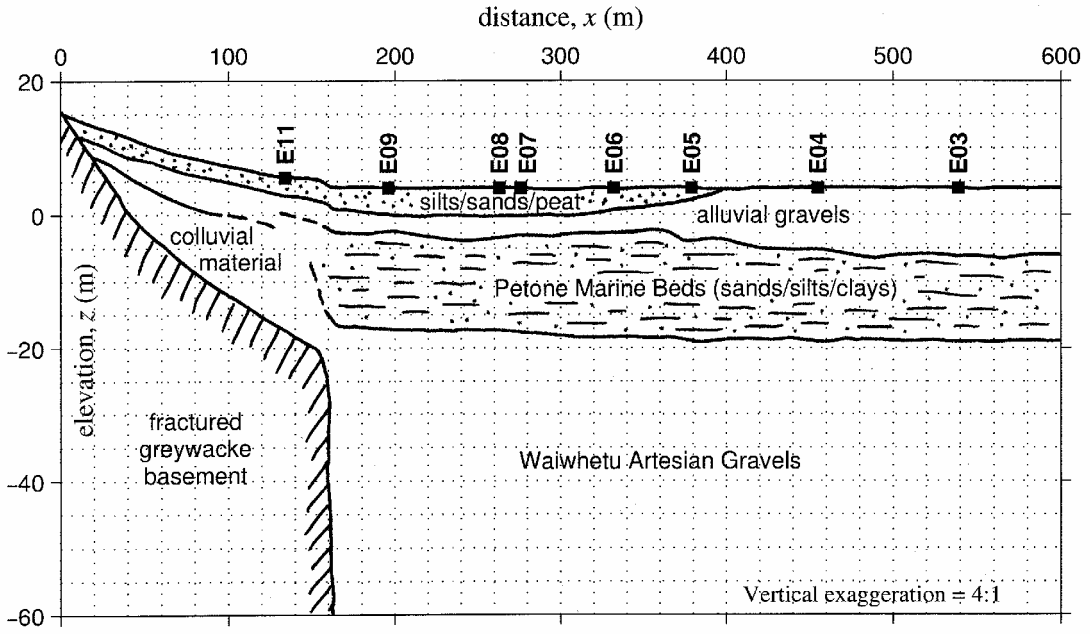

Figure 9.4. An estimated geological cross-section through the top 60 metres of stratigraphy beneath the array. Based on nearby borehole data and constructed with the help of Peter R Wood and Nick Perrin (Institute of Geological and Nuclear Sciences, Lower Hutt). The location of the cross-section is shown on Figure 9.1. Note the vertical exaggeration.

The area of land extending 200-300 metres across the valley on the down-thrown side of the fault trace was the site of the Te Momi Swamp in the early 1800's. In 1855 the Wairarapa Earthquake raised the Hutt Delta some 1.8-2.1 metres and drained the swamp (Stevens, 1974). Generally the top 3-4 metres extending out to x = 400 metres consists of silts and sand with some peat. Below and beyond this layer are alluvial deposits of loose sandy and silty gravels to a depth of approximately 8-10 metres above marginal marine deposits of fine sands, silts, clays and gravels (the Petone Marine Beds) to a depth of 20-22 metres. Below this are the Waiwhetu Artesian Gravels dating back to the last glacial.

9.1.3 RECORDED EVENTS

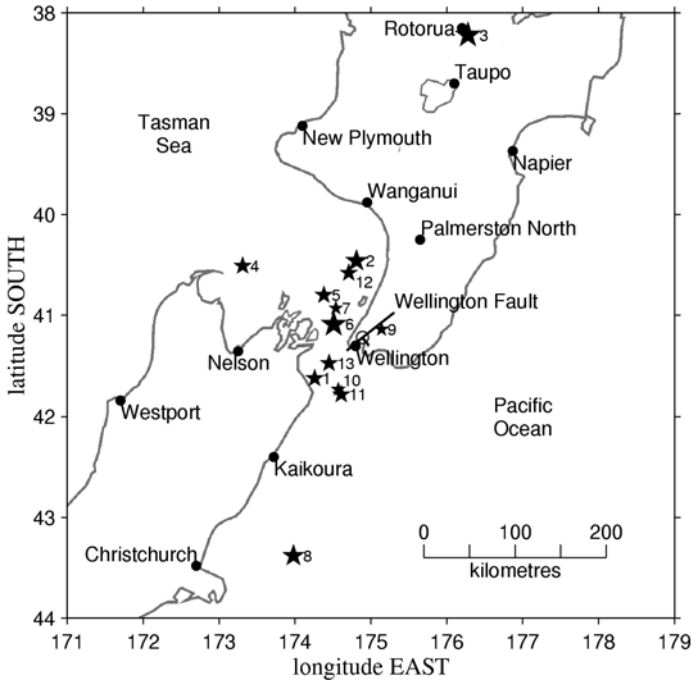

Figure 9.5. Location of the 13 earthquakes used in this study. The size of the star corresponds with the magnitude given in Table 9.2. The location of the array is shown with an open circle along the Wellington fault trace.

Thirty two earthquakes were recorded on the array between 18 December 1998 and 30 January 1999, and of these 13 were selected (Osborne, 1999) for use in this study. Table 9.2 lists details of these 13 events including their incoming azimuth and angle of incidence. Figure 9.5 shows the epicentral locations with respect to the array across the Wellington Fault. The angles of incidence were calculated using average crustal velocities from the IASPEI 91 global travel time model (J. Taber, pers comm.).

Three components of velocity were recorded at each station, the horizontal (north and east) components of which were subsequently rotated by 52 degrees clockwise into edge normal (EN) and edge parallel (EP) components, while the vertical component (UD) was left unaltered. The uncorrected velocity records have been subsequently integrated into approximate displacement time histories (errors exist below 0.5Hz due to instrument response). Figure 9.6 shows a six-second length of the shear wave from each event as recorded at station E01. Displacement records have been normalised to give equal peak amplitude for each event.

Table 9.2. Details of the 13 events selected for analysis. Azimuth is the angle of the epicentre from the array, measured clockwise from north. θ_i is the estimated angle of incidence that the incoming wave field has with respect to the vertical.

Event	Date	Origin	Latitude East	Longitude North	Azimuth (°)	Distance (km)	Depth (km)	θ_i (°)	Mag
1	18-Dec-98	Clifford Bay	41.62	174.26	230	63	5	66	3.8
2	21-Dec-98	Offshore Foxton	40.46	174.81	355	77	75	32	4.8
3	29-Dec-98	Rotorua	38.22	176.28	19	318	162	37	5.7
4	01-Jan-99	Farewell Spit	40.51	173.31	301	143	172	27	4.4
5	03-Jan-99	N Cook Straight	40.80	174.38	321	63	66	32	4.2
6	03-Jan-99	N Cook Straight	41.09	174.51	304	33	57	25	5.5
7	08-Jan-99	N Cook Straight	40.93	174.54	318	39	5	65	3.1
8	09-Jan-99	Pegasus Bay	43.38	173.98	198	226	12	41	4.9
9	11-Jan-99	N Rimutakas	41.14	175.14	65	27	6	64	2.6
10	12-Jan-99	S Cook Straight	41.73	174.57	205	56	31	51	3.2
11	20-Jan-99	S Cook Straight	41.78	174.61	203	59	31	51	3.6
12	21-Jan-99	Offshore Foxton	40.58	174.71	348	67	66	33	3.7
13	25-Jan-99	S Cook Straight	41.47	174.45	234	63	24	63	3.7

The thirteen events that were chosen represent a wide range of hypocentral depths (5-172km), distances (27-318km) and low to moderate magnitudes (M 2.6-5.7). Incoming wave fields thus show considerable variation in length and shape of the record, peak ground motion and frequency content. Figure 9.7 presents smoothed Fourier amplitude spectra of the EN, EP and UD shear wave displacements recorded at station E01. A heavily smoothed RMS average of the horizontal components is also shown.

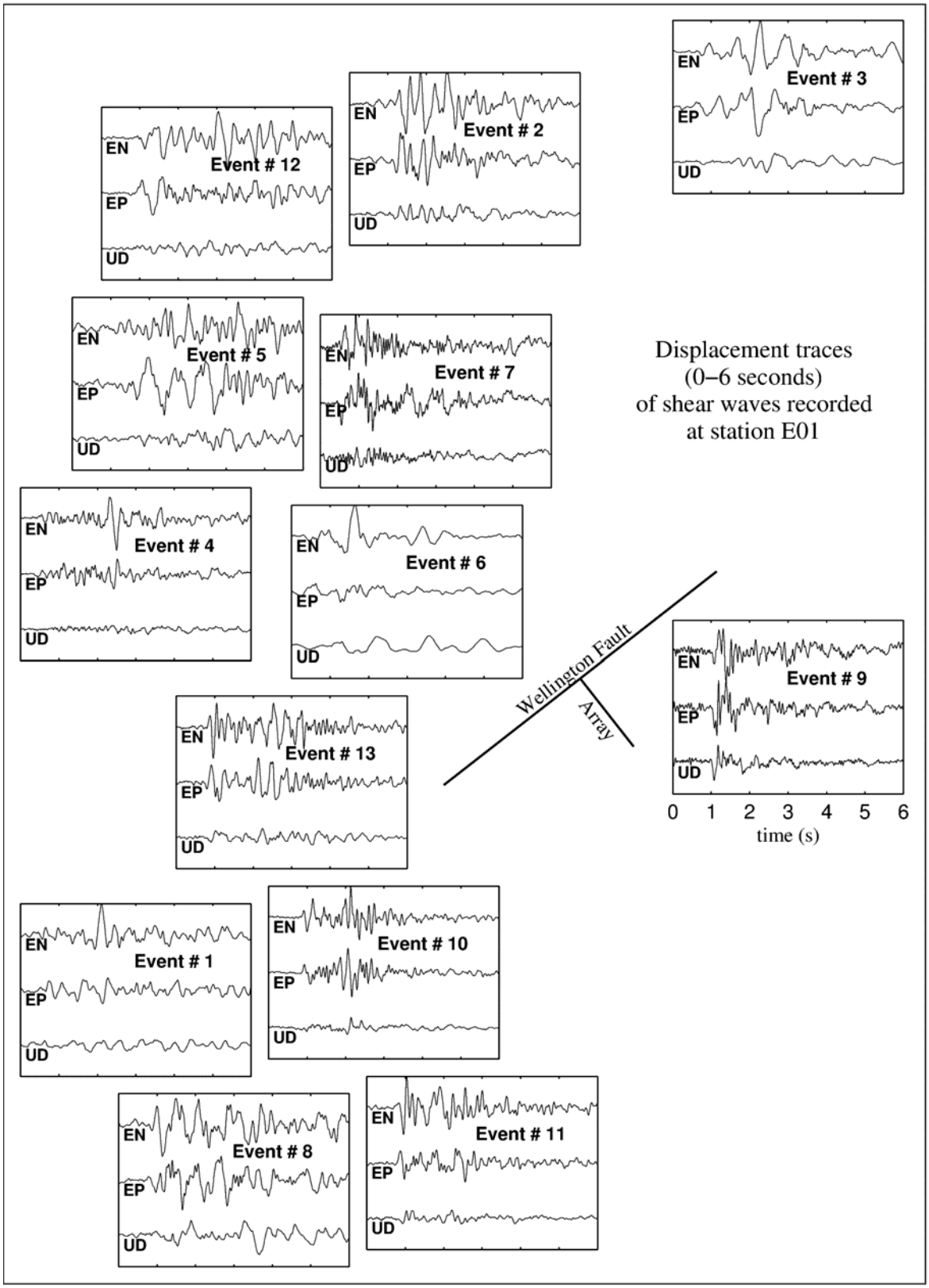

Figure 9.6. Displacement traces recorded at the rock site, E01, and presented in an approximate azimuthal distribution with respect to the array. Displacement amplitude is normalised such that all events have the same peak value.

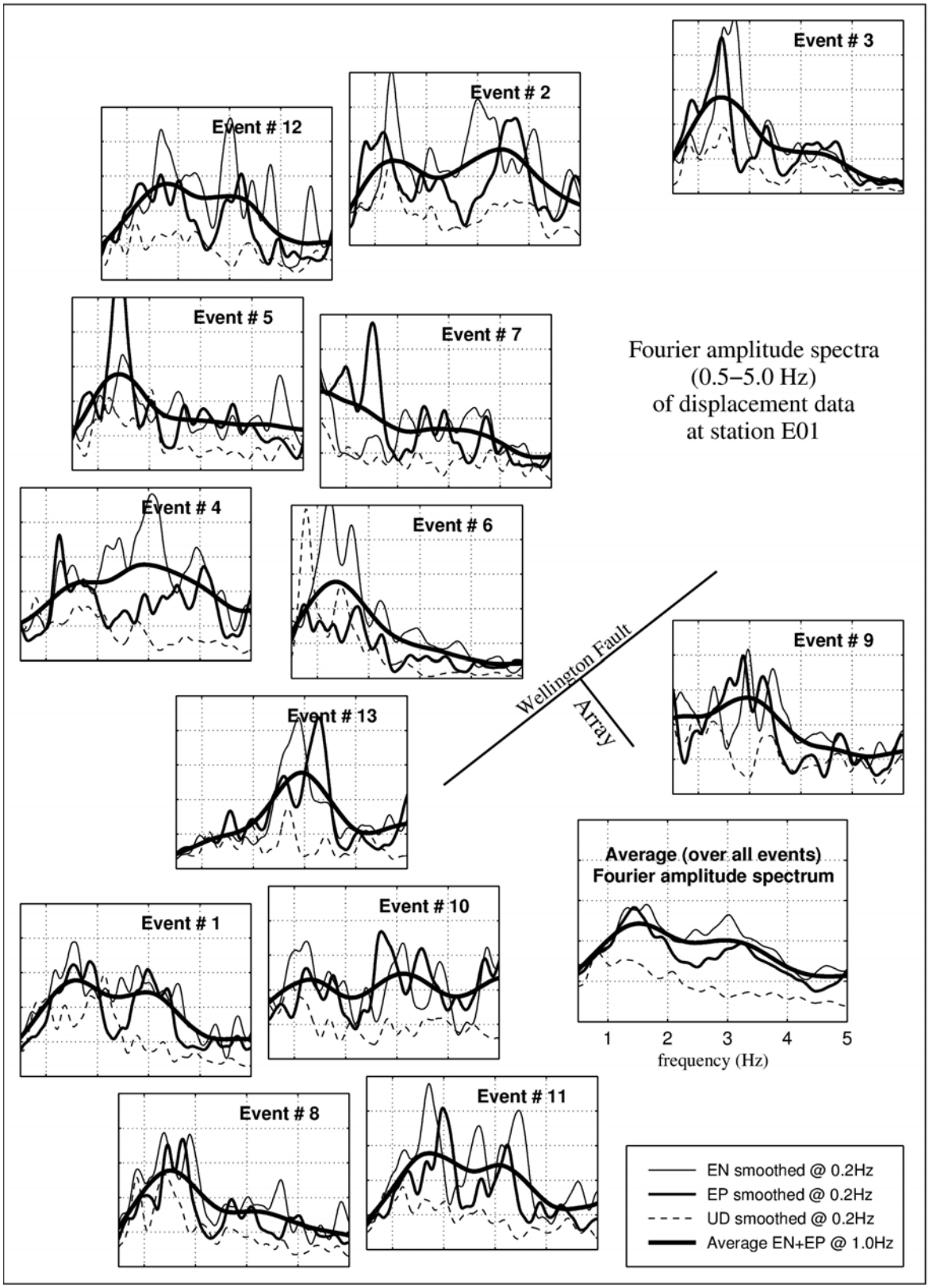

Figure 9.7. Fourier amplitude spectra recorded at the rock site, E01, for each event. Amplitude is normalised against the RMS horizontal maximum. Presented in an approximate azimuthal distribution with respect to the array.

The events can be roughly divided by azimuth. Events 2, 4, 5, 6, 7 and 12 originate from the northwest, approximately perpendicular to the fault-bounded valley edge, and arrive with estimated angles of incidence between 26° and 65° (measured from the vertical). Events 1 and 13 both arrive from the southwest, almost directly up the line of the Wellington Fault and with shallow angles of incidence (66° and 63° respectively); while events 8, 10, and 11 originate from the south with angles of incidence between 41° and 51°. Finally, Event 3 is a deep focus subduction zone earthquake from the central North Island, and Event 9 is a small shallow rupture centred only 27km to the northeast. Information on the source mechanisms of these events is unknown.

With the exception of events 2, 3, 6 and 13, which were felt weakly in the Wellington region, ground motions were very small. It is assumed herein that no non-linear permanent ground deformation occurred and the recorded motions are compatible with an elastic analysis. In general the larger magnitude events (eg. events 3, 6 and 8) contain noticeably more energy in the form of low frequency pulse-like motions, while the smaller events contain mainly high-frequency shaking.

9.1.4 DATA PROCESSING

A 20-second long window of the shear wave from each event was selected visually such that it starts approximately one second before the shear wave arrives across the majority of the array. The timing at station E04 was faulty and has been corrected visually with reference to the records at adjacent stations. It is therefore not accurate for timing purposes to less than ~0.2 seconds. Since none of the events were able to trigger all 11 stations there are many gaps in the data set. Displacement traces were integrated from velocity records by the trapezoidal method and then corrected for baseline errors. The units of velocity and displacement are in all cases normalised against the peak at station E01.

Prior to Fourier analysis and the calculation of Fourier spectral ratios (FSR, otherwise called a *sediment to rock spectral ratio*, SRR), a Hanning (cosine shape) taper was applied to 2% of each end of the trace to reduce the Gibbs effect. Station E01 is chosen as the rock site over E13 because of its location at the base of the hill where the shaking is much smaller. The results from E13 appear to be influenced by a topographic or similar effect leading to a strong amplification in several events. Some form of site effect however, also influences ground motions recorded at station E01. The edge-parallel records often contain

smaller peak amplitudes in both the time and frequency domains (see Figures 9.6 and 9.7), than those in the edge-normal orientation. Large pulses from events 1, 4 and 6 that feature strongly in the EN component are significantly smaller in the EP. Both horizontal components show on average two peaks in the frequency domain, one at 1.5Hz and one at 3.0Hz, with perhaps some form of deamplification between them at around 2.1-2.5Hz.

In order to minimise the contamination of the FSR by site effects at E01, the Fourier amplitude spectra from site E01 were first smoothed with a 1Hz moving triangular window. The two horizontal components (EN and EP) were then combined using an root-mean squared (RMS) average, the result of which is shown for each earthquake in Figure 9.7. Fourier amplitude spectra from the remaining stations were then smoothed with a 0.2Hz moving triangular window prior to the calculation of FSR. This heavy initial smoothing and horizontal averaging of the rock spectra has had the effect of reducing peaks and troughs in the ratio that are more a result of site conditions at the rock site E01 than amplifications due to sediments in the valley. There is, however, some loss of resolution and a possible generation of erroneous peaks and troughs in the result.

9.2 Analysis of Array Recordings

9.2.1 Displacement Time Histories

Figures 9.8 and 9.9 present 10-second windows of the rotated horizontal displacement traces obtained for events 1 and 5. In each case, the window starts approximately one second before the shear wave arrives at most stations. A full catalogue of displacement traces from all 13 events may be found in Appendix 2.1.

Ground motions at deep sediment sites within the valley (E03 to E09) are greatly amplified compared with those recorded at the rock site, E01. Displacement traces from E11 on the up-thrown side of the fault are also considerably amplified, yet not to the same extent as the deep sites. The records from E13 on the hill above the array also show very strong amplification, almost comparable to that at the deep sediment sites for some earthquakes.

While there is considerable variation between the displacement traces recorded at adjacent stations, it is evident that many of the pulses correspond with one another. This is most noticeable for the lower frequency (wide) pulses. In general the pulses that correspond

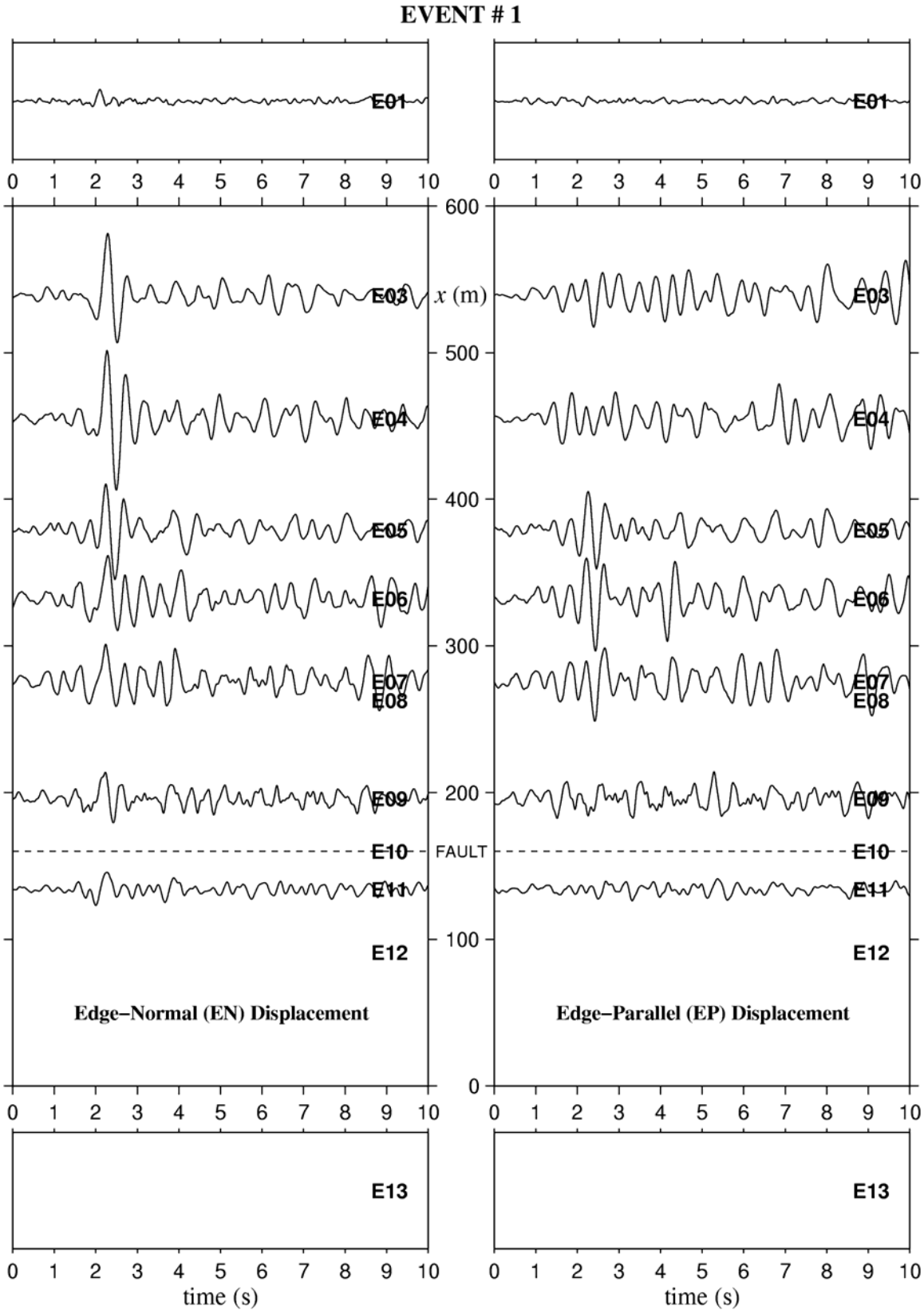

Figure 9.8. Displacement traces showing the first 10-seconds of the shear-wave recorded across the array during Event 1. Horizontal components only are shown. Amplitude is normalised against the peak at station E01.

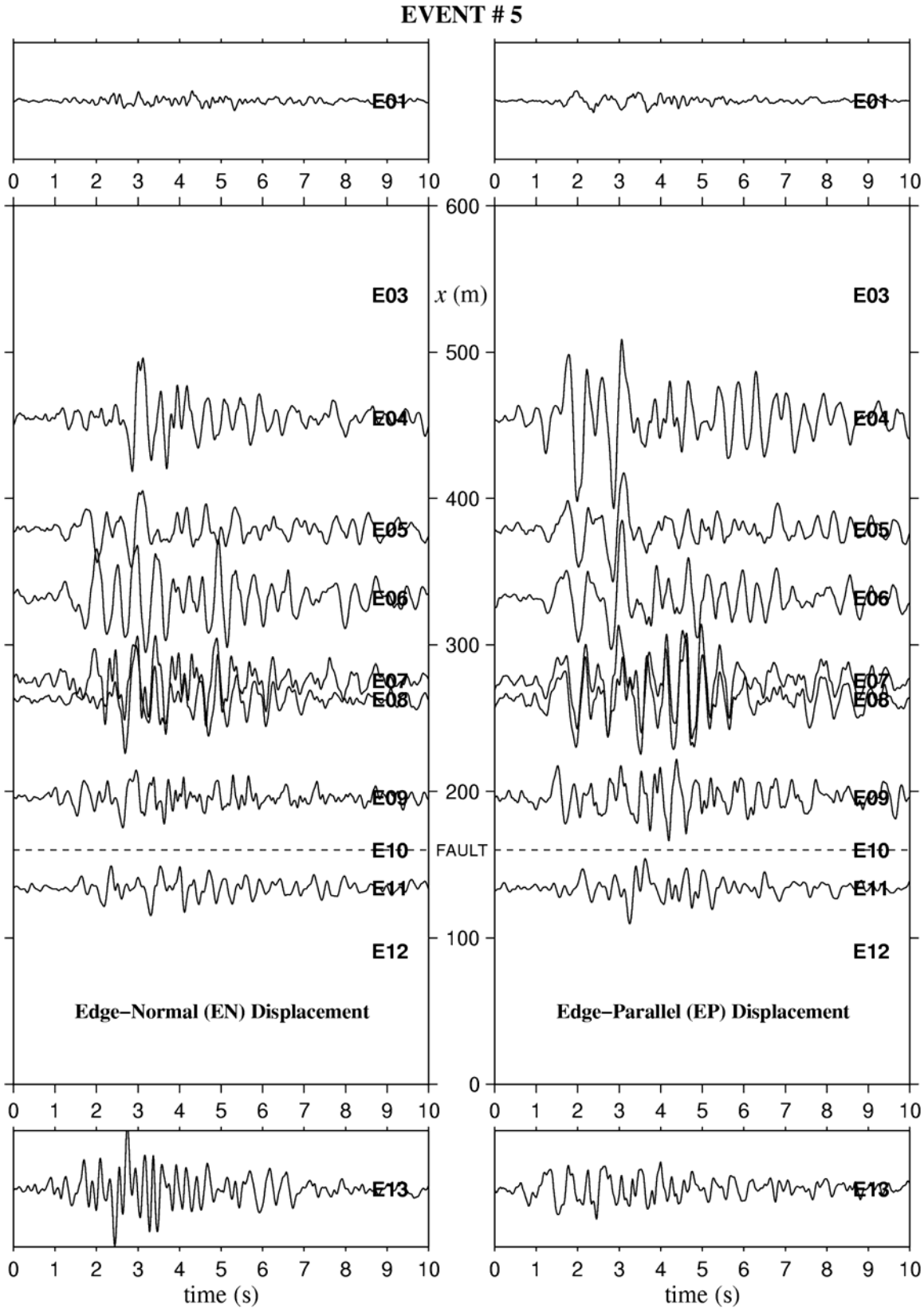

Figure 9.9. Displacement traces showing the first 10-seconds of the shear-wave recorded across the array during Event 5. Horizontal components only are shown. Amplitude is normalised against the peak at station E01.

between stations occur at approximately the same time across the array (E08-E03) on deep sediments. The peaks do, however change shape between stations, possibly as a result of a local scattering effect in the surrounding soil mass, or of surface waves travelling horizontally across the valley.

Figure 9.10 shows expanded detail of the maximum edge-parallel displacement peaks for three different events (4, 6 and 12). The near-vertical solid lines represent apparent velocities of body wave pulses arriving at the surface from below. The wave field of each of the three events shown, arrives at the site from the northwest with an estimated angle of incidence between 25° and 33°. The apparent velocities shown (between 2500m/s and 5800m/s) are not unreasonable considering that the apparent velocity for SH wave incidence is given by $\beta_{rock}/\sin\theta \approx 3000$m/s. The sloping solid lines represent possible phase velocities (between 169m/s and 175m/s) of high-frequency surface wave pulses travelling across the array. These are, however, very tenuous and more an indication of the possibility of phase propagation at this velocity than an observation of it.

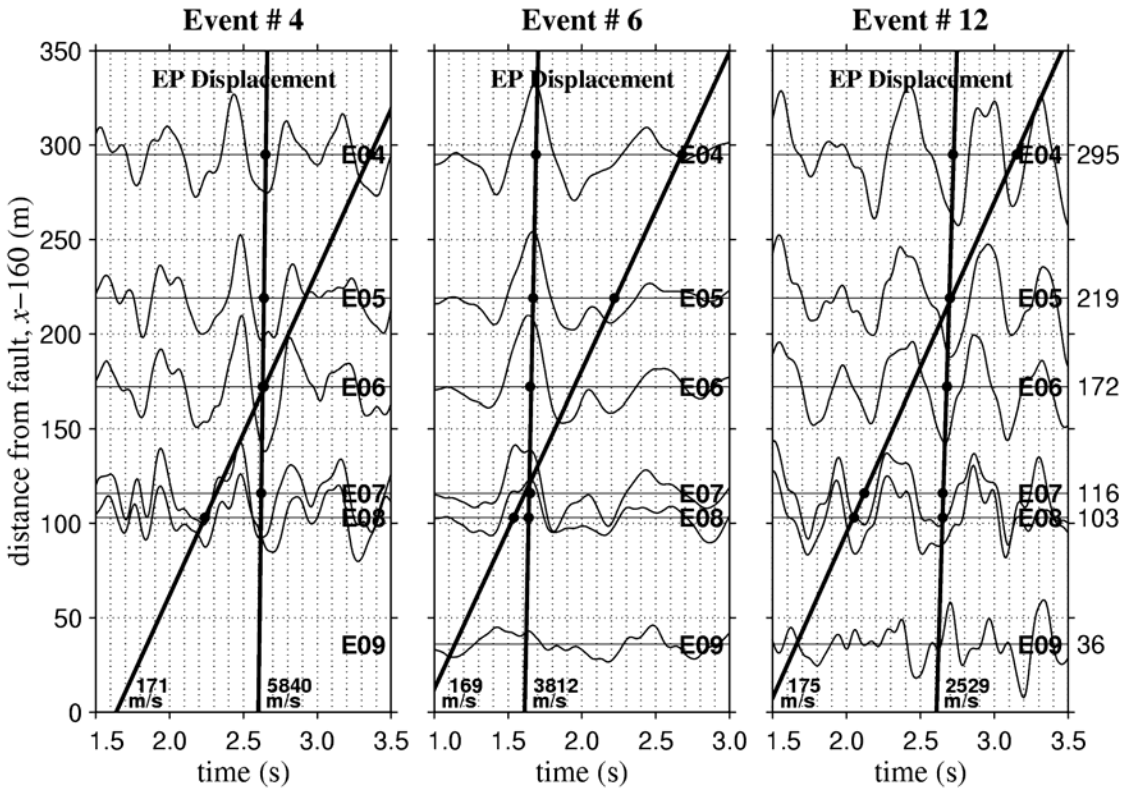

Figure 9.10. Expanded detail of parts of the shear-wave displacement recorded during Events 4, 6 and 12. The time axis values corresond to that given in Appendix 2.1. Only the motion recorded on the down-thrown side of the fault is shown.

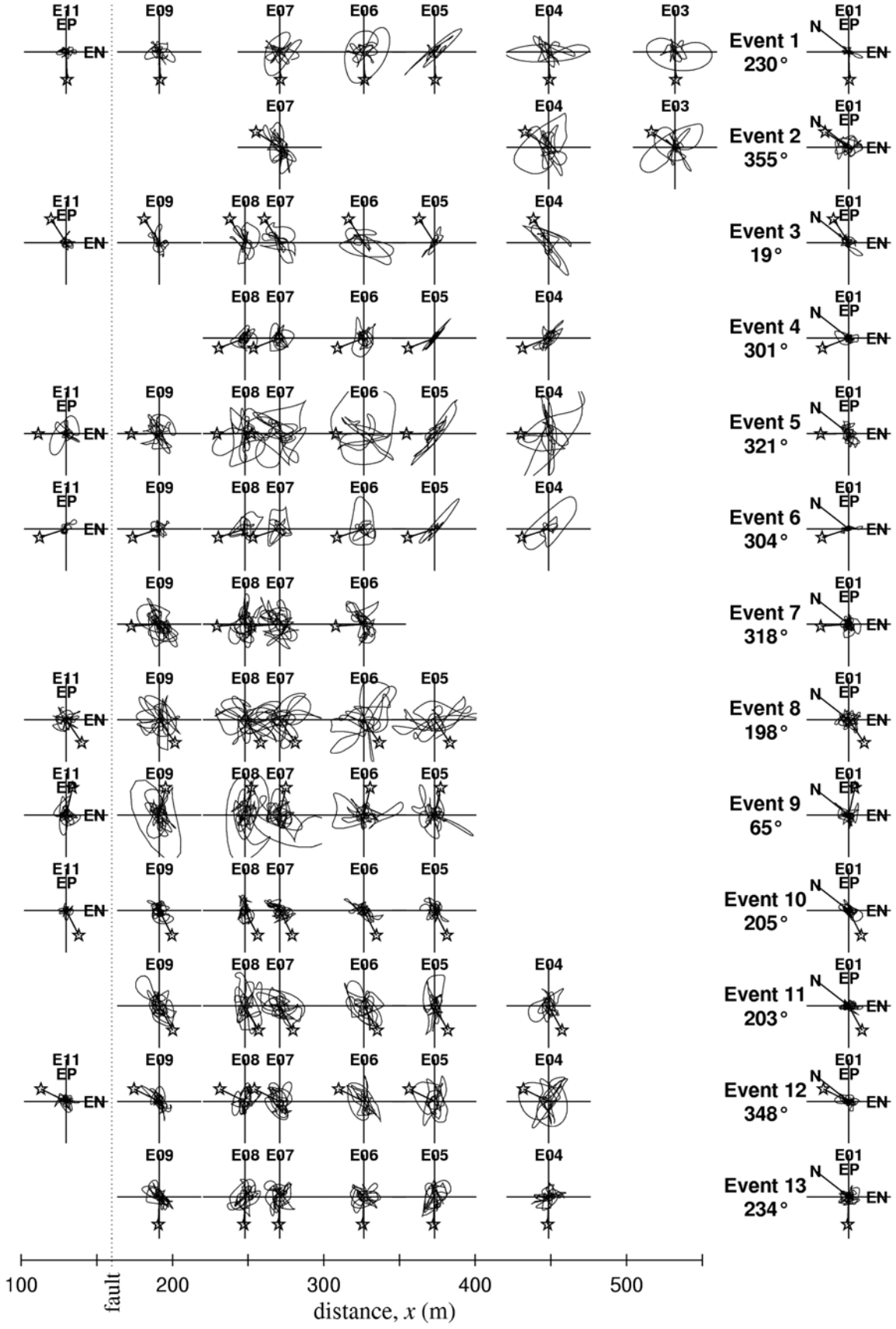

Figure 9.11. Particle motion in the horizontal plane plotted relative to the position of the recording stations. The star indicates the direction to the epicentre with respect to the EP and EN axes.

Figure 9.11 shows particle motion in the horizontal EN-EP plane. The first three seconds of the shear wave (t = 1-4s in Figures 9.8 and 9.9 and Appendix 2.1) have been plotted for each array station and for all 13 events. The position of the star indicates the direction to the earthquake epicentre with respect to the EN and EP orientations. Most noticeable is the large difference in particle motion experienced at adjacent stations such as E05 and E06 (47 metres apart) or E04 and E05 (76 metres apart). Neither is there much correlation between that recorded at the rock site (E01) and the other sites. Stations E07 and E08 on the other hand (only 13 metres apart) show reasonable correlation.

Events 4, 5 and 6 all arrive from a similar northwest direction. Although relative amplitudes are quite different, each event shows a strong EP pulse at station E06, and strong east-west (right diagonal) motion at E05 and E04. Stations closer to the fault show no particular preference in orientation. Event 1 from the southwest shows a similar pattern, with EP motion dominating stations E07 and E06, east-west at E05, and this time strong EN motion at E04 and E03. EP particle motion at station E06 is always stronger than the EN, with the exception of events 3, 9 and 10 that all show dominant EP motion closer to the edge.

9.2.2 PEAK GROUND MOTIONS

Figure 9.12 shows peak ground displacement (PGD) plotted against distance across the array for each event. Peak displacement is normalised against that at E01. Amplification of the PGD is generally less than a factor of 2.0 on the up-thrown side of the fault at station E11, while above the deep sediments amplification ranges between a factor of 1.5 and 8.0, averaging at around 3.0-4.0. Several events (eg. 4, 10 and 13) do not generate PGD amplification greater than 3.0 times that of the rock, while other events (eg. 5 and 9) generate maximum amplifications in the order of 6.0 or more over a number of stations. Different events show different positions of maximum peak amplification, ranging from station E08 (103 metres from the fault) out to E04 (295 metres from the fault).

Event 1, containing a single large pulse in the EN component and arriving with a shallow angle of incidence of approximately 66° from the southwest, has produced a single strong peak in the EP component at E06, and a less well-constrained peak in the EN component at E04. Because the incoming path of propagation is up the line of the Wellington fault, the angle of incidence with respect to a valley cross-section is effectively 0° (vertical

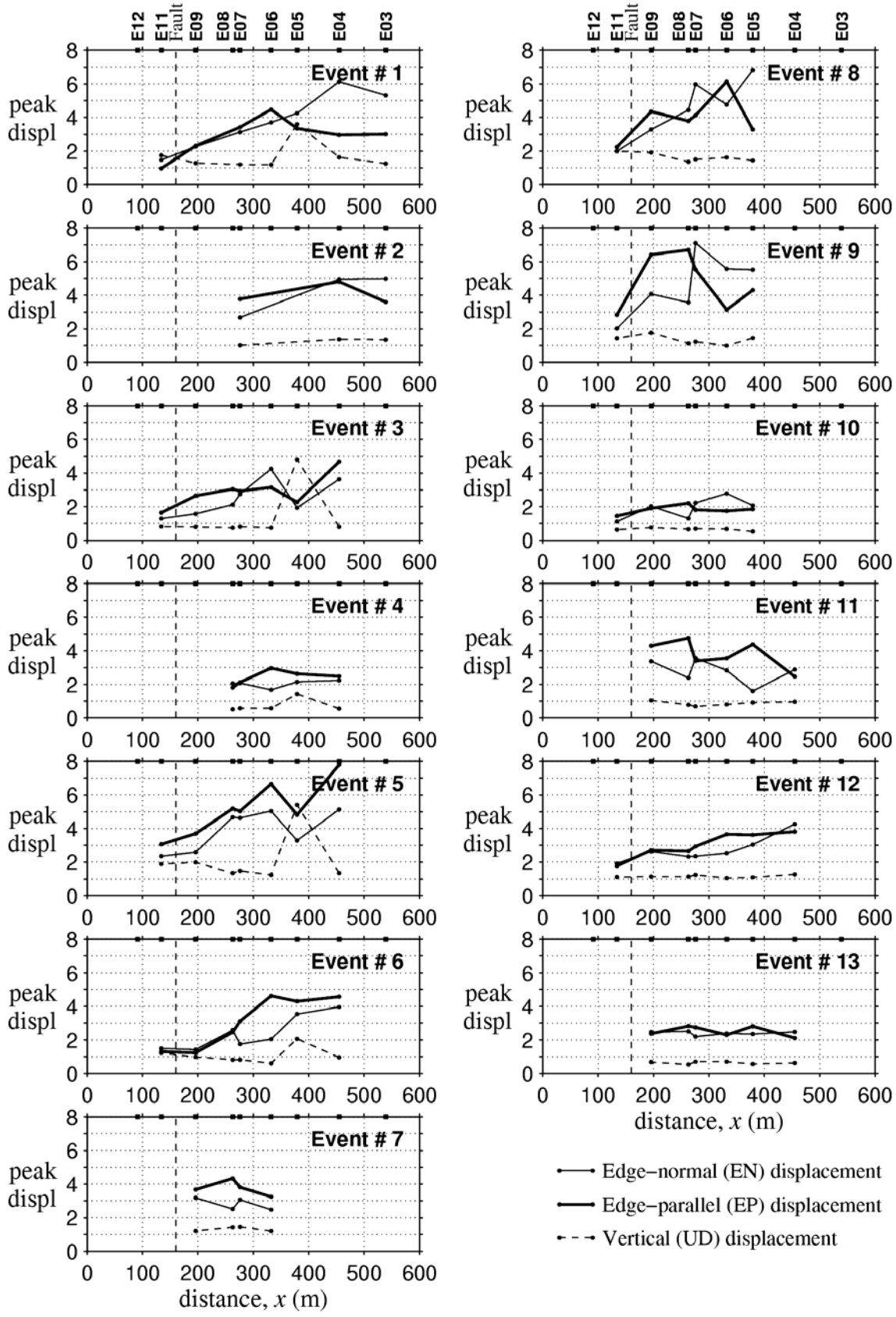

Figure 9.12. EN, EP and UD peak ground displacements (PGD's) plotted vs distance across the array for each event. PGD is normalised against that at E01.

incidence). These characteristics make Event 1 perhaps the most closely related of all the recorded events to the angle of input we may expect to see from a rupture on the Wellington fault.

Event 6 also contains a single strong pulse in the rock record, again most noticeable in the EN component at E01. It arrives from the northwest with a steep angle of incidence of 25° with respect to the vertical. While the EP component again reaches a maximum at station E06 of 4.6 times the PGD at E01, it does not drop off again like Event 1. The EN component reaches a maximum of 4.0 at the last recording station, E04.

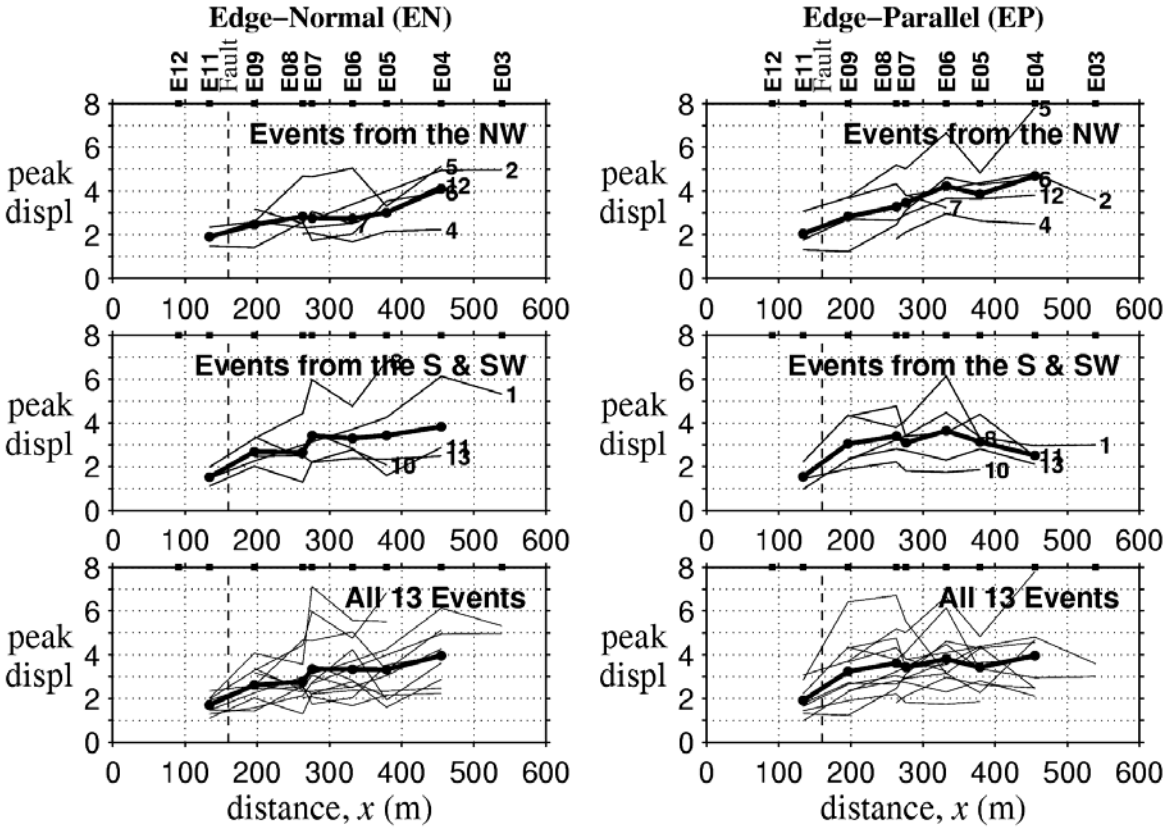

Figure 9.13. Horizontal peak ground displacements (PGD's) across the array grouped by incoming azimuth. The dark line is an average of each plot. An average over all events is shown in the lower two plots. PGD is normalised against that at E01.

Event 5 has generated the largest PGD, in the EP component at station E04. The wavefield from this event (containing several large pulses) also arrives from the northwest with an incident angle of 32°. Both horizontal components show a local maximum at station E06, and an even greater maximum at station E04, the latter of which may be related to

constructive interference of the first large pulse in the surface wave with the second pulse in the direct arrival (although that is strictly speculation). Nevertheless, the strongly pulse-like nature of the input has lead to very large amplification of PGD at stations E06 and E04.

Figure 9.13 shows the same data as in Figure 9.12, yet this time grouped according to incoming azimuth. The dark line shows an average for each component over events from the northwest, southwest, and all-events. The edge-parallel PGD from events to the southwest is the only example of the average peak amplification reaching a local maximum some distance across the array (at E06, 172 metres from the fault), and then decreasing further out. Average edge-normal PGD for events from the northwest, and from all azimuths show a maximum PGD at station E04 (295 metres from the fault). Limited data from station E03 indicates that the PGD remains constant or slightly decreases still further from the edge.

Plots of normalised peak ground velocity (PGV) in a similar form to Figures 9.12 and 9.13 are shown in Appendix 2.2. While the amplitudes are sightly lower, the shape remains very similar to the plots of PGD. As such, the observations given above all apply equally well to PGV.

9.2.3 PHASE AND GROUP VELOCITY ESTIMATION

While edge-generated surface waves are obvious in the results of numerical modelling, they are much more difficult to observe in recorded data. The strong yet variable amplification recorded at sites within the valley is, however, a strong indicator of edge-generated surface wave propagation. While it is difficult to see surface wave propagation paths from a visual inspection of the recorded data (eg. Figure 9.10), we are able to show the frequency-dependant propagation of wave packets (group velocity) by narrow band-pass filtering. At the same time, the tangled nature of the records containing both vertically and horizontally travelling waves has resulted in limited success at estimating phase velocities.

The science of seismology provides various techniques for the determination of phase and group velocities from surface wave recordings. Most of these have, however, been developed for teleseismic situations where the surface wave arrivals are separated in time

from each other and from body wave arrivals, and for surface waves travelling through the full depth of the crust at very high velocities. The case of edge-generated surface waves presents a whole new situation. The seismographs in the array measure ground motion at distances of less than 400 metres from the fault structure where the surface pulses originate. The waveforms recorded at these close distances are essentially a mix of both refracted and reflected body waves and horizontally propagating surface waves.

Larger basins are generally better for observing surface wave propagation. Hatayama et. al. (1995), for examaple, have measured dispersive phase velocities in array data from the 50km-wide Osaka Basin in Japan which match theoretical dispersion curves for Love waves in the 800m-deep basin structure. At the other extreme, Haines and Yu (1997) describe a high degree of spatial-incoherency in observed weak-motion wavefields within the shallow 500m-diameter Alfredton basin in New Zealand, while a similar lack of correlation was found between observed seismograms in the 2km-wide Kaminokuni basin in Japan (Nagumo and Sasatani, 1998).

To our advantage in the somewhat two-dimensional case of Lower Hutt, edge-generated surface waves can (in theory) be separated into Rayleigh and Love waves by their respective particle motions. The horizontal shearing motion from a Love wave will be found entirely in the EP orientation, out of the plane of propagation; while the elliptical particle motion of the Rayleigh wave should be found entirely in the EN and UD components. Here we have postulated that the locally-generated surface waves propagate perpendicularly away from the edge, an assumption quite valid on average a least, and for events arriving from the northwest, southeast or vertically. For the purposes of this study we are most interested in the Love wave propagation, and will hence investigate the EP component of motion for phase and group velocities.

The most significant contribution to the surface motion, however, appears to be from direct shear-wave arrivals. The EP particle motion is expected to be dominated by direct SH and Love waves for events originating from the northwest and southeast. On the other hand, for events originating from the southwest or northeast it will be the SV polarisation that dominates the EP record. P-waves generated by reflection and refraction may also be significant in the latter case.

Time variant cross-multiplication (Bloch and Hales, 1968) between any two stations on the array was employed to determine Love wave phase velocities in the EP records. A technique (see below) for the removal of direct body waves in the records prior to cross-multiplication was also adopted with the hope of producing traces rich in surface wave pulses, without so much interference from the body waves that currently appear to dominate the records. Unfortunately, no useful phase velocity information was obtained from this process, a result perhaps related to strong resonance in the soft Holocene sediments (see section 9.2.5) creating surface records that are correspondingly rich in body wave motion.

The technique for direct wave removal involved subtracting one record from another such that the direct arrivals in both traces cancel out. A slight advantage is gained by determining the apparent velocity of the direct arrival and making a small time shift adjustment to account for it. The second record can then be subtracted from the first or a third adjacent record, and the resulting two traces cross-multiplied. Another technique that was briefly investigated (with little success) was the subtraction of a synthetically generated body wave time-history (using a 1-D transfer function and an assumed basement motion such as E01) from the record at each station.

Group velocity has been calculated by separating each seismogram into frequency components and then tracking the propagation of wave packets across the array. Figure 9.14 shows a stack of seismograms calculated by narrow bandpass filtering at increments of frequency between 1.0 and 5.0 Hertz, for 3 different stations in event 11. In a typical teleseismic situation it is possible to directly see clear dispersion curves on a plot such as this, and be able to calculate the frequency dependant group velocity from the distance to the epicentre.

In this situation, we can see only fragments of several dispersion curves. The transient frequency distribution of energy in these recordings is much more related to the distribution of energy in the incoming wave field than it is to surface wave dispersion. For this reason, we can see similar fragmented patterns occurring at each of the three stations across the array. It appears that the 1.5-2.0Hz energy in the incoming wave field arrives first, and is followed by several packets of higher frequency energy arriving slightly later.

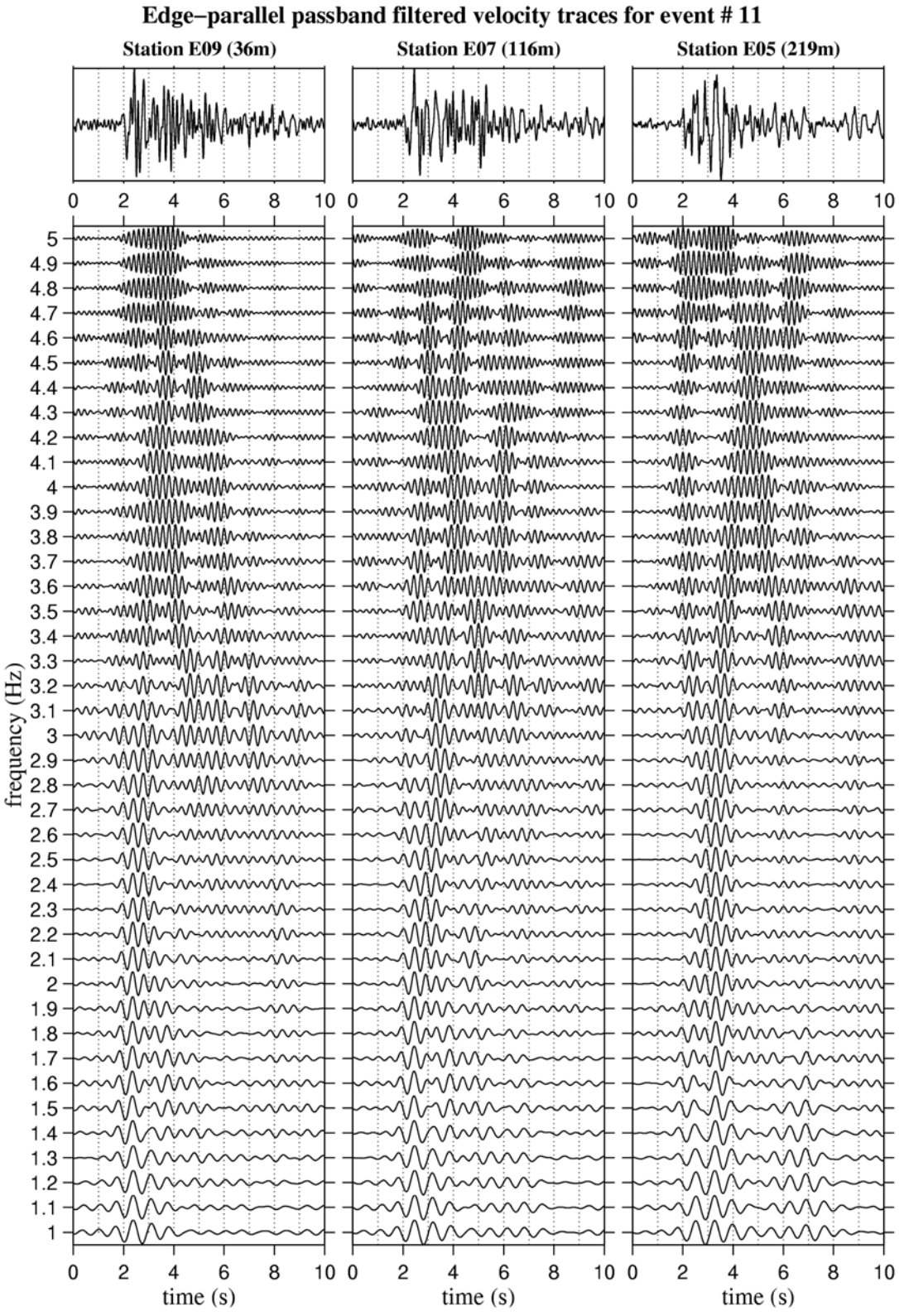

Figure 9.14. EP velocity traces from stations E09, E07 and E05 during event 11, bandpassed with a 0.5Hz 1st-order Chebychev filter. Amplitudes are adjusted to give equal peaks at all frequencies. The top plot shows the original unfiltered trace.

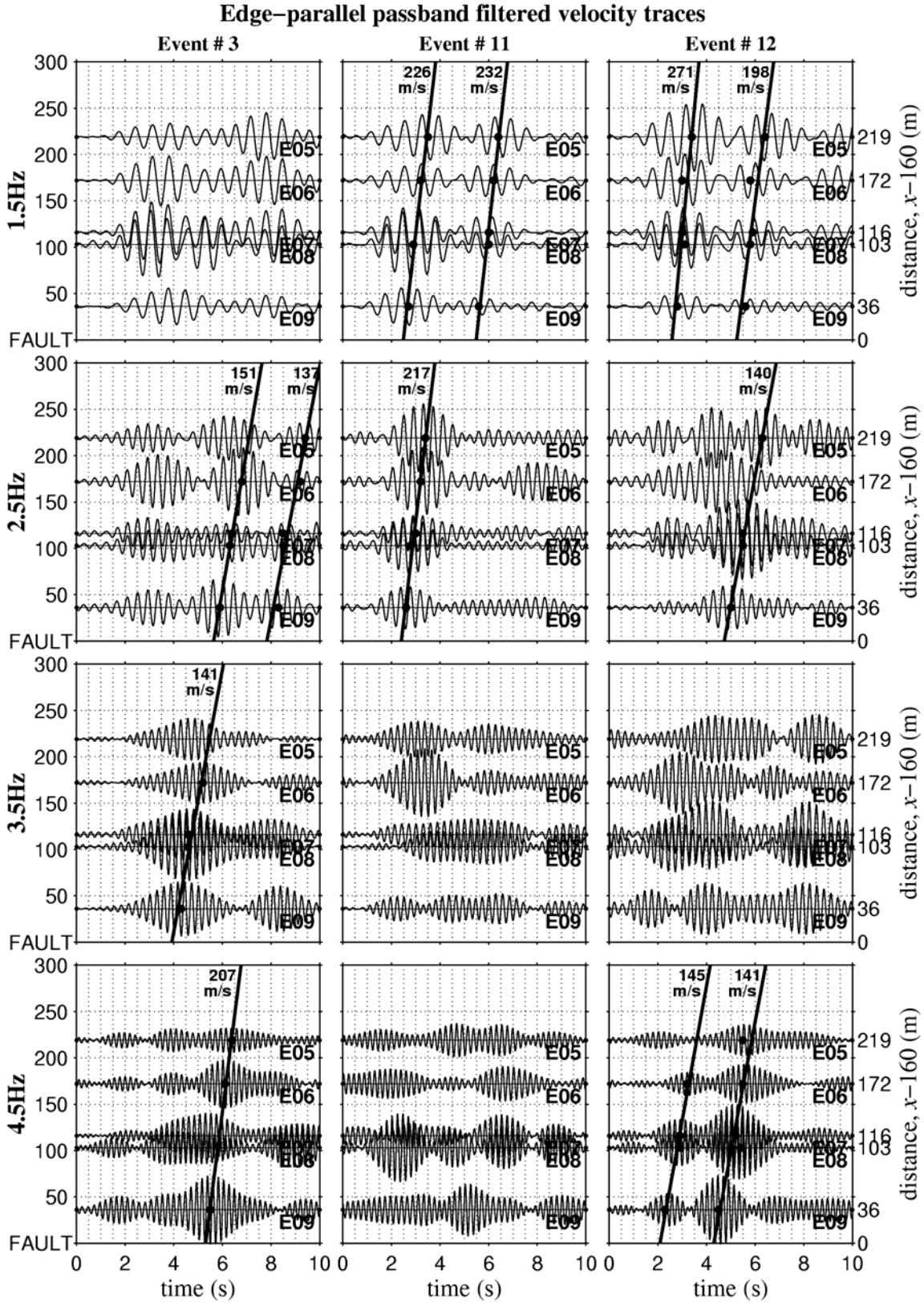

Figure 9.15. Bandpassed EP velocity records from Events 3, 11 and 12 plotted with respect to distance out from the fault trace, such that the movement of wave packets may be tracked across the array to give a group velocity at each frequency. A more comprehensive analysis is presented in Appendix 2.3.

With a series of stations, it is possible to measure the relative movement of energy across the array and calculate group velocity. Figure 9.15 shows the movement of wave packets across the array for events 3, 11 and 12 at four different frequencies. The solid lines show estimated values of group velocity at each frequency. Most plots show that some wave packets remain stationary, while others have a clear linear movement across the array. Several plots show a quite chaotic movement of energy with no clear linear distribution; presumably a result of interference between stationary and transient energy.

Group velocity estimates from Figure 9.15 and a number of other frequencies shown in Appendix 2.3 have been plotted atop a theoretical dispersion curve in Figure 9.16. While the distribution of measured group velocity is not tight, it does sit roughly around the theoretical group velocity curve calculated for the 20-metre thick layer of Holocene sediments immediately beneath the array. The minimum in the measured group velocity corresponding to the 1st mode Airy phase lies at a frequency of 2.0-2.5Hz.

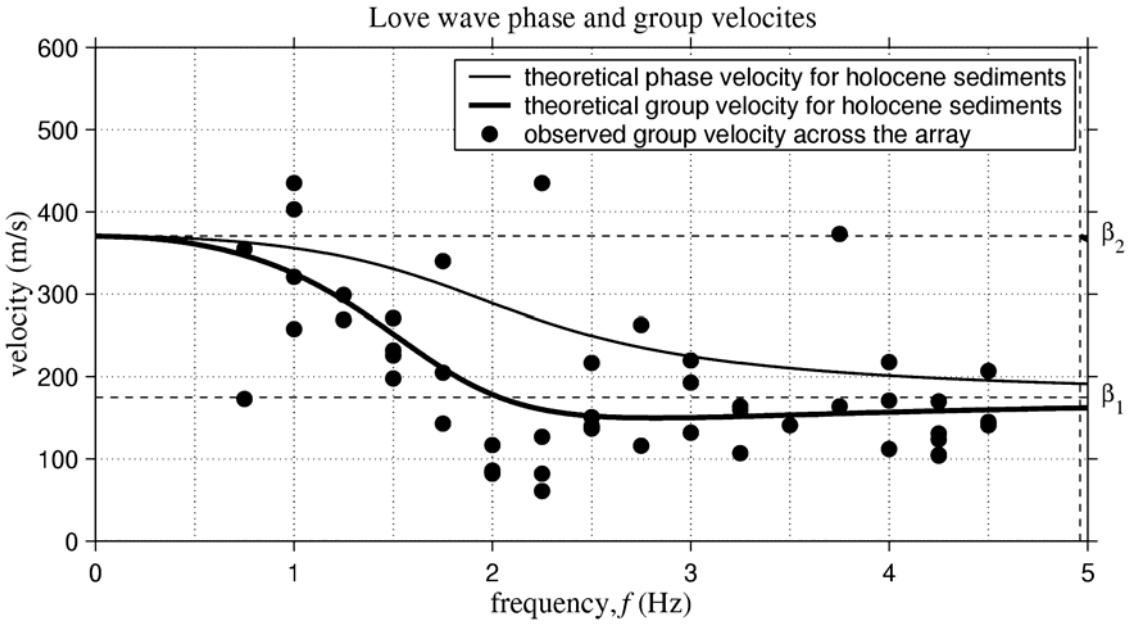

Figure 9.16. Measurements of group velocity made in Figure 9.15 and Appendix 2.3 plotted atop a theoretical dispersion curve of a Love wave travelling in the 20-metre thick Holocene layer. β_1 and β_2 are the shear wave velocities of layers B and C in the geological model in Chapter Ten.

9.2.4 TIME-FREQUENCY ANALYSIS OF DISPLACEMENT DATA

Figures 9.17 and 9.18 show spectrograms of transient Fourier amplitude spectra (FAS) over the horizontal components of displacement from events 1 and 5. Spectrograms have been constructed with a 1.0 second moving Hanning window over each of the 10-second shear wave displacement traces plotted in Figures 9.8 and 9.9. Fourier amplitude has been normalised against the peak of the horizontal components at station E01. A catalogue of spectrograms for all 13 events can be found in Appendix 2.4.

Spectrograms of the rock sites in most events show a wide range of frequency with one or two strong pulses near the start of the shear wave. A single 2.45Hz pulse occurs at E01 in Event 1, while other events have produced initial shear wave pulses at various frequencies between 1.30Hz (Event 5) and more than 5Hz (Event 10).

The deep sediment sites have tended to only amplify the lower frequencies (below ~4Hz). The prominent initial pulse of Event 1 is amplified strongly across the array, again most notably at E04 in the EN component, and at E06 in the EP component, as was observed in the measurements of peak displacement in Figure 9.12. The spectrograms show, however, a change in the dominant frequency of the initial shear-wave pulse. For Event 1, the 2.45Hz pulse occurring in E01 is amplified at slightly lower frequencies across the array stations (between 1.75Hz and 2.40Hz). For Event 5 the initial 1.30Hz pulses are amplified at slightly higher frequencies across the array stations (between 1.65 and 2.30Hz). The general trend indeed for all events is for the initial pulse(s) in the record to be amplified across the array most strongly at frequencies tending toward 2.0-2.2Hz, no matter the frequency of the initial pulse(s) in the rock. Later arrivals recorded at deep sediment sites also appear to be rich in 2Hz motion.

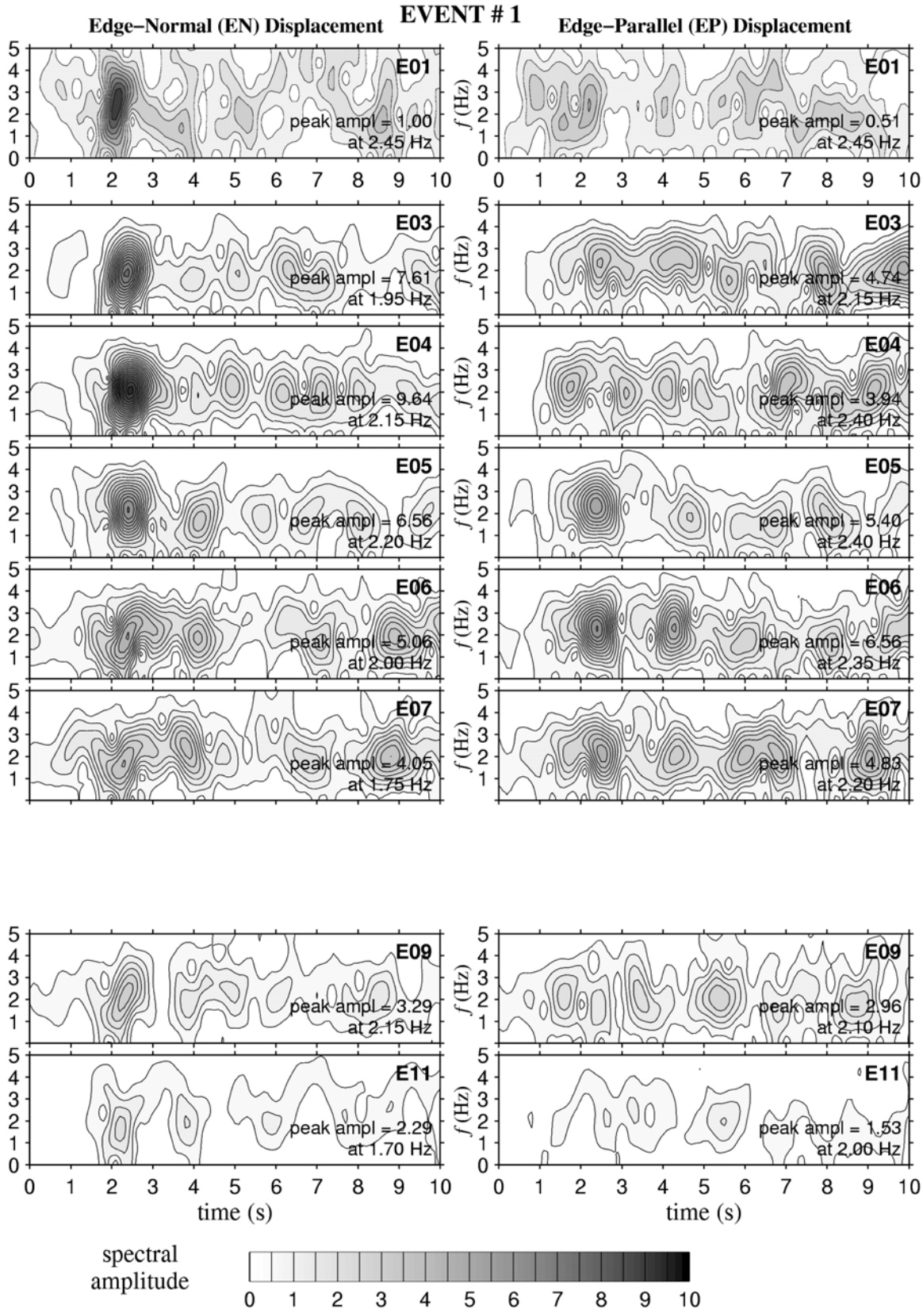

Figure 9.17. Spectrograms of horizontal shear-wave displacement recorded during Event 1. Spectral amplitude is normalised against the peak at E01 and contours are plotted at intervals of 0.5, except at station E01 where the contour interval is 0.1.

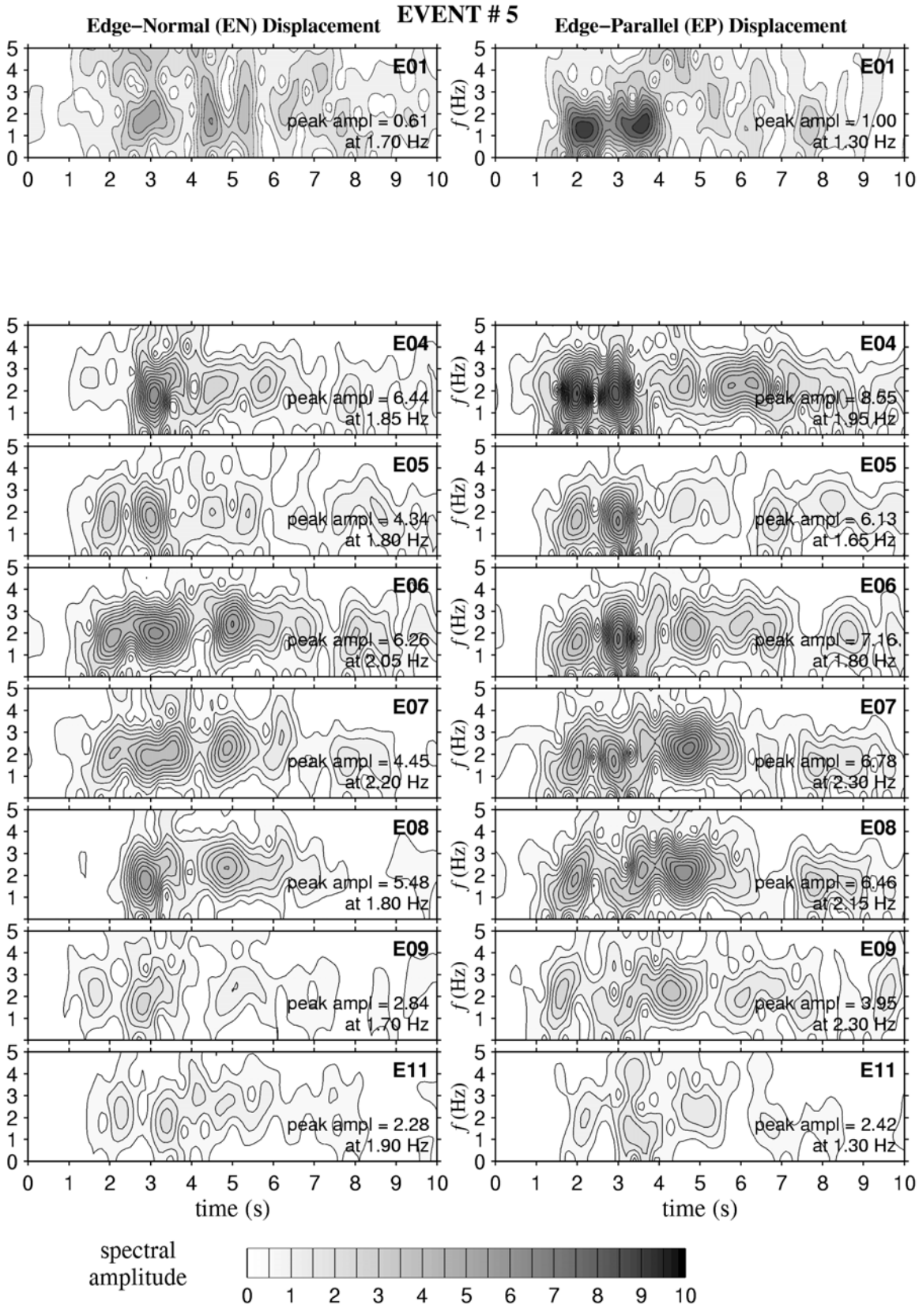

Figure 9.18. Spectrograms of horizontal shear-wave displacement recorded during Event 5. Spectral amplitude is normalised against the peak at E01 and contours are plotted at intervals of 0.5, except at station E01 where the contour interval is 0.1.

9.2.5 SOIL TO ROCK FOURIER SPECTRAL RATIOS

After assuming the shaking recorded at station E01 to be representative of the incoming wave-field, Fourier spectral ratios (FSR) are used to investigate the spectral amplification due to the sediments infilling the valley. Fourier spectral ratios for EN, EP and UD components are shown in Figure 9.19. The solid line on each plot gives the average FSR.

The horizontal components of all deep sediment stations (E09-E03) have a peak ratio at a frequency between 2.0 and 2.5Hz. Strong amplification above a factor of 5 occurs in general between 0.5 and 3.0Hz. The largest values of FSR occur in the edge-parallel component at stations E06 and E04 (11.0 and 11.5 respectively). Only two recordings at E03 mean the average FSR at this station is of poor quality. The FSR observed in the vertical component of station E05 for Events 1, 3, 5 and 6 is anomalously high in the 0.5-3.0Hz range. This is suggestive of some form of instrument error, since all other events recorded at this station show FSR of similar shape to adjacent stations E04 and E06.

The edge-parallel component displays three distinct resonant frequencies that remain relatively constant across stations E09-E03. The first and lowest is at 0.7Hz, the second at 1.4Hz and the third and highest at 2.2Hz. A fourth peak appears at 2.5Hz over most of the stations except E09 (2.7Hz) and E06 where it constructs with the 2.2Hz resonance to show a maximum at 2.4Hz. Station E11 on the up-thrown side of the fault exhibits a much lower peak FSR at 4.2Hz, indicative of stiff shallow sediments.

The edge-normal orientation develops slightly lower FSR than the EP. A single peak at 2.2-2.5Hz is observed at most of the deep sediment sites. The vertical component is much less amplified than the horizontal, with a FSR of 4-5 for frequencies between 1.0 and 5.0Hz. A 1.2Hz resonant frequency is noticeable over stations E08-E03, while E09, E08 and E07 show another peak between 4.0 and 5.0 Hz.

9.3 DISCUSSION

While there are many similarities to be found in the motion observed at each of the stations across the array, there are also significant differences. The array covers three quite different geological zones. The first is at sites E01 and E13 where the greywacke basement rock is almost at the surface, and these two sites show severely different ground responses as a result of topographic differences. The second is the narrow strip of land on the up-

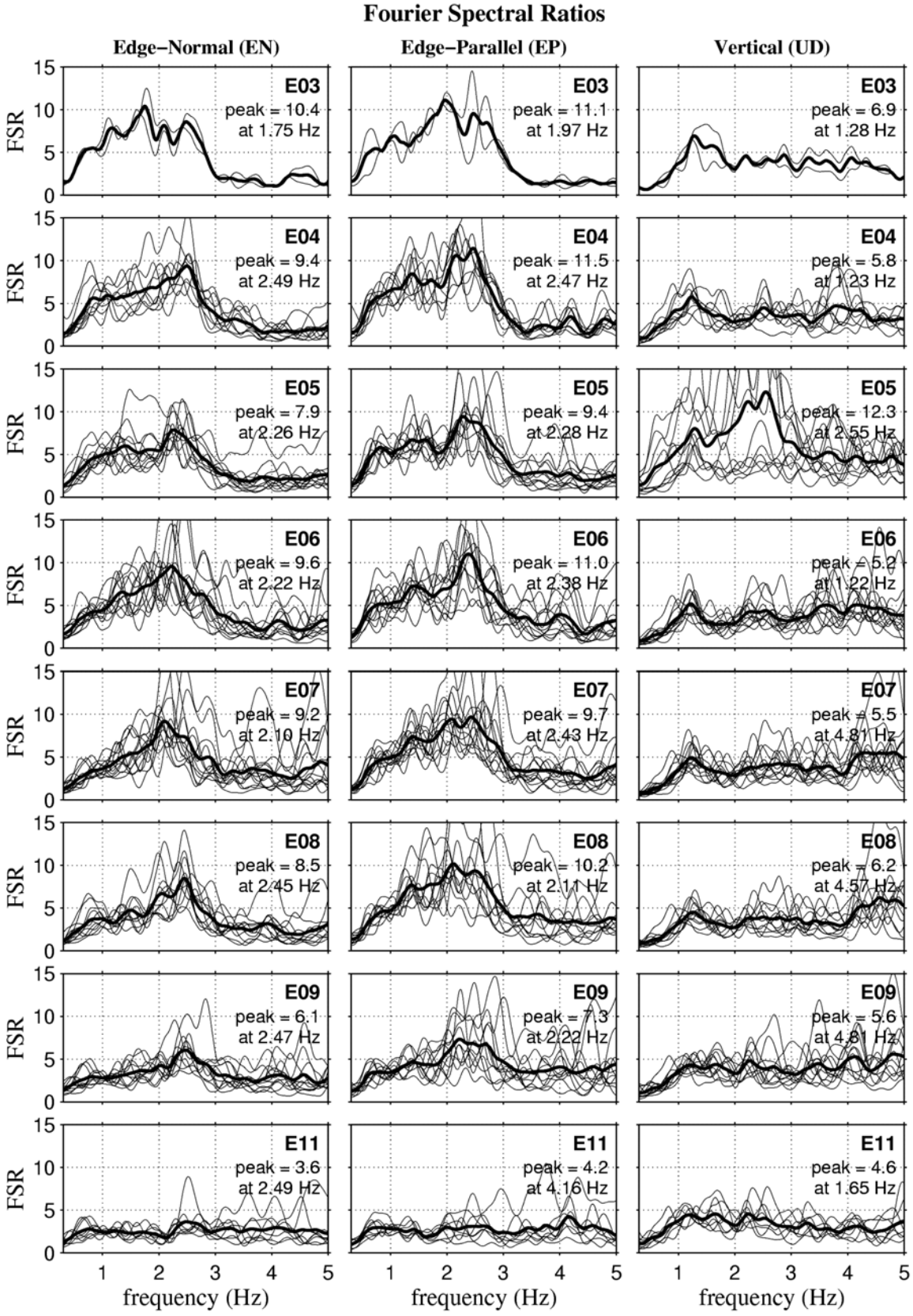

Figure 9.19. Fourier spectral ratios (FSR) separated into EN, EP and UD components, and averaged over all 13 events at each array station. Spectral amplitude at the soil and rock sites have been smoothed with 0.2Hz and 1.0Hz moving triangular windows, respectively.

thrown side of the fault where the basement rock lies below a depth of less than 25m of stiff colluvial and other deposits. The ground response here is quite different to the rock sites, and to the third zone of interest, the deep sediments on the down-thrown side.

Even amongst the seven stations on the deep sediments, there are large spatial variations in ground motion recordings. This is most clearly seen in the plots of particle motion in the horizontal plane in Figure 9.11, where the ground movement at any point in time may be in quite dissimilar directions at neighbouring stations within 50 metres of each other. The peak ground displacements in Figure 9.12 also show change across the array, again sometimes quite significantly between neighbouring stations.

Variable stratigraphy in the near-surface Holocene sediments will have had some influence in generating different ground responses at adjacent stations. The cross-section in Figure 9.4 gives only a general picture of the many inter-woven beds and lenses of a large variety deposits evident in the borehole data. The existence of a thin layer of silt, sand and peat on the surface out to station E05 is likely to effect only the high frequency motions due to its shallow depth. In fact, the maximum peak ground motions have been shown in Figure 9.13 to occur on average at stations E06 and E04, on the far edge of, and outside this recent fine deposit. The impedance contrast at the base of the Holocene layer and its resonant action as a whole is perhaps much more important than its internal heterogeneities.

As a result of the SH wave modelling in the previous chapter, it seems likely that the constructive basin-edge effect will be shown to be a significant contributor to the observed differential ground motion. The effect is essentially a mechanism leading to a constructive combination of arrival time, phase and frequency content at a given location and time. It is therefore most likely to be observed in the magnitude of peak ground motions. The drawback of using peak ground motions from recorded data, however, is that they are likely to be strongly influenced by other (somewhat random) physical effects such as the localised focussing and scattering of direct arrivals. The constructive effect occurs only over a period of time where the arrival times match; and because the same surface waves that generate the basin-edge effect travel across the whole array, we do not expect to see a peak in the Fourier spectral ratios.

9.3.1 AMPLIFICATION IN THE FREQUENCY DOMAIN

The frequencies amplified by the deep sediments are very similar across all seven stations; a result best seen in the average FSR in Figure 9.19. The EP component at each deep sediment station exhibits three clear peaks, at frequencies most likely associated with resonant modes of the deep valley structure. A fourth peak in frequency occurring quite close to the third is also of interest as the highest FSR is found in the region of these latter two peaks between 2.0 and 2.5Hz.

The existence of two high peaks at this frequency suggests the likelihood of at least two mechanisms contributing to the strong amplification. The first of these is probably a 3rd mode resonance of the 300 metre deep sediments, pointed to by the existence of the 1st and 2nd modes at 0.7Hz and 1.4Hz. Another mechanism that undoubtedly acts at this frequency is resonance of the top 20 metres or so of soft Holocene sediments above the stiffer artesian gravels. Using Equation 4.19, the SH resonant frequency of an infinite homogeneous flat layer of depth 20m and shear wave velocity 175m/s, is 2.19Hz. The strength of this latter resonance relative to that of the deep sediments is likely to depend on the impedance contrast at the base of the Holocene layer; a sharp contrast generating the highest amplification.

Variations in amplitude of FSR across the array appear to be relatively minor. Osborne (1999) shows the average horizontal spectral amplification (AHSA) – an average FSR between 0.5 and 3.0Hz over both horizontal components – to increase to a stable value of approximately 6.8±0.5 from station E07 out across the valley. Across the same location, the peak average FSR in Figure 9.19 – occurring in the 2.0-2.5Hz range – maintains a value of 10.5±1.0. Horizontal to vertical noise ratios (HVNR) from measurements made along Beaumont Street (Osborne, 1999) also show a 2Hz peak of fairly constant amplitude across this part of the valley.

The Fourier amplitude of the initial pulses in each event (Figures 9.17 and 9.18), on the other hand, show significant spatial variability across the deep sediment stations, very similar to the variation in PGD in Figure 9.12. The dominant frequency of these initial pulses consistently tends to occur at around 2.0-2.2Hz across the deep sediments. This happens even when the dominant frequency of the initial pulse at the rock site is quite different (Event 5 in Figure 9.18 is a good example). While a rapid development of vertical

resonance in the Holocene layer probably accounts for much of the amplification at this frequency, it cannot explain the spatial variability in the amplitude of these initial peaks.

9.3.2 AMPLIFICATION IN THE TIME DOMAIN

Ground motion time histories measured across the array show large variations in amplitude between stations. The peak generally occurs within the first few pulses of the shear wave arrival at the surface, and at a frequency shown by the spectrograms as tending toward 2.0-2.2Hz. The peak amplitude is a quantity that is inherently somewhat random in nature. It is essentially the summed response of a large number of physical influences. The time of arrival, phase, and frequency content of various pulses in an incoming wave field are of utmost importance in constructing the peak ground motion recorded at any given station. A slight variation in any of those three parameters may have a huge influence on its magnitude and nature.

A visual inspection of the displacement traces in Figure 9.10 suggests that the highest peak across the array exists due to a favourable combination of constructive interference occurring at that location in space and time. The form, if not timing, of many of the pulses is quite regular between stations. Certainly the largest contribution to the peak amplitude is from pulses with a high or infinite apparent horizontal velocity, in other words pulses that have arrived at the surface with a slightly inclined or vertical paths of propagation. What is not clear, however, is the transient nature of the waveforms that construct with the vertical arrivals to generate the peak motions.

There is a possibility that the additional contribution is due largely to scattering and focussing of direct and reflected body waves. If this were occurring within the localised soil mass beneath each station, the fluctuations in peak amplitude would probably be fairly chaotic and random across the array. If, on the other hand, the scattering and focussing occurred due to the geometry of the basement rock forming the deep valley, there would more likely be the consistency in the nature of the pulses that does exist in the results. The chief problem with this explanation however, is the lack of physical evidence for any suitable lens-like structure in the geological basement model; certainly not with the ability to produce the sharp spatial amplifications that exist in the peak displacements.

A more plausible explanation is that the additional contribution to pulse amplitude (over and above the direct arrivals) is due largely to edge-generated surface waves propagating across the array. In the EP component these would necessarily be Love waves, while in the EN and vertical components, Rayleigh waves. If this were the case, we would expect to be able to trace pulses across the EP time-histories travelling at some phase velocity of a Love wave in the sediments. While the sloping lines sketched in Figure 9.10 do appear to follow pulses travelling at the lower end of the expected range of Love wave velocity (175m/s, estimated from the assumed shear wave velocity structure), they by themselves are less than convincing as to the existence of surface waves.

The action of edge-generated surface waves in the valley, however, is verified by the arrival of packets of energy at successive frequency-dependant time intervals across the array. Group velocity observations made in this way and plotted in Figure 9.16 suggest a local minimum in the dispersion curve and corresponding Airy phase amplification at 2.0-2.5Hz. The Airy phase develops as the frequencies around the local minimum travel with the same group velocity and interfere constructively with each other. An interaction of this travelling Airy phase with the direct arrivals through the sediments would certainly lead to amplification in the 2.0-2.2Hz initial pulses over a short width of the array. A constructive basin-edge interference effect of this kind between direct and surface waves indeed seems necessary to explain the spatial variation in peak ground motions at the frequencies observed.

While there is a large difference between events in the position, shape and magnitude of the maximum PGD in Figure 9.12, it is not an unlikely result given the variability in the input motions. The angle of incidence of the wave field on the valley is likely to have a significant effect on the nature of the basin edge effect and the resultant peak ground motions at the edge. Since we are able to test the effect of different angles of incidence (in the plane of a valley cross-section) with the FEM modelling, an analysis will be left for the next chapter. Input from azimuths other than the plane of a valley cross-section undoubtedly adds to the variability.

Another major contributor to the nature of the constructive basin edge effect is the make-up of the input wave field. Strong amplification in a narrow zone is most likely to be generated by an incoming wave field containing a single pulse of energy, much larger in amplitude than the rest of the input. The amplification resulting from such a pulse is

unlikely to be significantly reduced by the somewhat random interaction with other pulses in the wavefield. In contrast, for input signals containing no single significant pulse, it is unlikely that a narrow band of amplification would result. Rather we would expect to see a wider zone of peak ground motions, variably amplified by the multi-pulse basin-edge effect described in Chapter Six. In agreement with this argument, the wavefield recorded at the rock site KBU during the Hyogo-ken Nanbu earthquake contains a very significant strong pulse. The worst damage from this earthquake occurred within a well-defined narrow zone.

While none of the displacement traces shown in Figure 9.6 contain a single pulse of energy quite so prominent as in the KBU record, or the simple Ricker wavelet used in the modelling, some (eg. Events 1, 4 and 6) do have a less prominent single pulse. Of these, the maximum edge-parallel PGD occurs near the recorder stations E07-E06 (116-172m from the fault) while the maximum edge-normal PGD occurs nearer E04 (295m from the fault). Other records (eg. Events 3, 5 and 8) contain several large pulses, while many of the rest contain no one large pulse that stands out significantly in amplitude. It is therefore more likely that we should see the wide band amplification of peak ground motions found on average in Figure 9.13.

9.4 SUMMARY

Significant differences are evident in the particle motion observed at neighbouring stations, sometimes less than 50 metres apart. Edge parallel motion dominates the records at stations E07-E06, 116-172 metres from the fault, while edge-normal motion dominates the records at stations further out from the fault. Maximum PGD from single-pulse events also occurs at stations E07-E06 in the edge-parallel component, and at station E04 (295 metres from the fault) in the edge-normal component. The multiple-pulsed nature of the majority of events and the range of angles of incidence, however, produce on average a wide-band amplification of peak ground motion across the array.

While scattering and focussing by the geometry of the basement rock may contribute to amplified arrivals across parts of the valley, it cannot account for the observed sharp variations in peak ground motion. Likewise, neither do the local variations in near-surface geology correspond with the observed variations in peak ground motion. The most plausible explanation to account for local amplifications across the array is a constructive

interference between direct shear-wave arrivals and edge-generated surface waves, the basin-edge effect.

Amplification of peak ground motions by the basin-edge effect is strongest at the Airy phase frequency, at which significant surface wave energy travels with the same velocity. The Airy phase for edge-generated Love waves in the Lower Hutt appears to be approximately 2.0-2.5Hz, corresponding to a minimum group velocity of around 100-150m/s. The group velocity observations roughly correspond to the theoretical 1st mode dispersion curve of a Love wave in the Holocene layer. The prevalence of 2Hz energy in the incoming wave fields may also contribute to the basin-edge effect occurring most strongly at this frequency.

Frequencies amplified in the Fourier spectral ratios correspond to resonant frequencies of both the deep sedimentary valley and the 20-metre thick Holocene layer. In the edge-parallel component, eigenfrequencies at 0.7Hz, 1.4Hz and 2.2Hz – corresponding the first three vertical resonant modes of the deep sedimentary valley – are clearly visible across stations E09-E04. A fourth peak observed at 2.4-2.7Hz is close to the fundamental vertical frequency of the Holocene layer. Anomalously strong resonance in the range 2.0-2.5Hz is a result of constructive interference between these two modes of resonant behaviour.

Chapter 10: REVISED FEM MODELLING OF LOWER HUTT

Using results from Chapter Nine, the near-surface stratigraphy and material properties of the Lower Hutt Central cross section (from Chapter Eight) has been adjusted to match the conditions in the location of the array. A comprehensive set of FEM results from the revised model is then presented to show the response of the valley as a whole and at the fault-bounded edge under input pulses of various frequencies and angles of incidence. In Section 10.5 a comparison is made between the modelling results and the array observations. Section 10.6 then comments on the applicability of using a two-dimensional linear-elastic analysis of wavelet propagation for the study of seismic response of the Lower Hutt.

10.1 METHOD OF ANALYSIS

10.1.1 MODIFICATIONS TO THE GEOMETRICAL AND VELOCITY MODEL

The geometry of the valley at the site of the array (Figure 8.1) is very similar to the cross section through Lower Hutt Central. For this reason the cross-section through the array has been constructed with the same basic geometry as cross-section BB in Figure 8.2. Near surface stratigraphy on the left-hand side of the model has been altered to match the geological cross-section at the position of the array in Figure 9.4, and the velocity model presented in Table 8.1 has been adjusted to match the resonant frequencies observed in the array results.

A significant difference in stratigraphy between the array site and cross-section BB is on the up-thrown side of the fault where only a thin layer of recent sediments overlies an older colluvial deposit. This is a change from the soft deposit of artificial fill that was modelled in cross-section BB and that produced the strongly resonant response seen in Figure 8.4(a). Borehole data also suggests a depth of only 20m to the aquifer gravels on the down-thrown side, as opposed to the 25m modelled in Lower Hutt Central. The fault-bounded edge of the new geometrical model revised for the array site is shown in Figure 10.1, along with

the location of the array instruments. The rest of the cross-section is as for cross-section BB in Figure 8.2.

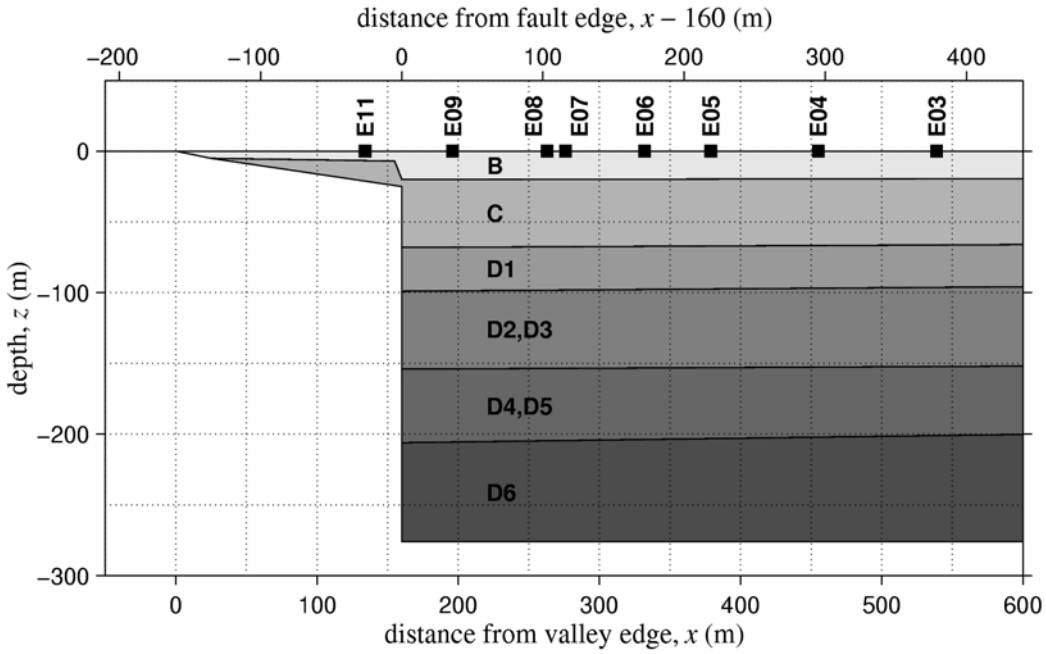

Figure 10.1. Part of the geological model developed from cross-section BB (Figure 8.2) for FEM modelling in the position of the array. The locations of the seismographs in Chapter Nine are also shown.

Average edge-parallel Fourier spectral ratios recorded at many of the stations above deep sediments all show a similar shape (Figure 9.19), with small peaks at 0.7Hz and 1.4Hz, and a large peak in the 2.0-2.5Hz range. It seems likely that these correspond to the first three resonant frequencies of the deep basin structure. The strong amplification between 2.0-2.5Hz is hypothesised to be a result of the fundamental frequency of the Holocene surface layer coinciding with the 3rd resonant frequency of the deep basin structure.

The resonant frequencies observed on the array are thus higher than those observed in the 2D modelling of the Lower Hutt Central cross-section, suggesting that the shear-wave velocity of the sediments must be higher than was estimated for the original simulations (Table 8.1). A one-dimensional analysis was thus made of the deep stratigraphic column adjacent to the fault to determine the likely increase in shear-wave velocities required to coincide the 3rd resonance of the deep sediments with the fundamental, f_0, of the Holocene layer in the region 2.0-2.5Hz. The result is shown in Figure 10.2, where the response of the original model through Lower Hutt Central is shown with the thin dashed and solid lines.

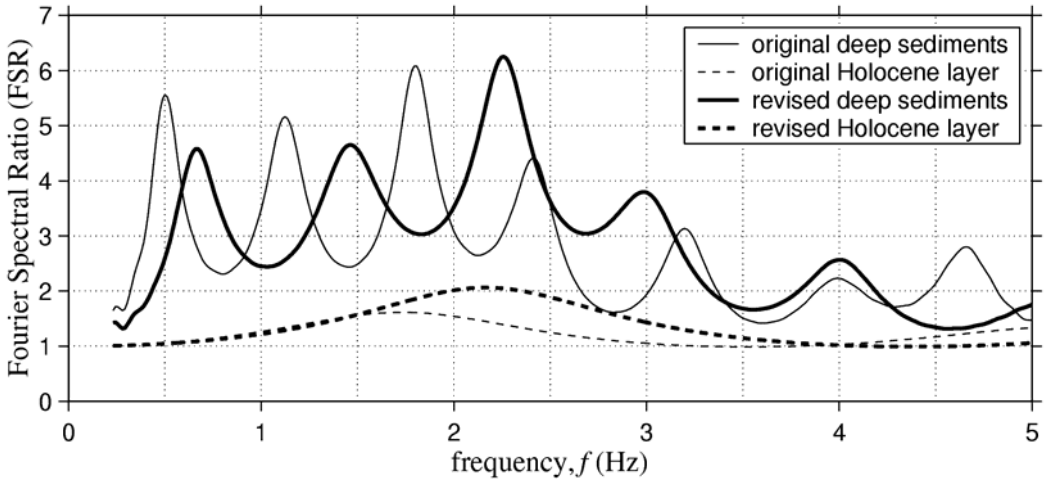

Figure 10.2. Results of a one-dimensional analysis used to revise the velocity model. Dashed lines show the 1-D response of the Holocene layer, while solid lines show the 1-D response of the full depth of sediments.

In order to achieve the result in Figure 10.2, the shear-wave velocities of layers 2-6 have been increased by a factor of 1.3, while the depth of the top layer has been reduced to 20m. Total depth to bedrock remains the same at 276m. The revised shear-wave velocities and sediment depths adjacent to the fault are presented in Table 10.1.

Table 10.1: Model parameters adjacent to the Wellington Fault in the original model (Chapter Eight) and in the revised model through the array in Alicetown. Damping, ζ = 2% in sediments (n = 1-6) and ζ = 0 in basement rock (n = 7).

n	Preliminary		Revised			Layer	
	h_n (m)	β_n (m/s)	h_n (m)	β_n (m/s)	ρ_n (kg/m^3)		
1	25.0	175.0	20.0	175.0	1750	B/Bb	Holocene Sediments
2	43.0	285.0	48.0	370.5	1800	C	Waiwhetu Artesian Gravels
3	31.0	325.0	31.0	422.5	1850	D1	Kaihinu Deposits
4	55.0	460.0	55.0	598.0	1900	D2/3	Waimea and Karoro Deposits
5	52.0	600.0	52.0	780.0	1950	D4/5	Moera Basal Gravels
6	70.0	675.0	70.0	877.5	2000	D6	Nemona Glacial Gravels
7	inf	1500.0	inf	1500.0	2700	E	Torlesse Basement Rock

The fundamental frequency of the 25m deep Holocene layer previously matched the 3rd mode of the deep sediments at around 1.6-1.8Hz. With a reduction in depth of the Holocene sediments (to 20m, as mentioned previously) its fundamental frequency

increases to 2.19Hz, still using the original shear wave velocity of 175m/s. This is a useful result since the 175m/s value is reasonably well constrained by SCPT testing in the Holocene layer (Stephenson and Barker, 1992). The shear wave velocities of the lower layers, however, have been scaled up by a factor of 1.3 to get the coincident amplification at around 2.2-2.3Hz shown in Figure 10.2.

Scaling up the shear-wave velocity of the deeper sediments by a factor of 1.3 is not an unreasonable change due to the lack of certainty involved in the original estimations. Increased stiffness in the lower stratigraphy will increase the velocity contrast at the base of the Holocene layer and enhance the amplification at 2.2Hz. It will also decrease the velocity contrast at the basement interface thus reducing the low-frequency resonant amplification of the deep basin structure that was not especially strong in the array results.

A vertically incident pulse will have a travel time through the sediments ($t_{S1} = 0.556$s) given by Equation 5.48 and through the rock ($t_{S2} = 0.184$s) given by Equation 5.49. The resultant time difference between arrivals at the surface is thus $t_{S1} - t_{S2} = 0.372$ seconds. In addition, the wavefront travelling up through the rock and sediments on the up-thrown side of the fault is expected to have an arrival delay given by $0.256\text{s} - t_{S2} = 0.072$ seconds. These times were calculated using the depths and velocities shown in Table 10.1.

The model has a velocity contrast between the deepest gravels and bedrock of only $\beta_7/\beta_6 = 1.7$. The contrast between the Holocene layer and the Waiwhetu aquifer is slightly higher than this at $\beta_2/\beta_1 = 2.1$. The depth-averaged shear wave velocity of the whole sedimentary column next to the fault is 613m/s giving an overall contrast with the basement of $\beta_7 / \overline{\beta}_{1-6} = 2.4$.

10.1.2 TESTING PROCEDURE

Several simulations with various inputs are made on the revised cross-section model described above. Initially, we simulate response due to a 2.0Hz vertically incident Ricker wavelet, as was used in the preliminary testing in Chapter Eight. The one-dimensional response across the valley is computed in order to compare with the two-dimensional result. The angle of incidence and characteristic frequency of the input are then varied in order to gauge the sensitivity of the response to these parameters. A full list of tests is given in Table 10.2.

Tests are continued for 4000 iterations with a time step of 0.005s to obtain 20 seconds of information, which is generally sufficient to reduce the amplitude of wave oscillations effectively back to nil. Transient displacement data is captured at each step from 200 points across the surface of the model, and in the case of the 2-D simulations, from another 4000 points below the surface in the vicinity of the edge.

Table 10.2. Summary of simulations made on the new Lower Hutt cross-section revised with results from the array analysis.

Analysis type	Test code	Characteristic frequency f_c (Hz)	Angle of incidence θ_i°
2-D	T1	0.50	0°
	T2	1.00	0°
	T3	2.00	0°
	T4	2.00	60°
	T5	2.00	30°
	T6	2.00	-45°
1-D	O1	2.00	-

The fundamental 1-D frequency of the full depth of sediments adjacent to the fault, $f_0^{\text{full depth}} = 0.67$Hz (Figure 10.2), while the fundamental 1-D frequency of the Holocene layer, $f_0^{\text{Holocene}} = 2.19$Hz. Using these to calculate the dimensionless frequencies (Equation 6.1) associated with the input it is possible to begin to envisage the likely edge response based on results from Part II. The dimensionless input frequencies are listed in Table 10.3.

Table 10.3. Characteristic frequencies of the input Ricker wavelets are converted to dimensionless forms based on both the fundamental frequencies of the deep sediments and the top (Holocene) layer.

Test	f_c (Hz)	$f_c/f_0^{\text{full depth}}$	$f_c/f_0^{\text{Holocene}}$
T1	0.50	0.746	0.228
T2	1.00	1.49	0.457
T3	2.00	2.99	0.913

The result of test T3 is presented in Section 10.2, where comparisons are made both with the preliminary test and with the 1-D simulation (01). Results from tests T1-T3 are then compared in Section 10.3 to determine the effect of the input frequency, while the results of tests T4-T6 are presented in Section 10.4 to determine the significance of the angle in incidence.

10.2 AMENDED RESULTS

Results are presented from simulation T3, which uses the same input (f_c = 2Hz and θ_i = 0°) as in the preliminary simulation in Chapter Eight. Surface response across the whole valley is first compared to the preliminary result, and then to the results of a one-dimensional analysis. We then look at the response just at the edge, including the propagation of pulses up through the cross-section.

10.2.1 WHOLE VALLEY RESPONSE

Figure 10.3 presents both the transient displacement response and the spectral ratio response of the whole valley for the two-dimensional analysis. Amplification across the full width of the valley is increased due to stronger resonance in the Holocene layer. Love waves generated at each edge have generally higher velocities than in the preliminary test; the two are compared in Table 10.4.

Table 10.4. A comparison of dominant group and phase velocities measured from surface displacement data for the preliminary test (Chapter Eight) and the revised test in this chapter. Subscripts *LHS* and *RHS* refer to the Love waves generated from the left-hand side (vertical edge) and right-hand side (sloping edge).

f_c (Hz)	θ_i°	Test	U_{LHS} (m/s)	c_{LHS} (m/s)	U_{RHS} (m/s)	c_{RHS} (m/s)
2.00	0°	Prelim	190	330	190	320
2.00	0°	T3	230	420	215	370

Amplification in the frequency domain still shows the classic pattern of two-dimensional resonance centred toward the deep side of the valley, yet the resonant frequencies are all higher than the preliminary result, as expected from the change to the velocity model. At least the first 15 horizontal modeshapes belonging to the fundamental vertical mode can be

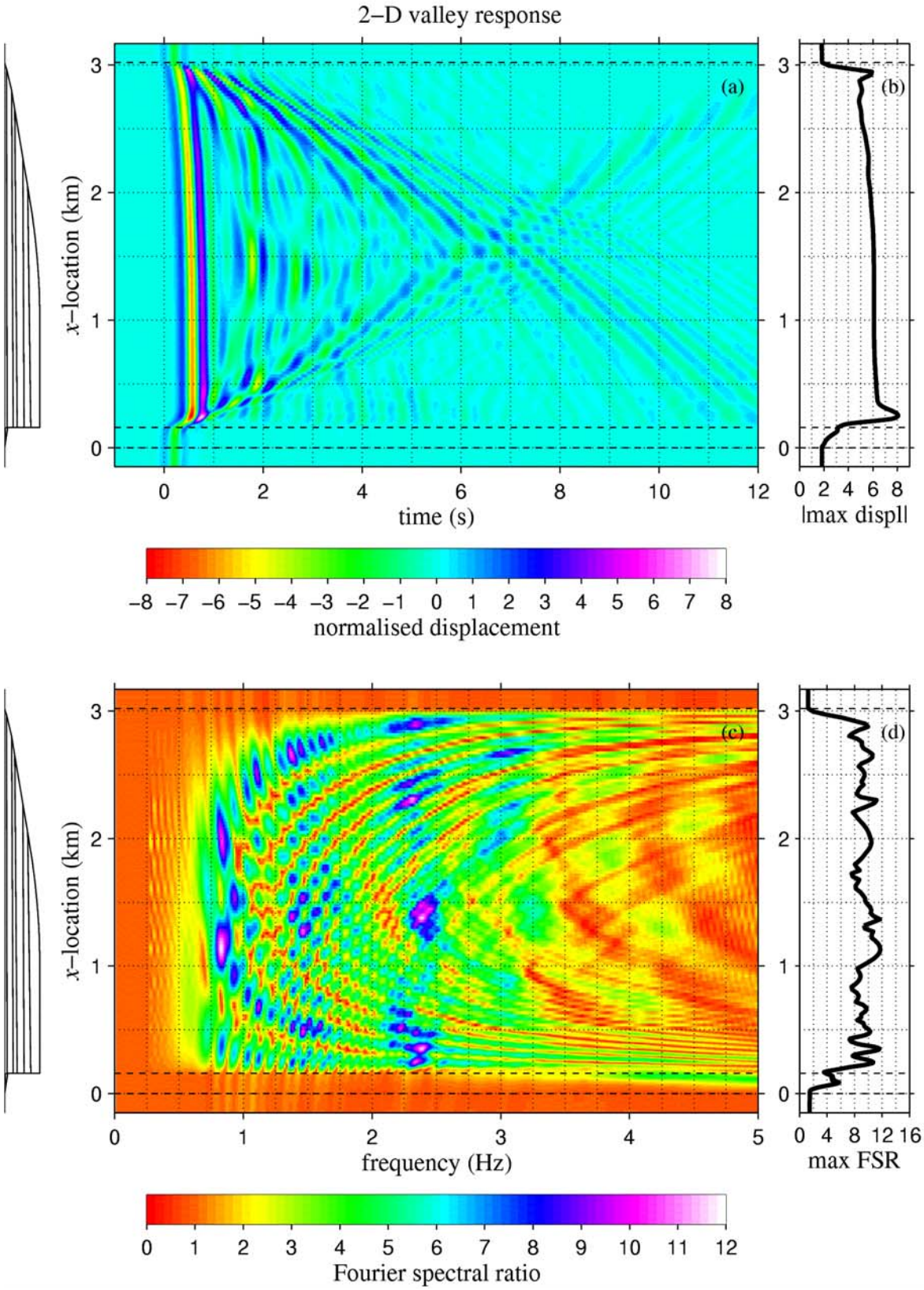

Figure 10.3. Results from the 2-D simulation T3 (f_c = 2.0Hz, θ_c = 0°) for comparison with the preliminary results in Chapter Eight. Axes (a) shows transient surface displacement. Axes (c) shows soil to rock Fourier spectral ratio. Peak displacement and FSR are shown on the narrow axes (b) and (d).

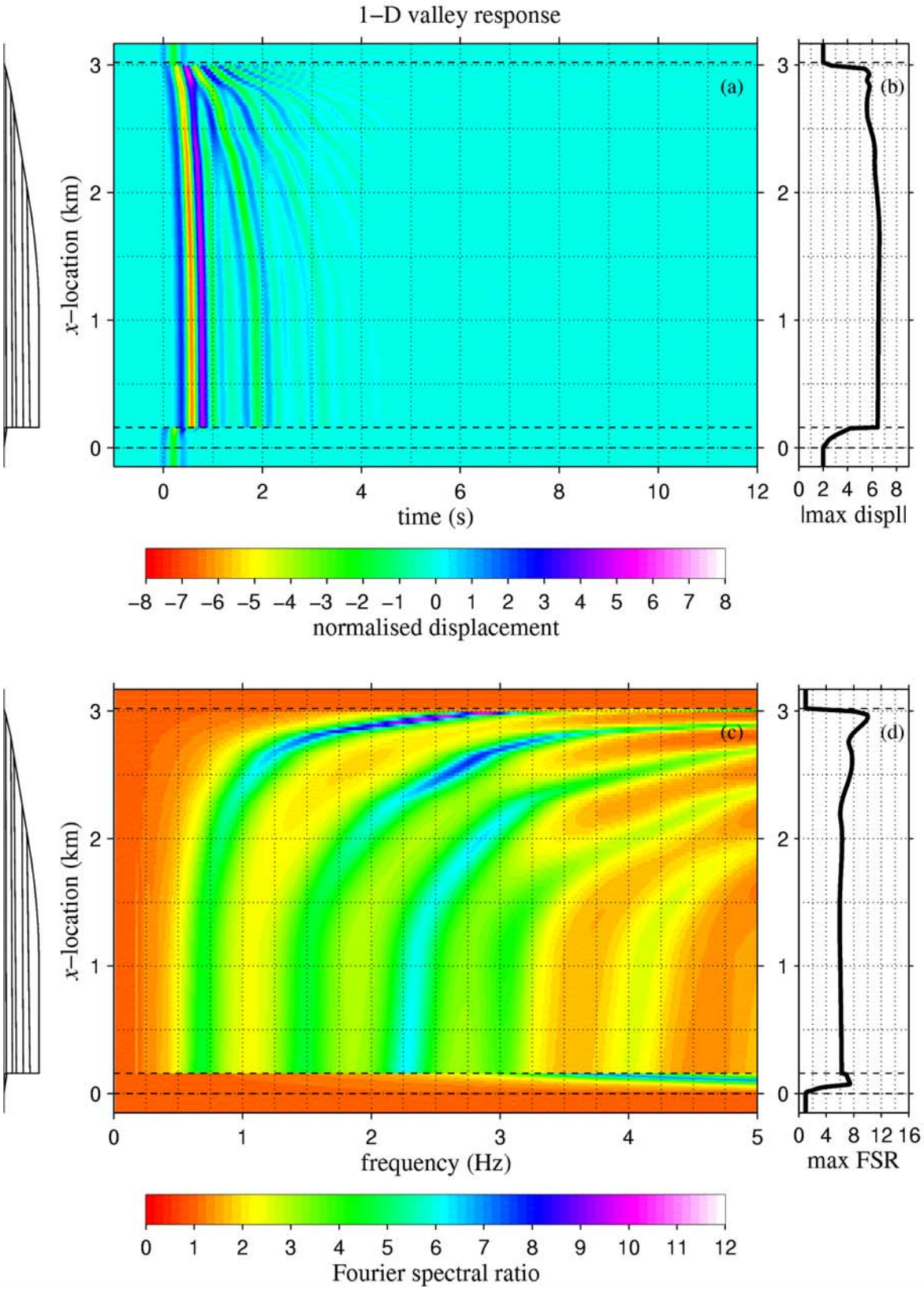

Figure 10.4. Results from the 1-D simulation O1 (f_c = 2.0Hz). Axes (a) shows transient surface displacement. Axes (c) shows soil to rock Fourier spectral ratio. Peak displacement and FSR are shown on the narrow axes (b) and (d).

identified. At the same time amplification associated with to 1st, 2nd and 3rd higher vertical modes are superimposed atop the fundamental at higher frequencies. Zones of strong FSR are the result of a complex interaction between these various resonant modes.

Comparison to a One-Dimensional Analysis

Figure 10.4 presents the 1-D analysis equivalent of Figure 10.3. The absence of surface waves leads to a much shorter duration of shaking. Peaks in displacement at each edge of the valley are also missing. Vertical resonant frequencies are continuous and smooth across the width of the valley, in contrast to the 2-D result which essentially contains the 1-D pattern superimposed with a strong pattern of horizontal resonance. Spectral amplification is correspondingly much higher in the 2-D and the pattern of amplification is significantly more spatially variable.

10.2.2 EDGE RESPONSE

Figure 10.5 presents surface displacement and spectral ratio detail from the edge of the plot shown in Figure 10.3. Shaded contours represent the amplitude of both displacement and FSR. Line plots on the right-hand axes compare peak displacement and FSR from the 2-D analysis (solid lines) to that from the 1-D analysis (dashed lines). Constructive interference between horizontally propagating pulses and the first arrival of the Ricker pulse at the surface generates amplified pulses in the displacement trace between x = 220-330m (peak at x = 250m), a feature not shown in the 1-D analysis. The horizontal phase velocity of the pulses in question is approximately 260-300m/s.

The highest Fourier spectral ratios at the edge of the valley (at x = 250m and x = 350m) are a result of superposition between the 1st and 2nd extremum lines of the fundamental resonant set, and the onset of the 3rd vertical mode. Both peaks correspond to positions of constructive interference between base-refracted pules and the edge-generated Love wave. Spectral amplification is very much a function of across-valley position and may vary as much as a factor of 10 in the space of 80 metres.

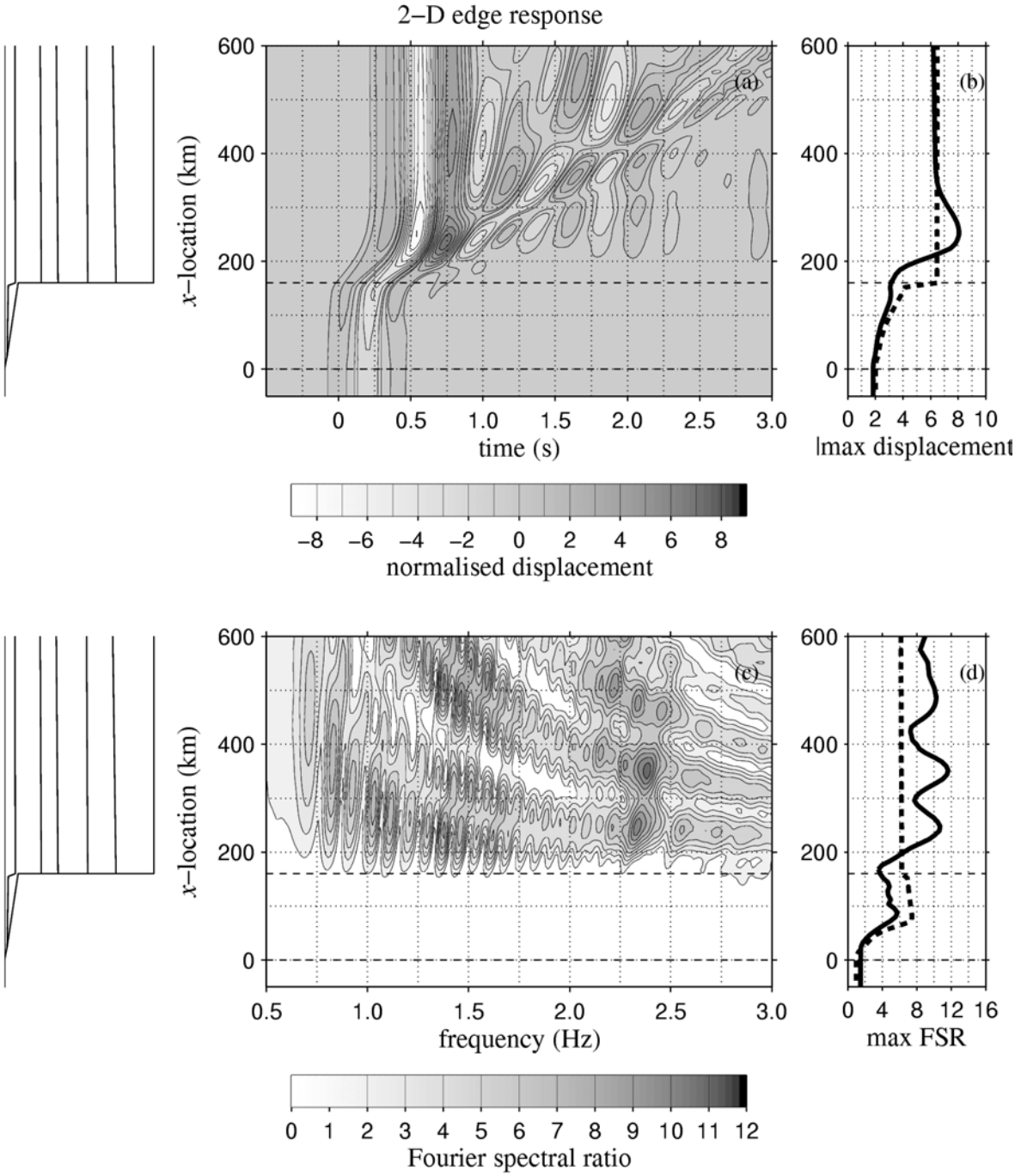

Figure 10.5. Expanded edge results from simulation T3 (f_c = 2.0Hz, θ_c = 0°). Axes (a) shows transient surface displacement. Axes (c) shows soil to rock Fourier spectral ratios. Peak displacement and FSR (solid lines) are compared with the 1-D result (dashed lines) on axes (b) and (d).

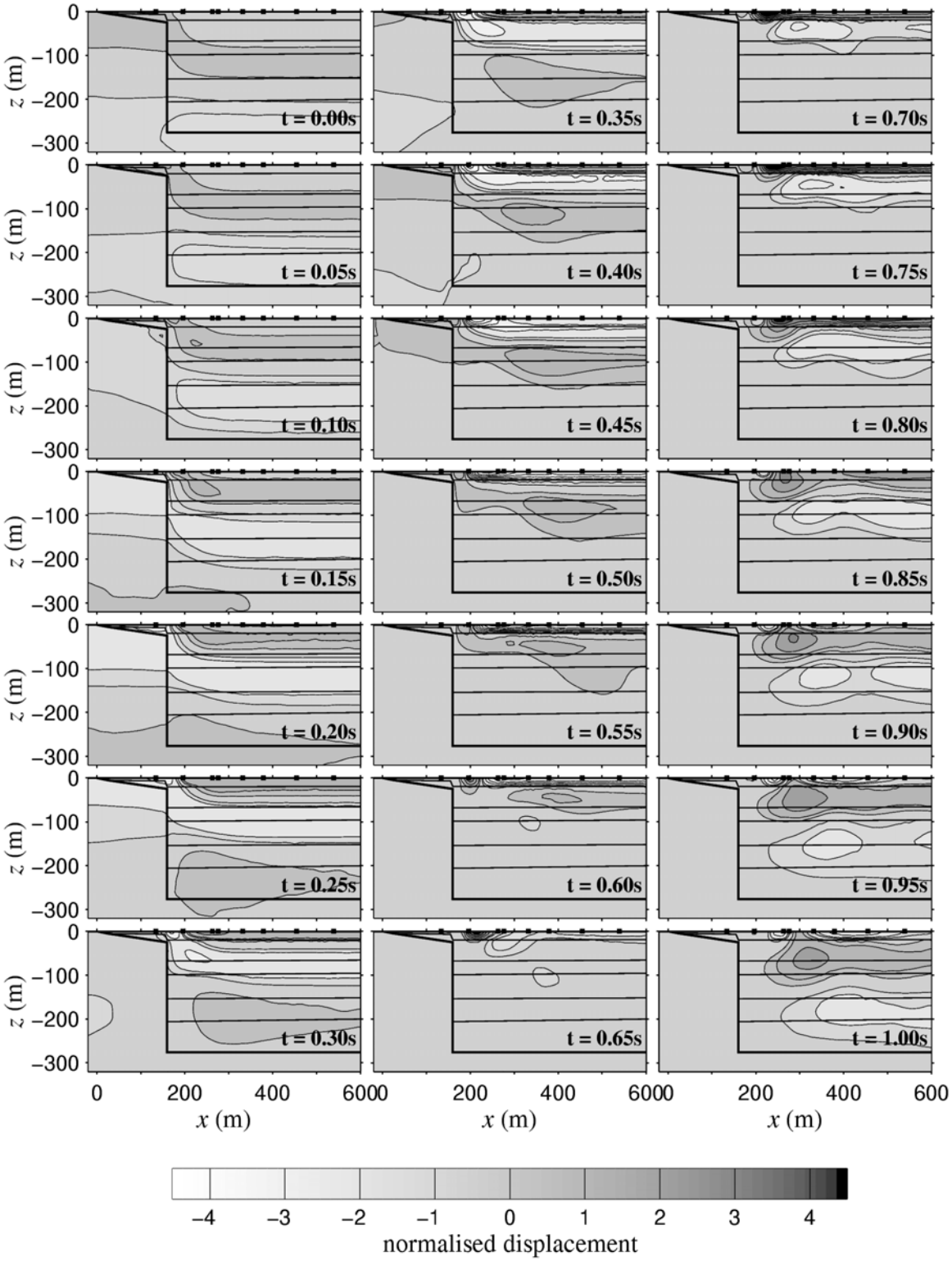

Figure 10.6. Consecutive frames of displacement in the *x*-*z* plane at the valley edge. Time *t* = 0 occurs when the first peak of the Ricker wavelet reaches the surface through the rock, and corresponds with the timing in Figure 10.5.

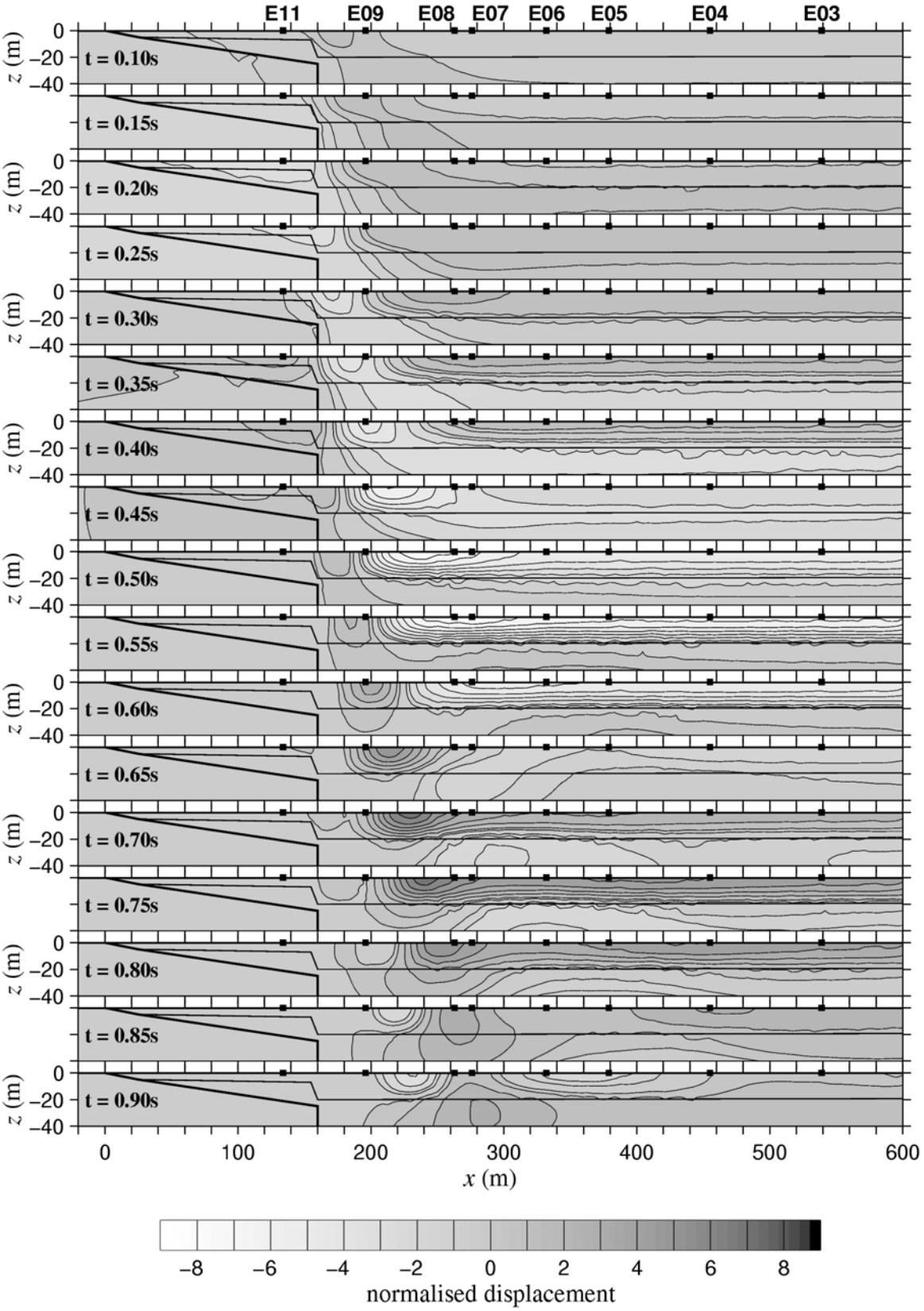

Figure 10.7. An expanded view of the top 40m of the frames in Figure 10.6. The location of the seismograph stations in Chapter Nine are also shown.

Pulse Propagation within the Cross-Section

Figure 10.6 presents consecutive frames of displacement showing the propagation of the 2.0Hz Ricker pulse past the deep vertical edge of the valley. As in previous modelling, the time coordinate is set to zero when the 1st peak of the Ricker pulse reaches the surface at the edge of the sediments, followed a short while later by the 2nd and 3rd peaks. The wavefront refracted into the sediments from the base is seen to decelerate as the shear-wave velocity increases. Weak points of constructive interference develop between the edge-refracted and base-refracted pulses once the latter reaches layer C (2nd from surface). The interferences then travel up toward the surface and merge with horizontally propagating pulses.

Frames in Figure 10.7 show expanded detail of the propagation through near surface Holocene sediments. The bulk of the surface wave energy appears to travel within the top (Holocene) layer and the next layer down (Waiwhetu gravels). Horizontally propagating pulses do not properly form at the shallow edge of the valley ($x = 0$), but rather above the deep vertical edge (at $x = 160$m). The bulk of the Love wave amplitude travels within the Holocene layer and meets the vertical arrival to generate peak displacement at $x = 250$m. This process occurs three times, once for each peak of the Ricker pulse. While the geometry of the problem in this example is significantly more complex than the simple layer edge in Chapter Six, the same basic mechanism of constructive interference is still apparent.

10.3 THE EFFECT OF INPUT FREQUENCY

Results are presented from tests T1-T3 for input Ricker wavelets of different characteristic frequencies ($f_c = 2.0$Hz, $f_c = 1.0$Hz and $f_c = 0.5$Hz). The angle of incidence is vertical in each simulation. The response of both the whole valley and just the edge are analysed in turn.

10.3.1 WHOLE VALLEY RESPONSE

Figure 10.8 shows colour plots of surface displacement and FSR across the whole valley for each of the three input frequencies. The result for $f_c = 2.0$Hz is as discussed in Section 10.2. The dominant group and phase velocities of the Love waves generated at each edge are listed in Table 10.5. When $f_c = 1.0$Hz both Love waves travel with similar or slightly

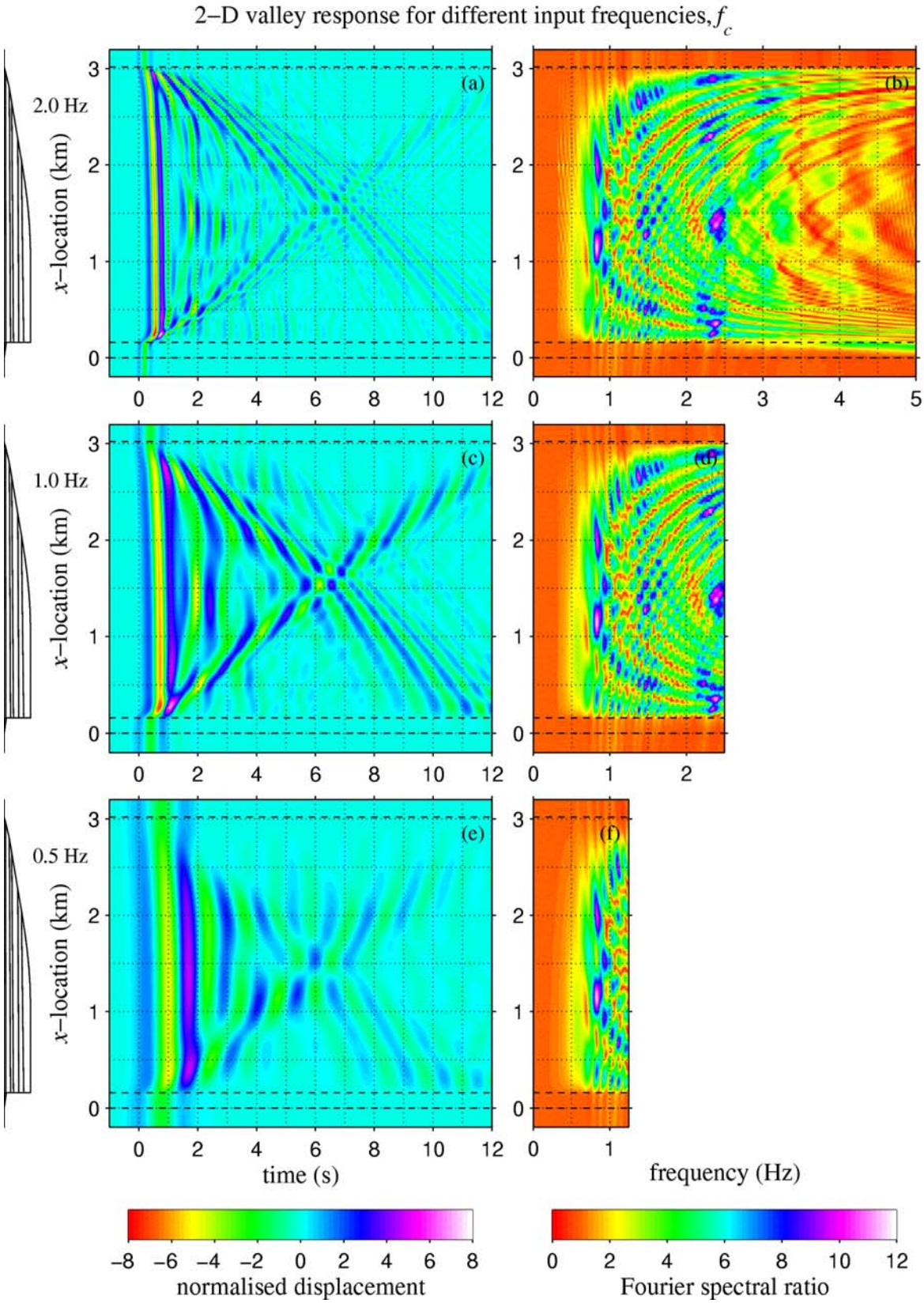

Figure 10.8. Transient surface displacement and FSR results across the full width of the valley for tests T3 (f_c = 2.0Hz), T2 (f_c = 1.0Hz) and T1 (f_c = 0.5Hz). The angle of incidence is vertical. FSR results are truncated at 2.5f_c.

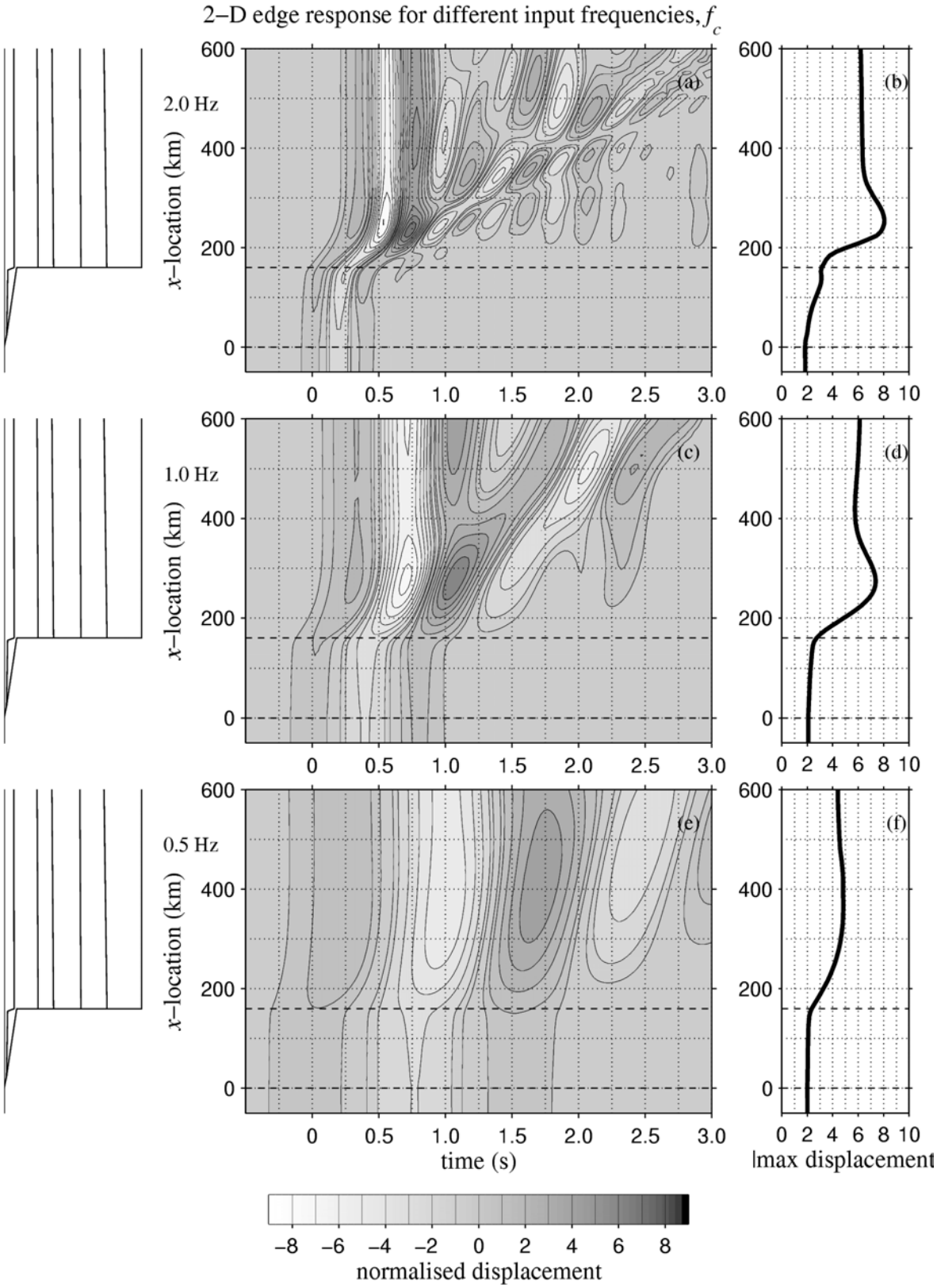

Figure 10.9. Transient surface displacement at the valley edge for tests T3 (f_c = 2.0Hz), T2 (f_c = 1.0Hz) and T1 (f_c = 0.5Hz). The angle of incidence is vertical.

higher phase and group velocities than for the higher frequency input. An input frequency of f_c = 0.5Hz, however, generates Love waves with significantly higher phase velocity and that have less effect at the edge.

Table 10.5. A comparison of predominant group and phase velocities measured from Figure 10.8 for different input frequencies.

f_c (Hz)	θ_i°	Test	U_{LHS} (m/s)	c_{LHS} (m/s)	U_{RHS} (m/s)	c_{RHS} (m/s)
0.50	0°	T1	240	580	250	660
1.00	0°	T2	230	430	230	430
2.00	0°	T3	230	420	215	370

Love waves leaving the fault-bounded edge have similar velocities to those from the sloping southeastern edge of the valley. Velocities are therefore apparently not controlled by the edge shape, by the layer properties. In the low frequency case, however, Love waves from the southeastern edge are noticeably higher than those from the fault-bounded edge due to more energy travelling within the shallow basement rock.

Fourier spectral ratios are exactly the same no matter the input frequency. Pulses with lower characteristic frequencies, however contain a narrower range of frequency components which can be studied.

10.3.2 EDGE RESPONSE

Figure 10.9 presents contour plots of transient surface displacement at the edge for the three different input frequencies. Table 10.6 lists the positions and value of the edge amplification. While not as strong as for the f_c = 2.0Hz input, the f_c = 1.0Hz Ricker pulse generates constructive interference between the vertical arrival and a horizontally-travelling phase moving at 360-400m/s, again lower than the dominant phase velocity of the Love wave. The f_c = 0.5Hz input produces only weak amplification at the edge and at a much greater distance.

Table 10.6. Positions of amplification by constructive interference and resultant values of peak displacement (normalised against the peak of the input).

f_c (Hz)	Test	x^c (m)	Peak displacement
0.50	T1	370	4.9
1.00	T2	270	7.1
2.00	T3	250	8.0

The distance to the point of constructive interference, x^c, increases in an apparently exponential fashion as the input frequency decreases. This can be explained with consideration of the results from FEM modelling in Part II. Input frequencies significantly lower than the fundamental of the layer tend to produce only weak amplification at a distance, while higher frequencies produce a sharp point of interference closer to the edge. An input frequency of 0.5Hz is less than the fundamental frequency of the basin (Table 10.3) and it is likely that most of the Love wave energy travels in deeper sediments or even the basement. The 2.0Hz input, on the other hand, is equivalent to three times the fundamental from which we would thus expect a sharp peak.

10.4 THE EFFECT OF ANGLE OF INCIDENCE

Results are presented for tests T4-T6 for 2.0Hz Ricker wavelets input at different angles of incidence ($\theta_i = 60°$, $\theta_i = 30°$ and $\theta_i = –45°$). The response of both the whole valley and just the edge are analysed in turn.

10.4.1 WHOLE VALLEY RESPONSE

Figure 10.10 shows colour plots of surface displacement and FSR across the whole valley for each angle of incidence. Table 10.7 lists the dominant group and phase velocity of the Love wave measured from the displacement plots in Figure 10.10. Velocities appear to remain similar no matter the angle of incidence.

A negative angle of incidence ($\theta_i = –45°$) is equivalent to seismic input from the southeast side of the valley, from a location perhaps beneath the southern Rimutaka ranges. The direct arrival reaches the rock on the right-hand side of the valley first, and approximately 1.5 seconds later the rock on the left-hand side. A strong surface wave is generated at the

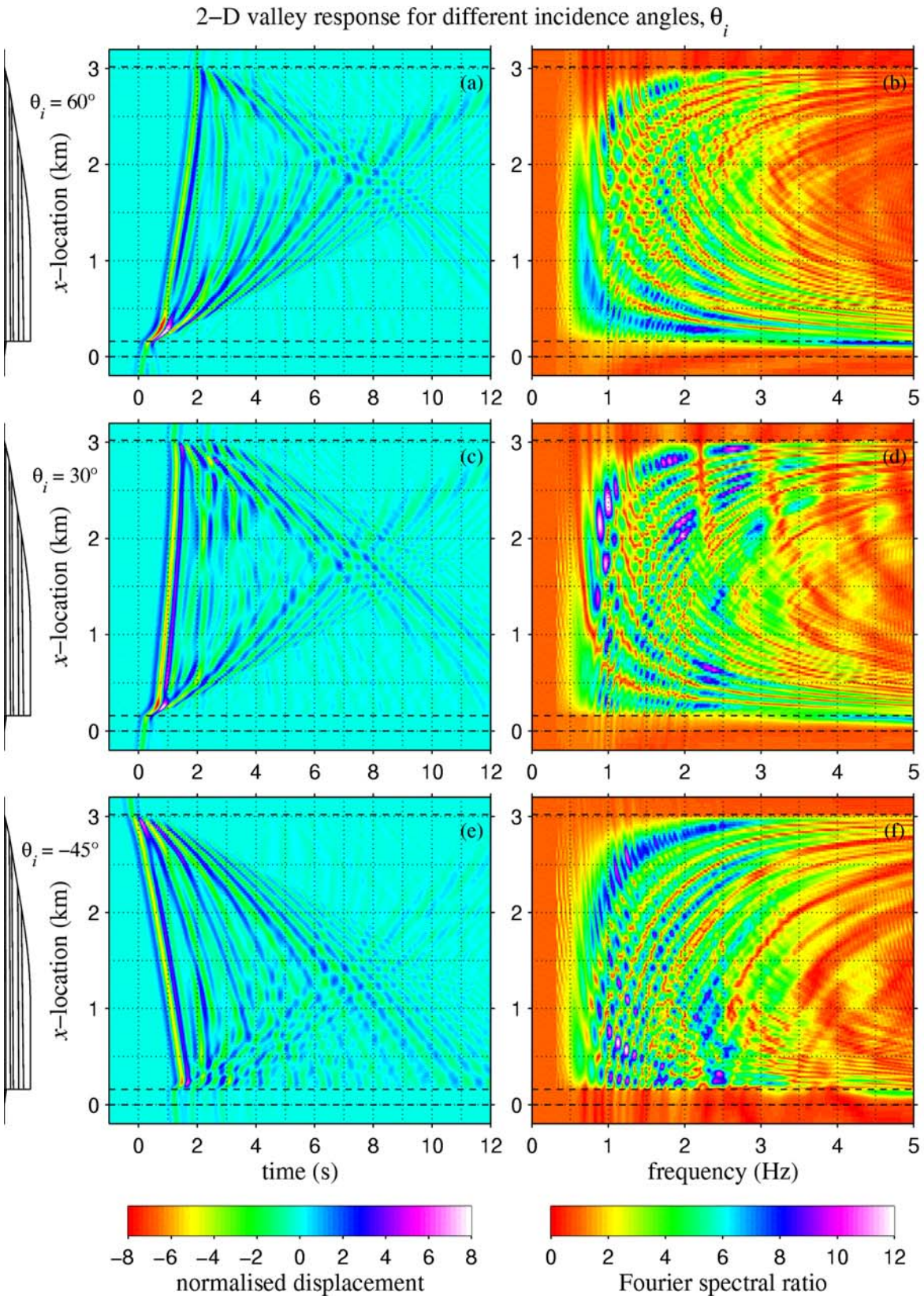

Figure 10.10. Transient surface displacement and FSR results across the full width of the valley for tests T4 (θ_c = 60°), T5 (θ_c = 30°) and T6 (θ_c = –45°) for an input frequency of 2.0Hz.

right-hand edge as the direct arrival is meets the sediments. The left-hand edge, on the other hand, is located in a shadow zone created by the deep basin-edge. It receives a de-focussed low-amplitude direct arrival and weak Love waves are instead generated by the total reflection of base-refractions at the edge, similar to the mechanism shown in Figure 5.3. As the initiation of the Love wave from the left is spread over several cycles of vertical reflection within the layer, it is difficult to define a dominant velocity.

Table 10.7. A comparison of dominant group and phase velocities measured from Figure 10.10 for different input frequencies.

f_c (Hz)	$\theta_i°$	Test	U_{LHS} (m/s)	c_{LHS} (m/s)	U_{RHS} (m/s)	c_{RHS} (m/s)
2.00	60°	T4	230	470	200	400
2.00	30°	T5	230	420	200	360
2.00	0°	T3	230	420	215	370
2.00	-45°	T6	-	-	230	410

Positive angles of incidence ($\theta_i = 60°$ and $\theta_i = 30°$) equate to a seismic input from the northwest, towards Porirua. The left-hand edge of the model is neither deep nor steep enough to generate a shadow zone, and strong Love waves are thus generated from both sides of the valley. Those from the left-hand side (nearest the input) are slightly stronger than those from the right.

In the frequency domain, the spatial location, frequency and relative amplification of resonant peaks shifts small amounts with the angle of incidence. Extremum lines associated with the Love wave generated from the closest edge dominate the pattern and spectral amplification is generally higher on the side of the valley opposite to that from which the wave propagates. FSR appears to be generally higher for angles of incidence closer to vertical.

10.4.2 EDGE RESPONSE

Figure 10.11 presents contour plots of transient surface displacement at the edge. Table 10.8 lists the positions and magnitude of the amplification caused by constructive interference. The magnitude increases as the angle of incidence increases from negative (SE) to positive (NW), as does the distance, x_c, and the width of amplification.

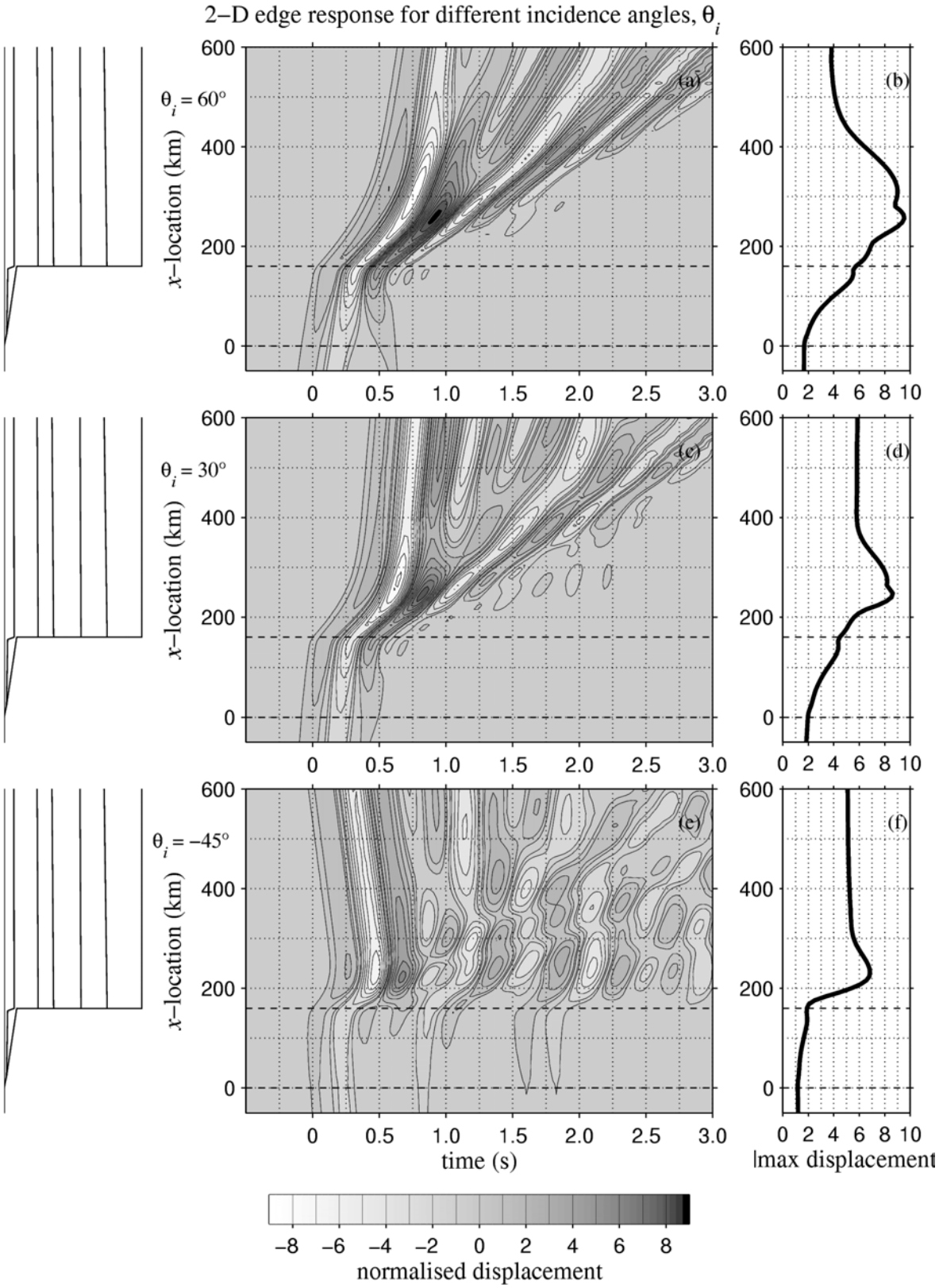

Figure 10.11. Transient surface displacement at the valley edge for tests T4 (θ_c = 60°), T5 (θ_c = 30°) and T6 (θ_c = –45°) with an input frequency of 2.0Hz.

Table 10.8. Positions of amplification by constructive interference and resultant values of peak displacement (normalised against the peak of the input).

$\theta_i°$	Test	x^c (m)	Peak displacement
60°	T4	260	9.5
30°	T5	250	8.7
0°	T3	250	8.0
-45°	T6	230	6.8

In most cases, it appears that the phase velocity of the edge-refracted peaks decreases with time (the 1st travels faster than the 2nd which is faster than the 3rd), such that the distance out to the point of constructive interference also decreases. The double peak in the maximum displacement plots for $\theta_i = 60°$ and $\theta_i = 30°$ is associated with two different occurrences of constructive interference. The first is related to the vertical arrival and horizontal pulse generated by the central (–ve) peak of the Ricker wavelet and takes place the furthest into the basin. The closer, narrower and more highly amplified peak is associated with the third (+ve) peak of the Ricker pulse and a Love wave pulse of higher phase velocity. This latter peak may also be related to vertical reflection of the Ricker pulse within the near-surface sediments.

10.5 Comparison between Observations and Modelling

A comparison of both Fourier spectral ratios and peak displacement is made between data observed across the array in Chapter Nine and results of FEM modelling in this chapter.

10.5.1 Fourier Spectral Ratios

Figure 10.12 shows a comparison of Fourier spectral ratios at the location of each recorder station over the range 0-5Hz. Thin grey lines show FSR calculated from the EP ground motion data from each of the 13 events, and the thick grey line represents the mean value. Observed FSR has been smoothed with a 0.1Hz moving triangular window. Black lines show FEM modelling results for four different angles of incidence.

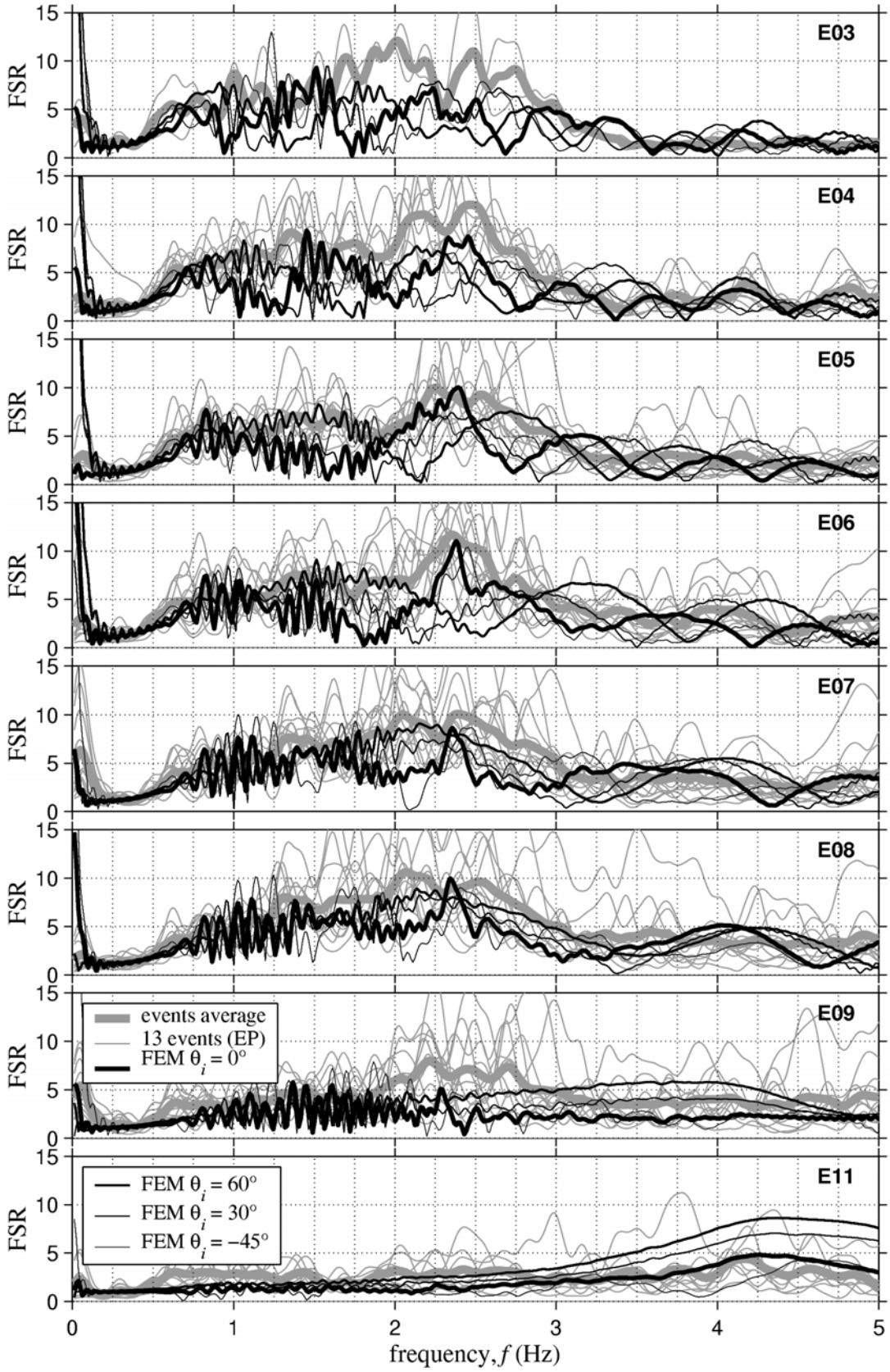

Figure 10.12. Soil to rock Fourier spectral ratios at each of the array recorder stations. A comparison between observed edge-parallel weak ground motions and the FEM results for various angles of incidence. The positions of each station were given in Table 9.1.

Both modelling and observations show, on average, strongly amplified ground motion between 0.5 and 3.0Hz. At the same time, there is a huge variation in FSR between the 13 recorded events, perhaps partly explained by the equally huge variation in FSR from modelling results for different angles of incidence. While there is obvious correlation between stations, significant spatial variation also exists across the short length of the array.

In Figure 10.13, an average FSR calculated from FEM modelling data over a width of the valley containing stations E08-E03 (x = 250-550m) is compared with recorded FSR averaged over stations E08-E03. In this way, the strong spatial variability seen in Figure 11.1 is averaged out of both the recorded and modelled data. Maximum values of FSR over the same range are also plotted with thinner lines. The average 2-D FSR (thick black line) is almost as low as the 1-D result (dashed line), due to averaging over peaks and troughs of the 2-D. A more realistic picture of the 2-D FEM modelling is thus given by the maximum FSR in the range x = 250-550m (thin black line). This maximum compares well with the general amplitude and shape of the recorded FSR.

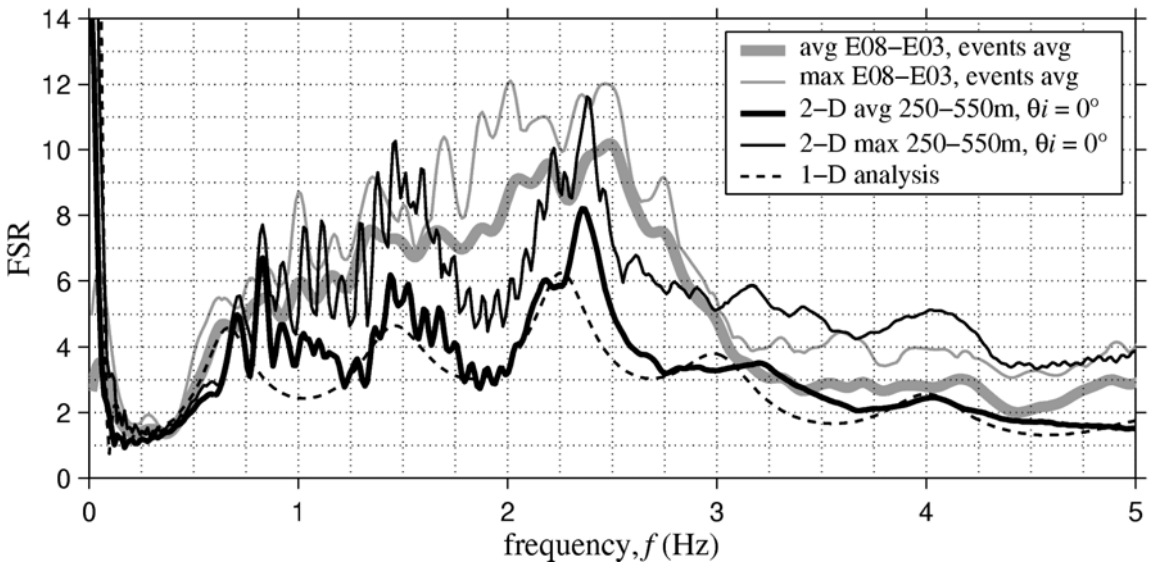

Figure 10.13. Soil to rock Fourier spectral ratios averaged over the positions of stations E08-E03 (x = 250-550m). Recorded data is compared with both 1-D and 2-D models.

Peak amplitudes occur in the range 2.0-2.5Hz. In the FEM analysis the peak is fairly narrow and distinct from the 1st and 2nd mode resonances, whereas the amplification in the

recorded data is more broad-band and the 1st and 2nd vertical modes are not well defined. On average, FSR calculated from the modelling result is slightly lower than recorded on the array, yet peak values are of a similar magnitude, as shown in Figure 10.14.

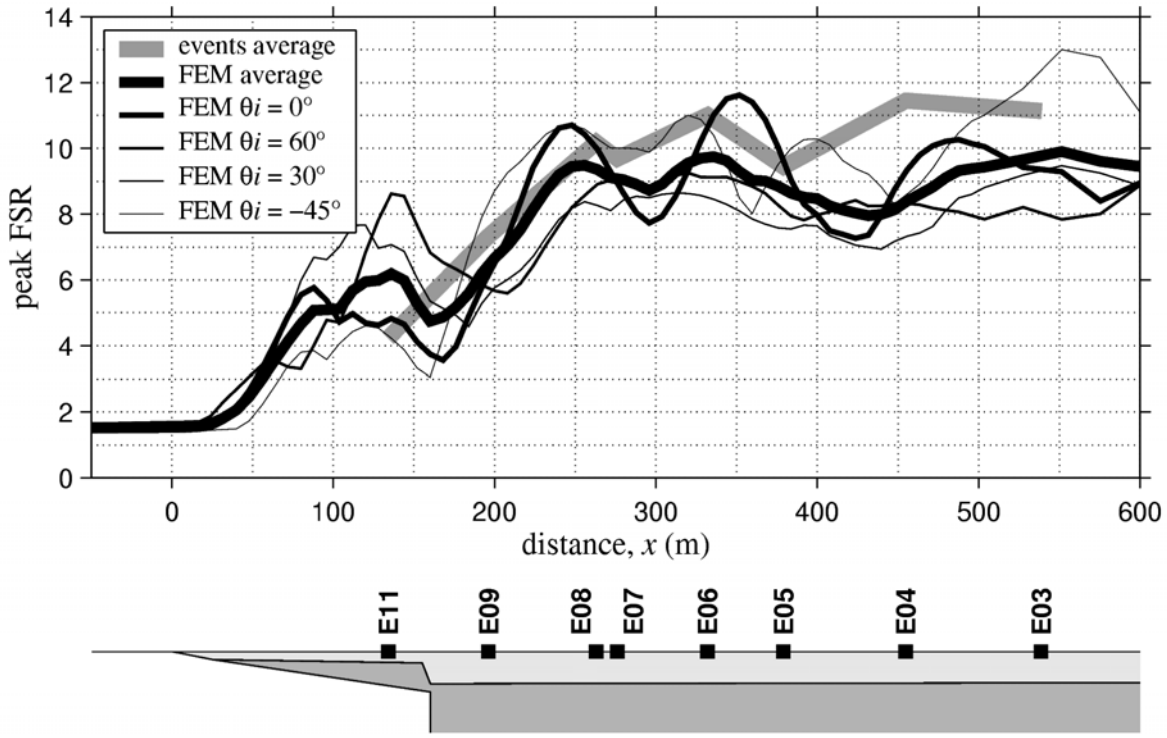

Figure 10.14. Peak FSR (in the range 0-5Hz) vs distance across the array. FEM 2-D data (black lines) compares well with the recorded data (thick grey line).

10.5.2 PEAK DISPLACEMENTS

Figure 10.15 shows the variation in peak displacement across the width of the array. Results from the 2-D FEM modelling have been plotted for all four angles of incidence, while peak displacements from each of the recorded events is also plotted. The general amplitude of average peak displacement is similar, yet the distinct peak in the modelling at $x = 250$m is not apparent in the recorded motions. Array data also shows a much wider range of peak displacement than does the modelling for different angles of incidence. Both these observations are, however, not surprising result considering the variety of input motion in the real ground motions.

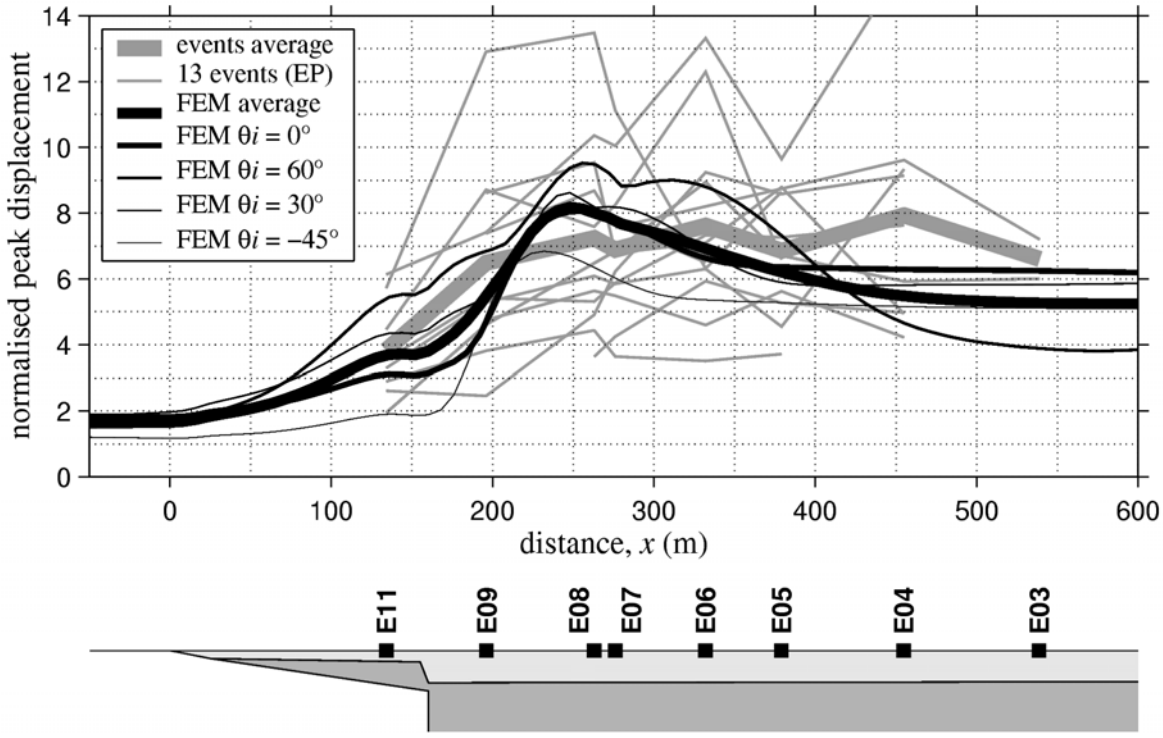

Figure 10.15. Peak ground displacement vs distance. 2-D modelling results are shown with black lines while recorded data is shown with grey lines.

10.6 Critique on the 2-D Elastic Analysis of SH Ricker Wave Propagation

The simplified nature of the FEM modelling means consideration must be given to its validity for use in real geological situations. In particular, a 2-D analysis has been used to model a 3-D geometry. Both the weak-motion analysis and the modelling assume an elastic response of the geological materials, while the modelling considers only a pulse-like anti-plane (SH) particle motion incident as a plane wavefront.

10.6.1 Multi-Dimensional Considerations

The use of 2-D rather than 1-D modelling has shown beyond doubt the significance of 2-D effects in magnifying and changing the form of the basin response. It is crucial then that we have some idea of how good our 2-D approximation is at modelling the real 3-D situation in the Hutt Valley. The geometry of the valley is essentially a triangular wedge of sediments extending 10km southwest from Taita Gorge, to reach a maximum width of 4.5km and depth of 300m at the Petone shoreline. The two sides of the wedge diverge at an

angle of approximately 21°, while the rock basement surface has a down-valley dip of approximately 1.5°. Similarly deep sediments extend out into Port Nicholson below the sea level, before terminating gradually near Wellington and the harbour entrance as basement rock rises to the surface.

The western side of the valley is relatively straight, following the vertical edge of the Wellington Fault. Several streams (such as Korokoro, Speedys and others) have incised into the surrounding hills triangular-shaped valleys draining into the Hutt Valley and forming small in-filled 'nicks' in the otherwise straight valley side. The eastern side of the valley forms a much more ragged edge as sediments have been deposited along the contour of the hill. One major irregularity on the eastern side is the Naenae basin, which widens the valley locally from 2.0 to 3.5km near the northern end. These irregular eastern hills also indicate that the base of the sediment wedge is likely to also have an irregular surface in the long-valley direction.

Although the valley does not extend in a perfect prismatic and cylindrical shape with constant cross-section to infinity in either direction, it is significantly longer than wide. In fact our cross-sections of width 3-4km and depth 0.3km are modelling a sediment wedge approximately 18km long, with deep sediments extending out into the Wellington Harbour. Marsh (1992) suggests that because 2-D effects become insignificant in the central regions of a cross-section for which the width is greater than 16 times the depth, it should be adequate to disregard 3-D effects when the out-of-plane distance to the basin edge is greater than 8 times the depth. For our 300m deep cross-section this would equate to only 2.4km, while there exists at least 8km in each direction.

Horizontal resonance and edge effects are both directly linked to the presence and amplitude of surface waves. Multi-dimensional behaviour will not occur at a site sufficiently distant from the basin edge, where the edge-generated surface waves have decayed to some insignificant amplitude. On the same note, true horizontal resonance can only occur when the sediment is constrained by bedrock in both directions, although surface waves propagating away from an edge have been shown in Part II to exhibit their own standing pattern of amplification. The open-ended nature of the Lower Hutt valley makes the presence of confined horizontal resonance in the longitudinal direction unlikely, yet surface waves propagating down-valley and creating additional amplification are a distinct possibility.

The open-ended nature of the Lower Hutt valley makes the presence of horizontal resonance in the longitudinal direction unlikely, although edge effects in this direction are a distinct possibility. The northern 4-5km of the valley and the Naenae sub-basin are very likely to exhibit a 3-D response due to the highly enclosed and irregular nature of their geometry; in addition to strong soft-soil effects in the Naenae swamp sediments (Dellow et. al., 1992). At the lower end of the valley, the 5km-long section from Avalon to Petone is quite open-ended in both directions, and likely to be dominated by 2-D cross-valley behaviour. Even the lower end of the valley is, however, expected to be influenced to some extent by surface waves propagating down-valley that were not able to be modelled with the 2-D method. In addition, irregularities along the eastern margin appear to have the potential to create localised out-of-plane edge waves that cannot be accounted for in the 2-D model.

Rupture propagation and energy radiation effects are also likely to be significant in the event of a Wellington Fault rupture, yet are unaccounted for by the 2-D model. Kawase et. al. (2000) shows that the distribution of peak ground motions even within the damage belt in Kobe is likely to have been variable in the third dimension due to both near source effects and changes to the basin-edge structure along its length. This is also likely to be the case in the Lower Hutt, yet for microzoning and engineering considerations the variation is likely to be insignificant.

10.6.2 NON-LINEAR AND INELASTIC SOIL BEHAVIOUR

Soft flexible basin sediments are expected to lose stiffness and behave in a non-linear manner during strong seismic excitation. Non-linear behaviour tends to increase the damping and reduce the shear modulus and shear-wave velocity, thus decreasing the natural frequencies of a basin. A reduction in the maximum displacements, velocities and accelerations and an increase in the duration of strong motion are also expected. Testing of soft cohesionless sands and gravels has shown that material damping increases dramatically above cyclic shear strains of 10^{-2} to 10^{-3} %, indicating the onset of inelastic behaviour (Beresnev and Wen, 1996; Isibashi and Zhang, 1993; Seed et. al., 1986). Non-linearity generally becomes apparent above PGA's of 0.1 to 0.2g, above which permanent soil deformation should be expected (Beresnev and Wen, 1996).

In this study we have used the computationally efficient linear method of analysis, assuming elastic behaviour of all modelled materials. In previous work, the author computed maximum shear strains of between 3×10^{-1} and 14×10^{-1} % on the surface of the section through Lower Hutt Central, under a Kobe (1995) type loading (Adams et. al., 1999). These suggest that the soft cohesionless soils would definitely exhibit highly non-linear behaviour during a major earthquake. There is, however, substantial evidence that results from an elastic analysis can be quite accurate at determining the spatial distribution, resonant frequencies and Fourier spectral ratios of amplification and to a lesser extent the form of the expected seismogram.

Larkin and Marsh (1991) and Marsh (1992) with their 2-D finite-difference modelling, compared linear and non-linear solutions, concluding that non-linear effects on basin response were important for large-magnitude earthquakes. At shear strains of 0.31%, non-linearity had the effect of stretching the duration of intense shaking by a factor of 2, while reducing the peak ground acceleration by a factor of 1.5 and reducing the acceleration response spectra by a factor of 2. A surprising result was the similarity of both amplitude and frequency in the Fourier spectra of the two analyses.

There is evidence (eg. King and Tucker, 1984; Borcherdt et. al., 1989) that linear results from elastic modelling or weak-motion recordings may be used successfully to predict both the amplified frequencies and to a lesser extent the amplitude of spectral ratio peaks for strong motion shaking up to at least 0.1 or 0.2g. Taber et. al. (1993) compare spectra from strong ground motion (0.05-0.1g) with weak ground motion recorded in the Lower Hutt and finds little evidence of non-linear behaviour. For higher PGA, Lermo and Chavez-Garcia (1994) conclude from studies in Oaxaca, Acapulco and Mexico City that micro-tremors can be used successfully to estimate at least the fundamental frequency of a site in the range 0.3 to 5.0 Hz. Weak motions have also been used to successfully predict zones of strong shaking in San Francisco during the Loma Prieta earthquake (Borcherdt and Glassmoyer, 1992), suggesting that the spatial variability of shaking observed in our elastic models will hold approximately during a major event.

In the Lower Hutt, the top 20-30m of soft Holocene sediments will develop the most significant non-linear behaviour. It would be expected that the amplification resulting from resonance within this top layer would decrease. So might the tendency for surface waves to travel within the Holocene sediments. Faster horizontal propagation velocities and lower-

frequency surface waves in deeper layers may predominate. It is likely that the lower-frequency whole-basin resonance modes may become more significant than in the elastic modelling and weak motion data. Results from our elastic analyses are, however, likely to be on the conservative side of reality in terms of peak response. Non-linear effects will probably lead to lower peak ground motions. The spectral ratios may be reasonably accurate, while the real duration of shaking is likely to be much longer than predicted.

10.6.3 INPUT MOTIONS

Simulations presented in this thesis are based on input motions in the form of a plane wavefront propagating up from below, with particle motion entirely in the anti-plane direction. This has been used both for simplicity and because the interest is in basin-structure effects rather than source effects. While a plane upward-travelling wavefront is perhaps a fair approximation of a wavefront that originates some distance from the site, it is not a realistic input motion for a near-field event such as a major rupture on the Wellington Fault.

A two-dimensional simulation cannot model the effects of rupture propagation or forward directivity which were shown to contribute to strong shaking in the 1995 Hyogo-ken Nanbu (Kobe) Earthquake (Pitarka et. al., 1998). Nor can it model the likely patterns of radiation that are emitted from a shear rupture. Limiting the analysis to SH motion means that the effects of in-plane particle motion and the generation of Rayleigh waves and subsequent in-plane basin-edge effects are also not considered.

The use of a Ricker wavelet (see Section 3.2.4) has proved to be very useful in the estimation of spectral amplification. A nice feature of using a simple pulse-type input is the ability to easily predict its appearance and arrival times at the surface for undispersed wavefronts, yet its shape in the time domain is not very representative of real ground motions, while the form of the input has been shown in Part II to be an important factor in amplification by basin-edge effects.

10.7 SUMMARY

Two-dimensional modelling of the Lower Hutt valley has identified several important features of seismic response. Love waves are shown to be generated from both sides of the

valley over a whole range of likely angles of incidence and input frequencies. A two-dimensional pattern of resonance develops across the width of the valley and amplification by constructive interference occurs at the fault-bounded edge.

A two-dimensional peaked spectral pattern develops across the width of the basin for all of the seismic inputs. The pattern probably develops by interference between the Love waves propagating from the edges, each with their own Love-wave edge pattern (Section 5.5.2). Spectral amplification is highly variable across the width of the valley. Zones of highest amplification are often associated with interference between the horizontal modes and the vertical resonant modes of the deep sediments.

Modelling of Ricker-pulse propagation shows the basin-edge effect to develop on the fault-bounded edge of the valley. A peak displacement in the order of 5-10 times the input is shown to occur at a distance $x = 220$-310 metres from the base of the hill (60-150m southeast of the fault trace). The zone of amplification may be up to 300 metres wide (ie. 0-300m from the fault trace). Peak ground displacement at the edge compares well in magnitude with that recorded on the array in Chapter Nine.

Fourier spectral ratios from recorded weak ground motions on the fault bounded edge show similar resonant frequencies to the modelling. Both recorded and modelled data show large spatial variability in spectral amplification. The FSR at any chosen position may also change significantly with changes to the angle of incidence.

In Section 10.6 a discussion was made of the limitations of using the weak motion data and the FEM modelling results to predict the seismic response of the Lower Hutt valley. It is expected that the two-dimensional nature of the modelling is a reasonable approximation in the lower end of the valley at least. Non-linear soil behaviour is expected to occur during damaging earthquakes and significantly alter the response of at least the Holocene sediments. The form of the input has been shown to have a major influence on the amplification of peak ground displacement. A sharp basin-edge effect occurs only for pulses of frequency 1Hz or greater.

PART IV

DISCUSSIONS AND CONCLUSIONS

Chapter 11: DISCUSSION ON THE NATURE OF BASIN-EDGE EFFECTS

All cases of anti-plane basin-edge effects noted in this thesis appear to be the result of constructive interference between various wavefields within the sediments. It is clear, however, that a distinction must be drawn between at least three types of basin-edge effects. The first we will continue to call the '*basin-edge effect*' after the name originally assigned by Kawase (1996) for amplification some distance from a steeply dipping basin edge. The second we will refer to as the '*wedge effect*', as it occurs above a shallow dipping edge. Finally, the third will be referred to as the '*Airy-phase edge effect*', which only occurs within a limited range of dimensionless frequency. Of these, it is the basin-edge effect that is of most interest and of primary concern in this discussion. We do, however, find occurrences of the wedge effect and the Airy-phase edge effect in the numerical modelling of both the semi-infinite layer and the Lower Hutt valley.

In Chapter Five, it was found that a discrete point of constructive interference may occur between refracted and undispersed wavefronts for certain combinations of edge slope and angle of incidence. The position of such interference may be exactly computed given a high-frequency input and simple plane-edge geometry. Finite-element modelling in Chapter Six, however, showed that the amplitude of interference between such undispersed wavefronts is insignificant compared to the constructive interference that develops between edge-generated dispersed wave fields and the delayed direct arrival.

In order to accurately predict the position of constructive interference it is necessary to understand the propagation characteristics of the edge-generated dispersed wavefields, and the subsequent set-up of a Love wave. An analytical development of such a problem has been beyond the scope of this thesis, yet we have attempted to make an overview and somewhat qualitative analysis of the problem through finite-element modelling of both the semi-infinite layer in Chapter Six and the fault-bounded edge to the Lower Hutt valley in Chapter Ten. Numerical modelling results are less than conclusive as to the exact nature of Love wave development at the edge, yet several useful generalisations can be made and will be discussed in this chapter. The aim of this discussion is to tie the ideas presented and

developed in Parts I, II and III into a more practical framework that may be useful to practitioners and researchers.

11.1 DEFINING THE MECHANISMS OF BASIN-EDGE EFFECTS

All three basin-edge effects that are defined above are essentially the products of some form of constructive interference. The basin-edge effect between independently propagating wavefronts, the Airy-phase edge effect between travelling and stationary resonance patterns and the wedge effect between various post-critically trapped rays.

11.1.1 THE BASIN-EDGE EFFECT

The basin-edge effect was initially defined by Kawase (1996) as an explanation for the belt of damage observed in Kobe; "… *amplification of ground motions 1 km away from the basin edge is caused by the coincidental interference of the primary S-wave with the basin-induced diffracted/surface waves which are generated at the basin edge and are radiated horizontally into the basin*." In its purest form, the basin-edge effect develops by constructive interference between two independently propagating wavefronts – one refracted up from the base and one generated at the edge – both originating from the same wavefront within the input signal. The constructive interference is discrete in both space and time and produces a well-defined local maximum in peak ground motion. Both the nature of the input signal and the geometry of the basin-edge have significant influence on the nature of this constructive interference and are the theme of discussion in Sections 11.2 and 11.3 of this Chapter.

11.1.2 THE AIRY-PHASE EDGE EFFECT

Amplification by the Airy-phase edge effect develops when the dominant frequency of the input signal is similar to the fundamental resonant frequency of the sedimentary column. Its mechanism of amplification is quite different to the basin-edge effect. Rather than being a discrete point of constructive interference, the Airy-phase edge effect is a coupling between surface waves travelling at the Airy phase and sub-critical resonance within the layer.

The Airy phase can be thought of as a form of post-critical travelling vertical resonance. Its nature is strongly dependent on the velocity contrast between the layer and the half-space.

As the velocity contrast increases, the Airy phase frequency trends towards the fundamental 1-D frequency of the layer, until we reach the Helmholtz case where the half-space is rigid and the two phenomenon are equivalent. The group velocity is now zero. As the velocity contrast increases, the Airy phase becomes much less prominent and the minimum group velocity tends towards the shear-wave velocity of the layer. It follows that the Airy-phase edge effect is also strongly dependent on the velocity contrast, being most noticeable in the modelling for high velocity contrasts.

Amplification by interference between the Airy phase of edge-generated surface waves and direct body waves is not a previously unknown phenomenon, having been proposed by Nagano (1998) and Niousha and Motosaka (1998) to have occurred in Kobe and Hanchinohe Cities, respectively. The FEM modelling in Chapter Six, however, suggests that for higher velocity contrasts the closeness of the Airy phase frequency to the fundamental frequency of the layer leads to a coupling between 1-D resonance and the Airy phase of the surface wave.

The width and position of the Airy-phase edge effect are controlled by interaction between the 1-D resonant frequency and the system of spectral extremum lines in the Love-wave edge pattern. In the frequency domain a large peak exists in the spectral pattern in the approximate position where the first extremum line of the Love wave coincides with the fundamental frequency of the layer (eg. Figure 6.6). This roughly corresponds to the position of local maxima in peak ground motions (eg. Figure 6.3b) that are most amplified close to the edge and decay with distance from the edge out to 8-9 times the depth of the layer.

11.1.3 THE WEDGE EFFECT

The distinction between the ‘basin-edge effect’ and the ‘wedge effect’ is made on the basis of the influence of the lower vertex. The wedge effect may occur in a wedge of infinite depth with no lower vertex, whereas the basin-edge effect is dependent on sediments of finite depth, bounded by an edge that is distinct from the base. The wedge effect becomes more important the shallower the edge-slope angle, while the basin-edge effect is most important in deep basins with a steeply-dipping edge.

Within a wedge, amplification does not occur where two independent wavefronts cross paths. Rather it builds up over the course of time and distance as the laterally propagating wavefield within the wedge travels away from the vertex, increasing in strength until reaching a peak some distance from the vertex, before then decaying in amplitude. The laterally propagating wavefield develops as energy is refracted in from the lower edge to become post-critically trapped within the wedge, with a positive horizontal phase velocity (ie. moving away from the vertex). This mechanism can be seen occurring in the FEM modelling above the shallow dipping edge for $\psi = 15°$ in Figure 6.12. Displacement within the apex of the wedge quickly decays as all incoming energy is directed away from the vertex.

Modelling results for an edge-slope angle of 15° (Figure 6.9a) show that the local maxima in peak ground motion due to the wedge effect occurs a distance of $2H$ from the edge, in the approximate position where the depth of the wedge corresponds to a 1-D resonant frequency equivalent to the central frequency of the input. It also occurs during the arrival of the edge-refracted wavefront at the surface (marked with a sloping line). In addition, the wedge effect can be seen to cause a local maximum in peak ground displacement on the southeastern edge of the Lower Hutt in Figure 10.3. A similar local maximum also occurs in the 1-D result (Figure 10.4) yet it is not as amplified as the 2-D case.

The cause for the local maximum is related to the frequency dependent properties of total reflection on the base of the layer. Hudson (1963) shows that a Love wave will develop in the wedge when the edge-angle is small (presumably with respect to the critical angle). For larger angles it is likely that there will also be some form of poorly-constrained total internal reflection within the wedge which may show many of the dispersive characteristics of the Love wave. This suggests the local maximum is probably a result of some form of Airy-phase phenomenon associated with the post-critically trapped wave reaching the dominant frequency of the input signal. Amplification would then occur between this laterally propagating Love-type wave and the first arrival of the undispersed edge-refraction at the surface. The undispersed edge-refraction, however, is not an independent waveform in that it is subsequently post-critically trapped to become part of the horizontally propagating Love-type wavefield.

The analytical solution of Sánchez-Sesma and Velázquez (1987) is made with the Helmholtz approximation of a rigid base. The time-domain results presented in their paper

agree with the mechanism of the wedge effect proposed here, where a highly dispersive wavefield generated within the widening wedge creates the largest amplification when it coincides with the undispersed arrival at the surface.

11.2 THE FORM OF THE INPUT SIGNAL

While the basin-edge effect mechanism is entirely a local phenomenon, created only by the geometry and material properties of the deep basin edge, its characteristics are highly dependent on the angle of incidence, the shape and frequency content of the time-history and the orientation of particle motion or type of wave involved.

11.2.1 THE NATURE OF THE INPUT TIME-HISTORY

It was reasoned in the wavefront analysis in Chapter Five that for a multi-pulsed input there could feasibly be a large number of positions across the basin where successive constructive interferences could take place. Given the multi-pulsed nature of most seismically-induced ground motions it seems reasonable to expect a zone of amplification wider than that generated by a simple Ricker pulse. The maximum extent of amplification would be limited by dispersive deamplification and stretching of the surface wave pulses, and loss of energy in the vertically reflecting wave by material damping and subcritical leakage into the basement. It would thus be expected that the first point of constructive interference would generally be the most significant. That is interference between a pulse in the delayed direct arrival and the matching pulse in the surface wave train, both originating from the same wavefront within the input. This appears to be the case in Lower Hutt modelling where the realistic combination of impedance ratios and material damping produce a single amplified zone.

The quality and strength of constructive interference is dependent on the match in not just the timing, but the shape of pulses. An input time-history containing a single prominent monotonic pulse would be expected to create a much more highly amplified and sharp zone of constructive interference than would an input of white noise. The resulting zone of amplification will have a width dependent on the dominant wavelength of the pulse. The more monotonic a pulse is, the less likely it will be distorted by dispersion and thus able to produce the most coherent constructive effect. For a multi-pulsed input signal, the quality of successive constructive interference would necessarily be dependent on a good match

between the shapes of successive peaks within the record. Interference between peaks originating from the same wavefront in the basement are expected to give the best match.

The time-history of ground motion at near-fault sites in the 1995 Hyogo-ken Nanbu Earthquake in Kobe was characterised by two major pulses, apparently associated with separate ruptures on the Rokko fault system (Toki et. al., 1995). A time-frequency analysis of the east-west component of motion recorded at Kobe University, situated on shallow stiff sediments above rock in the zone of forward directivity, is shown in Figure 11.1. Both large pulses (marked with a dot on the velocity record) can be seen to possess a frequency of approximately 0.7Hz, significantly higher than the fundamental frequency of the deep sediments (~0.25Hz).

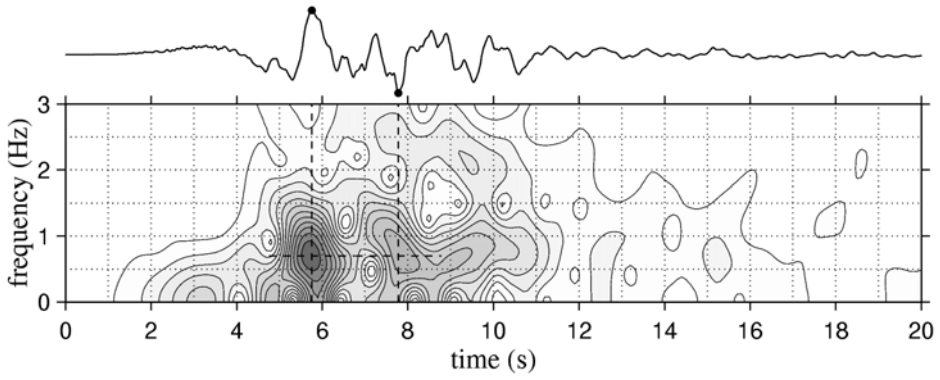

Figure 11.1. Spectrogram of the EW velocity record at Kobe University during the 1995 Hyogo-ken Nanbu Earthquake. The time-frequency distribution of Fourier amplitude spectra is calculated with a 2.0 second moving Hanning window. The uncorrected velocity trace is shown above. A prominent feature is two large 0.7Hz pulses.

The requirement for a strong pulse in the input record is met in Kobe with the directivity (bow-wave) effect from propagating ruptures generating these two large low-frequency pulses. It is not surprising that constructive interference between the surface wave and delayed direct arrival associated with each of these prominent pulses would create the strong belt of amplification evident in Kobe.

11.2.2 INPUT FREQUENCY

Based on the modelling in Chapter Six, it is obvious that both the width and position of the basin-edge effect are strongly dependent on the ratio of input frequency to the fundamental frequency of the basin-sediments. The results may be summarised as follows.

1. For $f < 0.75f_0$, little amplification occurs as most of the Love wave energy travels as a inhomogeneous wave in the basement.

2. For $f \approx f_0$, the Airy-phase edge effect develops amplification by a coupling between vertical resonance in the layer and the Airy phase of the Love wave. The extent of amplification is much wider than amplification associated with higher frequencies. For low velocity contrasts, however, this effect appears to be much less important.

3. For $f > 1.5f_0$, the basin-edge effect creates a discrete point of amplification by constructive interference. This is only expected to occur for frequencies greater than the fundamental of the layer.

The higher the frequency, the sharper and narrower the amplification. Higher frequency pulses are, however, generally not as prominent or well defined in most strong motion records. In the case of Kobe, the central frequencies of the causative peaks, although low, are approximately three times the fundamental frequency of the basin. The resulting basin-edge effect is hence both sharp and strongly amplified, as predicted by the semi-infinite layer modelling.

In the case of the Lower Hutt, we may reasonably expect strong pulses in the input from a Wellington Fault rupture to be of similar frequency to those in Kobe. Such pulses would coincide with the approximate fundamental frequency of the much smaller Lower Hutt valley (0.7Hz), yet since the average velocity contrast in Lower Hutt is only 2.4, strong amplification by Airy phase coupling is unlikely. It is nevertheless likely that any strong pulses in the input with central frequencies greater than 1Hz may produce a well-defined basin-edge effect a short distance from the fault trace.

11.2.3 SOURCE EFFECTS

The contribution of the source lies in controlling the wave type or orientation of particle motion that is incident on the basin, and in controlling the nature of the incident time-

history. The basin-edge effect occurs independently of any source effect, yet different rupture mechanisms and orientations and different hypocentral distances, depths and azimuth have significant effect on the type of wave field that is incident on the basin edge. While no specific investigation has been made in this thesis to quantify the effect of different source mechanisms on the nature of the input wave field, it is useful to consider these points here.

The 3-D shear-wave radiation pattern produced by a dislocation essentially controls the dominant particle motion in the far field. For example, the incident wave field in Lower Hutt from a NE-SW strike-slip rupture to the northwest of the valley would be expected to contain mostly edge-parallel (EP) particle motion; whereas the wave field from a similar rupture to the southwest is expected to contain mostly edge-normal (EN) particle motion. The shear-wave radiation pattern has also been shown to control the dominant particle motion at sites *close* to the rupture in damaging earthquakes such as San Fernando (1971), Imperial Valley (1979), Northridge (1994) and Kobe (1995).

At near fault sites, the incident shear motion is thus defined by a coupling between the shear-wave radiation pattern and the fault-fling or directivity effect. Sites located in front of a propagating rupture experience the effects of forward directivity (a large pulse associated with the bow wave of a rupture) with the dominant motion dictated by the shear-wave radiation pattern to lie in the fault-normal orientation. In the case of Kobe, the basin-edge lay within the zone of forward directivity generated by rupture on the basin-edge fault. The strongest components of ground motion of the incident wave were thus edge-normal, and in the form of a large double pulse, as shown in Figure 11.1. According to Kawase (1996), Motosaka and Nagano (1997) and many others, the strongest constructive interference thus took place between SV waves and Rayleigh waves, both propagating with some edge-normal particle motion.

At locations not influenced by forward directivity it may be either the edge-normal component or the edge-parallel component that is most amplified by the basin-edge effect. Ground motions within the damage zone at Santa Monica appear to be dominated by EP motion (Graves et. al., 1998). Santa Monica was located outside the lobe of forward directivity from the 1995 Northridge thrust event. The hypocentre was located some 20km north at a depth of 20km, and the rupture propagated up and northward, away from the

damage zone. The worst constructive interference thus occurred in the EP component between SH waves and some form of surface wave (Graves et. al., 1998).

The interference mechanism of the basin-edge effect appears to be entirely the same for both cases, with the only difference being the types of body waves (SH, or P-SV) and surface waves (Love or Rayleigh) involved. The question arises, however, as to the applicability of results from an SH wave analysis (as has been made in this thesis), when in zones of forward-directivity the basin-edge effect is almost certainly controlled by fault-normal ground motion in the form of P-SV and Rayleigh waves.

Kawase (1996) found that in Kobe the EP response showed similar characteristics to the EN response, yet that EP ground motions have much lower peak amplitudes, attributed directly to near-field forward directivity. Pitarka et. al. (1996, 1997) with a 2-D finite difference method to investigate incident plane and anti-plane wave fields in Kobe, show that although in-plane waves were dominant, both the SV- and SH-wave amplification patterns are influenced significantly by the 2-D effect of the basin structure. Peak amplification in the EN component occurs a greater distance from the edge than in the EP component, although both are near the region of the damage belt.

Similar results have been found by other modelling studies in two other Japanese locations. Niousha and Motosaka (1998) use 2-D modelling to show that that amplification of the EP component in Hachinohe City occurs closer to the edge than does amplification of the EN component. Tanaka et. al. (2000) use both 2-D and 3-D modelling in the Nobi Plain to also show that interference in the EP component occurs closer to the edge than in the EN component. Both papers attribute the difference to higher Rayleigh-wave phase velocities over the range of input frequency.

The differences in mechanism between an SV-Rayleigh-wave-controlled basin-edge effect and an SH-Love-wave-controlled basin-edge effect appear to be small, yet differences in its position are likely, owing to differences in the dispersive velocity distributions of the two types of surface waves. In the three examples outline above, the Rayleigh-wave phase velocities were higher than the Love-wave phase velocities within the causative frequency range, and thus the EN constructive interference occurs further from the edge than the EP. It is, however, necessary to look further at the velocity differences between Love and Rayleigh waves at a particular site before this can be assumed.

11.3 BASIN PROPERTIES

Given the same input motion, different sedimentary basins will generate different edge effects. Here the influence of the material properties and geometry of the edge are discussed. There are two main variables controlling the position of the basin-edge effect. The first is the difference in travel times between the direct arrival through the rock and the direct arrival through the sediments. A larger difference means that the surface wave has a greater length of time with which to travel across the basin before the delayed arrival reaches the surface. The second is the velocity and the position of initiation of the edge-generated surface wave. Higher velocities and more distant points of initiation shift the interference away from the edge.

11.3.1 SEDIMENTARY STRATIGRAPHY, BASIN DEPTH AND VELOCITY STRUCTURE

The depth and velocity of soft sediments adjacent to the basin edge control the travel time of vertically propagating shear waves, the fundamental resonant frequency of the layer and the dispersive velocity characteristics of horizontally-propagating Love waves. Deep basins and low-velocity sediments have low fundamental frequencies, and the corresponding ratio between the frequency of input pulses and the basin are higher. This leads to a sharper basin-edge effect as discussed in Section 11.2.2.

Deeper basins and softer sediments also delay the surface arrival of the wave travelling up through the sediments. The 900m depth of sediments below Kobe City delays the direct arrival by approximately 0.88 seconds (using the velocity model of Kawase, 1996), whereas the 300m depth of sediments in Lower Hutt creates only a 0.37 second delay. The shear-wave velocity contrast between the sediments and surrounding bedrock also influences the difference in arrival times. Bedrock surrounding the Osaka basin is granitic and much faster than the closely jointed and variably weathered Torlesse basement in the Wellington region, and aids the large arrival time difference in Kobe.

Just as important in defining the position of the basin-edge effect, is the surface-wave dispersive velocity distribution. Dispersion curves for near-surface sediments are a function of the material properties and depths of the sediments. For a given pulse frequency within the input, the sedimentary properties define the nature and velocity of the surface wave propagation, and hence the position of interference. Low frequency input

energy will be more likely to travel at higher velocities, while high frequency components travel at velocities closer to that of the near-surface layers.

Since the basin-edge effect only develops a sharp constructive interference for frequencies greater than the fundamental of the sediments, the group velocity of the critical Love wave is required to be less than the velocity of the sediments and the corresponding phase velocity will be higher, although in at least the same order of magnitude as the sediments. It has, however, been argued quite fairly that the causative surface wave in Kobe was a 1st (Kawase, 1996) or 2nd (Nagano, 1998) higher mode Rayleigh wave. Whatever the mode, the implication is that even at frequencies significantly higher than the fundamental of the basin, surface wave propagation may be much faster than expected, and the basin-edge effect may occur at a greater distance from the edge than expected using the fundamental-mode dispersion curve.

11.3.2 EDGE GEOMETRY

FEM modelling of the semi-infinite layer in Chapter Six shows that the edge-slope has little influence on the velocity of the Love wave that propagates away from the edge. Once the Love wave leaves the edge-region, its dispersive velocity characteristics depend only on the velocity structure of the sediments. These results agree both with the two-dimensional analytical work of Rodríguez-Zúñiga et. al. (1995), and numerical modelling of Shibuya (1992) who (along with others) have noted that surface-wave amplitudes are dependant on the seismic-velocity contrast between sediment and bedrock, yet vary little with the shape of the basin-edge.

While this may be true some distance from the edge, results from the preliminary modelling of two different cross-sections in Chapter Eight show that the shape of the edge plays a big role in determining the phase velocity of the initial edge-generated pulse causing the basin-edge effect. As discussed in the previous section, it is likely that the causative Love wave is actually a higher-mode Love wave. At least four modes of Love waves should theoretically exist within the band of frequencies excited by the 2.0Hz Ricker wavelet, and this would explain the high phase velocity associated with the causative Love wave modelled in the Lower Hutt.

In the single-layered case of a homogeneous semi-infinite layer, the apparent horizontal velocity of initial pulses leaving the edge is approximately the same as the dominant phase velocity of the fully developed Love wave. Consequently, it has been possible to develop the simple relationship in Equation 6.17 that accurately predicts the position of the first peak of constructive interference (see Figure 6.15a). The relationship also includes a term, x_i, which characterises the apparent position of the Love wave initiation. While the one-third rule (see Section 6.2.3) adequately describes the initiation point for edge-slopes greater than 45° and a 2.0Hz Ricker wavelet, it is probably of little relevance in any other situation. A general rule does exist, however, that a normal-sloping basin edge ($\psi < 90$) will push the point of initiation out into the basin, while a steeply overhanging edge will bring the point of initiation back. The point of initiation appears to have an approximately zero offset adjacent to a vertical edge.

The fault-bounded edge of the Lower Hutt is complex in that the near-surface sediments have a low-angled edge slope, whereas the rest of the deep sediments are bounded by a near-vertical rock wall. However, since the sediments on the up-thrown side of the fault are reasonably stiff in nature they appear to have little effect on the point of initiation of the edge-generated Love wave, which apparently lies approximately on the fault trace. It is likely also that diffraction at the lip of the vertical edge is significant in the development of the Love wave.

Observed amplification above the shallow dipping edges of both the semi-infinite layer and the southeastern edge of the Lower Hutt valley are good examples of the wedge effect. In the semi-infinite layer simulations this type of amplification above the sloping edge occurred only for edge-slope angles less than 30°. While it does not generate peak ground motions as high as the basin-edge effect near steeply dipping edges, wedge amplification is still a significant feature in the response of basins with shallow-dipping edges.

Chapter 12: DISCUSSION ON LOWER HUTT

Two-dimensional FEM modelling and analysis of weak motion data in the Lower Hutt has provided important insights into the seismic behaviour of both the whole valley and the fault-bounded edge. Gross simplifications – namely in the form of seismic input, the linear-elastic soil behaviour and the two-dimensional nature of the study – place limitations on the applicability of the research to estimating strong-ground motion during the major near-source ruptures, yet the value of the study lies more in the definition of certain mechanisms of valley response such as the basin-edge effect and two-dimensional resonance.

It is notable that various other sedimentary structures in the Wellington region such as Seatown, Rongotai, Te Aro, Thorndon, Upper Hutt, Wainuiomata and Porirua are also likely to amplify seismic motions by the mechanisms of multi-dimensional site effects, including resonance and constructive edge effects. Many of the observations of seismic response noted in this characterisation of the Lower Hutt may be applicable to other basins both in the Wellington region and further afield.

Relatively good matching of both the amplitudes and resonant frequencies between the modelling and array results has provided a much higher degree of confidence in the revised velocity model that was used in Chapter Ten for the sediments infilling the valley. It also gives credit to the 3D geological borehole database being developed at IGNS which was used to define the depth and properties of the Holocene layer in the specific position of the array, as well the geometry of lower stratigraphy and the basement interface.

12.1 LOVE WAVE PROPAGATION AND RESONANCE

It is visually obvious in the results of two-dimensional FEM modelling that strong Love waves are generated at each edge of the valley under seismic input, but this is not so easy to see in the array results. The action of edge-generated Love waves in the recorded data, however, is implicitly apparent due to several observations. Recorded data exhibits strong and variably amplified resonant peaks in the frequency domain. Such amplifications cannot

be explained simply as the result of one-dimensional resonance or focussing. The same argument is equally valid for the strongly amplified and spatially variable peak ground motions recorded across the array, or the high degree of differential motion observed between sites less than 50 metres apart. A more convincing and quantifiable observation is that of the movement of wave packets away from the edge with a frequency-dependent velocity close to the theoretical Love wave group velocity of the Holocene layer.

Such edge-generated Love waves are significant in Lower Hutt not only in that they are the primary cause of a significant constructive edge effect, but that they are likely to amplify ground motions by Airy phase amplification in the Holocene layer, and are the primary cause of multi-dimensional resonance within the deep sedimentary structure

12.1.1 VERTICAL RESONANCE AND AIRY-PHASE AMPLIFICATION IN THE HOLOCENE LAYER

The strongest amplification recorded on the array for stations on the down-thrown side of the fault occurs at 2.0-2.5Hz. The fundamental vertical frequency, f_0, of the Holocene sediments beneath the array clearly lies at approximately 2.2-2.3Hz, based on both these array observations and the 1-D flat layer approximation (Haskell, 1960) with borehole data for the depth of the layer (~20m) and SCPT measurements (Stephenson and Barker, 1992) for the shear-wave velocity (~175m/s). At the same time, FEM modelling shows that the bulk of the surface wave energy travels in the Holocene layer, while a lesser amount travels at higher velocities in lower layers.

In Chapter Six it was shown by FEM modelling that a strong coupling develops between the Airy phase of the Love wave and vertical resonance within the layer for input frequencies close to the fundamental of the layer and for a high velocity contrast. Thus given an input motion with significant excitation between $0.75f_0$ and $1.5f_0$ (1.65-3.3Hz), the Holocene layer would thus be expected to develop such a coupling causing amplified ground motions. For a velocity contrast of 10, the amplification would occur at a distance 1-8H from the fault trace (where H is the depth of the Holocene layer, x = 180-320m), in the same approximate position as the peak displacements observed in the modelling. The relatively low velocity contrast at the base of the Holocene layer will reduce the likely amplitude of this effect. Nevertheless, Airy phase amplification may be a factor in the

apparent width and lack of sharp maxima seen in the peak ground motions of events recorded across the array, as well as aiding to generate the very strong 2.0-2.5Hz spectral peak. The onset of non-linear soil behaviour in the soft Holocene sediments is expected to reduce the effect of Airy phase amplification during strong ground motions.

12.1.2 MULTI-DIMENSIONAL RESONANCE OF THE DEEP VALLEY STRUCTURE

Modelling results show a spatially variable pattern of amplification in the frequency domain that has many similarities to the analytical solution for two-dimensional resonance of anti-plane motion in a rectangular Helmholtz resonator (Bard and Bouchon, 1985; Bielak et. al., 1999). At the same time, the pattern could be explained as simply an interaction between two edge-generated Love wave amplification patterns (defined in Section 5.5.2 and shown in FEM modelling in Section 6.2.1) one from each side of the valley. Although most of the strongest spectral peaks in the 2-D pattern fall on the pattern of 1-D resonant frequencies, there is a significant difference between the two in that the 2-D spectral amplification is both stronger and more variable.

The question arises as to whether the spectral amplification is a result of 2-D resonance or simply due to interfering surface waves. Bard and Bouchon (1985) define a cut-off shape-ratio between valley behaviour being controlled by either 2-D resonance or surface wave propagation, based on an observation of the width of the valley where motion remains in-phase. With an average velocity-contrast and shape ratio of 2.4 and 0.12 respectively, the Lower Hutt valley falls well outside the requirements for 2-D resonance defined in Figure 12 of Bard and Bouchon (1985). Their criteria thus rejects the notion of 2-D resonance in the Lower Hutt valley, although it seems to be more a question of semantics rather than a difference in response.

The classic pattern of 2-D resonance could be defined as one where individual resonant peaks stand out clearly from the others and do not necessarily lie on the 1-D resonant peaks, such as the example shown in Figure 3.4 (which, incidentally also falls outside the realm of 2-D resonance defined by Bard and Bouchon, 1985). On the other hand, the classic pattern of edge-generated Love wave action and 1-D resonance is shown by the modelling in Chapter Six, where amplification is defined by extremum lines. The pattern which develops in the Lower Hutt obviously lies somewhere between these two “classic”

patterns, as the resonant peaks are well-defined yet are also strongly related to the extremum lines extending from each edge. Either way, there is a clear-cut lateral resonance pattern associated with Love-wave propagation, superimposed on a 1-D resonance pattern associated with vertical subcritical reflection. The spectral amplification in the Lower Hutt will thus be referred to as a pattern of two-dimensional resonance.

Because the deepest part of the valley is found adjacent to the fault along the western edge, the resonant modeshapes are all skewed westward. Higher resonant modes (both vertical and horizontal) have been attenuated in the soft soil, and have much lower amplitudes. In general, the soil exhibits spectral ratios up to 12 at certain locations across the entire width of the valley between 0.75 and 2.5 Hz, and ratios up to 4 over the whole frequency range shown (0.5-3.5Hz). This compares well not only with array data but with previously recorded data where FSR reaches values as high as 14 at deep sites in Petone (Taber and Smith, 1992).

Such anti-plane modes of resonance apparent in the modelling are in agreement with observations of Stephenson (1974, 1975, 1989b) who refers to resonant amplification being directed in the ~50° (long-valley) orientation. He notes strong directionality of 2.1-3.2Hz recorded motion, and associates it with horizontal resonance in the Holocene layer. The bias towards motion in the long-valley direction in observed data indicates the significance of the anti-plane modes that have been modelled in this study. Both modelling and array data, however, suggest that significant lower-frequency anti-plane resonant modes also exist and are associated with the full depth of sediments in the valley.

Although there is a neat and almost uniform pattern of resonant peaks in the 2-D spectral pattern, the level of amplification has a more chaotic distribution. It is often dictated by interference effects (Wirgin, 1995) between the fundamental and higher vertical-mode sets. The net effect is a complex patchwork of amplification, where the patches of greatest amplification lie approximately on the 1-D pattern. In a general sense we can thus characterise amplification by patches in *x-f* space, yet in a local sense the amplification is highly variable in both dimensions. A 0.1Hz change in frequency or a 80m change in cross-valley position may alter the spectral amplification by as much as a factor of 10. This strong variability is also evident in array data, although it is difficult to see a pattern to the amplification as we can see in the modelling results.

The angle of incidence effects both the amplification and spatial location of resonant peaks. Spectral amplification is, in general, strongest on the side of the valley opposite to the direction of incidence, strongest above the deep sediments near the fault-bounded edge, and strongest for near-vertical incidence. A worst case scenario for spectral amplification on the fault-bounded side of the basin is therefore steeply-incident input from the southeast. As the angle of incidence increases, the amplification pattern tends toward a Love-wave edge pattern originating from the side closest to the input, and amplification is predominantly associated with extremum lines rather than distinct resonant peaks.

The close spacing of vertical eigenfrequencies in the Lower Hutt Valley are a distinguishing feature separating it from smaller basins such as the nearby Te Aro Basin in Wellington (Adams et. al., 1999) or the Kirovakan Valley, Armenia (Bielak et al., 1999). The Lower Hutt thus contains this patchwork of spectral amplification created by interference effects between various modes that are not evident in the two above examples. On a similar note, the effect of the gentle down-valley slope of the basement in the Lower Hutt has the effect of lowering the resonant frequencies of sites closer to the Petone foreshore. This effect was noted in Chapter Eight where there was a 10% difference in resonant frequencies between the two cross-sections.

12.2 THE BASIN-EDGE EFFECT IN LOWER HUTT

Defining the possibility and characteristics of a Kobe-like basin edge effect in Lower Hutt was essentially the motivation for initiating this research. Indications are from both SH modelling and to a lesser extent from the array analysis, that a belt of higher peak ground motions generated by the basin-edge effect should occur along the whole length of the Lower Hutt Valley's western edge. While we can loosely define the characteristics of the expected amplification, it is likely to be quite different for different causative earthquakes.

12.2.1 FEM MODELLING RESULTS

The fault plane forming a vertical western edge to the valley lies between 100 and 300 metres from the base of the western hills. Modelling of the two different edge geometries in Chapter Eight suggests that it is this vertical edge and not the edge of the sediments that controls the position of interference. Well-defined pulses within the input with frequencies

greater than 1.0Hz are expected to produce strong constructive interference 0-300m out from the fault trace. Peak ground displacement (PGD) within this zone may be as much as 200% of that across the rest of the valley, but with most inputs closer to 130%.

Amplification within this belt is largest for earthquakes originating from the northwest and smallest for those from the southeast. Pulses of frequency 0.5Hz or less are expected to create little amplification, while those greater than the fundamental frequency of the sediments (0.7Hz) create a well-defined zone. The position and width of the zone are also strongly dependent on the pulse frequency and angle of incidence. A narrow belt of amplification close to the edge results from high frequency pulses and those from the southeast. Wider and more distant zones of constructive interference result from lower frequency pulses and those from the northwest.

The position of the edge effect seen in the modelling results can be roughly predicted with simple calculations based on estimated Love-wave velocities and the arrival delay of the direct wave in the sediments. From Section 10.1.1, the arrival delay is 0.37 seconds, and the Love-wave phase velocity in the Holocene layer will vary between 175m/s and 370m/s, or possibly higher due to stiffer and deeper sedimentary layers. Multiplying this range in velocity with the time delay gives a range in distance from the fault-edge of between 65 and 137 metres. This does not, however, give any indication of the likely width or level of the amplification.

12.2.2 Evidence from Weak Ground Motions and Observed Damage

On average, recorded weak motions across the array do not show a defined zone of greatly amplified peak ground motion. There is, however, ample evidence for the action of edge-generated Love waves in the recordings, and the peak ground displacements (PGD) are of similar magnitude to those found through numerical modelling. PGD in the edge-parallel direction from earthquakes to the south and southwest (Figure 9.13) show a peak on average some 30-180m from the fault trace, while the PGD in the edge-normal component and from earthquakes from other directions is stable or still increasing at 300m from the fault. These trends match those observed in the modelling, yet the width of amplification is perhaps larger than estimated by the Ricker pulse input. A longer array is obviously necessary to confirm this idea.

Reports from the 1934 Paihiatua earthquake (Table 7.1) indicate an anomalously high number of damaged brick chimneys adjacent to the Wellington fault in the Petone-Alicetown area of Lower Hutt (Downes et. al., 1999). There were two areas with the most significant damage. The first was in Railway Ave and Aglionby Street, not far from Lower Hutt Central and 125-250m from the fault trace. The second, in Petone, extended in a triangle from the Hutt Road (which runs almost parallel to the fault trace) out to Jackson Street and Nelson Street (up to 350m from the fault).

Both these observations of amplification adjacent to the fault result come from seismic inputs other than a Wellington Fault rupture. This indicates that the basin-edge effect in the Lower Hutt is not dependent on a propagating rupture source, nor is it dependent on strong ground motion. These observations also indicate the variability in response from real seismic events as opposed to smooth and well defined distributions of amplification in modelling results.

12.2.3 LIMITATIONS

Specific results discussed here almost exclusively imply linear elastic soil behaviour. Non-linear effects especially in the Holocene layer may limit high-frequency surface wave propagation near the surface, and the lower-frequency energy travelling through deeper layers at higher velocities may create the strongest interference at greater distances from the edge. While the position of the basin-edge effect estimated here applies only to peak ground displacement, indications are that velocity and acceleration show an almost identical trend (Adams et al., 1999). Displacements have been used in this study for the ease of physical interpretation.

The modelling results hold only for SH-Love wave interference resulting from edge-parallel input motions. While these may dominate the wave field arriving from many near and distant strong motion events, it is perhaps more likely that the dominating input motion from a propagating strike-slip rupture on the Wellington Fault will be the edge-normal component, and interference between SV and Rayleigh waves most important as was the case in Kobe. Indications are that the edge-normal interference will occur at a greater distance from the fault.

The shape of the input pulse is obviously an important controlling factor in the amplification pattern. Large coherent pulses (such as the modelled Ricker wavelet) in the 1-2Hz range apparently produce a strong and well-defined basin-edge effect. Multiple pulses, on the other hand, may create a much wider band of amplification, and this may be one of the reasons for the lack of a defined peak in the recorded peak ground motion across the array. Forward directivity from a propagating rupture has been shown to generate a large pulse in the time history, and is thus expected to produce a well-defined belt of strong motion in the Lower Hutt.

12.2.4 TWO TYPICAL SCENARIOS OF A BASIN-EDGE EFFECT IN LOWER HUTT

A Wellington Fault Earthquake

Recent three-dimensional finite difference modelling (Benites and Kozuch, 2000; Olsen and Benites, 1998; Benites, pers. comm.) has shown the importance of directivity on ground motions in the Wellington region during a major strike-slip rupture on the Wellington Fault. They estimate peak ground velocities in excess of 90-160cm/s at some near-fault sites from a M7.25 earthquake, without taking into account near-surface low velocity sediments. Directivity effects are thus expected to dominate the wave field arriving in the Lower Hutt in this type of event.

As was the case in Kobe, the dominant motion will likely be in the edge-normal orientation, and thus the dominant constructive edge effect controlled by SV and Rayleigh wave propagation. Given a coherent rupture, forward directivity is expected to generate a significant pulse in the input wave field. Then, provided the pulse is of a frequency greater than the fundamental of the deep sediments (0.7Hz), a significant edge-normal basin-edge effect is expected to occur. While further investigation needs to be made concerning the difference between Rayleigh wave and Love wave propagation in the Lower Hutt sediments, based on Japanese studies the EN amplification is expected to occur a greater distance from the fault than what is estimated for the EP case.

A Hikurangi Subduction Zone Earthquake

A major rupture on the Hikurangi subduction interface would likely produce an input to the Lower Hutt similar to that which occurred in Santa Monica during the Northridge

earthquake, with respect to the dominant particle motion at least. This comparison is made considering the roughly similar orientations of the rupture plane with respect to the strike of the basin edge. In any case, assuming dominant EP motion in the input, we would expect to observe a basin-edge effect to develop by interaction between an edge-generated Love wave and the delayed arrival of the SH, and strongly amplified long-valley peak ground motions.

12.2.5 SUMMARY

Taking all the above factors into account, we may loosely define the position of the basin-edge effect in Lower Hutt to occur between 0-300m from the fault trace, given edge-parallel particle motion, a single and well-defined pulse in the record, and linear soil response. Edge-normal motion, multiple pulses in the input time-history, non-linear soil behaviour and real variability in the ground shaking are all likely to increase the distance and width of strong amplification, perhaps to as much as 600 or more metres from the edge. In any case, the basin-edge in Lower Hutt is expected to be significant, and coincident with residential, commercial and industrial development up the entire length of the valley.

Chapter 13: CONCLUSIONS

Two-dimensional numerical modelling of the semi-infinite layer and the Lower Hutt valley, observations from a weak motion array, and a critique of current literature have lead to the following conclusions.

13.1 BASIN-EDGE EFFECTS ON ANTI-PLANE MOTION

- The seismic response at a basin edge is controlled by edge-generated wavefields. Such edge-generated wavefields are produced by refraction, diffraction and/or total reflection of an incoming seismic wavefield at the basin edge. In the anti-plane case, they quickly develop into horizontally propagating Love waves by total internal reflection.

- Love waves propagating through a homogeneous layer away from an edge set up distinctive interference patterns in both the time and frequency domains. Both patterns are strongly dependent on the shear-wave velocity contrast at the base of the layer. In the frequency domain, the spectral pattern is characterised by extremum lines associated with the wavelength of edge-generated Love waves. In the time domain, the surface response is characterised by apparently curving phase velocities.

- Edge-generated Love waves are much smaller in amplitude than the direct arrivals through the sediments. This makes it difficult to see wave propagation in recorded data.

- Basin-edge effects are localised zones of amplification occurring near the edge of sedimentary basins during seismic events. They develop by constructive interference at the free surface between various wavefields within the sedimentary basin. This thesis defines between three different types of basin-edge effects, based on mechanism of occurrence:

    1. The basin-edge effect occurs adjacent to a steeply dipping edge, by constructive interference between a delayed arrival through the full depth of sediments and an edge-generated wavefield.

2. The Airy-phase edge effect develops by constructive interference between subcritically-trapped SH waves and the Airy phase of an edge-generated Love wave, when the dominant frequency of the input is close to the fundamental frequency of the layer.

3. The wedge effect occurs some distance from the apex of a sedimentary wedge where constructive interference within the post-critically trapped Love-type wavefield develops amplification above the sloping basement.

- The frequency of the input signal with respect to the fundamental vertical frequency of the layer controls the form of amplification at the edge. An input frequency significantly less than the fundamental will produce little edge amplification. An input frequency close to the fundamental will create an Airy-phase edge effect, provided the velocity contrast is high. Finally, an input frequency significantly higher than the fundamental will generate the basin-edge effect.

- For a given input signal, the basin-edge effect amplification will be strongest and most well-defined for very deep basins, and for those with a sharp velocity contrast between the sediments and the basement rock.

- The position of the basin-edge effect is essentially given by the difference in surface arrival times (between waves travelling through the sediments and those travelling through the rock) multiplied by the (dispersive) velocity of the edge-generated Love wave. The edge-slope angle, however, controls the apparent position of Love wave development, and thus the distance of the basin-edge effect from the edge. Normal edge-slopes push the basin-edge effect further out from the edge, while reverse edge-slopes bring it closer to the edge.

- The nature of the input motion controls both the width and the quality of constructive interference. A prominent and monotonic pulse within an input signal will generate the strongest amplification. The width of amplification is controlled by the wavelength of the pulse. A multi-pulsed input with a good match in shape between successive pulses will generate a wider zone of amplification.

- The basin-edge effect has also been shown to occur between *undispersed* edge- and base-refracted wavefronts, yet its amplitude is generally insignificant compared to that

which develops between the edge-generated *dispersed* wavefield and the base-refraction. The position of constructive interference between undispersed wavefronts may, however, be calculated with simple geometrical expressions.

- The edge-parallel (SH-Love wave) basin-edge effect (that we have restricted this study to) will be strongest when the incoming wavefield is dominated by edge-parallel particle motion. Basin-edge effects associated with edge-normal and vertical particle motion appear to develop by the same constructive effect, yet at different distances from the basin edge.

13.2 SEISMIC RESPONSE OF THE LOWER HUTT VALLEY

- The anti-plane seismic response of the Lower Hutt Valley is characterised by two-dimensional resonance across its width, and a constructive basin-edge effect adjacent and parallel to the Wellington Fault.

- Two-dimensional resonance which develops due to edge-generated surface waves describes the anti-plane spectral behaviour of the full width of the valley. Frequencies within the range 0.5-3.5Hz are variably amplified up to a Fourier spectral ratio (FSR) as high as 12. The distribution of amplification is highly variable with both location and frequency. Resonant interference effects are the cause of strong amplification generally centred near the first three 1-D vertical modes of the full depth of sediments.

- Especially strong amplification in the frequency band 2.0-2.5Hz results from a coincidence of the fundamental resonant mode of the Holocene layer and the 2nd higher mode of the deep sediments. In addition, amplification near the edges in this frequency band may be associated with Love waves propagating at the fundamental Airy phase.

- Strong differential motion is an outstanding feature in array recordings. Large variations exist in the particle motions recorded at sites within 50 metres of each other has significant implications for the behaviour of large structures in the valley.

- Constructive interference between edge-generated surface waves and the direct arrival of the shear wave through the sediments is expected to create strong displacement, velocity, and acceleration pulses in ground motion parallel to the fault-bounded valley edge. The position, strength and width of this Kobe-like basin-edge effect depends

heavily on the form of seismic input. It is estimated to occur between 0 and 600m from the Wellington Fault trace, and may double the peak ground motions.

- Although we are using linear methods to model soils that will probably behave in a highly non-linear fashion, our results can be applied to strong-motion shaking. The elastic model should conservatively over-predict values of peak ground motion and peak spectral amplification. It should provide a reasonable estimate of the frequency content of shaking and the FSR values. The model should also accurately determine the important spatial distribution of amplification. We do however expect it to under-predict the duration of shaking

- Limitations aside, this two-dimensional linear analysis simulating the propagation of anti-plane SH waves has proved to be a substantial step toward the determination and understanding of the seismic behaviour of the Lower Hutt Valley. It would be prudent for planners and developers to be aware of the risks associated with urban development within the Lower Hutt, and to ensure adequate protection is available to withstand the type of strong ground shaking outlined above.

13.3 SUGGESTIONS FOR FURTHER RESEARCH

Several suggestions are made which may aid the direction of future research. The seismic behaviour of the Lower Hutt valley would be better understood with:

- A denser, longer and two-dimensional array of instruments across the valley for better capture of surface wave effects.

- An extension of the numerical analysis to edge-normal and vertical particle motion (to include P, SV and Rayleigh waves), to three-dimensional effects (including a 3-D velocity model and fault-rupture effects) and to non-linear soil models.

- Consideration given to the effect of topography surrounding the valley.

The methods of analysis used in the Lower Hutt could also be applied to other site-specific response studies in similar basin-edge and sedimentary valley locations, where an understanding of the spatial distribution of ground shaking would be helpful (for example in Napier, Christchurch or Nelson)

The understanding of basin-edge effects would improve with further research leading on from that presented here, such as:

- A much more comprehensive numerical analysis of SH wave propagation within simple basin-edge shapes.
- An extension of this thesis to an analysis of the SV-Rayleigh wave basin-edge effect.
- An extension of the solution to the wedge problem (Sanchez-Sesma and Velaquez, 1987) to include a finite layer depth and a lower vertex.
- Analytical work to develop a relationship between the 2-D anti-plane resonance pattern within a rectangular Helmholtz resonator (Bard and Bouchon, 1985) and the Love-wave spectral edge pattern in a semi-infinite layer (presented here).
- Further exploration on the relationship between the Love-wave spectral edge pattern and the basin-edge effect.

REFERENCES

Abo-Zena, A.M. and King, C.Y. (1973) SH Pulse in an Elastic Wedge. *Bull. Seism. Soc. Am.* 63 (5): 1571-1582.

Abramovici, F.; Le, L.H.T. and Kanasewich, E.R. (1989) The Evanescent Wave in Cagnaird's Problem for a Line Source generating SH Waves. *Bull. Seism. Soc. Am.* 79: 1941-1955.

Adam, M. and Takemiya, H. (1997) Site Topography Effects in Kobe During the 1995 Hyogo-ken Nanbu Earthquake: The Nonlinear Analysis. *Proc. 8th Intl. Conf. Soil Dyn. Earthq. Eng.* Istanbul, Turkey, 1997 (SDEE '97).

Adams, B.M. and Jaramillo, J.D. (2000) A Two-Dimensional Study on the Seismic Response of the Aburrá Valley, Medellín, Colombia. *Submitted to the Bull. N.Z. Nat. Soc. Earthq. Eng*., June 2000.

Adams, B.; Davis, R. and Berrill, J. (2000) A Two-Dimensional Study on the Seismic Response of the Aburrá Valley, Medellín, Colombia. *Civil Engineering Research Report* 2000-2. University of Canterbury, Christchurch, NZ.

Adams, B.; Davis, R.; Berrill, J. and Taber, J. (1999) Two-Dimensional Site Effects in the Hutt Valley - Similarities to Kobe. *Civil Engineering Research Report* 1999-3. University of Canterbury, Christchurch, NZ.

Ahmad, S.; Fishman, K.L. and Xue, H. (1995) Response of Alluvial Valleys to Incident SH, SV and P Waves. *Proceedings of the Third International Conference on Recent Advances in Geotechnical Earthquake Engineering and Soil Dynamics*, St Louis, April 1995. Paper No. 10.17, Vol II: 709-714.

Aki, K. (1988) Local Site Effects on Strong Ground Motion. *Proc. Earthquake Eng. Soil Dyn.* II: 103-155.

Aki, K. (1993) Local Site Effects on Weak and Strong Ground Motion. *Tectonophysics* 218: 93-111.

Aki, K. and Larner, K.L. (1970) Surface Motion of a Layered Medium Having an Irregular Interface due to Incident Plane SH Waves. *J. Geophys. Res*. 75: 933-954.

Aki, K. and Richards, P.G. (1980) *Quantitative Seismology: Theory and Methods*. Vols I & II. WH. Freeman and Company, USA. 932p.

Alex, C.M. and Olsen, K.B. (1998) Lens-Effect in Santa Monica? *Geophys. Res. Lett*. 25 (18): 3441-3444.

Al-Hunaidi, M.O. (1989) Numerical Modelling of the Radiation Condition of Unbounded Media. In: *Engineering Seismology and Site Response: Proceedings of the 4th International Conference on Soil Dymanics and Earthquake Engineering*, Mexico City, Mexico, October 1989. Editors: A.S. Cakmak and I. Herrera.

Bao, H.; Bielak, J.; Ghattas, O.; Kallivokas, L.F.; O'Hallaron, D.R.; Shewchuk, J.R. and Xu, J. (1998) Large-Scale Simulation of Elastic Wave Propagation in Heterogeneous Media on Parallel Computers. *Computer Methods in Applied Mechanics and Engineering*. 152: 85-102. Elsevier Science S.A.

Bard, P.Y. and Bouchon, M. (1980a) Seismic Response of Sediment Filled Valleys Part 1: The Case of Incident SH Waves. *Bull. Seism. Soc. Am*. 70 (4): 1263-1286.

Bard, P.Y. and Bouchon, M. (1980b) Seismic Response of Sediment Filled Valleys Part 2: The Case of Incident P and SV Waves. *Bull. Seism. Soc. Am*. 70 (4): 1921-1941.

Bard, P.Y. and Bouchon, M. (1985) The Two-Dimensional Resonance of Sediment-Filled Valleys. *Bull. Seism. Soc. Am*. 75: 519-541.

Bard, PY. (1994) Effects of Surface Geology on Ground Motion: Recent Results and Remaining Issues. *Proc. 10th European Conference on Earthquake Engineering*, 1: 305-325.

Bardet, J.P.; Kapusker, M.; Martin, G.R. and Proubet, J. (1992) Marina District: Site-Response Analyses. *U.S. Geological Survey Professional Paper* 1551-F ppF85-F140.

Begg, J.G. and Mazengarb, C. (1996) *Geology of the Wellington Area*, Scale 1:50,000. Institute of Geological and Nuclear Sciences Geological Map 22. 1 sheet + 128p. Lower Hutt, NZ: IGNS Ltd.

Benites, R.A. and Kozuch, M.J. (2000) *A simulated rupture of the Wellington fault*. Presentation to the inaugural GNS Earthquake Short Course, Wellington, New Zealand.

Ben-Menahem, A. and Singh, S.J. (1981) *Seismic Waves and Sources*. Springer-Verlag, New York. 1108p.

Beresnev, I.A. and Wen, K.L. (1996) Review: Non-Linear Soil Response - A Reality? *Bull. Seism. Soc. Am*. 86 (6): 1964-1978.

Berryman, K.R. (1990) Late Quaternary Movement on the Wellington Fault in the Upper Hutt Area, New Zealand. *NZ. J. Geol. Geophys*. 33: 257-270.

Bielak, J. and Christiano, P. (1984) On the Effective Seismic Input for Nonlinear Soil-Structure Interaction Systems. *Earthq. Eng. and Struct. Dyn*. 12: 107-119.

Bielak, J.; Hisada, Y.; Bao, H.; Xu, J. and Ghattas, O. (2000) One- vs Two- vs Three-Dimensional Effects in Sedimentary Valleys. *Proc 12th World Conf. Earthquake Eng.*, Auckland, New Zealand. Paper No. 2689.

Bielak, J.; Xu, J. and Ghattas, O. (1999) Earthquake Ground Motion and Structural Response in Alluvial Valleys. *J. Geotechnical and Geoenvironmental Engineering, ASCE*. 125 (5): 413-423.

Block, S. and Hales, A.L. (1967) New Techniques for the Determination of Surface Wave Phase Velocities. *Bull. Seism. Soc. Am*. 58 (3): 1021-1034.

Boore, D.M. (1970) Love Waves in Nonuniform Wave Guides: Finite Difference Calculations. *J. Geophys. Res*. 75 (8): 1512-1527.

Boore, D.M. (1972) Finite Difference Methods for Seismic Wave Propagation in Heterogenous Materials. In: *Methods in Computational Physics*, 11: 1-36. Ed. BA. Bolt, Academic Press, New York.

Boore, D.M.; Larner, KL.; Aki, K. (1971) Comparison of Two Independent Methods for the Solution of Wave Scattering Problems: Response of a Sedimentary Basin to Incident SH Waves. *J. Geophys. Res*. 76: 558-569.

Borcherdt, R.D. (1970) Effects of Local Geology on Ground Motion Near San Fransisco Bay. *Bull. Seism. Soc. Am*. 60 (1): 29-61.

Borcherdt, R.D.; Glassmoyer, G.; Andrews, M.; Cranswick, E. (1989) Effects of Site Conditions on Ground Motion and Damage. In: Armenia Earthquake Reconnaissance Report. *Earthquake Spectra*. Special Supplement: 23-42.

Borcherdt, R.D. and Glassmoyer, G. (1992) On the Characteristics of Local Geology and their Influence on Ground Motions Generated by the Loma Prieta Earthquake in the San Fracisco Bay Region, California. *Bull. Seism. Soc. Am*. 82: 603-641.

Bouchon, M. (1995) Site Response: Physics and Modelling. *Proc. 5th Intl. Conf. Seismic Zonation*, part III: 1869-1877.

Bouchon, M. (1996) The Discrete Wavenumber Formulation of Boundary Integral Equations and Boundary Element Methods: A Review of Applications to the Simulation of Seismic Wave Propagation in Complex Geological Structures. *Pure and Applied Geophysics*. 148(1/2): 3-20.

Bouchon, M. and Aki, K. (1977) Discrete Wave-number Representation of Seismic-Source Wave Fields. *Bull. Seism. Soc. Am*. 67(2): 259-277.

Bouden, M.; Datta, S.K. and Shah, A.H. (1989) Dynamic Amplification of Seismic waves by Alluvial Valleys in Layered Medium. In: *Engineering Seismology and Site*

Response: Proceedings of the 4th Intl. Conf. on Soil Dyn. and Earthq. Eng., Mexico City, Mexico, October 1989. Editors: A.S. Cakmak and I. Herrera.

Bravo, M.A.; Sanchez-Sesma, F.J.; Chavez-Garcia, F.J. (1988) Ground Motion on Stratified Alluvial Deposits for Incident SH Waves. *Bull Seism. Soc. A*. 78 (2): 436-450.

Bravo, M.A.; Sanchez-Sesma, F.J.; Chavez-Perez, S. (1989) A Hybrid Approach to Study the Seismic Response of Soft-Soil Sedimentary Basins. In: *Engineering Seismology and Site Response: Proceedings of the 4th Intl. Conf. on Soil Dyn. and Earthq. Eng.*, Mexico City, Mexico, October 1989. Editors: A.S. Cakmak and I. Herrera.

Brekhovskikh, L.M. (1980) *Waves in Layered Media*. 2nd Ed. Academic Press, New York. 503p.

Chavez-Perez, S.; Ramos-Martinez, J. and Sanchez-Sesma, F.J. (1989) Seismic Response of Three-Dimensional Alluvial Basins of Axisymmetric Shape. In: *Engineering Seismology and Site Response: Proceedings of the 4th Intl. Conf. on Soil Dyn. and Earthq. Eng*., Mexico City, Mexico, October 1989. Editors: A.S. Cakmak and I. Herrera.

Constantino, C.J. Wachowski, A.; Barnwell, U.L. (1967) Finite Element Solution for Wave Propagation in Layered Media Caused by Nuclear Detonation. *Proc. Intl. Symp. on Wave Propagation and Dynamic Properties of Earth Materials*, Mexico. pp 59-70.

Cotton, C.A. (1912) Recent and Sub-Recent Movements of Uplift and Subsidence near Wellington, New Zealand. *Scottish Geographical Magazine*. 28: 306-312.

Cotton, C.A. (1960) Hutt Valley Fault Scarps. *NZ. J. Geol. Geophys*. 3:218-221.

Cowan, M. and Hatherton, T. (1968) Gravity Surveys in Wellington and Hutt Valley. *N.Z. J. Geol. Geophys*. 11 (1): 1-15.

Cremonini, M.G.; Christiano, P. and Beilak, J. (1988) Implementation of Effective Seismic Input for Soil-Structure Interaction Systems. *Earthquake Engr. Struct. Dyn*. 16: 615-625.

Dellow, G.D.; Read, S.A.L.; Begg, J.G.; Van Dissen, R.J. and Perrin, N.D. (1992) Distribution of Geological Materials in Lower Hutt and Porirua, New Zealand: A Component of a Ground Shaking Hazard Assessment. *Bull. N.Z. Natl. Soc. Earthquake Eng*. 25 (4): 332-344.

Dezfulian, H. and Seed, H.B. (1970) Seismic Response of Soil Deposits Underlain by Sloping Rock Boundaries. *Journal of the Soil Mechanics and Foundations Division, ASCE* SM6: 1893-1916.

Dezfulian, H. and Seed, H.B. (1971) Response of Nonuniform Soil Deposits to Travelling Seismic Waves. *Journal of the Soil Mechanics and Foundations Division, ASCE* SM1: 27-46.

Douglas, A. (1970) Finite Elements for Geological Modelling. *Nature*. 226: 630-631.

Downes, G.; Dowrick, D.; Smith, E. and Berryman, K. (1999) The 1934 Paihiatua Earthquake Sequence: Analysis of Observational and Instrumental Data. *Bull. Natl. Soc. Earthquake Eng*. 32 (4): 221-245.

Drake, L.A. (1972a) Love and Rayleigh Waves in Non-horizontally Layered Media. *Bull. Seism. Soc. Am*. 62: 1241-1258.

Drake, L.A. (1972b) Rayleigh Waves at a Continental Boundary by the Finite Element Method. *Bull. Seism. Soc. Am*. 62: 1259-1268.

Dravinski, M. (1982a) Scattering of SH Waves by Subsurface Topography. *J. Eng. Mech. Div., Proc. ASCE* 108 (EM1): 1-17.

Dravinski, M. (1982b) Scattering of Elastic Waves by an Alluvial Valley. *J. Eng. Mech. Div., Proc. ASCE* 108 (EM1): 19-31.

Dravinski, M. (1982c) Influence of Interface Depth upon Strong Ground Motion. *Bull. Seism. Soc. Am*. 72 (2): 597-614.

Dravinski, M. (1983) Scattering of Plane Harmonic SH Wave by Dipping Layers of Arbitrary Shape. *Bull. Seism. Soc. Am*. 73 (5): 1303-1319.

Dravinski, M. and Mossessian, T.K. (1987) Scattering of Plane Harmonic P, SV and Rayleigh Waves by Dipping Layers of Arbitrary Shape. *Bull. Seism. Soc. Am*. 77 (1): 212-235.

Drijkoningen, G.G. and Chapman, C.H. (1988) Tunneling Rays using the Cagnaird-De Hoop Method. *Bull. Seism. Soc. Am*. 78 (2): 898-907.

Espinosa, A.F.; Algermissen, S.T.; De las Casas, J. (1977) The Lima Earthquake of October 3, 1974: Intensity Distribution. *Bull. Seism. Soc. Am*. 67: 1429-1439.

Ewing, M.W.; Jardetzky, W.S.; Press, F. (1957) *Elastic Waves in Layered Media*. McGraw-Hill, New York. 380p.

Fah, D. (1996) Hybrid Methods for Simulating Site Effects. *Proc. 11th World Conf. Earthquake Eng*. Paper no. 2039.

Field, E.H. (1996) Spectral Amplification in a Sediment-Filled Valley Exhibiting Clear Basin-Edge-Induced Waves. *Bull. Seism. Soc. Am*. 86(4): 991-1005.

Finn, W.D.L.; Byrne, P.M.; Evans, S. and Law, T. (1996) Some Geotechnical Aspects of the Hyogo-ken Nambu (Kobe) Earthquake of January 17, 1995. *Can. J. Civ. Eng.* 23 (3):778-796.

Frankel, A. (1993a) Effects of Three-Dimensional Bedrock Topography on Earthquake Motions in Sedimantary Basins. In: *Earthquake Induced Ground Failure Hazards*. National Academy Press, Washigton, D.C. pp1-8.

Frankel, A. (1993b) Three-Dimensional Simulation of Ground Motion in the San-Bernandino Valley, California, for Hypothetical Earthquakes on the San Andreas Fault. *Bull. Seism. Soc. Am*. 83 (4): 1020-1041.

Frankel, A. and Vidale, J. (1992) A Three Dimensional Simulation of Seismic Waves in the Santa Clara Valley, California from a Loma Prieta Aftershock. *Bull. Seism. Soc. Am*. 82 (5): 2045-2074.

Fuchs, K. and Schulz, K. (1976) Tunneling of Low-Frequency Waves through the Subcrustal Lithosphere. *J. Geophys*. 42: 175-190.

Gao, S.; Liu, H.; Davis, P.M. and Knopoff, L. (1996) Localized Amplification of Seismic Waves and Correlation with Damage due to the Northridge Earthquake: Evidence for Focussing in Santa Monica. *Bull Seism. Soc. Am*. 86: S209-S230

Grant-Taylor, T.L. (1959) Geology of the Hutt Valley. *Proceedings of the N.Z. Ecological Society*. 6:31-35.

Grant-Taylor, T.L. (1967) Fault Movement and Deformation on the Wellington Fault in the Wellington Region. *NZ. Geol. Survey Rep*. 27, 14p.

Graves, R. and Somerville, P. (1995) Seismic Zonation of Urban Regions Located in Sedimentary Basins. *Proc 5th Intl. Conf. Seismic Zonation*, Nice, France. pp 1035-1042.

Graves, R.W. (1993) Modelling Three-Dimensional Site-Response Effects in the Marina District, San Francisco, California. *Bull. Seism. Soc. Am*. 83(5): 2045-2074.

Graves, R.W. (1995) Preliminary Analysis of Long Period Basin Response in the Los Angeles Region from the 1994 Northridge Earthquake. *Geophys. Res. Lett*. 22 (2): 101-104.

Graves, R.W.; Pitarka, A. and Somerville, P.G. (1998) Ground Motion Amplification in the Santa Monica Area: Effects of Shallow Basin-Edge Structure. *Bull. Seism. Soc. Am*. 88 (5): 1224-1242.

Hartzell, S.; Cranswick, E.; Frankel, A. and Meremonte, M. (1997) Variablility of Site Response in the Los Angeles Urban Area. *Bull. Seism. Soc. Am*. 87: 1377-1400.

Haskell, N.A. (1953) The Dispersion of Surface Waves on Multi-Layered Media. *Bull. Seism. Soc. Am*. 43: 17-34.

Haskell, N.A. (1960) Crustal Reflection of Plane SH Waves. *J. Geophs. Res*. 65 (12): 4147-4150.

Helmberger, D.V. and Vidale, J.E. (1988) Modelling Strong Ground Motions Produced by Earthquakes with Two-Dimensional Numerical Codes. *Bull. Seism. Soc. Am*. 78: 109-121.

Higashi, S. (2000) Simulation of Strong Motion During the 1995 Hyogo-Ken Nanbu Earthquake by using the 2D/3D Pseudospectral Method. *Proc 12th World Conf. Earthquake Eng.*, Auckland, New Zealand. Paper No. 1751/4/A.

Hill, J.; Harley, B.; Murphy, M. and Schuster, G. (1990) Propagation and Resonance of SH Waves in the Salt Lake Valley, Utah. Bull. *Seism. Soc. Am*. 80 (1): 23-42.

Hisada, Y. and Yamamoto, S. (1996) One-, Two- and Three-Dimensional Site Effects in Sediment-Filled Basins. *Proc. 11th World Conf. Earthquake Eng.*, Acupulco, Mexico. Paper No. 2040

Hisada, Y.; Aki, K. and Teng, T.I. (1993) Three-Dimensional Simulations of Surface Wave Propagation in the Kanto Sedimentary Basin, Japan. Part 2: Application of the Surface Wave BEM. *Bull. Seism. Soc. Am*. 83: 1700-1720.

Hisada, Y.; Bao, H.; Bielak, J.; Ghattas, O. and O'Hallaron, D.R. (1998) Simulations of Long-Period Ground Motions during the 1995 Hyogoken-Nanbu (Kobe) Earthquake using 3D Finite Element Method. *Proc. 2nd Intl. Symposium on the Effect of Surface Geology on Seismic Ground Motion*, Yokohama, Japan, Dec. 1-3, 1998.

Hudson, J.A. (1962) The Total Internal Reflection of SH Waves. *Geophys. J. Royal Astr. Soc*. 6: 509-531.

Hudson, J.A. (1963) SH Waves in a Wedge-shaped Medium. *Geophys. J. Royal Astr. Soc*. 7 (5): 517-546.

Hudson, J.A. (1980) *The Excitation and Propagation of Elastic Waves*. Cambridge University Press, UK. 224p.

Hudson, J.A. and Knopoff, L. (1964) Transmission and Reflection of Surface Waves at a Corner: 1. Love Waves. *J. Geophys. Res*. 69 (2): 275-280.

Ingham, C.E. (1971) Elastic Properties of Rock: Wellington Urban Motorway Tunnel. *Department of Scientific and Industrial Research Geophysics Division Report* No. 71. N.Z.

Inoue, T. and Miyatake, T. (1997) 3-D Simulation of Near-Field Strong Ground Motion: Basin Edge Effect Derived from Rupture Directivity. *Geophys. Res. Lett*. 24 (8): 905-908.

Ishibashi, I. and Zhang, X. (1993) Unified Dynamic Shear Moduli and Damping Ratios of Sand and Clay. *Soils and Foundations* 33 (1): 182-191.

Jackson, P.S. (1971) The Focussing of Earthquakes. *Bull. Seism. Soc. Am*. 61: 685-695.

Kato, K.; Aki, K. and Teng, TL. (1993) Three-Dimensional Simulations of Surface Wave Propagation in the Kanto Sedimentary Basin, Japan. Part 1: Application of the Surface Wave Gaussian Beam Method. *Bull. Seism. Soc. Am*. 83: 1676-1699.

Kawase, H. (1988) Time-Domain Response of a Semi-Circular Canyon for Incident SV, P and Rayleigh Waves Calculated by the Discrete Wavenumber Boundary Element Method. *Bull. Seism. Soc. Am*. 78: 1415-1437.

Kawase, H. (1996) The cause of the Damage Belt in Kobe: “The Basin-Edge Effect”, Constructive Interference of the Direct S-Wave with the Basin Induced Diffracted/Rayleigh Waves. *Seismol. Research Lett*. 67 (5): 25-34.

Kawase, H. and Aki, K. (1989) A Study on the Response of Soft Basin for Incident S, P and Rayleigh Waves with Special Reference to the Long Duration Observed in Mexico City. *Bull. Seism. Soc. Am*. 79 (5): 1361-1382.

Kawase, H. and Aki, K. (1990) Topography Effect at the Critical SV-Wave Incidence: Possible Explanation of Damage Pattern by the Whitter Narrows, California Earthquake of 1 October 1987. *Bull. Seism. Soc. Am*. 80: 1-22.

Kawase, H. and Iwata, T. (2000) Simultaneous Simulation for Kobe: What we have learned at ESG98. *Proc. 12th World Conf. Earthquake Eng.*, Auckland, New Zealand. Paper No. 2684.

Kawase, H.; Matsushima, S.; Graves, R.W. and Somerville, P.G. (2000) Strong Motion Simulation of Hyogo-ken Nanbu (Kobe) Earthquake Considering both the Heterogeneous Rupture Process and the 3-D Basin Structure. *Proc. 12th World Conf. Earthquake Eng.*, Auckland, New Zealand. Paper No. 0990.

Kawase, H.; Matsushima, S.; Graves, R.W. and Somerville, P.G. (1997) Does the "Basin-Edge Effect" depend on the Incident Wavefield? *Seismol. Res. Lett*. 68 (2): 311 (abstract).

Kazuyoshi, K. (1995) Practical Estimates of Site Response: State-of-Art-Report. *Proc. 5th Intl. Conf. Seismic Zonation*, Part III: 1878-1907.

Keller, J.B. and Rubinow, S.I. (1960) Asymptotoic solution of eigen value problems. *Ann. Phys*. 9: 24-75.

Khair, K.R.; Datta, S.K. and Shah, A.H. (1989) Amplification of Obliquely Incident Seismic Waves by Cylindrical Alluvial Valleys of Arbitrary Cross-Sectional Shape: Part I: Incident P and SV Waves. *Bull. Seism. Soc. Am*. 79 (3): 610-630.

Khair, K.R.; Datta, S.K. and Shah, A.H. (1991) Amplification of Obliquely Incident Seismic Waves by Cylindrical Alluvial Valleys of Arbitrary Cross-Sectional Shape: Part II: Incident SH and Rayleigh Waves. *Bull. Seism. Soc. Am*. 81 (2): 346-357.

Kim, J. and Papageorgiou, A.S. (1993) Discrete Wavenumber Boundary Element Method for 3-D Scattering Problems. *J. Eng. Mech. Div., Proc. ASCE* 119 (3): 603-624.

King, J.L. and Tucker, B.E. (1984) Observed Variations of Earthquake Motion Across a Sediment-Filled Valley. *Bull. Seism. Soc. Am*. 74 (1): 137-151.

Kosloff, R. and Kosloff, D. (1986) Absorbing Boundaries for Wave Propagation Problems. *J. Comp. Phys*. 1 (63): 363-376.

Kouoh-Bille, L. and Wirgin, A. (1995) On the Validation of Resonance Frequencies of Sedimentary Basins using Semi-Classical (EBK) Method for Discretezed Domain. *Proc 5th Intl. Conf. Seismic Zonation*, Nice, Frace, October 1995. Vol. 2: 1611-1618.

Kubo, K. and Isoyama, R. (1980) Damage to Buried Utility Pipes in the 1978 Miyagiken-Oki Earthquake. *Proc 7th World Conf. Earthquake Eng*., Istanbul, Turkey, vol 8, pp 225-232.

Kuhlemeyer, P.L. and Lysmer, J. (1973) Finite Element Method Accuracy for Wave Propagation Problems. *J. Soil Mech. and Foundations Division, ASCE.* 199 (SM5): 421-427.

Larkin, T. and Marsh, J. (1991) 2-D Non-Linear Site Response Analysis. *Bull. N.Z. Natl. Soc. Earthquake Eng*. 25 (3): 222-229.

Lermo, J. and Charvez-Garcia, E.J. (1994) Are Micro-tremors Useful in Site Response Evaluation. *Bull. Seism. Soc. Am.* 84 (5): 1350-1364.

Lensen, G.J. (1958) The Wellington Fault from Cook Straight to Manawatu Gorge. *NZ. J. Geol. Geophys*. 1: 178-196.

Lewis, K.B. (1989) A Reversal of Throw and Change of Trend on the Wellington Fault in Wellington Harbour. *N.Z. J. Geol. Geophys*. 32: 293-298.

Ling, H. and Rial, J.A. (1994) Asymptotic Analysis of SH-wave Modes in Geologic Resonators (Sedimentary Basins) of Non-Separable Geometry. *Wave Motions,* 19: 245-270.

Lomnitz, C.; Flores, J.; Novaro, O.; Seligman, T.H. and Esquivel, R. (1999) Seismic Coupling of Interface Modes in Sedimentary Basins: A Recipe for Disaster. *Bull. Seism. Soc. Am*. 89 (1): 14-21.

Loo, H.Y. and Jin, X.S. (1984) Finite-Element Analysis for Ground Motion of 1976 Tangshan Earthquake. *Proc. 8th World Conf. Earthquake Eng*., Vol II: 343-400.

Love, A.E.H. (1911) *Some Problems of Geodynamics*. Cambridge University Press.

Luco, J.E. and De Barros, F.C.P. (1995) Three-Dimensional Response of a Layered Cylindrical Valley Embedded in a Layered Half-Space. *Earthq. Eng. and Struct. Dyn*. 24: 109-125.

Luokakis, K.E. and Bielak, J. (1995) Seismic Response of 2D-Valleys: Local Site Effects. *Proc. 3rd Int. Conf. Recent Adv. in Geotechnical Earthquake Eng. Soil Dyn*. vol II: 595-599.

Lysmer, J. and Drake, L.A. (1971) Propagation of Love Waves Across Non-Horizontally Layered Structures. *Bull. Seism. Soc. Am*. 61: 1233-1251.

Lysmer, J. and Drake, L.A. (1972) A Finite Element Method for Seismology. In*: Methods in Computational Physics*. 11: 181-215. Ed. BA. Bolt, Academic Press, New York.

Lysmer, J. and Kuhlemeyer, R.L. (1969) Finite Dynamic Model for Infinite Media. *Journal of the Engineering Mechanics Division, ASCE*. 95 (EM4): 859-877.

Lysmer, J. and Waas, G. (1972) Shear Wave in Plane Infinite Structure. *Journal of the Engineering Mechanics Division, ASCE*. 98 (EM1): 85-105.

Lysmer, J.; Udaha, T.; Tsai, C.F. and Seed, H.B. (1975) *FLUSH: A Computer Program for Approximate 3-D Anaylsis of Soil Structure Systems*. Report EERC 74-4, Earthquake Engineering Research Center, University of California, Berkley, 83p.

Manoogian, M.E. and Lee, V.W. (1995) Scattering of SH-Waves by Arbitrary Surface Topography. *Proceedings of the Third International Conference on Recent Advances in Geotechnical Earthquake Engineering and Soil Dynamics*, St Louis, April 1995. Paper No. 10.03 Vol II: 665-670.

Marsh, E.J. (1992) Two Dimensional Nonlinear Seismic Ground Response Studies. *Research Report* No. 536, School of Engineering, University of Auckland, N.Z.

Maruo, Y.; Iwata, T. and Irikura, K. (1998) Site effects of Kobe Large Earthquake Disaster Belt using aftershock data. *Proc. 2nd Intl. Symposium on the Effects of Surface Geology on Seismic Ground Motion*, Yokohama, 1998, pp 537-544.

Mathworks (1997) *MATLAB Version 5.1: The Language of Technical Computing*. The Mathworks Inc, Natick, MA.

McKay, A. (1892) On the geology of Marlborough and Southeast Nelson. Part 2. *NZGS Reports of Geological Explorations During 1890-91* (21): 1-28.

Moczo, P. and Bard, P.Y. (1993) Wave-Diffraction, Amplification and Differential Motion Near Strong Lateral Discontinuities. *Bull. Seism. Soc. Am*. 83 (1): 85-106.

Motosaka, M. and Nagano, M. (1995) Effects of Deep Irregular Underground Structure and Shallow Surface Geology on the Amplification Characteristics of Ground Motions in Kobe City. *Trans. AGU*. 76 (4b): S21F-12.

Motosaka, M. and Nagano, M. (1996) Analysis of Ground Motion Amplification Characteristics in Kobe City Considering Deep Irregular Underground Structure - Interpretation of the Heaily Damaged Belt Zone During the 1995 Hyogo-Ken Nambu earthquake. *J. Phys. Earth* 44: 577-590.

Motosaka, M. and Nagano, M. (1997) Analysis of Amplification Characteristics of Ground Motion in the Heavily Damaged Belt Zone During the 1995 Hyogo-Ken Nanbu Earthquake. *Earthq. Eng. and Struct. Dyn*. 26: 377-393.

Nagano, M. (1998) Amplification characteristics of ground motions in deep irregular underground structure with vertical discontinuity. *Proc. 2nd Intl. Symposium on the Effects of Surface Geology on Seismic Ground Motion*, Yokohama, 1998, pp 859-866.

Niousha, A. and Motosaka, M. (1998) Analysis of the Ground Motion Directionality Focused on Irregular Undrground Structure. *Proc. 2nd Intl. Symposium on the Effects of Surface Geology on Seismic Ground Motion*, Yokohama, 1998, pp 867-872.

Ohtsuki, A. and Harumi, K. (1983) Effect of Topography and Subsurface Inhomogeneities on Seismic SV Waves. *Earthquake Eng. Struc. Dyn*. 11: 441-462.

Olsen, K.B. and Archuleta, R.J. (1996) Three-Dimensional Simulation of Earthquakes on the Los Angeles Fault System. *Bull. Seism. Soc. Am*. 86: 575-596.

Olsen, K.B. and Benites, R.A. (1998) 3-D Simulations of Earthquakes on the Wellington Fault. http://www.crustal.ucsb.edu/~kbolsen/Wellington/wel_rep.html.

Osborne, N. (1999) The Basin Edge Effect in the Lower Hutt, Wellington using Weak Ground Motions. *BSc Honours Thesis*, School of Earth Sciences, Victoria University of Wellington, New Zealand.

Papageorgiou, A.S. and Pei, D. (1994) 3-D Response of Cylindrical Valleys of Arbitrary Cross-Section to Seismic Waves Incident from any Azimuthal Direction. *Proc. 5th US Nat. Conf. On Earthquake Eng*., Chicago. Vol III: 45-54.

Park, R.; Billings, IJ.; Clifton, GC.; Cousins, J.; Filiatrault, A.; Jennings, DN.; Jones, LCP.; Perrin, ND.; Rooney, SL.; Sinclair, J.; Spurr, DD.; Tanaka, H. and Walker, G. (1995) The Hyogo-ken Nambu Earthquake (The Great Hanshin Earthquake of 17

January 1995): Report of the NZNSEE Reconnaissance Team. *Bull. NZ. Natl. Soc. Earthquake Eng*. 28 (1): 1-9.

Pei, D. and Papageorgiou, A.S. (1993) Study of the response of Cylindrical Alluvial Valleys of Arbitrary Cross-Section to Obliquely Incident Seismic Waves using the Discrete Wavenumber Boundary Element Method. *Proceedings of the 6th Intl. Conf. on Soil Dyn. and Earthq. Eng*., Bath, 1993.

Pitarka, A. and Irikura, K. (1996) Basin Structure Effects on Long-Period Strong Motions in the San Fernando valley and the Los Angeles Basin. *Bull. Seism. Soc. Am*. 86 (1B): S126-S137.

Pitarka, A.; Irikura, K. and Iwata, T. (1997) Modelling of Ground Motion in the Higashinada (Kobe) area for an Aftershock of the 1995 January 17 Hyogo-ken Nanbu, Japan, Earthquake. *Geophys. J. Int*. 131: 231-239.

Pitarka, A.; Irikura, K.; Iwata, T. and Kagawa, T. (1996) Basin Structure Effects in the Kobe Area Inferred from the Modeling of Ground Motions from Two Aftershocks of the January 17, 1995, Hyogo-ken Nanbu Earthquake. *J. Phys. Earth*: 44: 563-576.

Pitarka, A.; Irikura, K.; Iwata, T. and Sekiguchi, H. (1998) Three-Dimensional Simulation of the Near-Fault Ground Motion for the 1995 Hyogo-ken Nanbu (Kobe), Japan, Earthquake. *Bull. Seism. Soc. Am*. 88 (2): 428-440.

Pitarka, A.; Takenaka, H. and Suetsugu, D. (1994) Modelling Strong Motion in Ashigara Valley for the 1990 Odawara, Japan Earthquake. *Bull. Seism. Soc. Am*. 84 (5): 1327-1335.

Poceski, A. (1969) The Ground Effect of the Scopie July 26 1963 Earthquake. *Bull. Seism. Soc. Am*. 59 (1): 1-22.

Prescott, W.H. (1982) Circumstances Surrounding the Preparation and Suppression of a Report on the 1868 California Earthquake. *Bull. Seism. Soc. Am*. 72 (6): 2389-2393.

Rassem, M.; Ghaobarah, A. and Heinebrecht, A.C. (1997) Engineering Perspective for the Seismic Site Response of Alluvial Valleys. *Earthq. Eng. and Struct. Dyn*. 26: 477-493.

Rayleigh, Lord (1885) On Waves Propagated along the Plane Surface of an Elastic Solid. *Proceedings of the London Mathematical Society*, 17: 4-11.

Rial, J.A. (1989a) Geologic Resonators of Arbitrary Geometry: Chaotic Behavior of Trapped Seismic Waves. In: *Engineering Seismology and Site Response: Proceedings of the 4th Intl. Conf. on Soil Dyn. and Earthq. Eng*., Mexico City, Mexico, October 1989. Editors: A.S. Cakmak and I. Herrera.

Rial, J.A. (1989b) Seismic Wave Resonances in 3-D Sedimentary Basins. *Geophys. J. Int*. 99: 81-90.

Rial, J.A. and Ling, H. (1992) Theoretical Estimation of the Eigenfrequencies of 2-D Resonant Sedimentary Basins: Numerical Computations and Analytical Approximations to the Elastic Problem. *Bull. Seism. Soc. Am*. 82 (6): 2350-2367.

Rial, J.A.; Saltzman, N.G. and Ling, H. (1992) Earthquake Induced Resonance in Sedimentary Basins. *American Scientist* 80: 566-578.

Ricker, N. (1940) The Form and Nature of seismic Wavelets and the Structure of Seismograms. *Geophysics* 5: 348-366.

Rodriguez-Zuniga, J.L.; Sanchez-Sesma, F.J. and Perez-Rocha, L.E. (1995) Seismic Response of Shallow Alluvial Valleys: The Use Of Simplified Models. *Bull. Seism. Soc. Am*. 85 (3): 890-899.

Sanchez-Sesma, F. (1987) Site Effects on Strong Ground Motion. *Soil Dyn. Earthquake Eng*. 6: 124-132.

Sanchez-Sesma, F. and Luzon, F. (1995) Seismic Response of Three-Dimensional Alluvial Valleys for Incident P, S, and Rayleigh Waves. *Bull. Seism. Soc. Am*. 85 (1): 269-284.

Sanchez-Sesma, F.; Chavez-Garcia, F. and Bravo, M. (1988) Seismic Response of a Class of Alluvial Valleys for incident SH Waves. *Bull. Seism. Soc. Am*. 78: 83-95.

Sanchez-Sesma, F.; Chavez-Garcia, F.; Suarez, M.A.; Bravo, M. and Perez-Rocha, L.E. (1988) On the Seismic Response of the Valley of Mexico. *Earthquake Spectra*. 4: 569-589.

Sanchez-Sesma, F.; Heitz, J.-F.; Bravo, M. (1989) Ground Motions on Stratified Alluvial Basins. In: *Engineering Seismology and Site Response: Proceedings of the 4th Intl. Conf. on Soil Dyn. and Earthq. Eng.*, Mexico City, Mexico, October 1989. Editors: A.S. Cakmak and I. Herrera.

Sanchez-Sesma, F.; Ramos-Martinez, J.; Perez-Rocha, L.E. (1993) The Seismic Response of Shallow Alluvial Valleys. *Proceedings of the 6th Intl. Conf. Soil Dyn. Earthq. Eng.*, Bath, 1993.

Sanchez-Sesma, F.J. (1985) Diffraction of Elastic SH Waves by Wedges. *Bull. Seism. Soc. Am*. 75 (5): 1435-1446.

Sanchez-Sesma, F.J. and Esquivel, J.A. (1979) Ground Motion on Alluvial Valleys under Incident Plane SH Waves. *Bull. Seism. Soc. Am*. 69: 1107-1120.

Sanchez-Sesma, F.J. and Velazquez, S.A. (1987) On the Seismic Response of a Dipping Layer. *Wave Motion* 9: 387-391.

Sanchez-Sesma, F.J.; Benites, R. and Bielak, J. (1996) The assessment of strong ground motion: What lies ahead. *Proc. 11th World Conf. Earthquake Eng*., Acapulco, Mexico. Paper no. 2014.

Schrivner, C.W and Helmberger, D.V. (1994) Seismic Waveform Modelling in the Los Angeles Basin. *Bull. Seism. Soc. Am*. 84 (5): 1310-1326.

Seed, H.B.; Idriss, I.M. and Dezfulian, H. (1970) Relationships between Soil Conditions and Building Damage in the Caracas Earthquake of July 29, 1967. *Earthquake Engineering Research Center Report* No. EERC 70-2.

Seed, H.B.; Wong, R.T.; Idriss, I.M. and Tokimatsu, K. (1986) Moduli and Damping Factors for Dynamic Analyses of Cohesionless Soils. *ASCE Journal of Geotechnical Engineering* 112 (11): 1016-1032.

Seki, T. and Nishikawa, T. (1988) Absorbing Boundaries for Wave Propagation Problems (Using Kosloff's Method in Absorbing Region. *Proc. 10th World Conf. Earthquake Eng*. vol II: 629-634.

Seligman, T.H.; Alvarez-Tostado, J.M.; Mateos, J.L. and Flores, J. (1989) Resonant Response Models for the Valley of Mexico-I; The Elastic Inclusion Approach. *Geophys. J. Int*. 99: 789-799.

Semblat, J.F.; Duval, A.M. and Dangla, P. (1999) BEM Analysis of Seismic Wave Amplification in Caracas. *Proc. 7th Intl. Symp. On Numerical Models in Geomechanics*, Graz, Austria, pp 275-280.

Shewchuck, J.R. (1996) Triangle: Engineering a 2D Quality Mesh Generator and Delaunay Triangulator. *First Workshop on Applied Computational Geometry* (Philidelphia, PA.), pp124-133, ACM, May 1996.

Shibuya, J. (1992) Amplitude of Surface Waves in Ground Motion on Alluvial Basins. *Proc. 10th World Conf. Earthquake Eng*. vol II: 629-634.

Smith, W.D. (1974) A Non-Reflecting Plane Boundary for Wave Propagation Problems. *J. Comp. Phys*. 15: 492-503.

Smith, W.D. (1975) The Application of Finite Element Analysis to Body Wave Propagation Problems. *Geophys. J. Astr. Soc*. 42:747-768.

Stephenson, W.R. (1974) Earthquake Induced Resonant Motion of Alluvium. *Bull. N.Z. Natl. Soc. Earthquake Eng*. 7 (3): 144-146.

Stephenson, W.R. (1975) Cellular Normal Modes of Alluvium Response. *Bull. N.Z. Natl. Soc. Earthquake Eng*. 8 (4): 245-254.

Stephenson, W.R. (1989a) Normal Modes of a "Cylindrical Valley of Alluvium. *Bull. N.Z. Natl. Soc. Earthquake Eng*. 22 (2): 76-80.

Stephenson, W.R. (1989b) Observation of a Directed Resonance in Soil Driven by Transverse Rock Motion. *Bull. N.Z. Natl. Soc. Earthquake Eng*. 22 (2): 81-89.

Stephenson, W.R. and Barker, P.R. (1992) Evaluation of the Sediment Properties in the Lower Hutt and Porirua Areas by Means of Cone and Seismic Cone Penetration Tests. *Bull. N.Z. Natl. Soc. Earthquake Eng*. 25(4):265-285.

Stevens, G.R. (1956a) Hutt Valley Artesian System. *N.Z. J. Sci. Tech*. 38B (3): 149-156

Stevens, G.R. (1956b) Stratigraphy of the Hutt Valley, New Zealand. *N.Z. J. Sci. Tech*. 38B (3): 201-235.

Stevens, G.R. (1958) The Wellington Fault. *Trans. Roy. Soc. NZ*. 85.

Stevens, G.R. (1990) *Rugged Landscape: The Geology of Central New Zealand*. DSIR, Wellington, New Zealand.

Stevens, G.R. (1991) *On Shaky Ground*. A Geological Guide to the Wellington Metropolitan Region. DSIR, Lower Hutt, New Zealand.

Stritharan, S. and McVerry, GH. (1992) Microzone Effects in the Hutt Valley in Records from a Strong-Motion Acceleograph Array. *Bull. N.Z. Natl. Soc. Earthquake Eng.* 25 (4): 246-264.

Taber, J.J. and Smith, E.G.C. (1992) Frequency Dependant Amplification of Weak Ground Motions in Porirua and Lower Hutt, New Zealand. *Bull. N.Z. Natl. Soc. Earthquake Eng*. 25 (4): 303-331.

Taber, J.J.; Stritharan, S.; McVerry, G.H. and Ansell, J.H. (1993) Site Effects from Seismic Shaking: A comparison of Strong and Weak Ground-Motion in Wellington City and the Hutt Valley. A Report to Earthquake and War Damage Commission.

Takemiya, H. and Adam, M. (1996) Why the Heaviest Damages Occurred in Kobe During the Hyogo-Ken Nanbu Earthquake. In: *The Kobe Earthquake: Advances in Earthquake Engineering*. Chapter 3: pp 39-58. Editor C.A. Brabbia. Computational Mechanics Publications, UK.

Takemiya, H. and Fujiwara, A. (1994) SH-Wave Scattering and Propagation Analyses at Irregular Sites by Time Domain BEM. *Bull. Seism. Soc. Am*. 84 (5): 1443-1455.

Tanaka, K.; Kurimoto, O. and Fukuwa, N. (2000) Effects of Underground Topographical Irregularity to Seismic Amplification in the Nobi Plain. *12th World Conference on Earthquake Engineering*, Auckland, New Zealand. Paper No. 805.

Thompson, W.T. (1950) Transmission of Elastic Waves through a Stratified Solid Medium. *J. Applied Physics*. 21: 89-93.

Toki, K.; Irikura, K. and Kagawa, T. (1995) Strong Motion Records in the Source Area of the Hyogoken-Nambu Earthquake, January 17, 1995, Japan. *J. Nat. Disaster Sci*. 16 (2): 23-30.

Tolstoy, I. (1973) *Wave propagation*. McGraw-Hill, USA. 466p.

Toshinawa, T. and Ohmachi, T. (1992) Love Wave Propagation in a Three-Dimensional Sedimentary Basin. *Bull. Seism. Soc. Am*. 82: 1661-1667.

Touhei, T. and Yoshida, N. (1988) A Coupled Boundary and FEM for the Time Marching Analysis. *Proc. 9th World Conf. Earthquake Eng*. II: 623-628.

Trifunac, M.D. (1971) Surface Motion of a Semi-Cylindrical Alluvial Valley for Incident Plane SH Waves. *Bull. Seism. Soc. Am*. 61: 1755-1770.

Tucker, B.E. and King, J.L. (1984) Dependance of Sediment-Filled Valley Response in Input Amplitude and Valley Properties. *Bull. Seism. Soc. Am*. 74(1): 153-165.

Van Dissen, R.J. and Berryman, K.R. (1990) Seismic Hazard Assessment of the Wellington-Hutt Valley Segment of the Wellington Fault. *Regional Natural*

Disaster Reduction Plan - Seismic Hazard, 1989 Study, Part 5. Department of Scientific and Industrial Research.

Van Dissen, R.J. and Berryman, K.R. (1991) Timing, Size and Reccurence Interval of Prehistoric Earthquakes in the Wellington Region, New Zealand. In: *Proceedings, Pacific Conference on Earthquake Engineering*, Auckland, New Zealand 3: 239-249.

Van Dissen, R.J. and Berryman, K.R. (1996) Surface rupture earthquakes over the last ~1000 years in the Wellington region, New Zealand, and implications for ground shaking hazard. *J. Geophys. Res*. 101 (B3): 5999-6019.

Van Dissen, R.J.; Berryman, K.R.; Pettinga, J.R. and Hill, N. (1992a) Paleoseismicity of the Wellington-Hutt Valley Segment of the Wellington Fault, North Island, New Zealand. *N.Z. J. Geol. Geophys*. 35: 165-176.

Van Dissen, R.J.; Taber, J.J.; Stephenson, W.R.; Stritharan, S.; Read, S.A.L.; McVerry, G.H.; Dellow, G.D. and Barker, P.R. (1992b) Earthquake Ground Shaking Hazard Assessment for the Lower Hutt and Porirua Areas, New Zealand. *Bull. N.Z. Natl. Soc. Earthquake Eng*. 25 (4): 286-302.

Vidale, J.E. and Helmberger, D.V. (1988) Elastic Finite Difference Modelling of the 1971 San Fernando, California Earthquake. *Bull. Seism. Soc. Am*. 78 (1): 122-141.

Weinstein, L.A. (1969) *Open Resonators and Open Waveguides*. The Golem Press, Boulder, Colorado.

Weischet, W. (1963) The Distribution of the Damage Caused by the Earthquake in Valdivia in Relation to the Form of the Terrane. *Bull. Seism. Soc. Am*. 53 (5): 1259-1262.

Wirgin, A. (1995) Resonant Response of a Soft Semi-Circular Cylindrical Basin. *Bull. Seism. Soc. Am*. 85 (1): 285-299.

Wong, T.L. And Trifunac, MD. (1974) Surface Motion of a Semi-Elliptical Alluvial Valley for Incident Plane SH Waves. *Bull. Seism. Soc. Am*. 64: 1389-1408.

Yamanaka, H.; Seo, K. and Samano, T. (1989) Effects of Sedimentary Layers on Surface-Wave Propagation. *Bull. Seism. Soc. Am*. 79 (3): 631-644.

Yuan, Y.; Yang, B. and Huang, S. (1992) Damage Distribution and Estimation of Ground Motion in Shidian (China) Basin. *Proc. Int. Symp. Effects of Surface Geology on Seismic Motion*, 25-27 March, Odawara, Japan. vol 1, pp 281-286

Zahradnik, J. and Hron, F. (1987) Seiesmic Ground Motion of Sedimentary Valleys: Example La Molina, Lima, Peru. *J. Geophys*. 62: 31-37.

Zeng, Y. and Benites, R. (1998) Seismic Response of Multi-Layered Basins with Velocity Gradients upon Incidence of Plane Shear Waves. *Earthq. Eng. and Struct. Dyn*. 27: 15-28.

Zhang, B. and Papageorgiou, AS. (1995) Seismic Response of a Linear, 2-D Model of the Marina District. *Proc. 3rd Int. Conf. Recent Adv. in Geotechnical Earthquake Eng. Soil Dyn*. Vol II: 567-570.

Zhou, T. and Dravinski, M. (1994) Resonance Prediction of Deep Sediment Valleys Through an Eigenvalue Method. *Geophs. J. Int*. 117: 749-762.

Appendix 1: ADDITIONAL RESULTS FROM FEM MODELLING IN Chapter 6

1.1 FOURIER SPECTRAL RATIOS FOR DIFFERENT EDGE-SLOPE ANGLES

Figures A1.1.1 – A1.1.3. Contour plots of Fourier spectral ratios (FSR) for simulations S1-S9 (see Table 6.1), each with different edge-slope angles. Maximum FSR is shown to the right while the edge-slope geometry is shown to the left of the main plot.

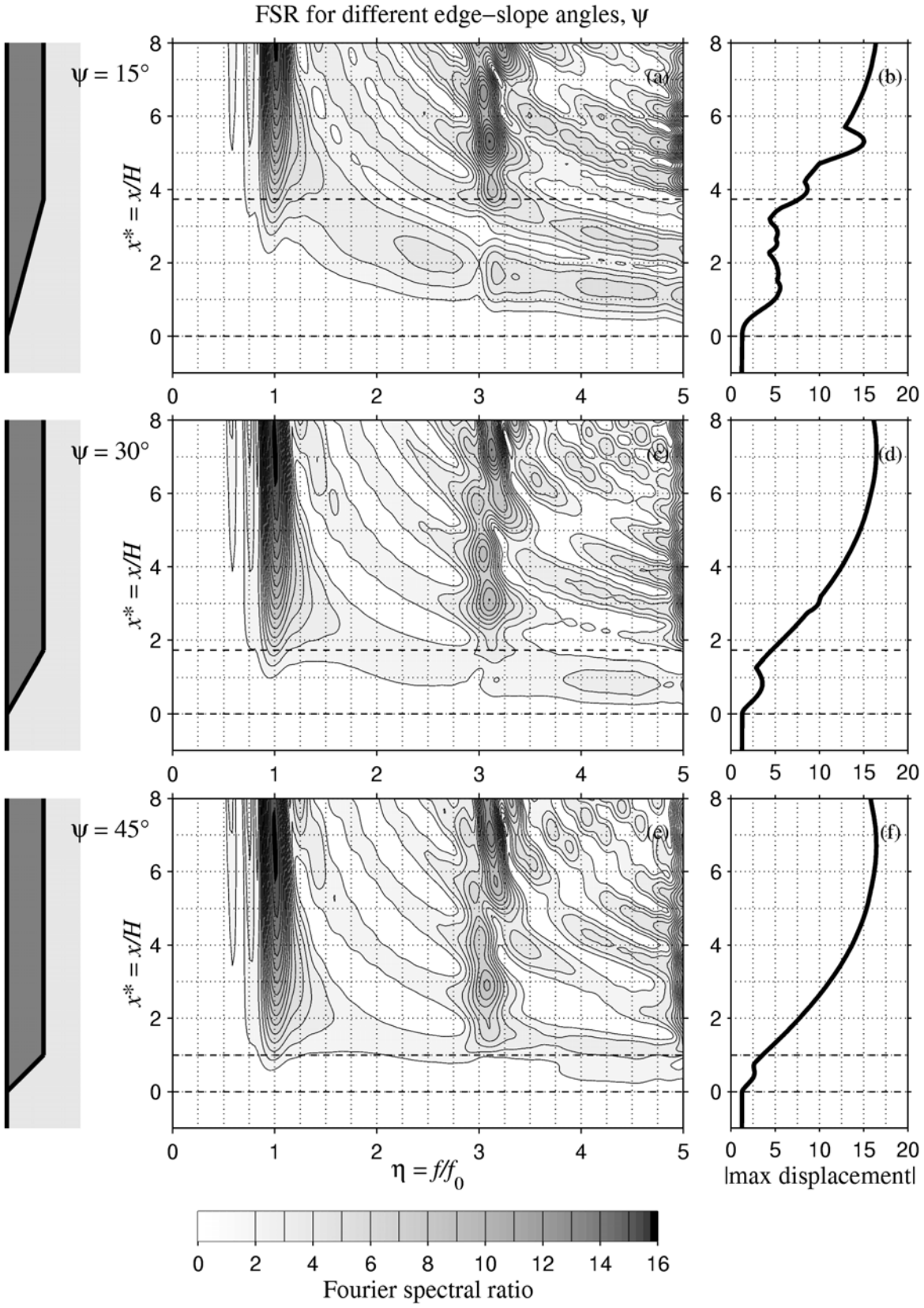

Figure A1.1.1. Simulations S1 (ψ = 15°), S2 (ψ = 30°) and S3 (ψ = 45°).

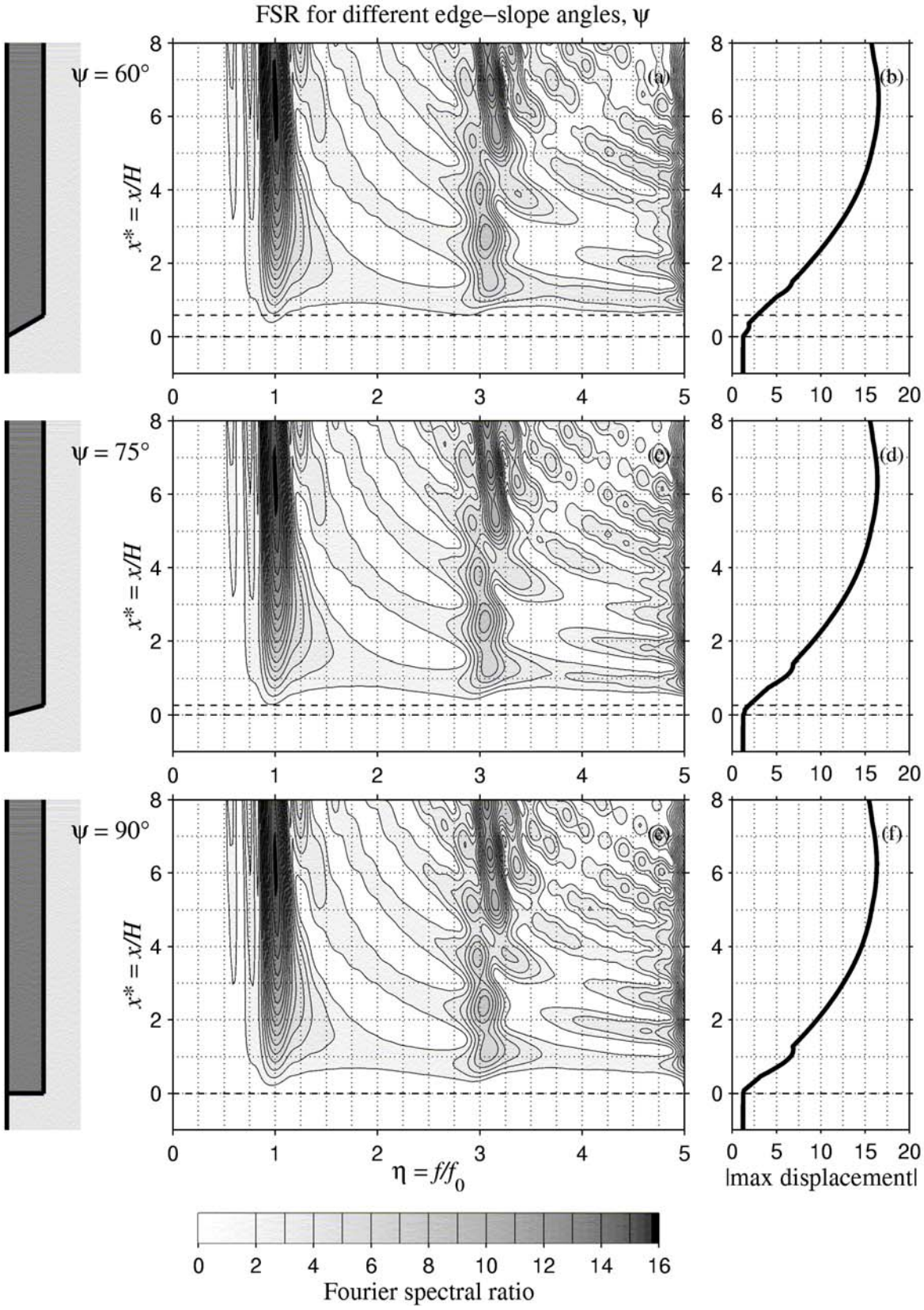

Figure A1.1.2. Simulations S4 ($\psi = 60°$), S5 ($\psi = 75°$) and S6 ($\psi = 90°$).

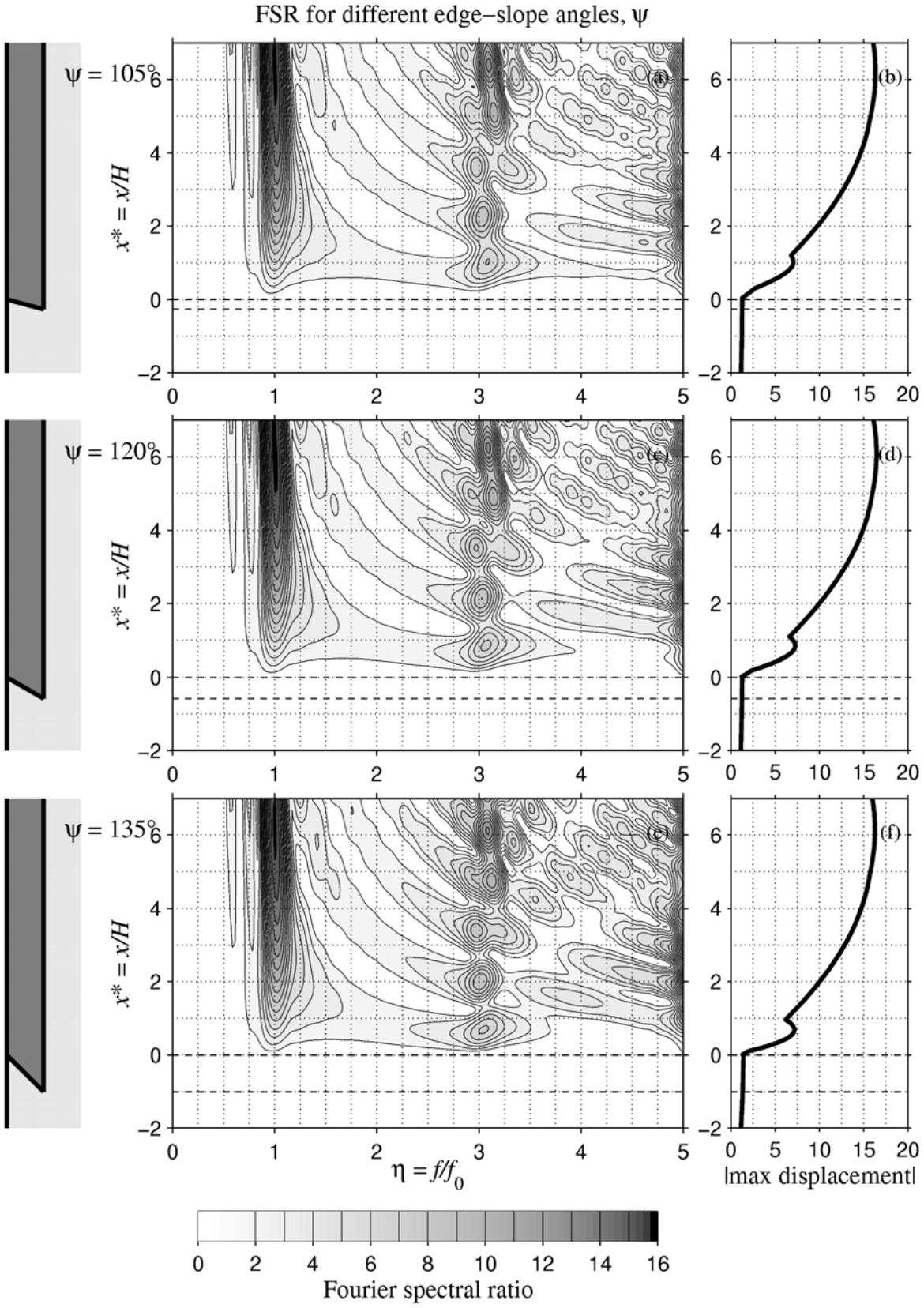

Figure A1.1.3. Simulations S7 (ψ = 105°), S8 (ψ = 120°) and S9 (ψ = 135°).

Appendix 2: CATALOGUE OF RESULTS FROM THE ARRAY IN Chapter 9

2.1 DISPLACEMENT TIME HISTORIES

Figures A2.1.1 – A2.1.13. A 10-second window of the displacement time histories generated by the arrival of the shear wave is shown for each of the 13 earthquakes selected for analysis in Chapter 9. Displacement has been calculated by integration from the recorded velocity trace. The horizontal components shown have been rotated 52° clockwise from north and east into edge-normal (EN) and edge-parallel (EP). Displacement amplitude is normalised against peak horizontal displacement in the recording at the rock site, Station E01. Traces have been positioned on the page with respect to the distance of the recorder to the edge of the valley. Table 9.2 gives details on each recorded event, while Figure 9.5 indicates the epicentral location. Table 9.1, Figure 9.1 and Figure 9.4 provide details on the positioning of the array recording stations.

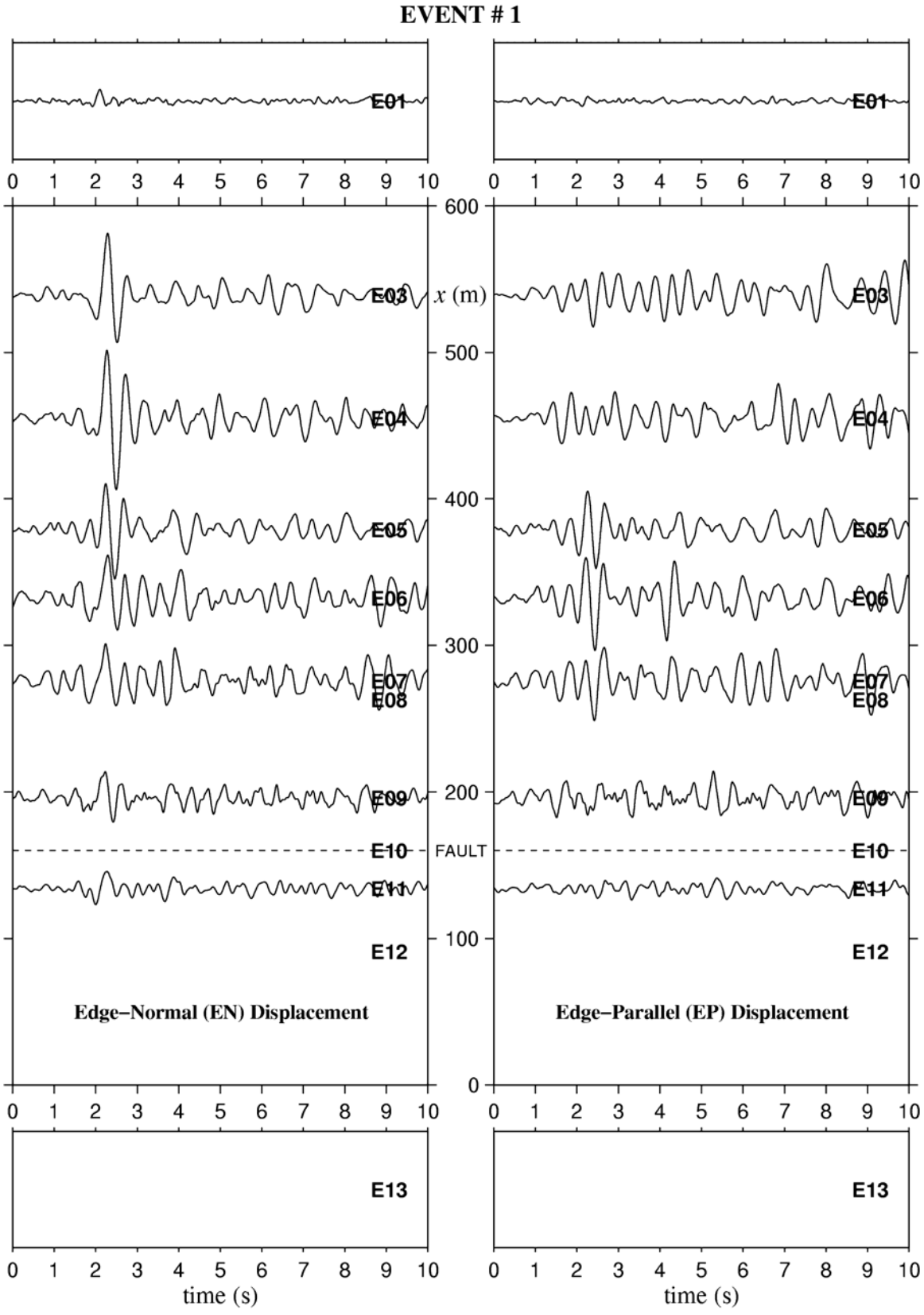

Figure A2.1.1. Shear-wave displacement from Event 1.

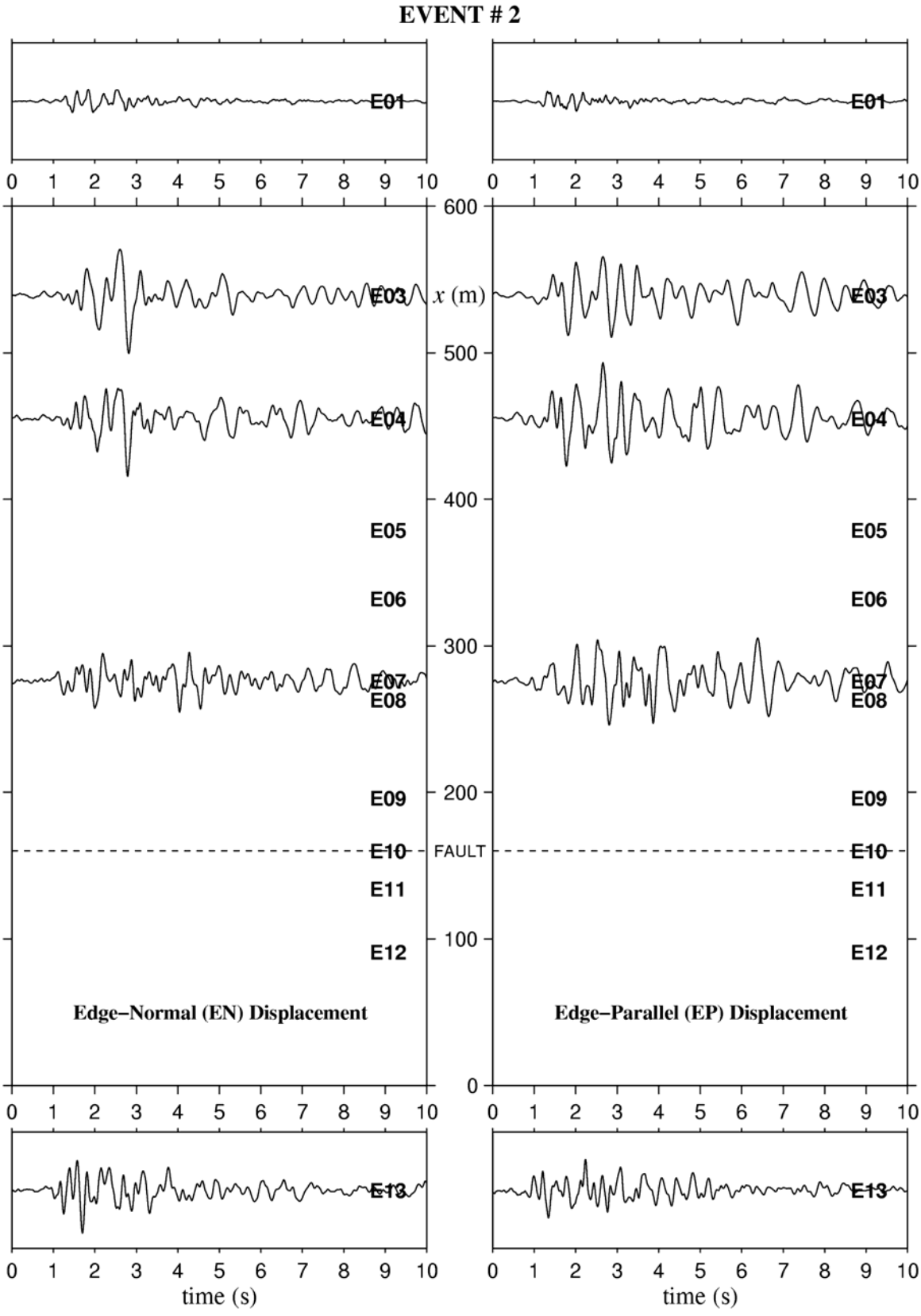

Figure A2.1.2. Shear-wave displacement from Event 2.

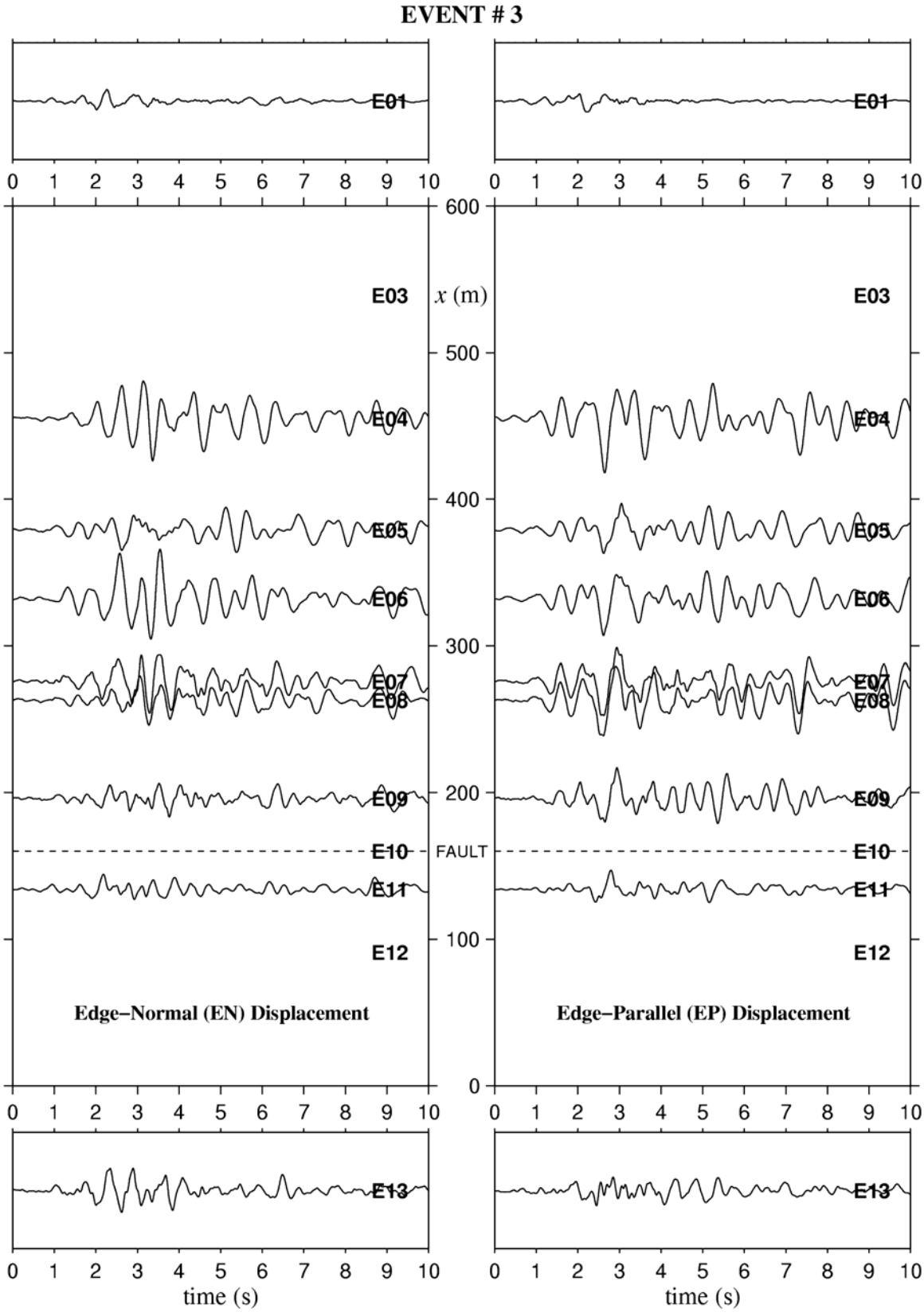

Figure A2.1.3. Shear-wave displacement from Event 3.

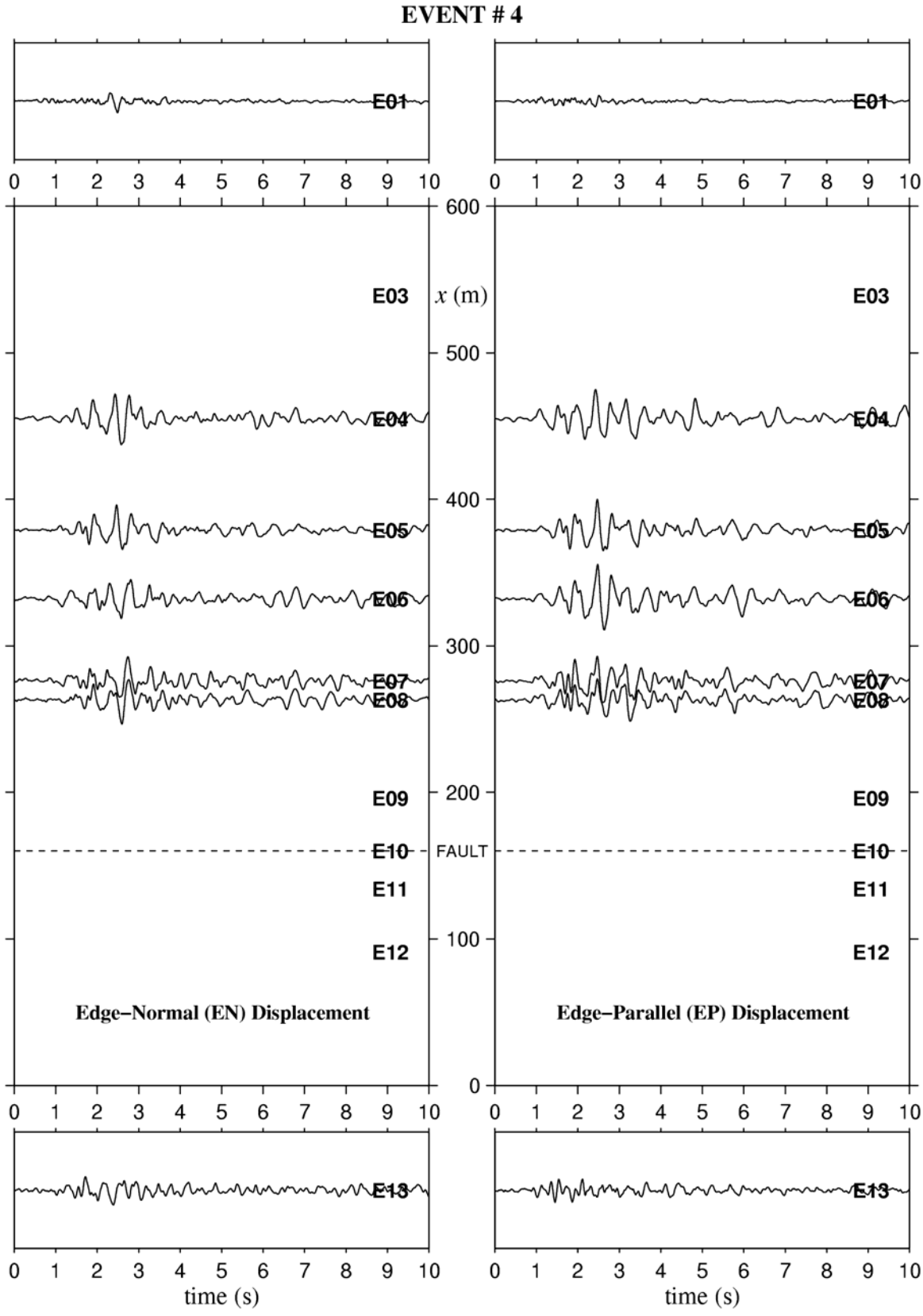

Figure A2.1.4. Shear-wave displacement from Event 4.

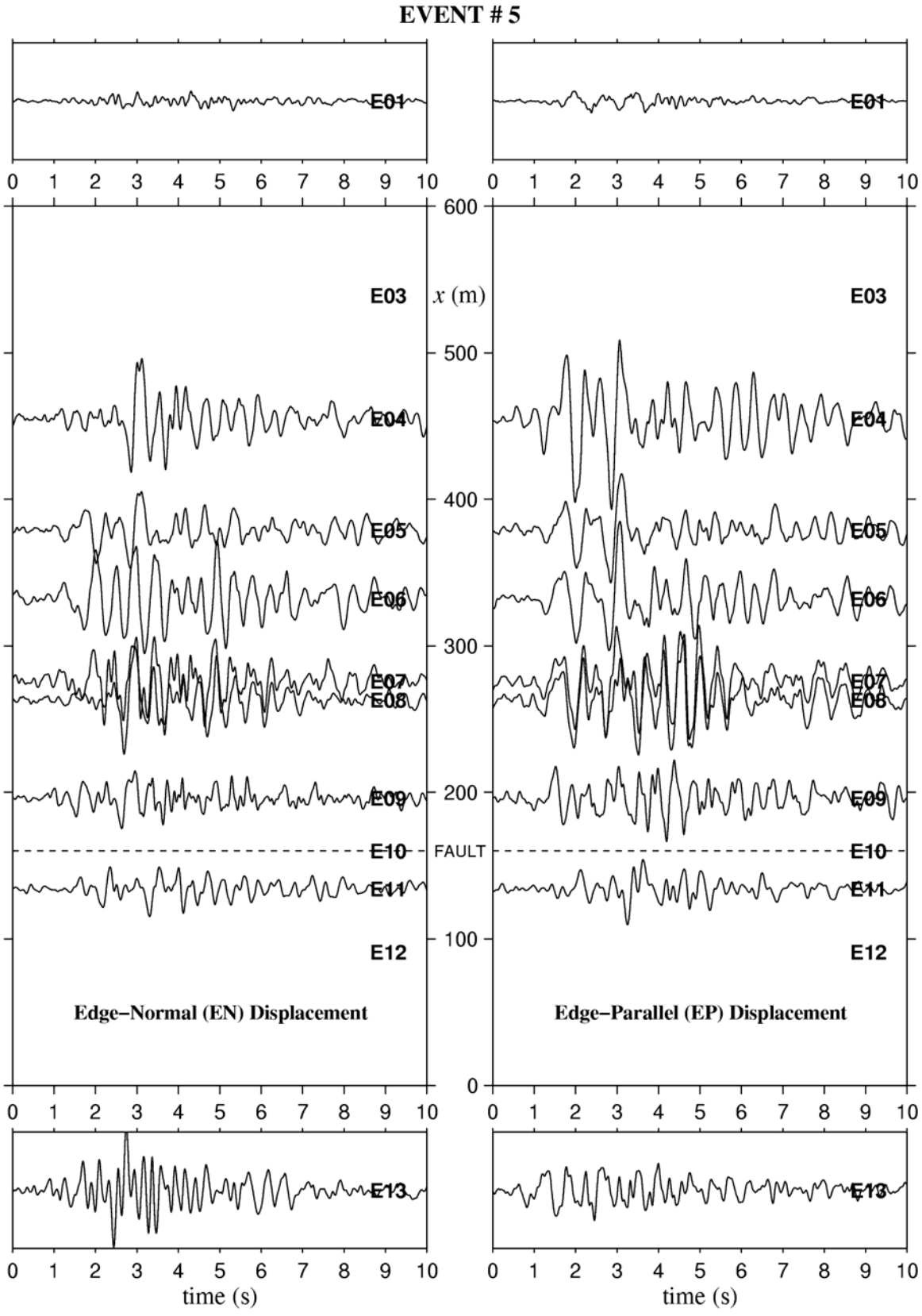

Figure A2.1.5. Shear-wave displacement from Event 5.

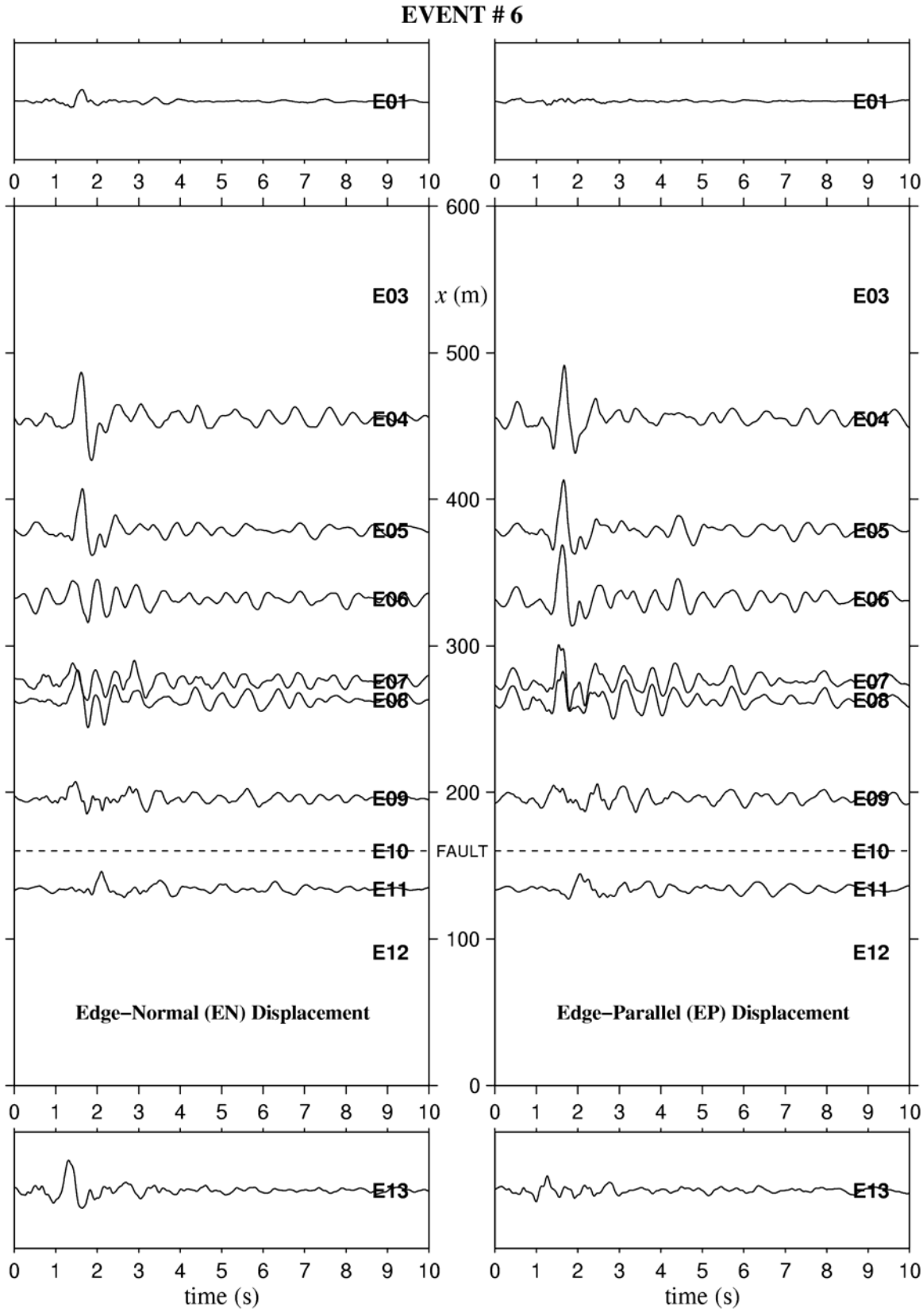

Figure A2.1.6. Shear-wave displacement from Event 6.

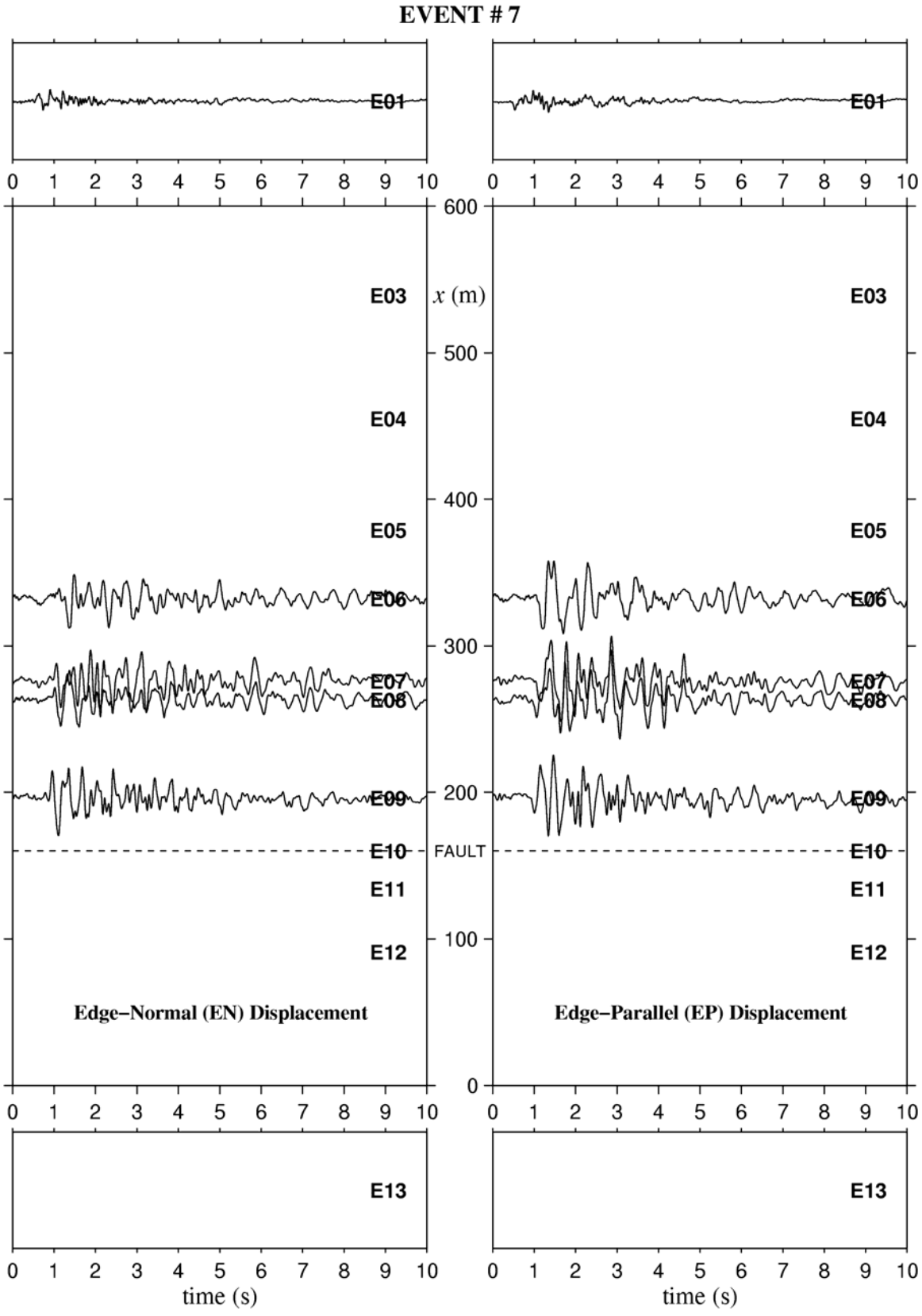

Figure A2.1.7. Shear-wave displacement from Event 7.

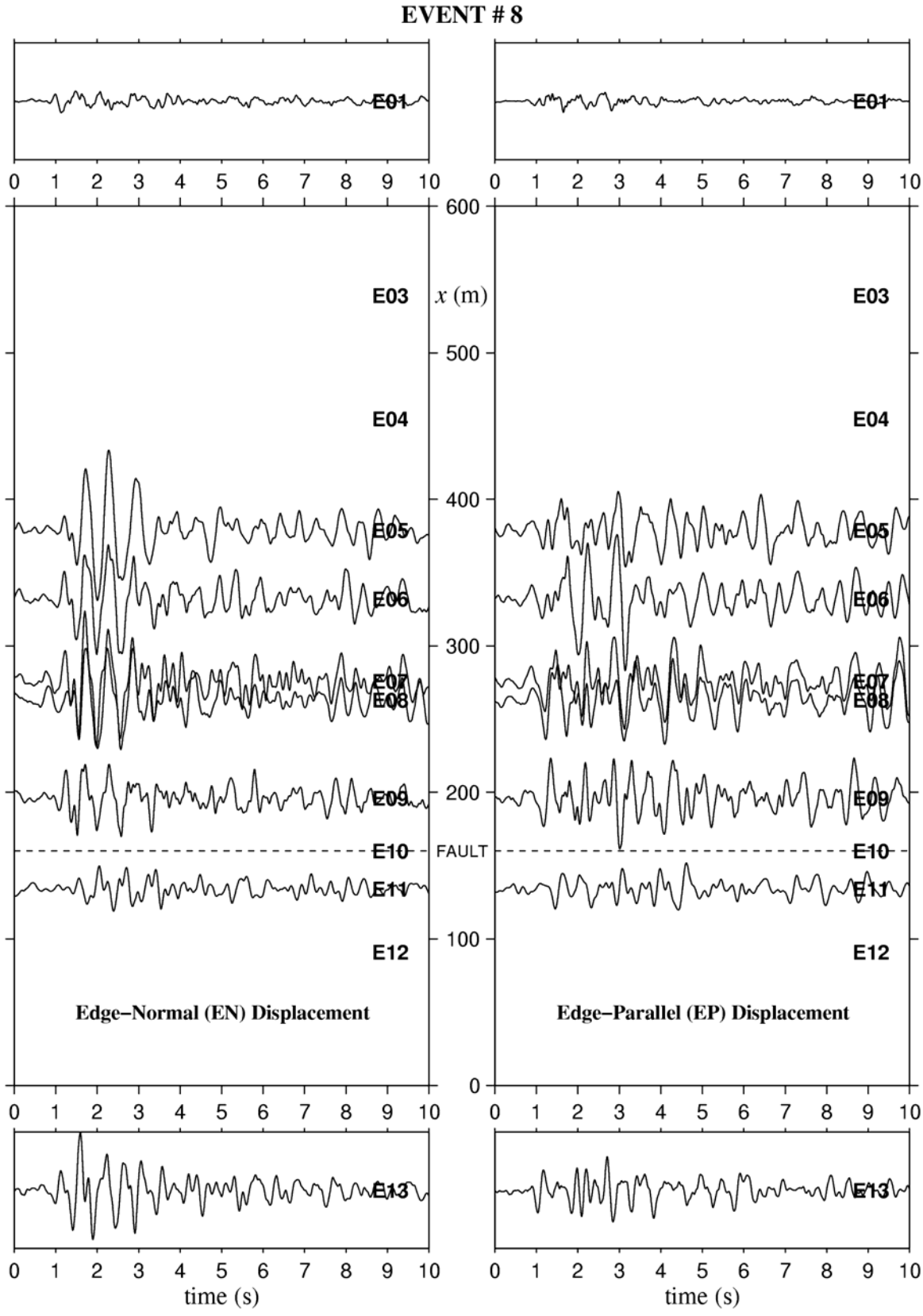

Figure A2.1.8. Shear-wave displacement from Event 8.

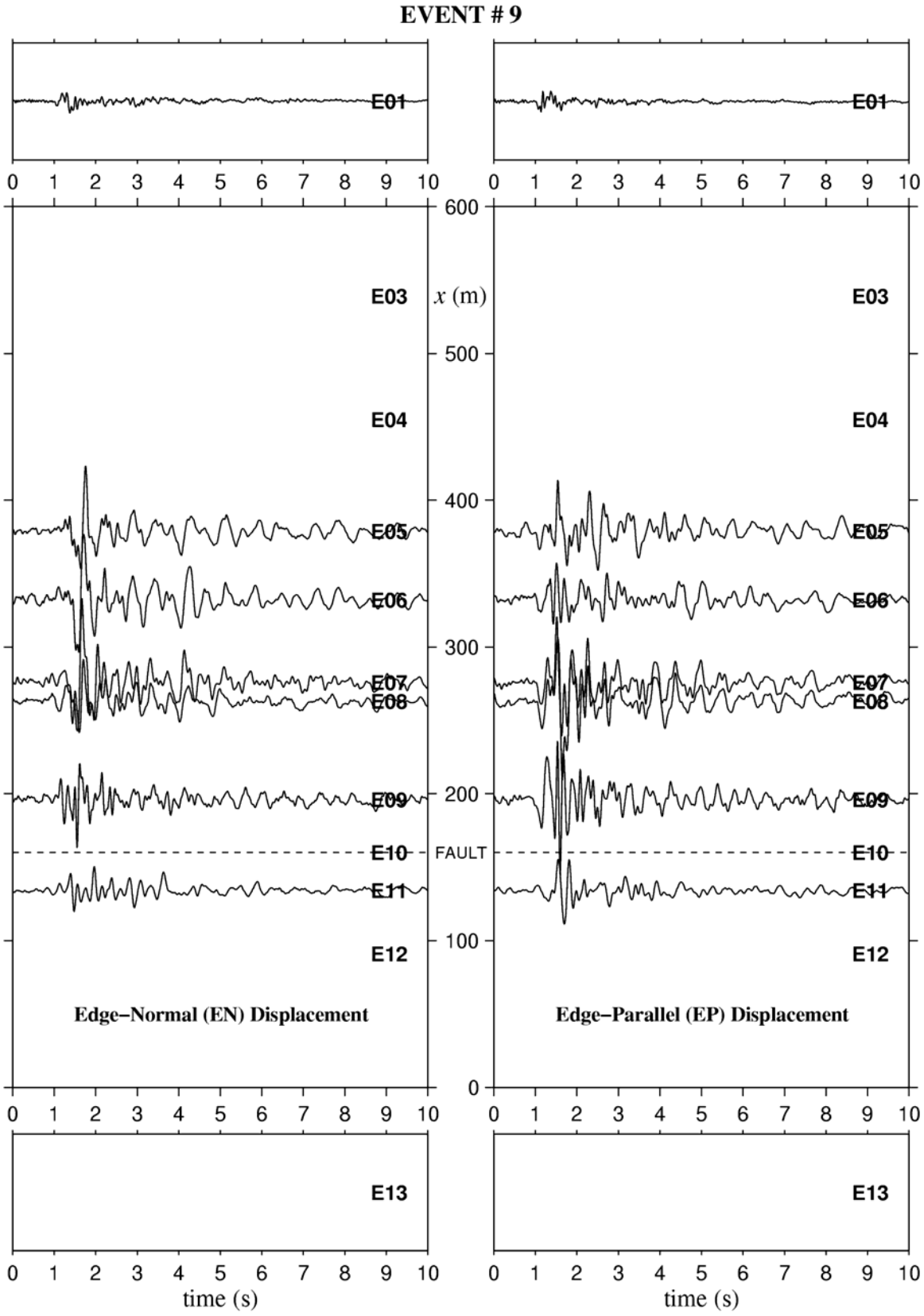

Figure A2.1.9. Shear-wave displacement from Event 9.

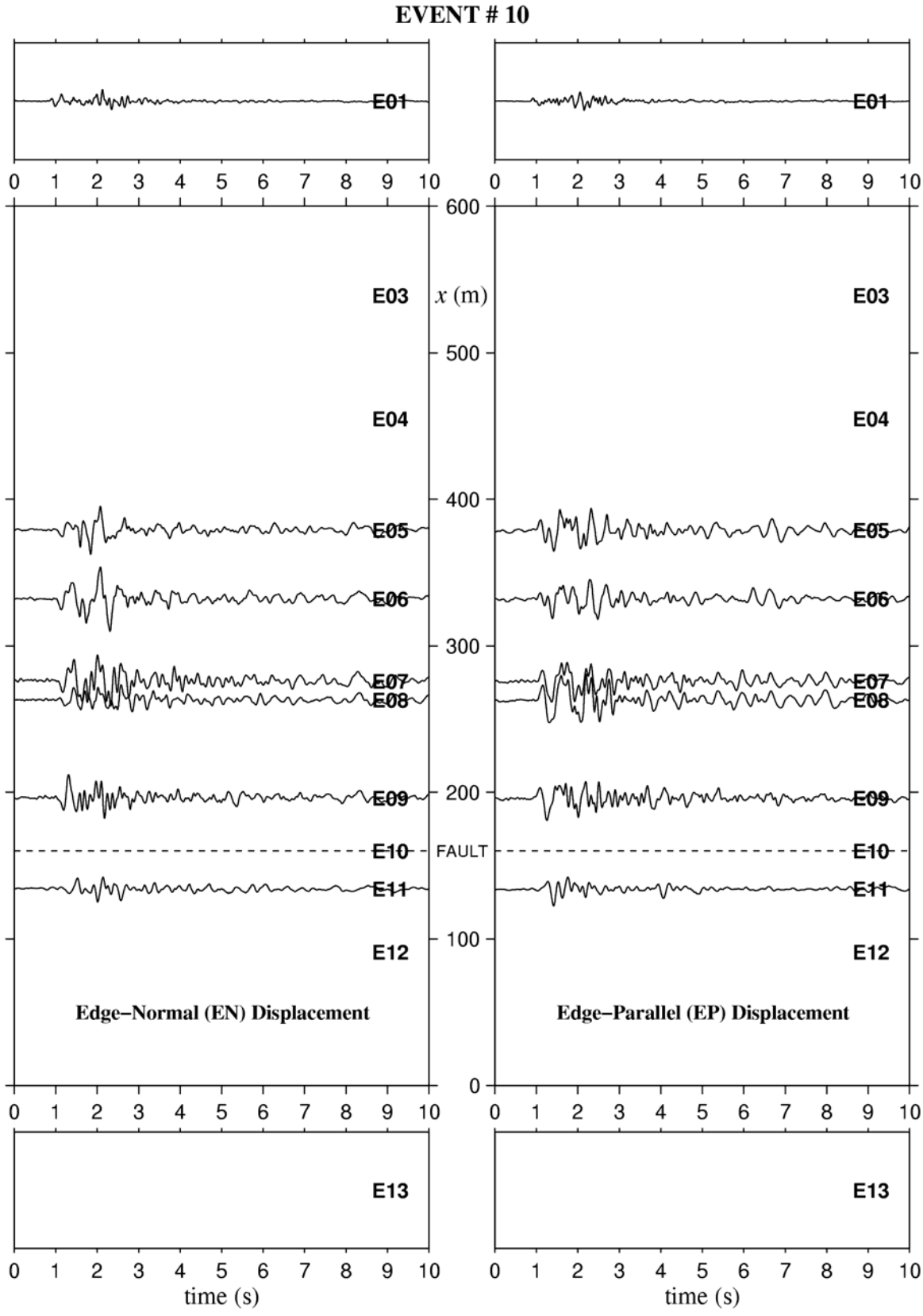

Figure A2.1.10. Shear-wave displacement from Event 10.

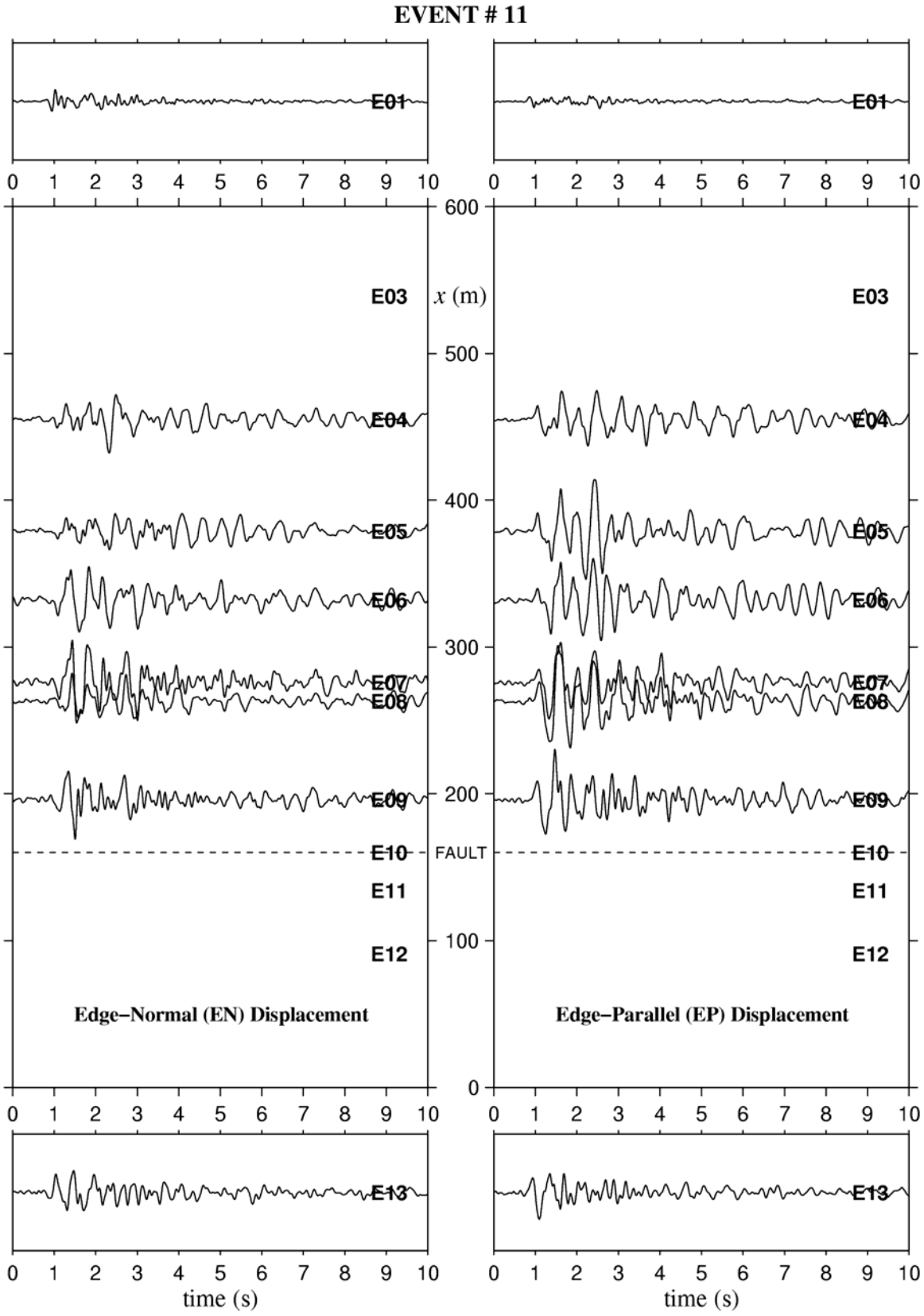

Figure A2.1.11. Shear-wave displacement from Event 11.

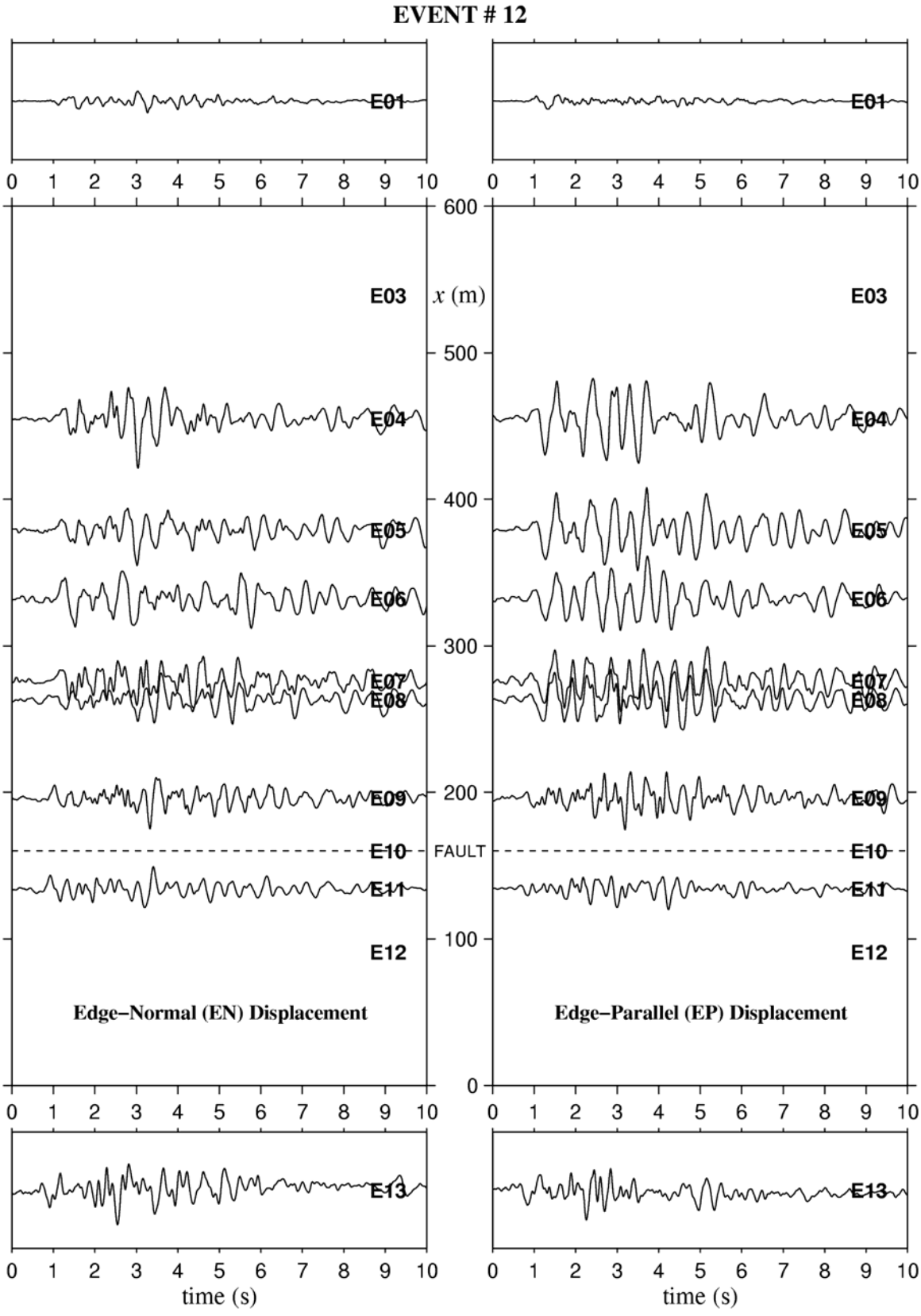

Figure A2.1.12. Shear-wave displacement from Event 12.

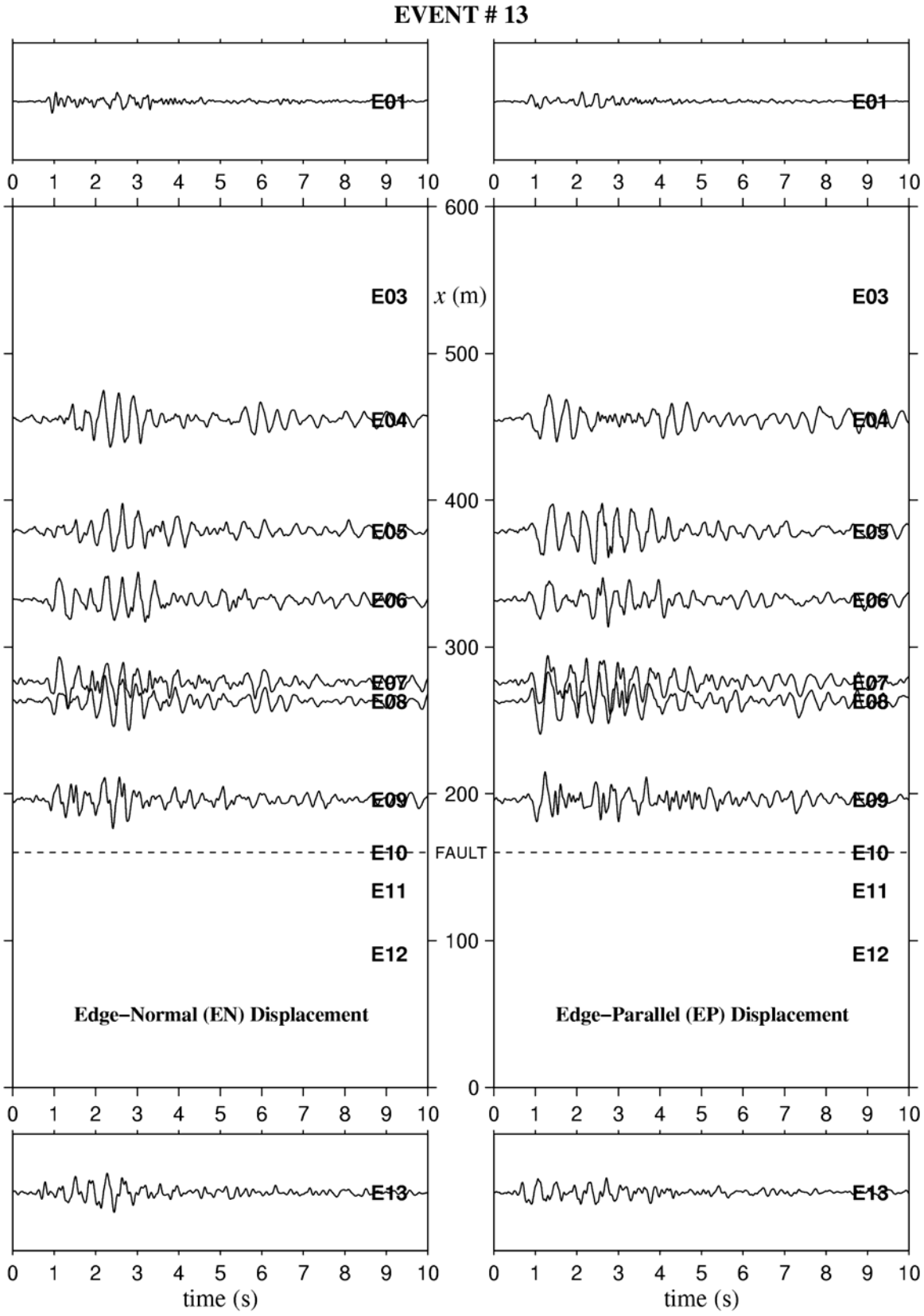

Figure A2.1.13. Shear-wave displacement from Event 13.

2.2 PEAK GROUND VELOCITY

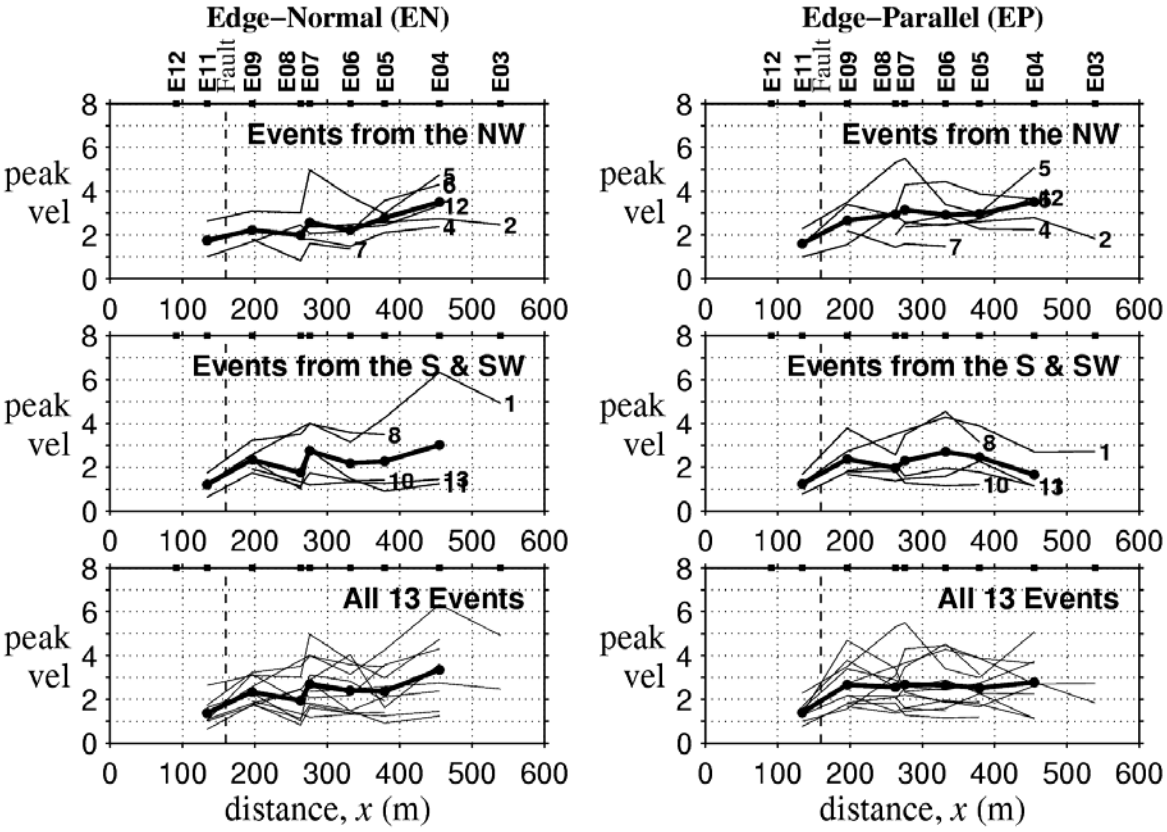

Figure A2.2.1. Peak ground velocity (PGV) across the array grouped by incoming azimuth. The dark line is an average of each plot. An average over all events is shown in the lower two plots. PGV is normalised against that recorded at E01.

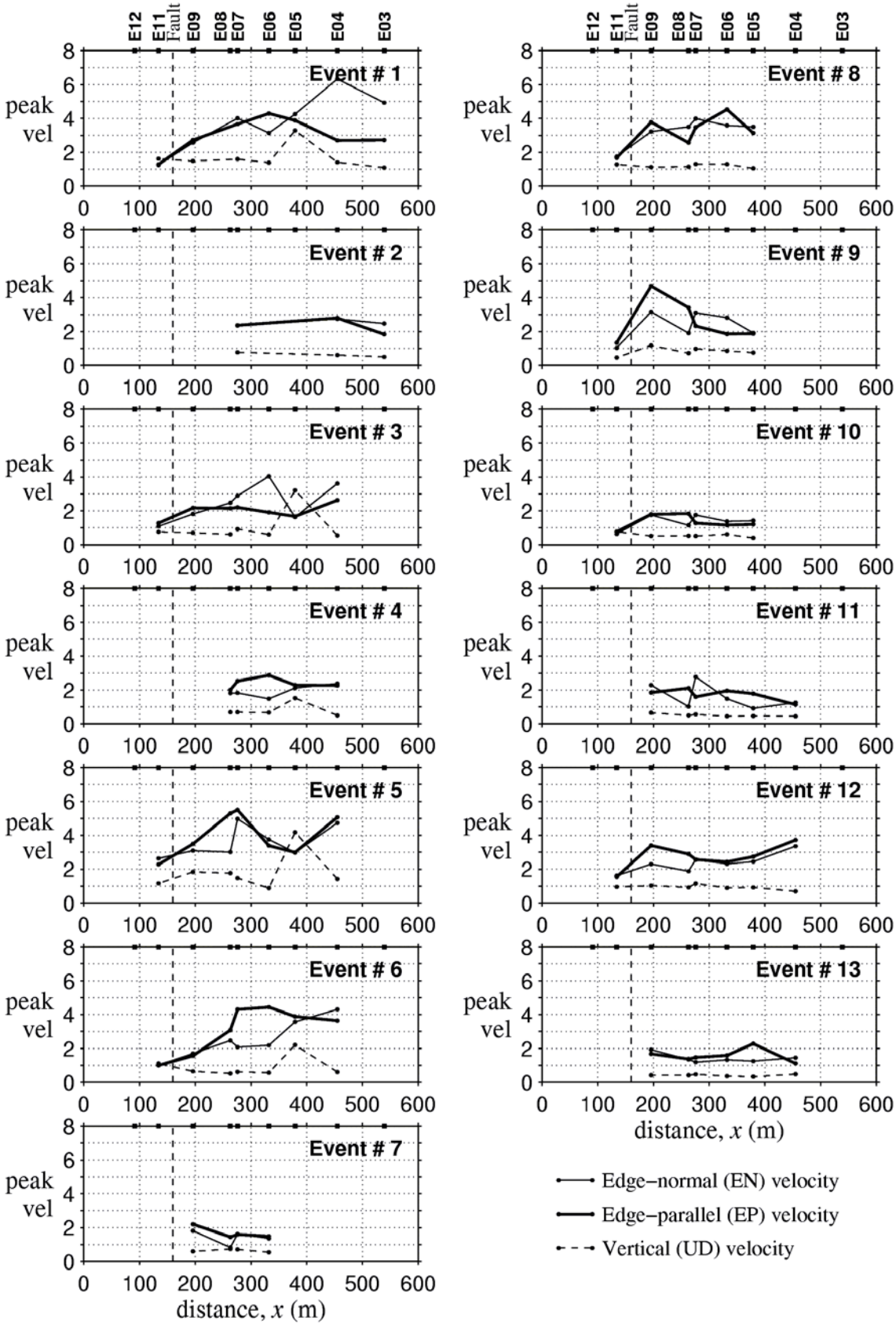

Figure A2.2.2. EN, EP and UD components of peak ground velocity (PGV) plotted against distance across the array for each event. PGV is normalised against that recorded at E01.

2.3 GROUP VELOCITY ESTIMATES

Figures A2.3.1 – A2.3.4. Bandpassed edge-parallel velocity records from Events 3, 11 and 12 plotted with respect to distance out from the fault trace, such that the movement of wave packets may be tracked across the array to give a group velocity at each frequency. A full set of graphs used to calculate data for the construction of Figure 9.16 is shown here.

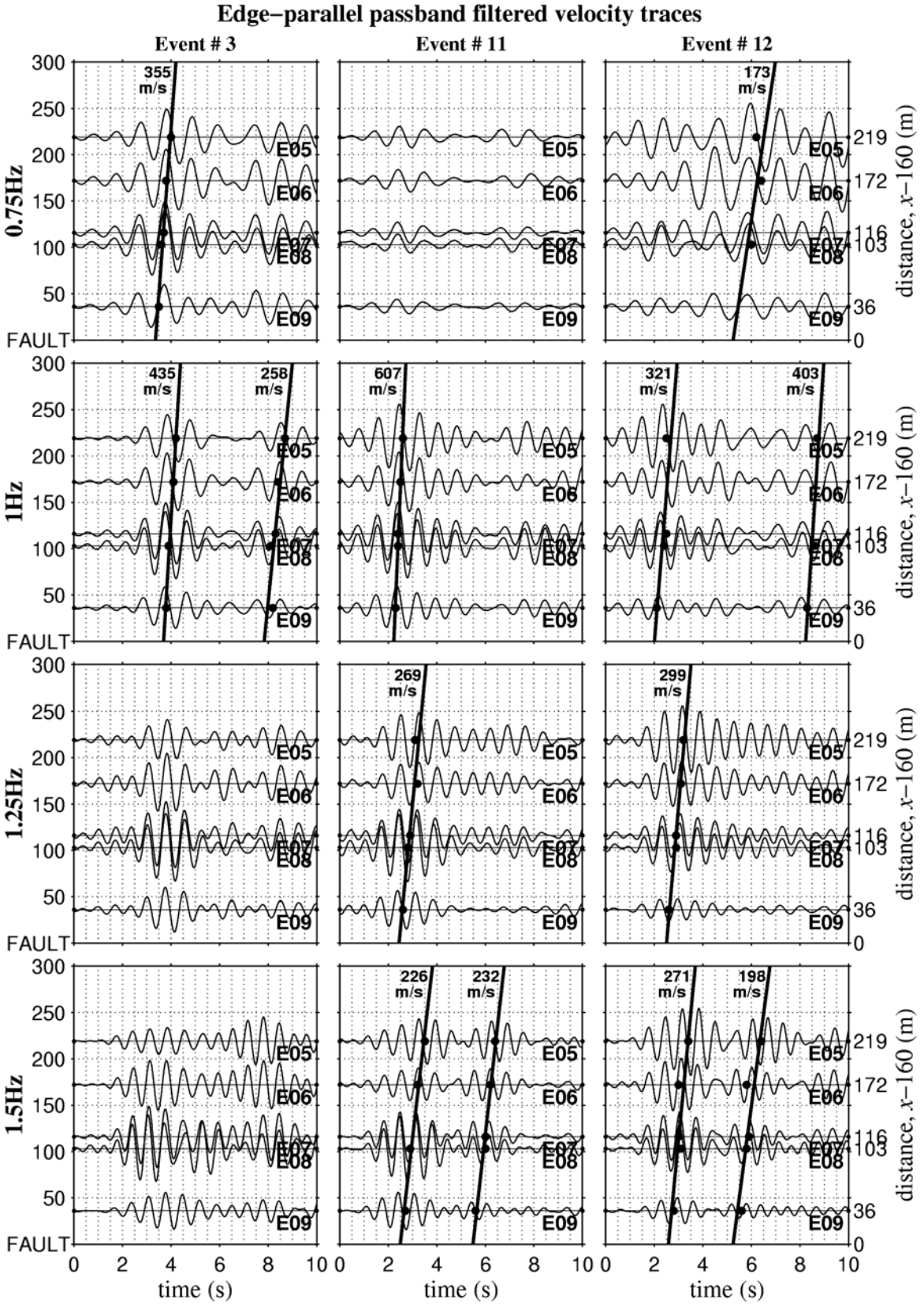

Figure A2.3.1. Group velocities for 0.75, 1.00, 1.25 and 1.50Hz.

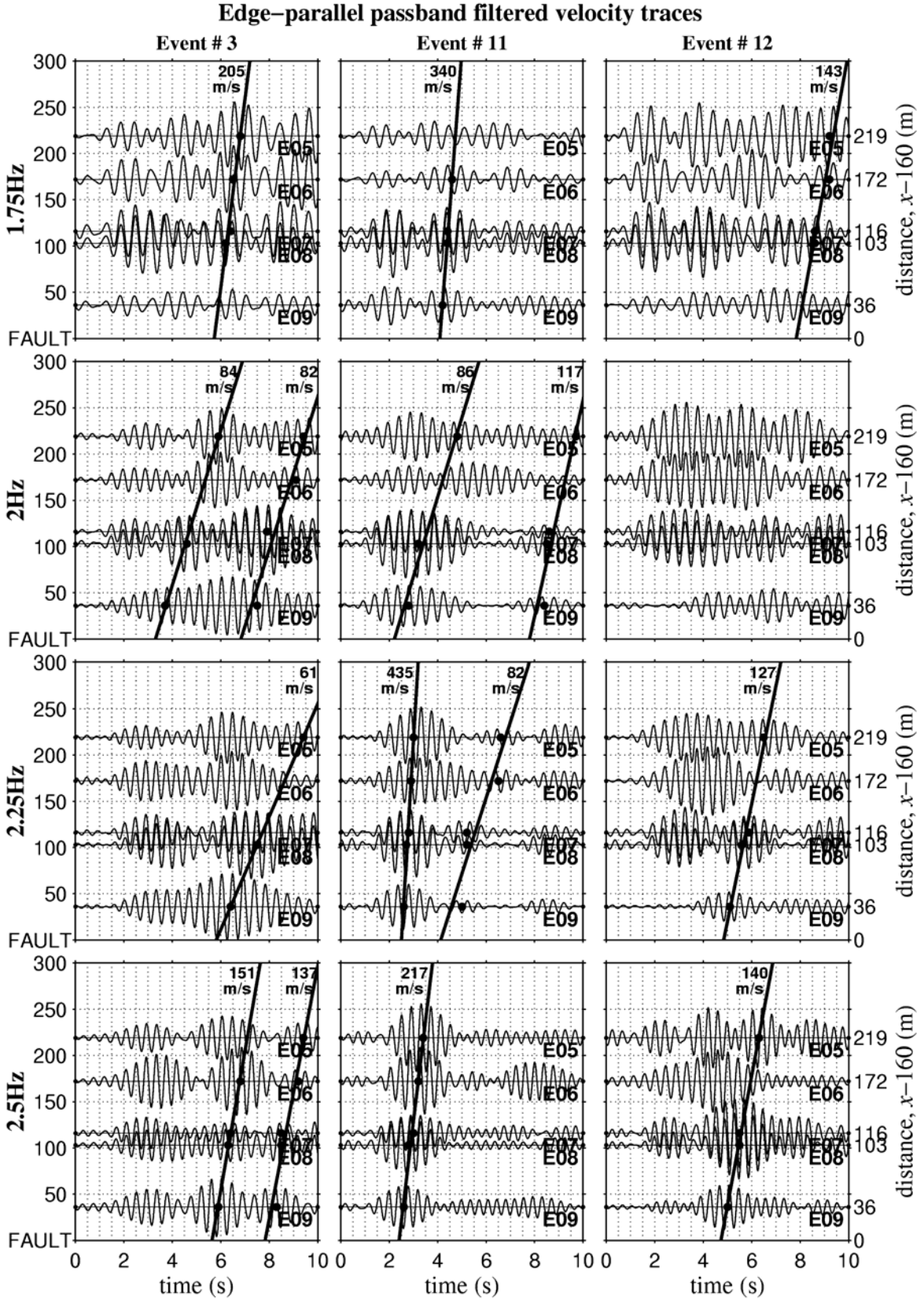

Figure A2.3.2. Group velocities for 1.75, 2.00, 2.25 and 2.50Hz.

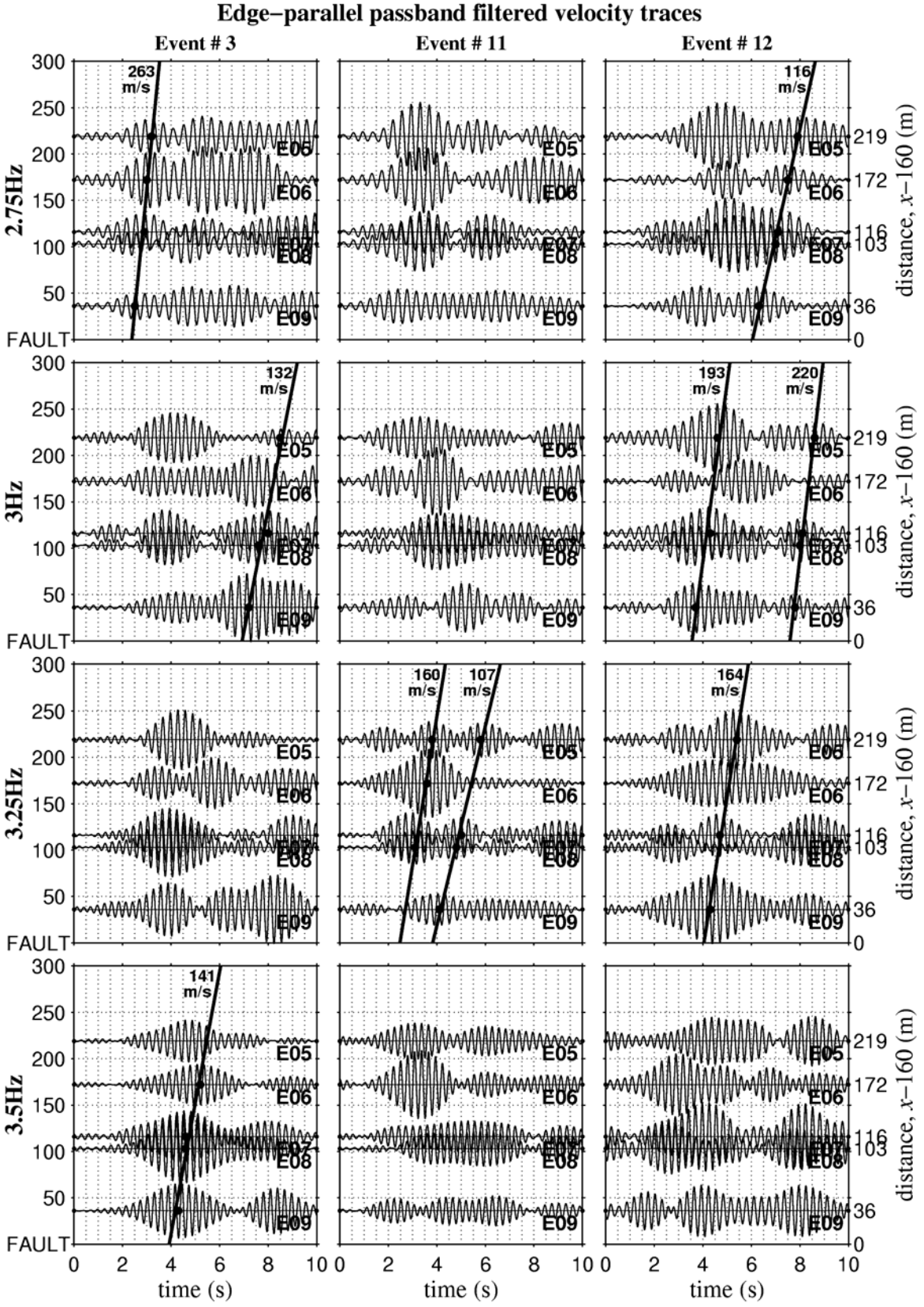

Figure A2.3.3. Group velocities for 2.75, 3.00, 3.25 and 3.50Hz.

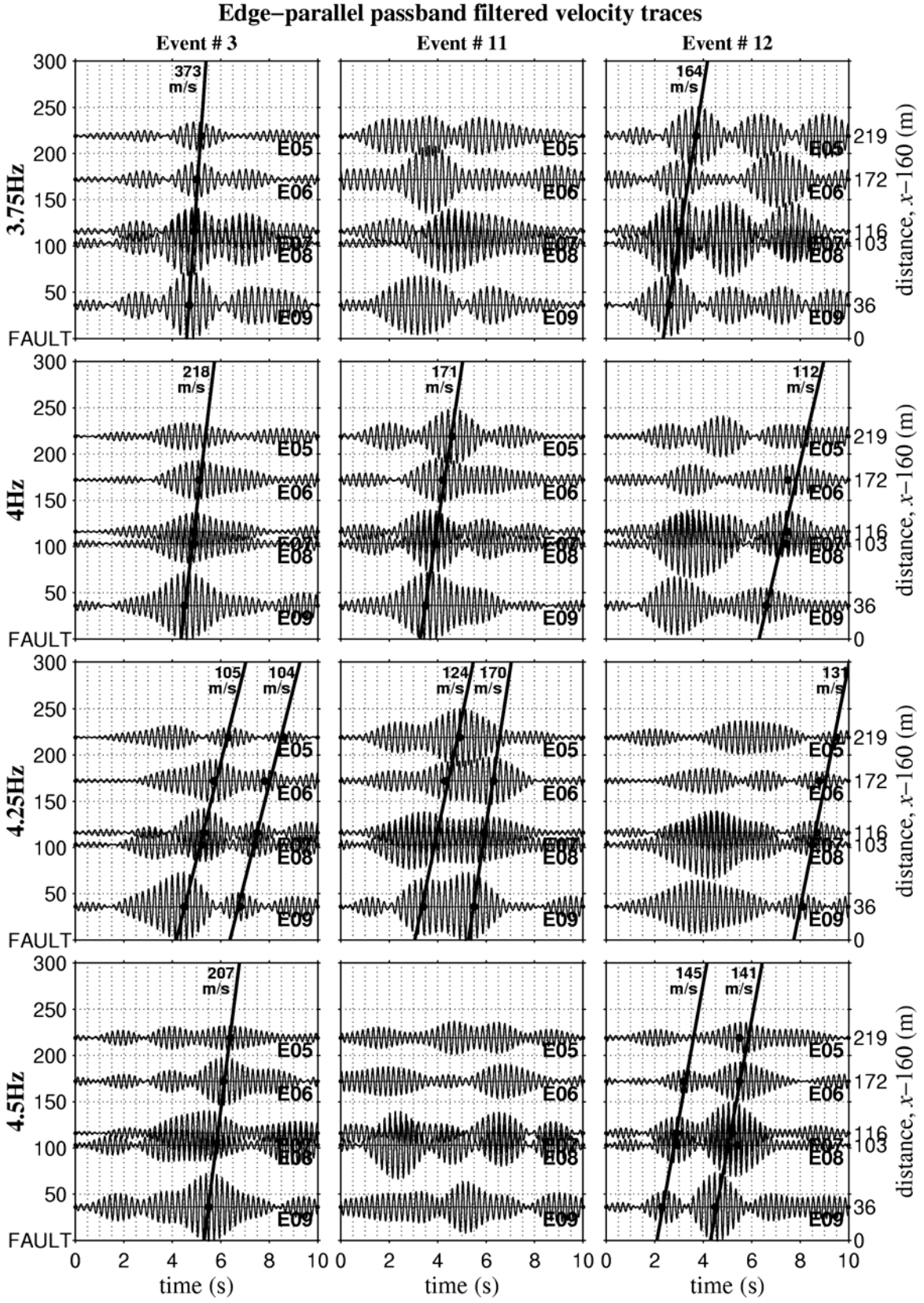

Figure A2.3.4. Group velocities for 3.75, 4.00, 4.25 and 4.50Hz.

2.4 SPECTROGRAMS OF DISPLACEMENT

Figures A2.4.1 – A2.4.13. Spectrograms showing the transient Fourier amplitude spectra (FAS) of the displacement traces presented in Appendix 2.1. Calculated with a 1.0 second moving Hanning window. Instantaneous FAS has been normalised against the peak of the horizontal components at Station E01. Contours of Fourier amplitude at Station E01 are at intervals of 0.1, while at intervals of 0.5 elsewhere.

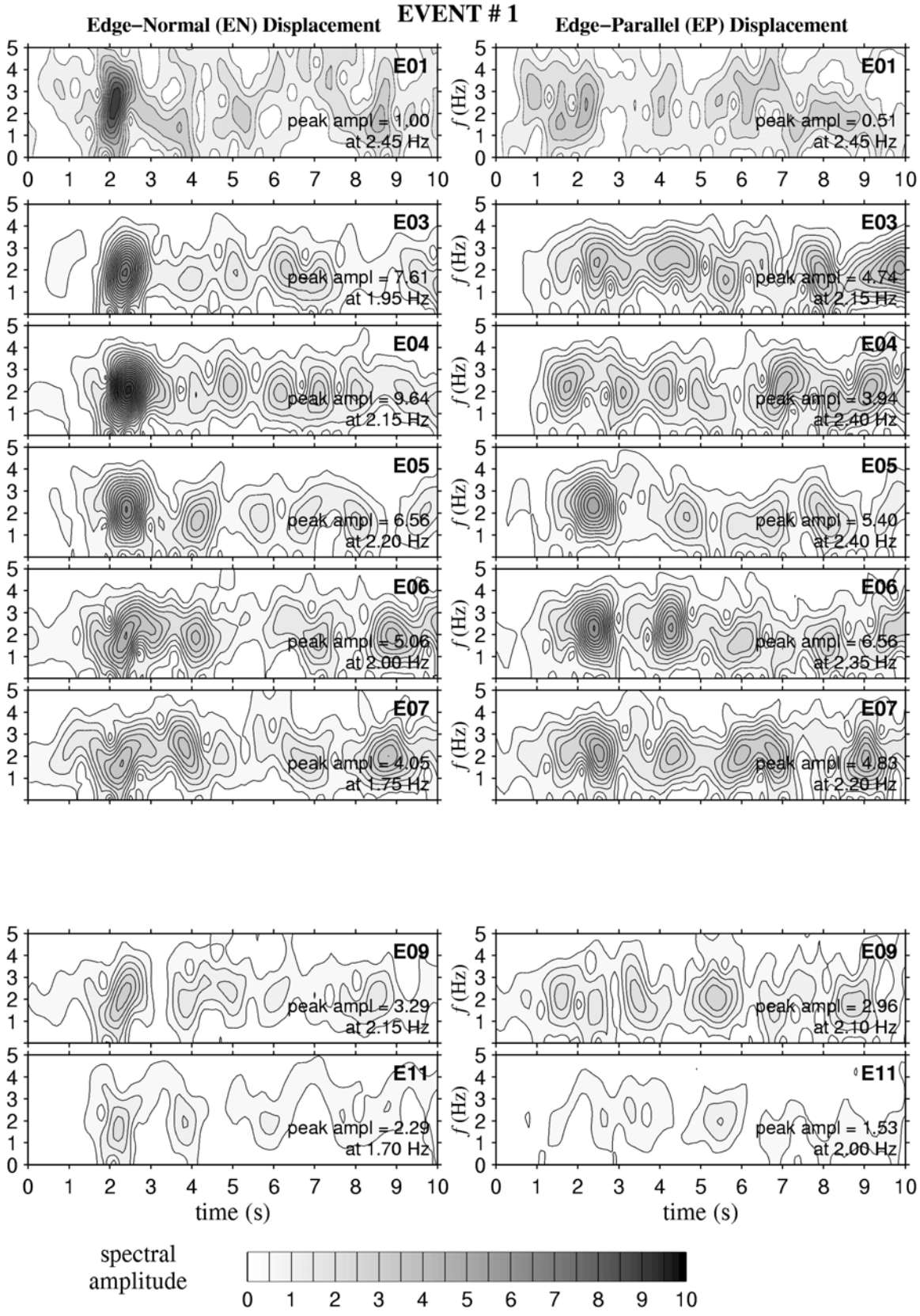

Figure A2.4.1. Spectrograms from Event 1.

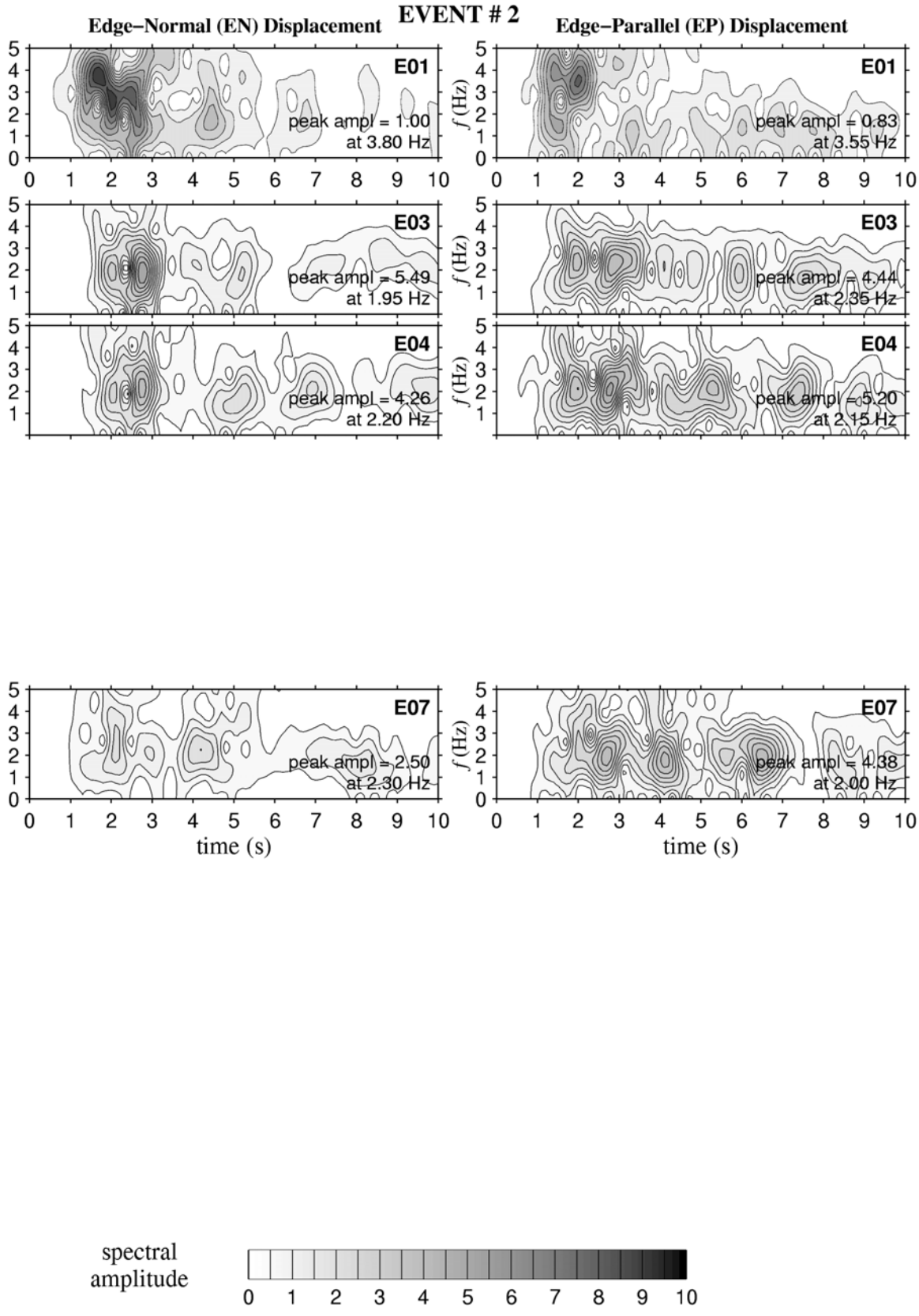

Figure A2.4.2. Spectrograms from Event 2.

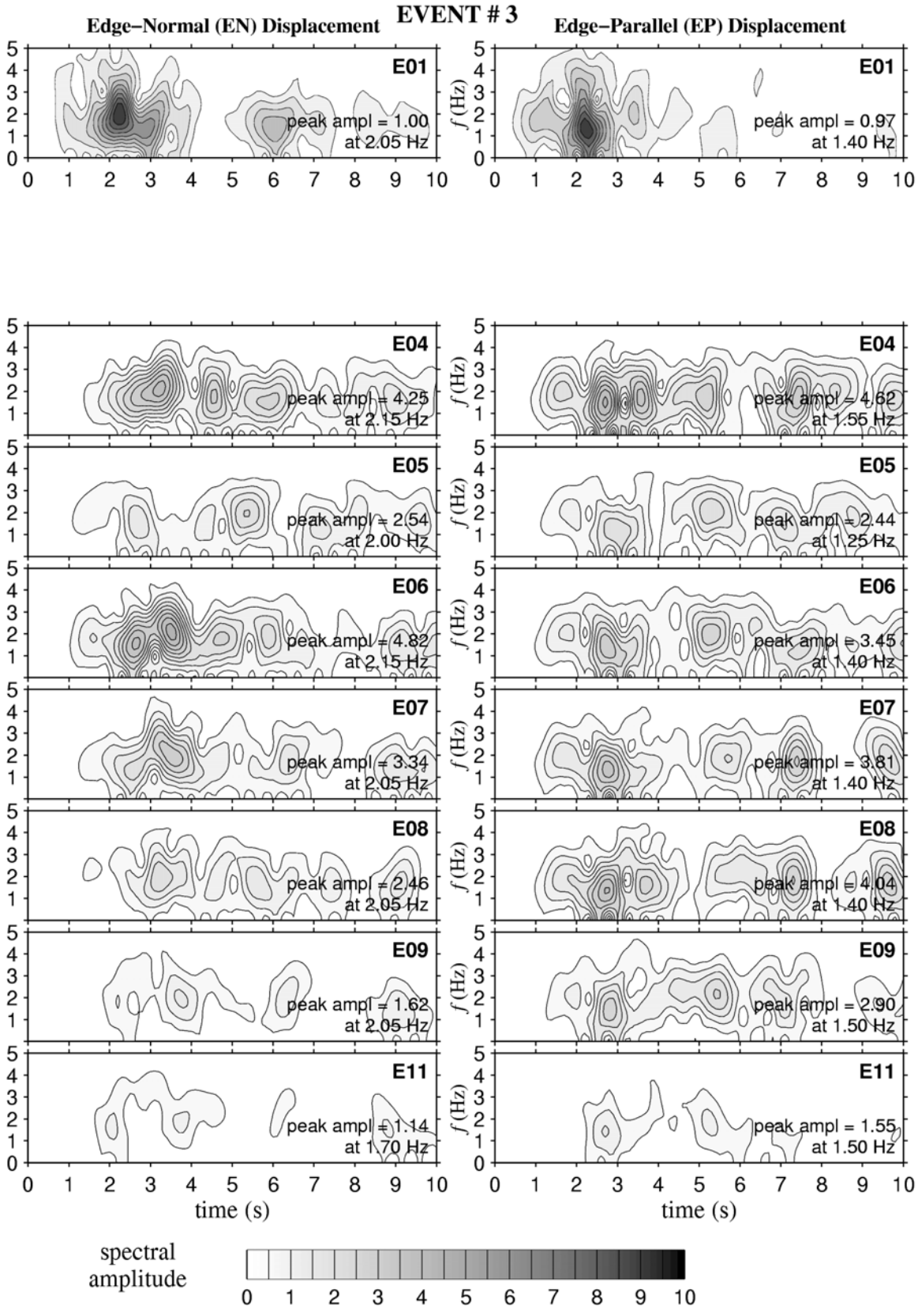

Figure A2.4.3. Spectrograms from Event 3.

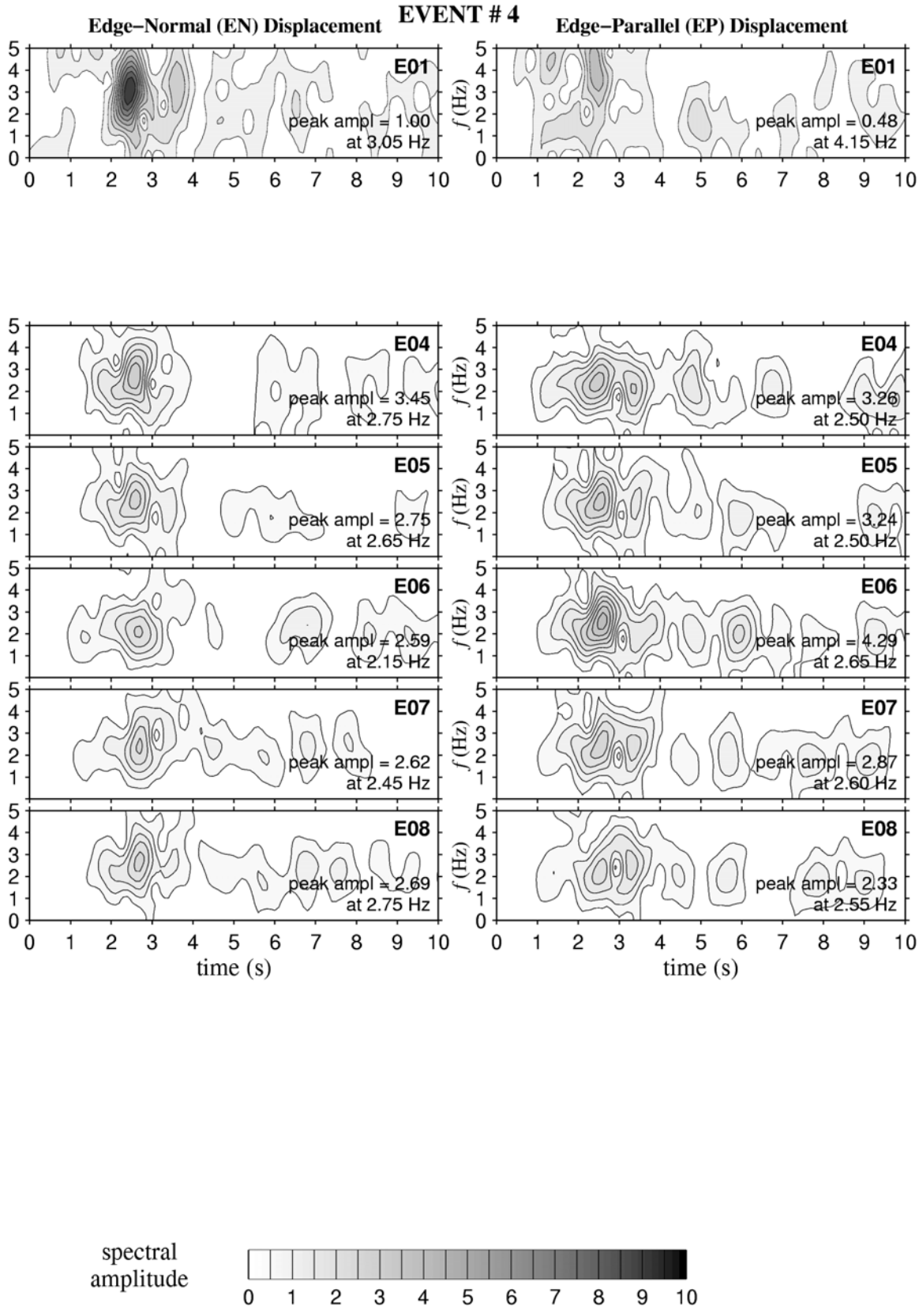

Figure A2.4.4. Spectrograms from Event 4.

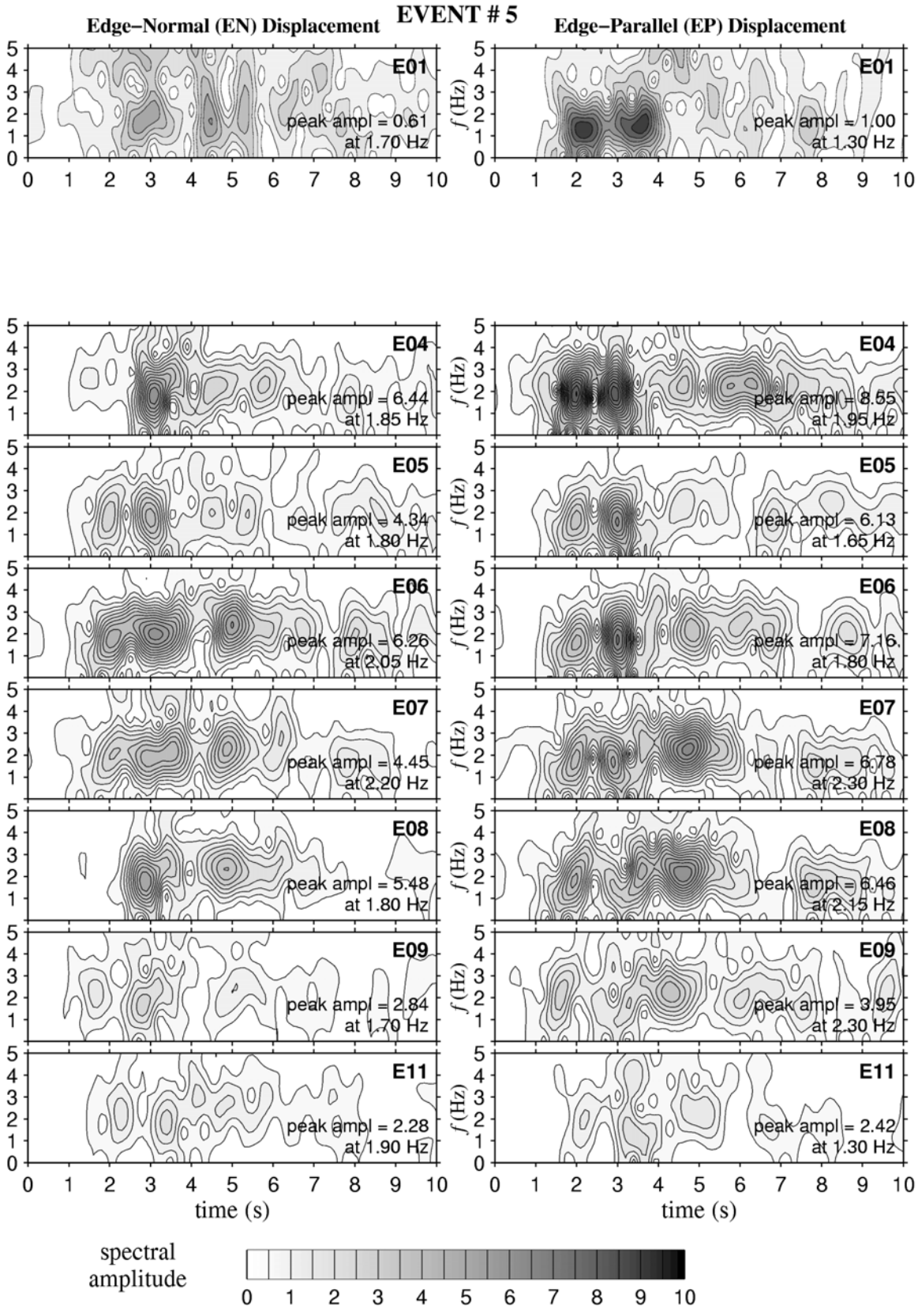

Figure A2.4.5. Spectrograms from Event 5.

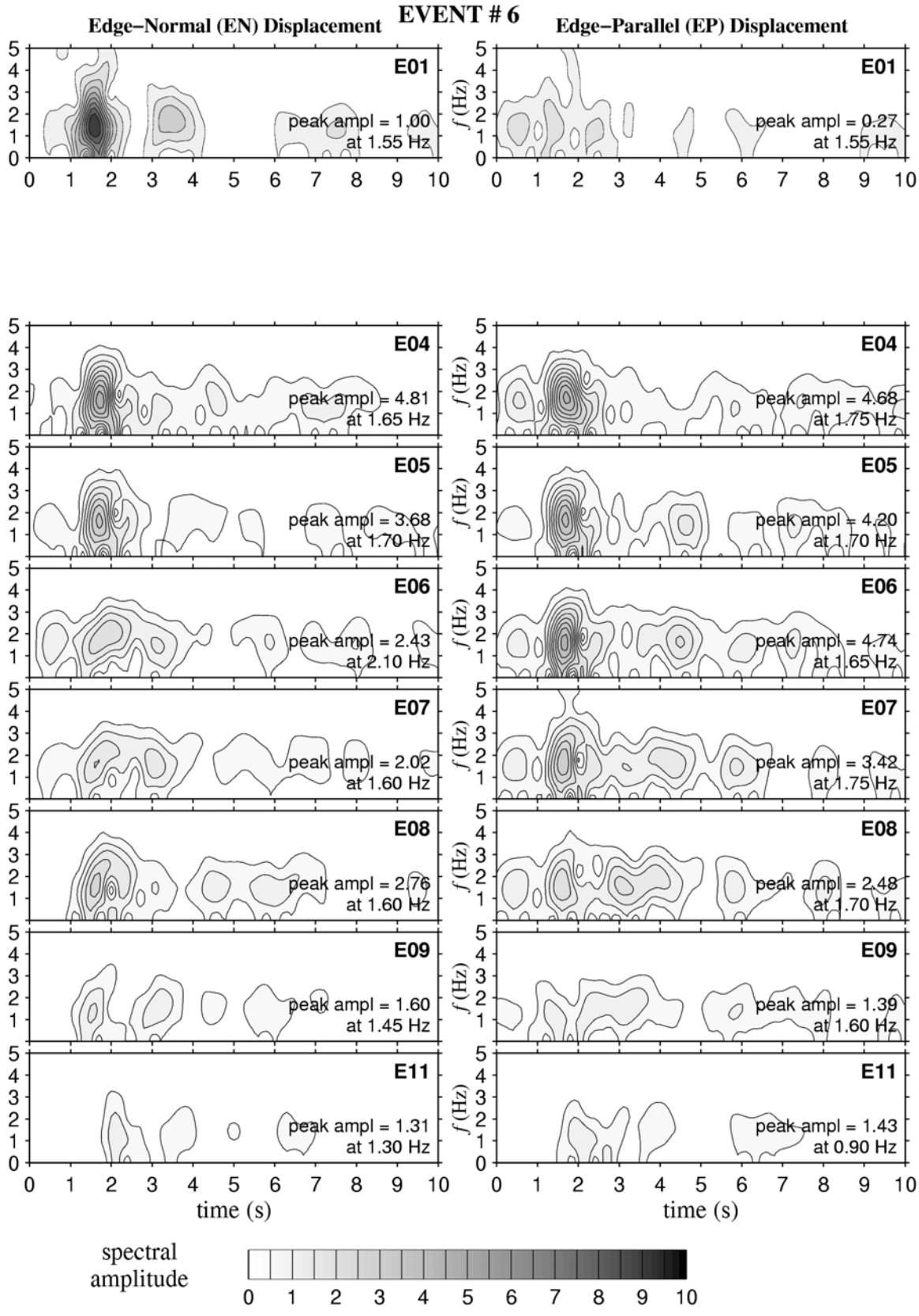

Figure A2.4.6. Spectrograms from Event 6.

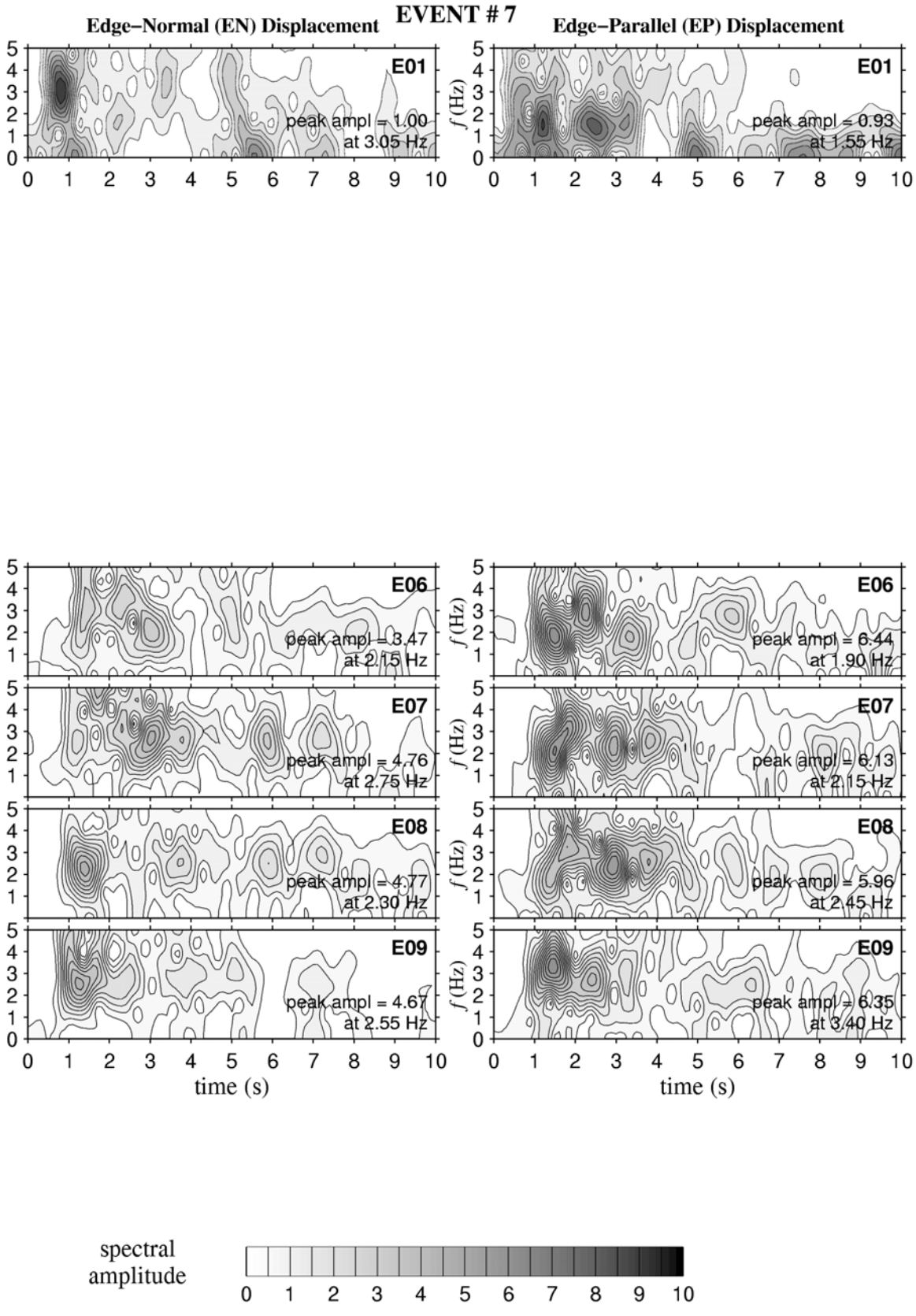

Figure A2.4.7. Spectrograms from Event 7.

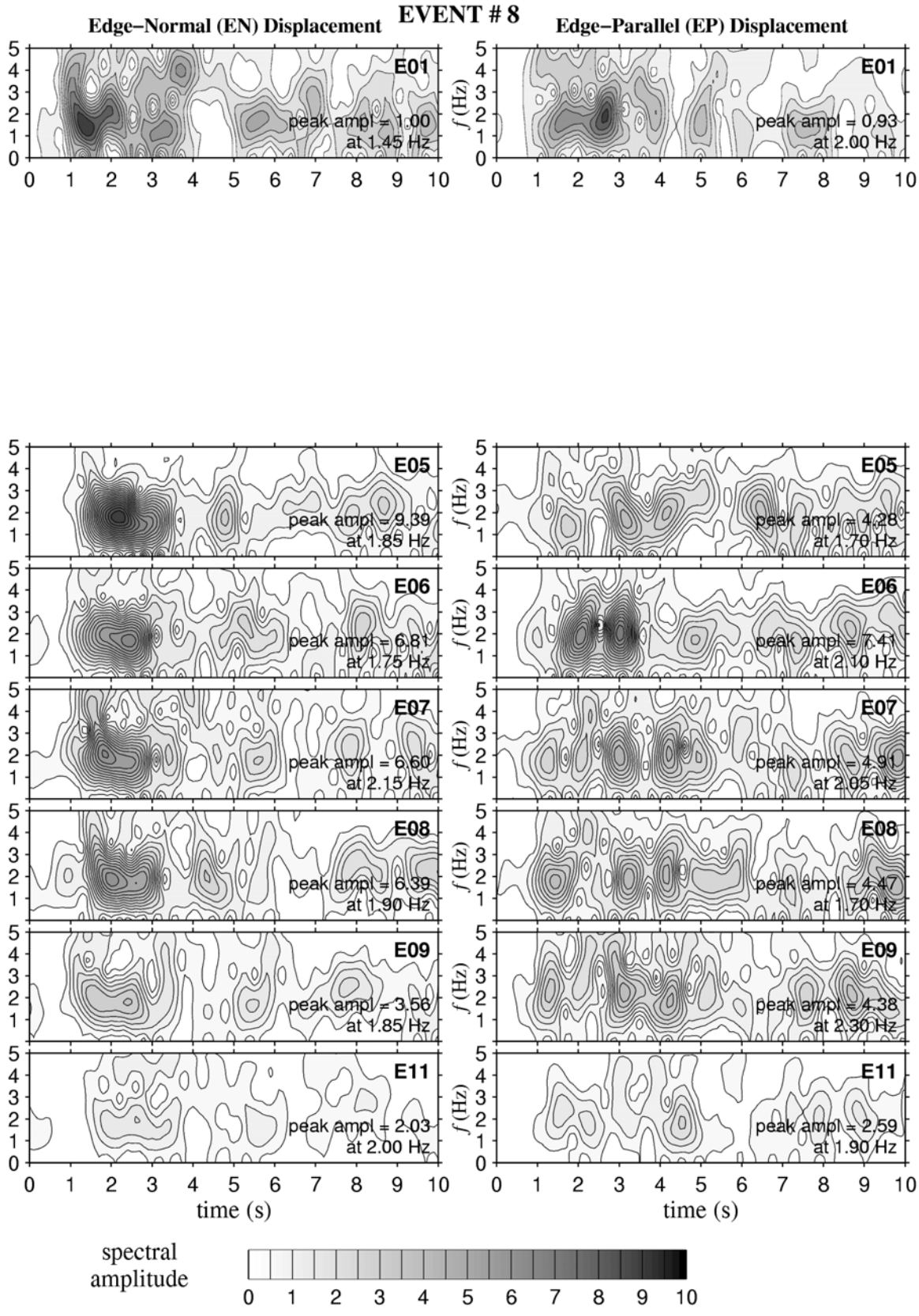

Figure A2.4.8. Spectrograms from Event 8.

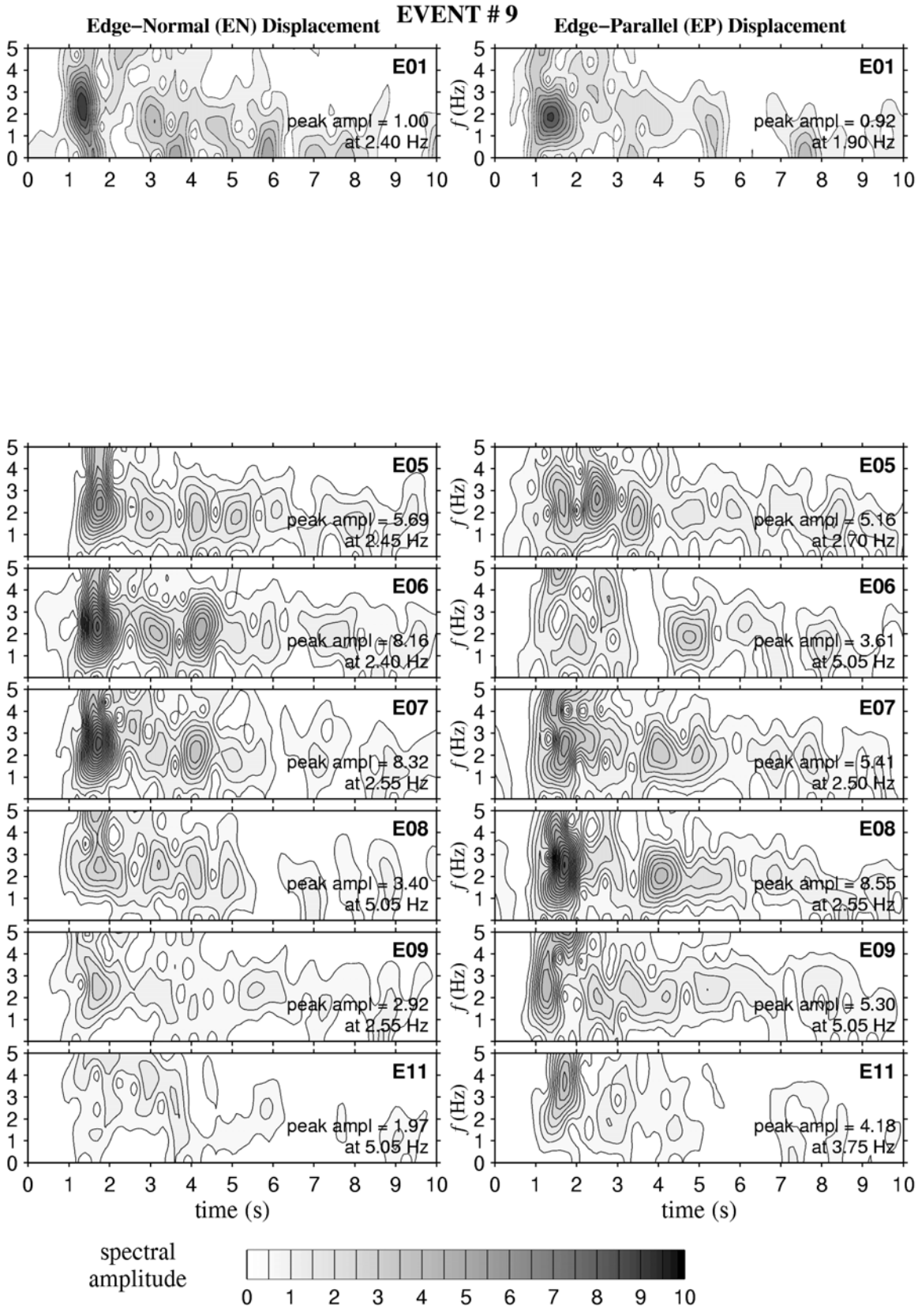

Figure A2.4.9. Spectrograms from Event 9.

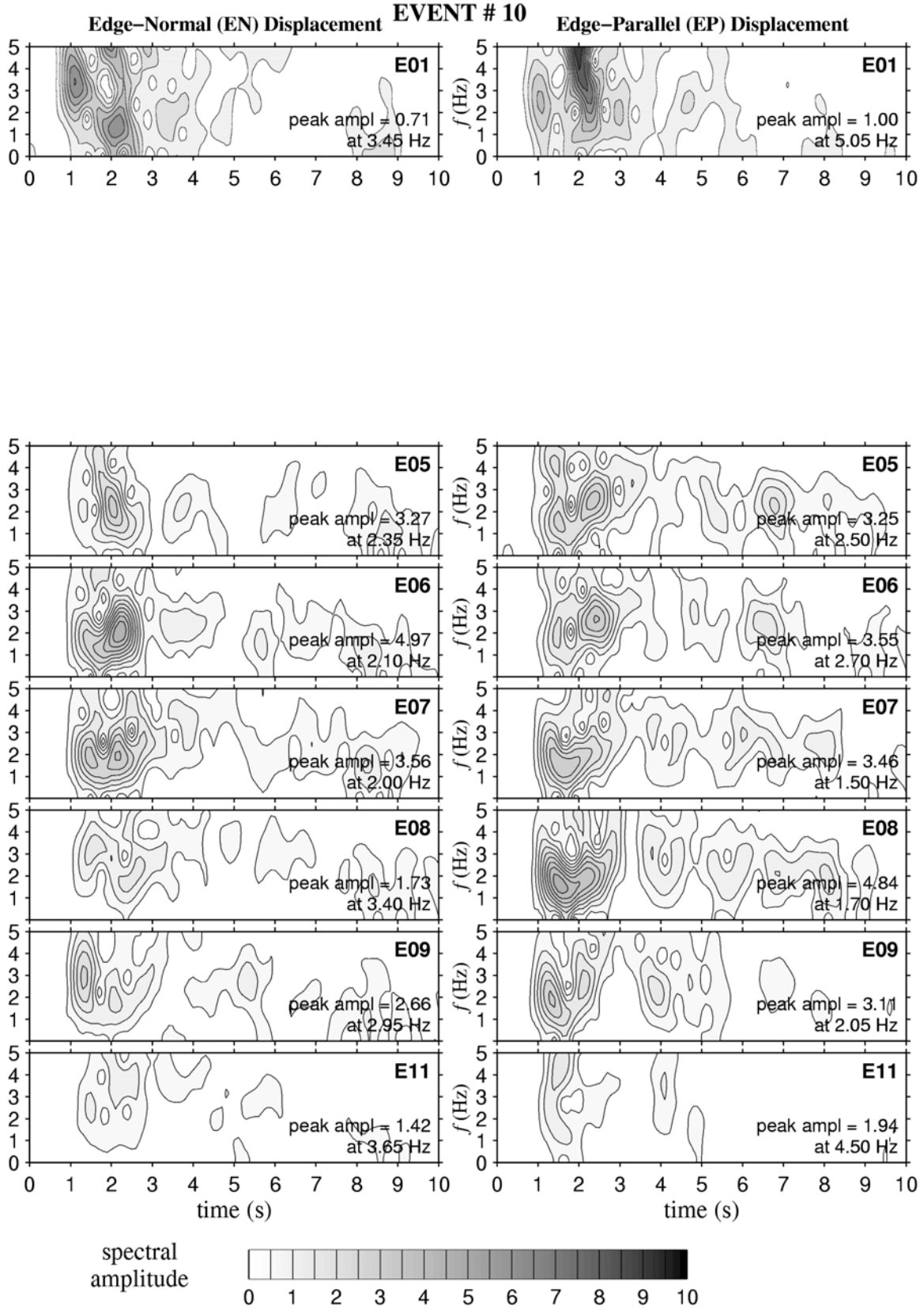

Figure A2.4.10. Spectrograms from Event 10.

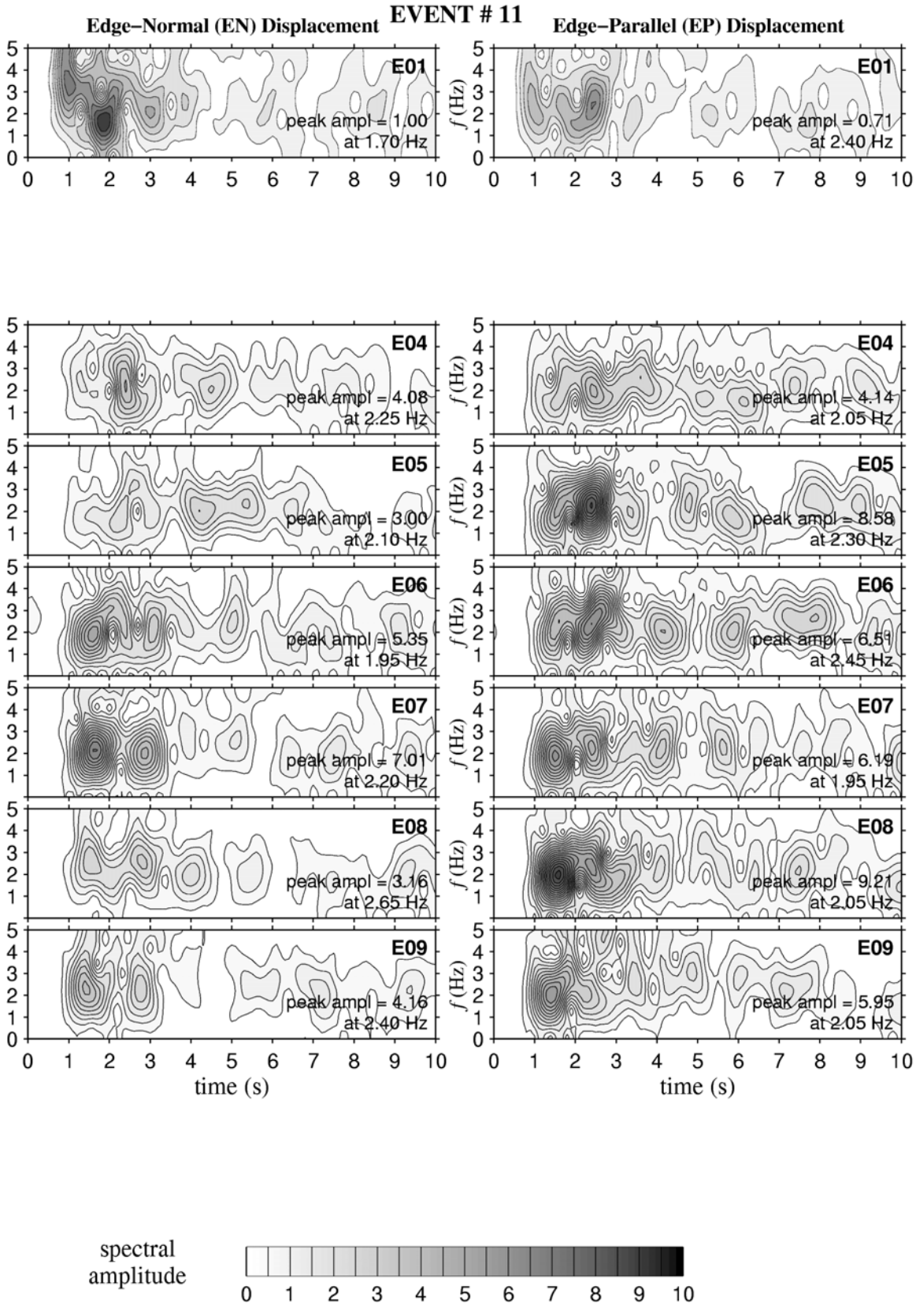

Figure A2.4.11. Spectrograms from Event 11.

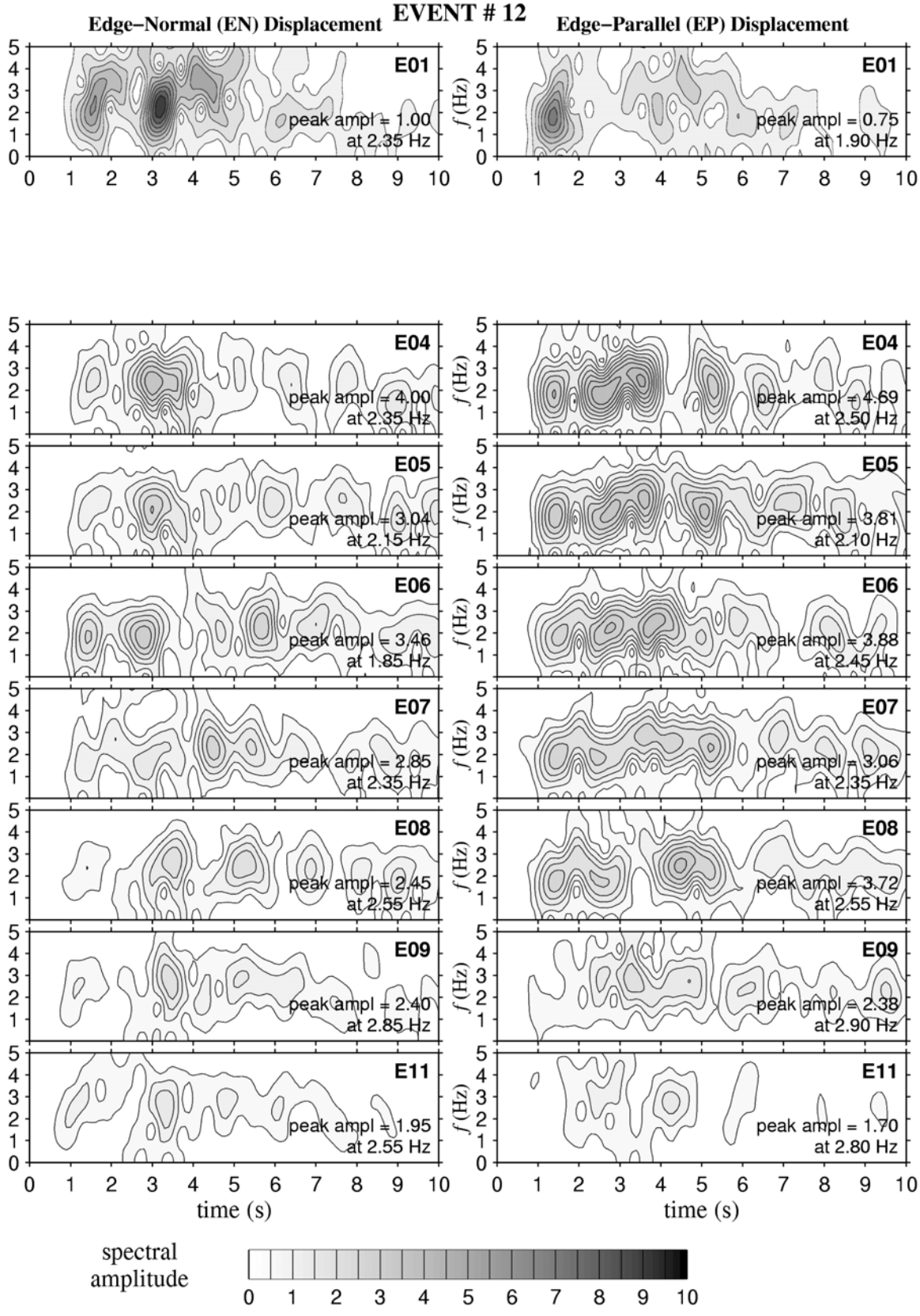

Figure A2.4.12. Spectrograms from Event 12.

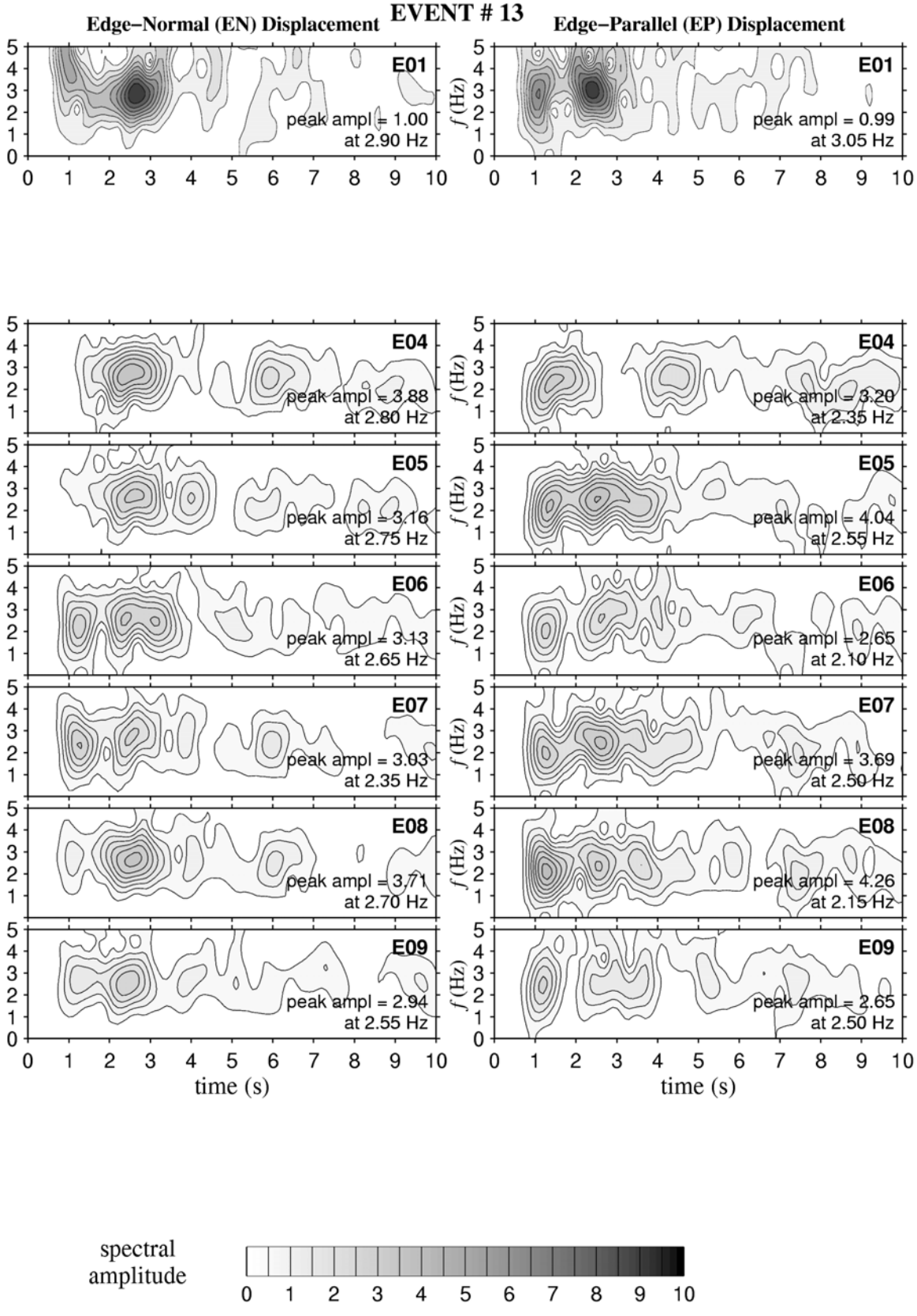

Figure A2.4.13. Spectrograms from Event 13.